16 State House Station
Augusta, Maine 04333

MaineDOT

Transportation Research Division

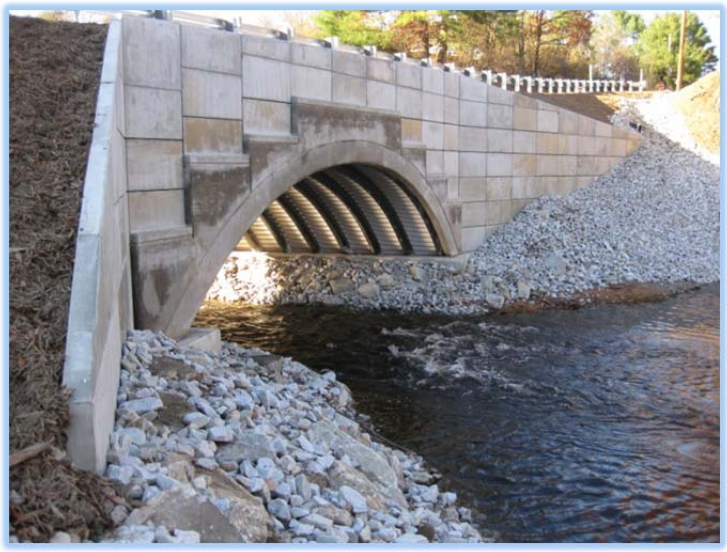

Technical Report 16-04

Bridge-in-a-Backpack™

Task 3.3: Investigate Soil-Structure Interaction – Modeling and Experimental Results of Concrete Filled FRP Tube Arches

Final Report – January 2016

Technical Report Documentation Page

1. Report No. ME 16-04	2.	3. Recipient's Accession No.	
4. Title and Subtitle Bridge-in-a-Backpack™ Task 3.3: Investigating Soil – Structure Interaction – Modeling and Experimental Results of the concrete filled FRP tubes arches.		5. Report Date December 2015 6.	
7. Author(s) Harold J. Walton, Ph.D. Candidate Bill Davids, Ph.D., P.E. Melissa Maynard, Ph.D		8. Performing Organization Report No. Report Number: 16-13-1023C	
9. Performing Organization Name and Address University of Maine – Advanced Structures and Composites Center		10. Project/Task/Work Unit No. Project 17891.00 – Task 3.3 11. Contract © or Grant (G) No. Contract # 20111223*2878	
12. Sponsoring Organization Name and Address Maine Department of Transportation		13. Type of Report and Period Covered 14. Sponsoring Agency Code	
15. Supplementary Notes			

16. Abstract (Limit 200 words)

This report includes fulfillment of Task 3.3 of a multi-task contract to further enhance concrete filled FRP tubes, or the Bridge in a Backpack. Task 3 is an investigation of soil-structure interaction for the FRP tubes. Task 3.3 is the modeling and experimental results of the concrete filled FRP tube arches.

This report presents experimental results and numerical analysis for short-span buried composite arch bridges whose main structural members are concrete-filled fiber reinforced polymer (FRP) tube arches (CFFTs). This investigation focuses on soil-structure interaction of the bridge system to expand understanding beyond isolated arch performance. Soil plays several roles: weight on the structure, restraining arch movement, and dissipating surficial truck loads.

Investigation focused on experimental and numerical analysis of subscale bridge systems. Four bridge systems were constructed with two different span-to-rise ratios (5:1 and 2.67:1) and two different materials (linear-elastic steel and CFFT). Tested systems were half-scaled from commercial bridge dimensions, and cross sectional properties were selected for scaled for the same lateral earth pressure coefficient under service loading.

17. Document Analysis/Descriptors Arch bridges, concrete filled FRP tubes, soil-structure interaction, Bridge-in-a-Backpack		18. Availability Statement	
19. Security Class (this report)	20. Security Class (this page)	21. No. of Pages 311	22. Price

Bridge-in-a-Backpack™

Task C (Deliverable 3): Behavior of Buried Composite Arch Bridges

Prepared for:

Dale Peabody P.E.
Director Transportation Research
Maine Dept. of Transportation
16 State House Station
Augusta, ME 04333-0016

University of Maine's Advanced Structures and Composites Center

Report Number: 16-13-1023C

December 17, 2015

Prepared by:

Harold Walton
Project Graduate Student and
Structural Engineer, HNTB, Westbrook, ME

Reviewed by:

Bill Davids, PhD PE
Professor and Chair
UMaine Civil Engineering

Melissa Landon, PhD
Associate Professor
UMaine Civil Engineering

ACCREDITED

An ISO 17025 accredited testing laboratory, accredited by the International Accreditation Service

EXECUTIVE SUMMARY

This report presents experimental results and numerical analysis for short-span buried composite arch bridges whose main structural members are concrete-filled fiber reinforced polymer (FRP) tube arches (CFFTs). This investigation focuses on soil-structure interaction of the bridge system to expand understanding beyond isolated arch performance. Soil plays several roles: weight on the structure, restraining arch movement, and dissipating surficial truck loads.

Investigation focused on experimental and numerical analysis of subscale bridge systems. Four bridge systems were constructed with two different span-to-rise ratios (5:1 and 2.67:1) and two different materials (linear-elastic steel and CFFT). Tested systems were half-scaled from commercial bridge dimensions, and cross sectional properties were selected for scaled for the same lateral earth pressure coefficient under service loading.

Bridges were placed in a self-reacting timber soil box and were backfilled with compacted granular fill in alternating lifts to an elevation 610 mm above the apex. Bridges were subject to a series of live loads across the middle 60% of the span of the arches, replicating truck loading. Bridges were loaded at the apex until failure to find the capacity of the buried arch system.

The experimental testing process was numerically replicated with two finite element solvers: a soil-spring model implemented for design of commercial CFFT arch bridges and a soil-continuum model that mimics the governing physics. The soil-spring model separates vertical applied force (soil weight, surficial live loads) and horizontal soil resistance (deflection dependent soil springs). The soil-continuum model uses depth-dependent elastic moduli and

Mohr-Coulomb plasticity to model soil restraint and dilation in high-shear regions. Soil-structure interaction was governed by hard normal contact and frictional tangential contact.

The soil-spring model was conservative yet adequate for most of the experimental backfilling and live load steps. Negative foundation moment in a short rise arch due to 60% offset load was excessively conservative and warrants future consideration. The continuum model was more accurate for live load moments away from the point of load, but was unconservative in several tests for peak positive moment. The continuum model proved impractical as a design tool due to cost, development time, and run time.

TABLE OF CONTENTS

LIST OF TABLES

LIST OF FIGURES

CHAPTER 1. INTRODUCTION

1.1. Introduction

Concrete filled fiber reinforced polymer (FRP) tube (CFFT) arches are used as the main structural members in short span buried bridges (Bannon 2009, Dagher et al. 2012, Davids et al. 2012). Figure 1.1 illustrates the elements of the buried arch bridge system. Lightweight compared to traditional structural members, FRP shells provide tensile and hoop structural reinforcing for concrete and serve as stay in place formwork. Design of CFFT tubes for bridges is governed by a guide specification in AASHTO (2012). FRP also provides good environmental durability and is not subject to rust, potentially extending the lifespan of a bridge and reducing maintenance requirements. Soil adds structural capacity to a bridge system: it provides lateral restraint reducing arch deflections, and it distributes vehicular surface pressures over a larger area, reducing internal arch forces. However, soil also adds substantial dead load, typically higher load than service truck loads, and the progressive backfilling process may cause higher moments than the final soil configuration. Figure 1.2 shows a completed CFFT bridge in Bradley, Maine, during a live load test; the parallel CFFT arches are visible under the buried structure.

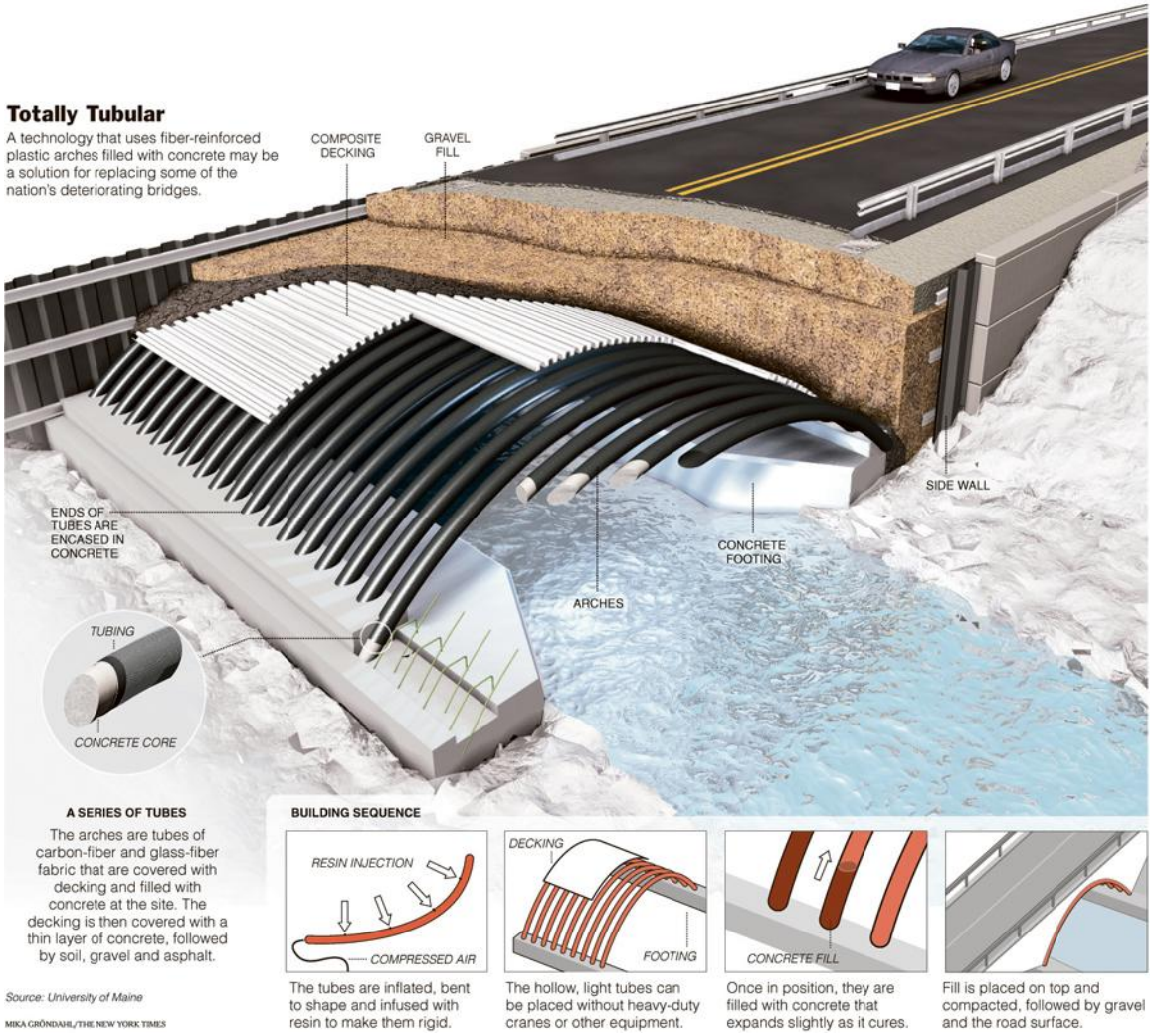

Figure 1.1. Composite Buried Bridge Components, the New York Times (2013)

Figure 1.2. Completed CFFT Bridge, Bradley, Maine

Prior research on the CFFT arch bridge system has focused on constructability of CFFT arches (El-Chiti 2004, Tomblin 2006), strength of individual CFFT members (Bannon 2009, Dagher et al. 2012), environmental durability of the FRP shell (Demkowicz 2011), and hollow capacity of the FRP shell as formwork (Walton 2011, Davids et al. 2012). Previous work has led to the development of a soil-spring model with nonlinear elastic arch and soil behavior. The model had been adapted to account for soil restraint based on the concept of soil springs used in retaining wall design (Barker et al. 1991). However, it is necessary to assess the behavior of the complete bridge system with multiple arches, decking, foundations, and soil and compare predictions of this soil-spring model with measured response. Prior field testing of full arch bridge systems suggests that current design practice is conservative and there is a need to improve the efficiency of the system by realistically assessing the structural role soil plays in a buried composite arch bridge (Quinn et al. 2013, Goslin et al. 2015). The objective of the research discussed in this report was to close the knowledge gap between behavior of an isolated

arch and behavior of the buried CFFT arch bridge system interacting with surrounding soil. This included verifying the use of soil-spring beam element modeling as an effective discretization method for buried CFFT arches.

Three approaches were used to investigate this problem: improvement to the current design method, relying on nonlinear soil springs, development of a 2D continuum-soil model using commercial finite element (FE) analysis, and experimental laboratory testing of four scaled arch bridge systems. Two of the scaled bridge systems were constructed using steel arches designed to remain in the linear elastic range for all loading cases other than ultimate apex load capacity. Steel arches provide reliable strain data and allow internal arch member force resultants to be accurately determined from test data, whereas CFFT arch behavior depends on prior concrete cracking, a highly localized and variable phenomenon that occurs at a low stress (CFFT arches begin to crack during backfilling). Steel arches were intended to provide a better basis for model comparison and evaluation.

1.2. Chapter Overviews

This report is divided into six main chapters. Two chapters address test development, two chapters address model development, and two chapters address test results and model comparisons.

1.2.1. Chapter 2. Scaling Procedure

Chapter 2 reports the scaling procedure for developing half-span arches to fit within limitations of available laboratory space. Testing is based on length scaling: span, rise and arch spacing are scaled uniformly for a typical 12.2 m bridge. Subscale material and cross sectional properties are chosen to produce the same lateral earth pressure coefficient, *K*, expected in a full-

scale structure. The response cannot be scaled for all load responses because of differing nonlinear relationships for the full scale and half scale bridges: the chosen load case for scaled response was the change in response due to an apex live load after completion of backfilling. Bridge response predictions needed to perform the scaling are developed with the soil-spring model discussed in detail in Chapter 4.

1.2.2. Chapter 3. Experimental Testing Procedures

Chapter 3 contains experimental testing procedures for the laboratory bridges. This chapter describes construction of a 12.2 m x 2.2 m x 3.9 m self-reacting timber soil box. Arches were fabricated, cast into concrete foundations, and placed in the soil box. Bridges were backfilled with soil in lifts alternating on each side of the bridge. Bridges were loaded with a series of seven uniform, full width, live loads evenly spaced over the middle 60% of the span, and were loaded to ultimate capacity at the apex. This chapter also describes instrumentation during testing.

1.2.3. Chapter 4. Soil-Spring Modeling

Chapter 4 details the development of the current design model and modifications to the model as part of the present research. The soil-spring model models progressive backfilling and subsequent live loading, with stored effects due to backfilling. The soil-spring model uses 1-dimensional beam and spring elements. The structural beam elements are given a nonlinear-elastic moment curvature relationship based on Burgueño's (1999) predicted response for axially loaded CFFT tubes filled with nonlinear concrete using a Mander (1988) model. Soil spring elements are given a nonlinear-elastic response based on traditional deflection-dependent retaining wall lateral earth pressures (Barker et al. 1991). New work on the CFFT model includes the development of a more representative foundation instead of simpler pinned at top of foundation and fixed at top of foundation models, expansion of the model to multiple soil

properties, and inclusion of large deformation analysis including a post-buckling solver to track failure response of steel arch bridges. Because all materials (arch, foundation, decking, and soil) in this model are nonlinear elastic (no plasticity) there is no hysteretic effect; the model returns to the end of backfilling base state after live load is removed.

1.2.4. Chapter 5. Soil-Continuum Modeling

Chapter 5 details the development of a 2D FE model for steel arch bridges. CFFT arches have a more complicated stress-strain relationship and are not modeled using this procedure at this time. Soil-continuum modeling allows the development of a more physically consistent soil model than used in soil-spring modeling. Soil is modeled using variable elastic modulus with depth based on Duncan-Selig values (Petersen et al. 2010). The soil is also given Mohr-Coulomb plasticity that allows for soil dilation when exceeding the internal elemental shear capacity of the soil. The Mohr-Coulomb model allows perfectly-plastic dilation, which is unable to be modeled using an implicit solver, because of the associated large change in elemental stiffness during dilation. Instead, this model uses an explicit dynamic solver with 5% damping to obtain a quasi-static result from a dynamic solver.

The soil-continuum model captures the same phenomena as the soil-spring model: it models staged backfilling, live loading with a series of offset load positions, and apex ultimate load. Staged backfilling requires a custom fit soil-continuum lift part for each stage to correctly match the current geometry of the deformed arch and prior soil lifts. The Abaqus analysis is driven from MATLAB to read the present geometry and write input files for the next analysis including the new part geometry. Each new lift analysis uses an import analysis that loads the prior deflections and stress states from the last increment of the prior model as the baseline value of the new model.

1.2.5. Chapter 6. Steel Arch Results

Chapter 6 examines results of steel arch bridge testing. Results are compared to both the soil-spring model and the soil-continuum model, which are detailed in Chapter 4 and Chapter 5 respectively. Selected test and model results are presented for three bridges: a tall rise (2.29 m) bridge with compacted soil, a tall rise bridge with under-compacted soil, and a short rise (1.22 m) bridge. Measured properties include soil pressure, arch deflection, arch axial load, and arch bending moment for soil backfilling, live load sequence, and ultimate load. An emphasis is given to bending moments, as these are critical design values. Attention is also given to lateral foundation thrust for the short arch bridge during backfilling, apex live load, and ultimate load, since lateral thrusts are a significant foundation design consideration. Comparisons are made between short and tall rise and between levels of soil compaction. Also, moment variation due to load sequence is considered for steel arches.

1.2.6. Chapter 7. CFFT Arch Results

Chapter 7 examines results of CFFT arch bridge testing and correlates results to soil-spring models. CFFT arch bridges are subject to backfilling loads, live load sequence, and ultimate apex load. Experimental strains are not calculated to moments and axial loads because of uncertainty in the moment curvature relationship. Instead, measured top and bottom strains are presented in this chapter, and modeled strains are computed from from the moment-curvature relationship assumed in the soil-spring model. The model predicted strains indicated a higher degree of nonlinearity during backfilling loads, and this is largely triggered by the moment-curvature relationship. To reduce side-to-side variability predicted by the models that was not observed experimentally, an additional symmetric model was created that simultaneously applies load to both sides of the structure, forcing a symmetric backfilling response.

1.2.7. Chapter 8. Conclusions

- Chapter 2: inefficient steel bar sections were required to get the same bending stiffness as cracked CFFT sections and still provide enough capacity to remain linear-elastic throughout service loading.
- Chapter 3: the timber soil box was structurally adequate, but inclusion of flexible plastic over rough-sawn timbers may have resulted in higher friction between the soil box wall and the soil mass than desired.
- Chapter 4: Modification to the soil-spring analysis indicates modest changes in model results from allowing foundation rotation versus a true fixed analysis. Small deformation analysis is critically unconservative for the subscale bridges, and may be unconservative for full-scale bridges due to axial load and P-delta effects. The model results with various friction angles indicate that larger friction angle results in meaningfully smaller arch moments, thus using accurate soil properties instead of conservative soil properties will reduce design requirements.
- Chapter 5: depth dependent soil stiffness produces meaningfully different arch moments than a uniform soil-stiffness model.
- Chapter 6: steel arches provide a good comparison to model results due to linear-elastic material behavior during service live load sequence. The continuum-soil model overpredicts the backfilling moment response, particularly near the foundation. The soil-spring model is accurate for apex load, but becomes progressively less accurate and conservative for the short bridge with increasing offset load. This response is likely due to inadequate soil restraint near the apex and improper soil modeling at the foundation line.

- Chapter 7: the nonlinear-elastic moment-curvature relationship used in design is accurate for determining capacity for isolated monotonic loads. The moment-curvature relationship only crudely approximates true plastic behavior, as it is a nonlinear elastic model and does not represent the permanent change in stiffness caused by concrete cracking. Cyclic loading and sequential loading may be poorly predicted due to a lack of knowledge on the current stiffness of previously cracked sections. The bending effect resulting from an offset load applied away from the apex is overpredicted by the soil-spring model and the soil-spring model did not converge in some instances; likely this is due to inadequate restraint near the apex.

CHAPTER 2. SCALING THE LABORATORY TEST

2.1. Introduction

The goal of this report is to improve the design efficiency of the buried concrete filled arch bridge system comprised of concrete-filled fiber reinforced polymer (FRP) tube (CFFT) arches through a detailed experimental and computational assessment of soil-structure interaction. Previous research (Bannon 2009; Dagher et al 2012) has assessed the load capacity of an isolated arch; this capacity depends on the tensile strength properties of the composite shell. For a given load or set of loads on the arch the behavior of an isolated arch is documented and predictable, but the soil cover and decking have a large influence on load distribution. Soil both dissipates patch loads from truck tires, spreading the load over a greater area of the arch, and restrains the arch from moving under load; both actions reduce the moment carried by the arch from a truck tire patch or point load. A better understanding of the interaction between the cover soil and the supporting structure is necessary to improve prediction of the loads on the arch and foundation. This project seeks to improve this understanding computationally and experimentally through the testing of subscale buried arch structures. Mimicking the soil-structure interaction response of full-scale structures in these laboratory tests is critical, and is the focus of this chapter.

Arches have been built with a variety of span to depth ratios; typical values range from 5:1 to 3:1. A bridge with a large span to depth ratio will have large footing thrust and small radial displacement compared to a taller arch with the same stiffness. A bridge with a 12 m span and 1.5 m spacing approaches the strength limit for 300 mm diameter arches based on typical truck and soil loading, but this bridge is too large for laboratory testing due to height and cost limitations. A subscale arch with half the height was required to load the arch with an overhead actuator. For the planned test setup soil is confined in a self-reacting timber and concrete box and

superimposed loads are applied to the soil surface. Details of the test setup are presented in Chapter 3.

2.2. Overview of Scaling Considerations

To achieve representative soil structure interaction in this test setup, the subscale bridge should have both the same load distribution and horizontal soil pressure as the full-scale bridge. Soil dead load is a major portion of the load on the arch and the distribution of this load must be preserved; the span and the spacing are scaled with the height of the bridge to maintain volume for a given percent bridge length. Live loads must also be scaled accordingly and are further discussed in the Scaling section. Horizontal soil pressure is dependent on deflection and position from the neutral soil position. There are too many parameters influencing arch stiffness to produce ideal horizontal pressures under all loading conditions, and as a result the lab scale structure was designed based on horizontal pressures caused by the scaled live loading positioned at the apex of the backfilled structure. This is not the only important pressure; alternatively the horizontal pressure profile at the end of backfill or during important truck loading positions could have been selected.

Apex live load is not the critical design live load for most buried bridges because the highest moments produced by apex load are positive beam sign convention moments (tension on bottom) at the apex, which opposes larger negative locked-in backfilling moments. Apex loading is preferable to critical design load locations as a scaling parameter because the moment response is large and the location is well defined; the apex is always in the same location for a given span regardless of rise. Peak positive moment response at the ‘shoulder’ occurs in varying span locations based on bridge shape, and due to lack of knowledge about load distribution there is

less confidence in offset load response. The response to apex load is close to symmetric, differing only by staged backfilling history from side to side on the bridge, and peak vertical pressure should be located directly under the load.

Ultimately, two global arch geometries were considered: a short arch with 6.1 m span, 1.2 m rise, 0.76 m spacing, and a tall arch with 6.1 m span, 2.28 m rise, and 0.76 m spacing. The two arch geometries were selected to provide both a high deformation small thrust arch and a low deformation large thrust arch. The scaled cross sections are introduced later in this chapter.

CFFT arches have a nonlinear moment curvature relationship; axial compression reduces the crack depth in the concrete making the section stiffer in bending. Concrete does carry some tensile stress before it is cracked; reloaded concrete will behave differently than uncracked concrete making the strain-moment relationship dependent on load history. An objective of this study is to validate the soil-spring model for predicting moment for buried arch bridges, and the strain to moment correlation of post-cracked concrete makes this difficult. Also, heavy braided FRP is a difficult material on which to measure strain with foil gauges due to variation in strain behavior between individual fiber tows and the small number of tows measured by a single foil strain gauge. Therefore, a steel arch was also developed for soil testing purposes. Steel, prior to yield, is a linear elastic material and the bending stiffness of a steel member is not dependent on axial load or prior loads. Because steel behaves as a uniform homogenous material foil strain gauges are effective at reading bending strain on steel. The steel arch needed to adhere to the same scaling guidelines as the FRP subscale: same load distribution and similar horizontal pressure.

2.3. Model Description

All preliminary modeling for this research program is based on the model used for commercial bridge design by Advanced Infrastructure Technologies originally developed by Clapp and Davids (2011). A more comprehensive description of the model is in Chapter 3 of this report. Throughout this chapter beam moment sign convention is assumed unless specifically designated: negative moment causes tension on the top of the arch, positive moment causes compression on the top of the arch. This section explains the differences between the model used for scaling the test and the model presented in more detail in Chapter 3 for correlation to experimental results. Part of the scope of this report is to show improvements to the soil-spring model, however the model had not been improved at the time of scaling, and the scaling results are presented in this chapter using the original model assumptions. A diagram of the model used with this study shown with a coarse mesh for visual clarity is presented in Figure 2.1.

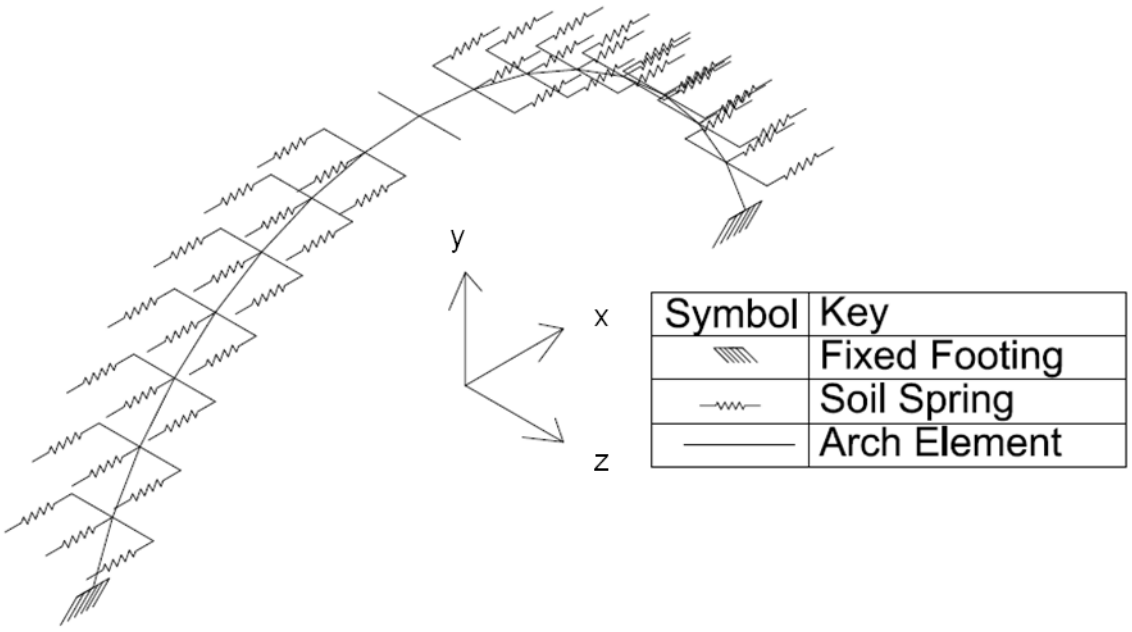

Figure 2.1. Soil-Spring Model Used in Scaling

The soil-spring model used for scaling the laboratory tests was based on a small deformation solver (equilibrium was established for the at-rest geometry of the arch). This was initially assumed adequate because the deformation during backfilling was estimated at approximately 50 mm for a full-scale 12.2 m span arch, which is less than 0.5% of the span. Service live load deflections are predicted to be approximately one-third as large as peak backfilling movement.

The arch was discretized with 60 equal-length, planar (*x*-*y* plane), end to end elements. Two transverse (*z* direction) decking elements were connected to all interior nodes (not at the foundations) and each decking element length is half of the spacing of the arches. The outer ends of the decking elements are given reflective boundary conditions, which assumed that the load on decking between adjacent arches is uniform. Horizontal soil springs (*x* direction) were connected to each arch or deck node. The soil spring modeling approach and the soil spring load-deformation relationship developed from NCHRP Report No. 343 (Barker et al. 1991) are given by Clapp and Davids (2011), and discussed in more detail later in this report. Soil was modeled using typical design assumptions: a medium density granular soil (2.0 Mg/m3) with a friction angle (ϕ) of 37° and an at-rest earth pressure coefficient (K_0) 0.45.

Soil is modeled as a series of nonlinear spring elements connected at each decking node and arch node with horizontal force dependent on the change in spring length (*x* displacement). The deflection is zeroed from the point where the node of interest was first buried and compacted; the zero position for a spring is not the zero deflection position for the arch.

2.3.1. Boundary Conditions

For simplicity, the arches are modeled as fixed at the footing for all pretest analyses. During field implementation arches are cast in a large reinforced concrete footing that restrains the arch end rotations and deflections. The concrete mass either acts as a spread footing to distribute the

vertical load into the underlying soil, while soil behind the footing prevents horizontal displacements, or the foundation is built on piles, which help transfer the vertical and horizontal arch loads to the soil. In lab testing the arches were cast into a concrete spread footing, but unlike a typical bridge there was no soil under the footings; the footings were supported by the rigid reinforced concrete lab floor.

Horizontal restraint was two opposite extremes to surround the real world conditions: rigidly linked footings and low base friction footings. During initial lab testing, the two footings were connected with steel bars that span the direction of the arch, and inline load cells measured the horizontal thrust between the footings. Implemented throughout backfill and during initial loading, this condition is equivalent to a rock anchored footing or a very rigid soil or pile foundation where basically no footing movement is allowed. The steel bars were removed after initial testing and additional live loads and the ultimate loads were applied with sliding footings. The untied footings were still fixed against rotation the end of the arch relative to the footing, only now the footing was allowed to move along the span direction with a thin plastic pad under the footing to reduce the base friction. Horizontal restraint was provided by the soil behind the footing. These two tested cases were intended to bound the possible soil to footing interactions of the arch bridge system. One discrepancy between real-world bridges and the experimental test is that the soil does not extend below the concrete floor, so less soil was mobilized by the footings than in an actual bridge, which reduces sliding footing restraint compared to a full scale bridge.

2.3.2. Soil

Currently, the bridges are designed using soil springs that do not account for additional stiffness from compaction and represent the transition from at-rest pressure to passive pressure with a single linear region (Clapp and Davids 2011). Compaction increases the at-rest earth

pressure, increasing spring stiffness. Soil passive response is expected to be nonlinear, gaining more stiffness with less deflection near at-rest pressure, before shear banding develops, than when soil pressures are close to fully passive. Vertical surcharge through the soil is based on the Boussinesq distribution for load acting on the surface of the soil (Holtz and Kovacs, 1981). This distribution assumes an elastic homogenous soil mass; the actual soil mass is compacted layers of fill and will tend to form stress layers, causing a lower load directly under the surface load and a greater load away from the surface load, closer to the Westergaard theory. Horizontal soil stress from a surcharge load is the vertical soil stress at a given point multiplied by the current horizontal pressure coefficient.

Soil dead load, the weight of the soil, is assessed using equivalent fluid pressure. The vertical soil stress at any point along the arch is the local soil depth multiplied by the soil density. Horizontal soil loads are more complicated because they are based on equivalent fluid pressure and the movement of the arches. When an arch moves away from the soil mass the soil is in the active region, decreasing the horizontal stress; when the arch moves toward the soil mass it is in the passive region increasing the horizontal stress. Active and passive regions are based on the NHCRP (Barker et al. 1991) curve for medium-dense sands behind a cantilever wall, with the plot shown in Figure 2.2, normalized with wall height (h); for this analysis the arch height is used as the wall height. Often the soil against the arch is neither fully active nor fully passive, and the soil stress and soil stiffness for a particular node are based on the movement of the node relative to the total arch height and are linearly interpolated from Figure 3. Typical bridge design uses the uncompacted soil curve, which is considered conservative, but is less likely to produce the actual laboratory displacements and stresses. When the displacement is greater than $0.009h$, the soil is fully active with $K = 0.25$, when displacement is less than $-0.016h$ it is fully passive

with K = 4.0. In between, there is a series of linear portions that approximate the NCHRP curve. Figure 2.2 compares the compacted and uncompacted soil curves. The horizontal pressure is the total vertical pressure (from live load and from soil loads) multiplied by the horizontal pressure coefficient calculated based on deflection.

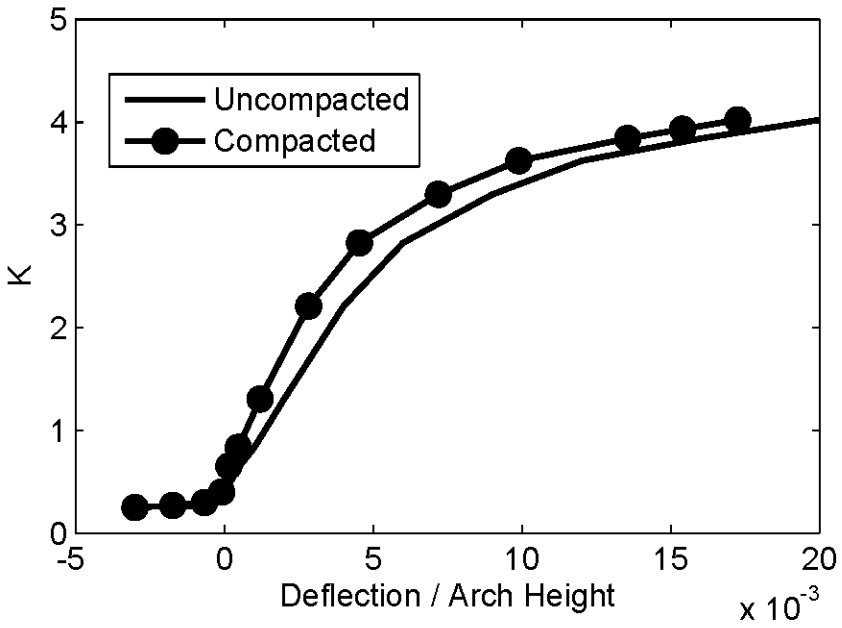

Figure 2.2. Comparison of Compacted and Uncompacted Soil Stiffness

Compacted and uncompacted soil assumptions produce different model outputs for a given arch. The difference is more pronounced for the taller arch, where the horizontal soil forces are higher because the arch is taller. During backfill, the stiffer compacted soil pushes harder on the arch and causes approximately 10% larger moments at the footing and larger displacements. Radial displacements caused by complete soil backfill are compared for compacted and uncompacted soils assuming a tall, full-scale arch in Figure 4 and assuming a short full-scale arch in Figure 5 with 5.8 m of soil over both footings and 1.22 m of soil over the apex. The change in displacement from a subsequent apex line live load with the design tandem load

described in the load section is also shown in Figure 2.3 and Figure 2.4. Notice that the displacements are as much as twice as large for the compacted soil arch, but subsequent live loading does not produce as much change. Both arches start with at-rest soil pressures, 2.5 times larger for the compacted soil, in the neutral position, but the soil load pushes the arch into a predominantly active position, particularly between the footings and the shoulders. This effect is larger for the compacted soil because it has higher horizontal loads. The change caused by live loading is about the same for both the compacted and uncompacted soil assumption; in both cases the soil is starting from a similar horizontal pressure, because the soil load moved most of the forces to active, requiring similar deflections to increase the horizontal pressure to the lowest stable position.

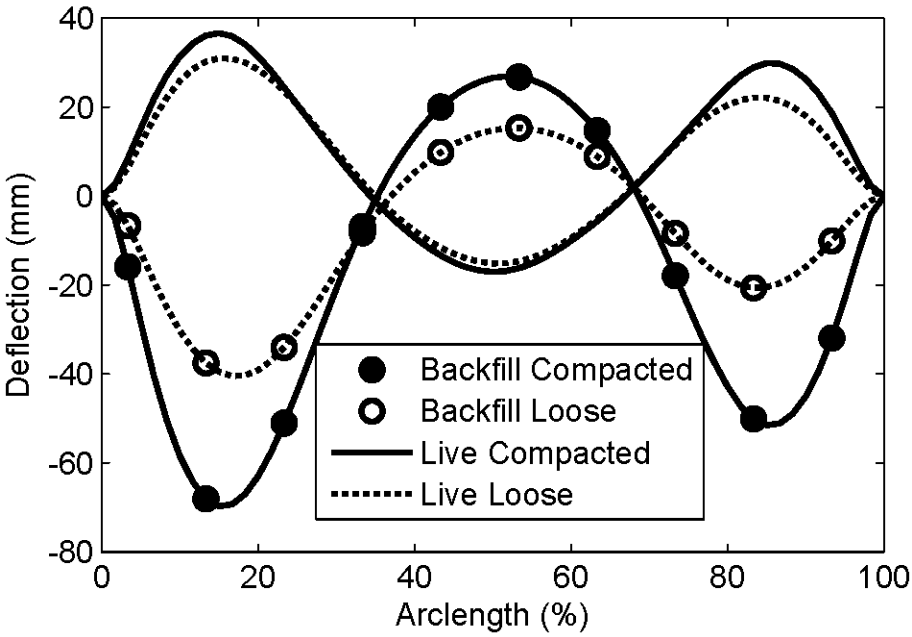

Figure 2.3. Deflection Behavior of Tall Arch, Compacted and Uncompacted

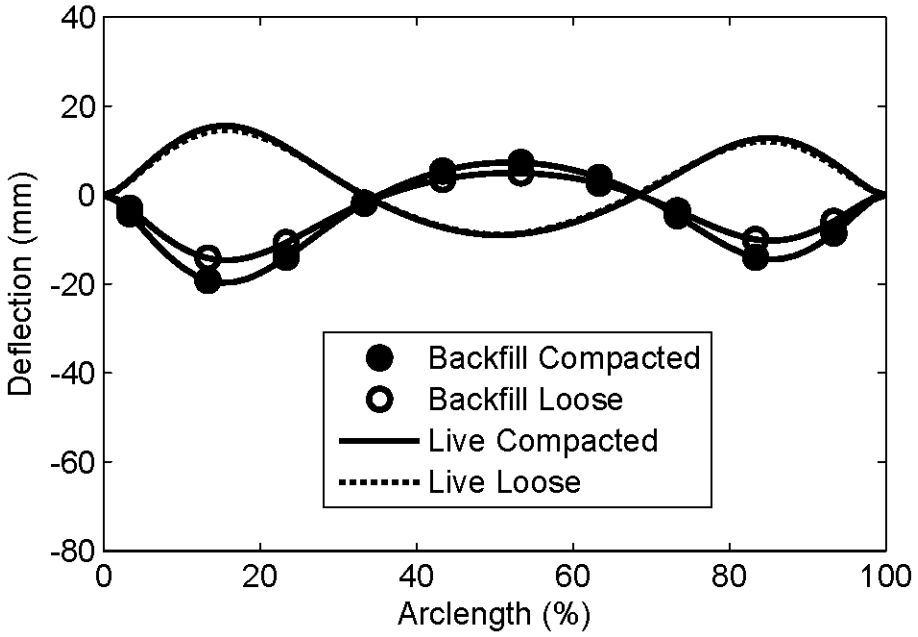

Figure 2.4. Deflection Behavior of Short Arch, Compacted and Uncompacted

2.3.3. FRP Properties

FRP properties are found using classical lamination theory for a thin multilayered plate. Classical Lamination Theory (CLT) with micromechanics was used to calculate the shear modulus and transverse (radial) and longitudinal moduli of the FRP shell (for further information on Classical Lamination Theory and micromechanics see Daniel and Ishai (2006)) by combining the properties of the fiber (carbon or glass) and the vinyl ester resin. For transverse modulus and shear modulus the Halpin-Tsai approximations were used (Daniel and Ishai, 2006). Fiber volume fraction was assumed to be 0.50. An additional complication is braid waviness; the braided fabric weaves over and under cross tows creating depth to the laminate inconsistent with the flat plate assumption; the 3D nature of the braid decreases the longitudinal modulus of the fiber. An approximation developed by Cox and Dadkhah (1995) based on a sinusoidal wave shape beam gives a longitudinal stiffness reduction factor. In Equation 1 t_f is the fiber thickness, λ is the

wavelength (measured at 18mm for the carbon), E_1 is the fiber elastic modulus in the fiber direction, G_{12} is the in-plane shear modulus, ν_{12} is the Poisson's ratio. This model showed good agreement with results of coupon-level stiffness tests conducted at the University of Maine on carbon fiber only (Bannon 2009) and on hybrid glass and carbon composites (Demkowicz 2011), predicting modulus to within 10%.

$$E_1(wavy) = E_1\left(1+2\left(\frac{t_f\pi}{\lambda}\right)^2\left(\frac{E_1}{G_{12}}-2(1-\nu_{12})\right)\right) \qquad \text{Equation 2.1}$$

Typically, only the axial compliance matrix is considered for the hollow arches. Classical Lamination Theory assumes a thin composite plate; when that plate is instead a hollow circle the bending stiffness is greatly increased. The moment of inertia of a thin plate is proportional to length times thickness cubed and the moment of inertia of a hollow annulus is proportional to thickness times diameter cubed. For a typical diameter to thickness ratio of 100:1 a hollow FRP arch shell moment of inertia is 7500 times larger than a plate moment of inertia with the same material. Bending stiffness and combined bending/axial stiffness terms in the CLT compliance matrix are far too small when predicted assuming a flat plate, and the most accurate results are obtained by discarding the combined term all together and using the axial compliance matrix only to calculate the axial moduli.

The FRP shell is only a portion of the total stiffness; much of the arch stiffness comes from concrete. The concrete filled arch uses a model developed for concrete filled FRP tubes (Burgueño 1999), which assumes a Mander model (1988) for confined concrete. Concrete in tension is assumed cracked, a conservative assumption for strength design that under predicts bending stiffness and over predicts deflection. The level of cracking during any particular load

cycle is difficult to ascertain because it depends on tensile stress in earlier load cycles, but the minimum bending stiffness occurs when concrete tensile strength is neglected. The Burgueño (1999) model also includes axial load; axial compression closes the cracks in concrete and increases the bending stiffness. Figure 2.5 contains a plot of the moment curvature relationship for a 300 mm arch with a variety of axial loads.

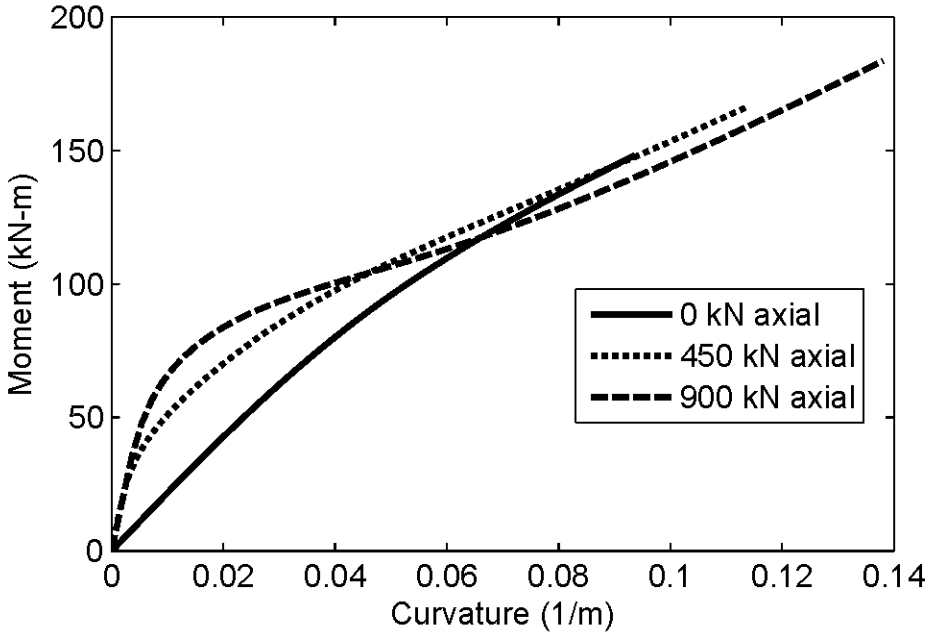

Figure 2.5. Moment-Curvature Relationship for a 300 mm Arch

Another source of axial stiffness in the system is the deck. Buried arch bridges constructed to-date have either a structural reinforced concrete deck or a structural FRP deck. The concrete deck provides noticeable axial stiffness; due to limited fasteners between the deck and the arch they are treated as separate entities without composite action. Deck stiffness is thus added to the arch stiffness at a given node. The FRP deck is much more compliant in the longitudinal direction and its stiffness is neglected. For subscale lab testing, a wood deck was used as explained later, which provides negligible longitudinal stiffness.

2.4. Scaling

Scale factor will be defined as the ratio of the full-scale bridge property to the equivalent subscale bridge property; e.g. for the 6.1 m span subscale of the 12.2 m assumed bridge the scale factor *S* for span is 2. The scaling objective was to maintain the same arch deflection while keeping load distribution and the contribution from live and dead loads proportional; scaling terms for the relevant terms follow. Soil dead loads, per unit length, w_s are cross sectional area dependent, which means they vary by a factor of S^2 (4). When this equation gets integrated with respect to length the scale factor will increase by an additional *S*, e.g. shears and reactions have a factor S^3 (8), moments have S^4 (16), and deflections have S^6 (64). As a first estimate of mimicking deflection the bending stiffness of the section *EI* (elastic modulus *E* times moment of inertia *I*) was reduced by a factor of 64 in the subscale.

The full-scale bridge used as the standard in this study is a conglomeration of typical bridge dimensions and characteristics; it does not match the exact parameters of any existing bridge. By pushing a bridge to the arch moment and decking moment limits, as proposed by current design methodology, the soil effects will be maximized and there will be the greatest opportunity to see arch strains and deflections under equivalent service level loads. The standard arch used is a 12.2 m span at 1.5 m with a 1.22 m depth of cover at the crown, a rise of 2.44 m for the short arch 4.57 m for the tall arch 1.22 m by 1.22 m footings that continuously span between the arches, and a 300 mm diameter cross-section. The composite shell has three total layers: an innermost layer of +/-81degree, 1.1 mm thickness, E-glass inner layer and two +/-21 degree, 0.74 mm thickness, carbon fiber layers combined with vinyl ester resin and an assumed 50% fiber volume fraction (total thickness 2.5 mm). The elastic moduli, based on classical lamination theory and

micromechanics, are 60 GPa longitudinal and 20 GPa transverse. The arches are filled with normal weight (2.3 Mg/m^3) concrete with a compressive strength of 35 MPa. The arches are covered with a reinforced concrete deck with properties based on a buried CFFT arch bridge built in Caribou, ME in 2011. The average deck thickness is 165 mm with minimum thickness 90mm, E is 26 GPa, I_{lp} (longitudinal positive) is 3250 mm^4/mm, I_{ln} (longitudinal negative) is 1080 mm^4/mm, I_t (transverse positive) is 52400 mm^4/mm.

2.4.1. Scaling the CFFT Arch

The subscale CFFT arch diameter cannot be half of the diameter of the larger arch; the shell stiffness and core stiffness vary with a different scale than deflection. Deflection varies with S^6, while I for the core varies with d^4 (the cracked concrete is not linear elastic – I is not valid, but it is a useful starting point), core area varies with d^2 (important because crack closing and bending stiffness depend on axial stress), and I for the shell and section modulus for the concrete vary with d^3. Using I for the core as the determining factor the diameter would be 107 mm; axial stress has the same scale factor. Nonlinear behavior changes the stiffness considerably; the concrete bending stiffness is more dependent on crack depth and estimated section loss than gross moment of inertia. If diameter were scaled by moment, scale factor 16, over section modulus, d^3, the required diameter is 120 mm. To compromise on these relationships the diameter was specified as 114 mm. Ideally, if all parameters were scalable, the crack depth should be identical for the subscale and the full-scale arch, but the required compromise between bending stress and deflection means that the crack depths are not identical and the difference is compensated with the transverse shell stiffness. Additional alteration allowed by changing the concrete density only slightly change the response of the arch, but changing the concrete strength

has multiple effects: it reduces the elastic modulus of the concrete and it changes the strength analysis altering the crack depth and the stiffness of the section.

The shell is linear elastic; to reduce the number of differences in the scaling process the shell bending stiffness should also be scaled. It is impossible to scale the shell thickness; a certain thickness per layer is required to maintain transverse strength and stiffness and keep fiber coverage for the part. Based on the cube of the relative diameter, the reduction of longitudinal stiffness, E_x-t, is slightly over 3.5. The total longitudinal elastic modulus E_x for the full-scale section based on CLT is 50 GPa and shell thickness t is 2.5 mm; longitudinal stiffness E_x-t is 130 kN/mm making the required subscale E_x-t 36 KN/mm. The lower longitudinal stiffness requires only a single outer layer of E-glass fiber reducing the thickness and the modulus while improving cost, manufacturability, and strain to failure. There are several different possible combinations of fiber angle and material thickness for both layers to produce the required longitudinal shell stiffness.

The shell was also designed to provide the correct confinement capability. Confinement pressure comes from the hoop stiffness of the shell wall E_r-t. At low curvatures the confinement contribution to the moment-curvature relationship is quite small, overwhelmed by other section parameters, but as the concrete is more cracked the transverse shell stiffness, which holds the cracked concrete together, noticeably affecting bending stiffness. To scale the response, the confinement potential was also scaled with the inverse of the discrepancy between theoretical and actual gross concrete moment of inertia. Because the compromised diameter produces a 30% smaller concrete I than the theoretical value, a 30% smaller confining pressure was needed to adjust the bending stiffness of the subscale for high strains. E_y-t for the full-scale arch is 50 kN/mm, scaled for the subscale's response it is 39 kN/mm.

The laminate chosen, using CLT and micromechanics, was an inner layer of E-glass +/-75 degrees, 1.0 mm thickness, and an outer layer of E-glass +/- 25 degrees, 0.89 mm thickness, with total thickness 1.9 mm and elastic moduli E_x of 19 GPa and E_y of 20 GPa. Micromechanics predictions can be accurate to within 10% for braided hybrid glass/carbon composites (Bannon 2009), but coupon level testing was performed to obtain better predictions which were unavailable when designing the test. Concrete strength can be slightly adjusted to change the moment-curvature relationship if the laminate proves to be either substantially stiffer or more flexible than predicted.

The moment-curvature relationship was calculated using the Mander model (1988) for confined concrete, using a program developed by Burgueño (1999). The same approach has been used to successfully model the bending response of carbon-glass hybrid CFFTs (Bannon 2009; Dagher et al 2012). This model uses a given axial stress and the previous outlined material properties for inputs. The model starts with compressive strain. It finds compressive stress based on the material properties and then finds the appropriate tensile stress and strain to balance the axial load. The stresses are used to compute moment and the strains are used to compute curvature. In the arch model the Burgueño moment-curvature relationship is precalculated and stored for several axial loads. For a given moment and axial load the curvature is linearly interpolated from the precalculated values. Bending stiffness (tangent modulus) is the local moment divided by curvature; this is calculated for each node.

2.4.2. Scaling the Steel Arch

One major advantage to using steel arches is that steel is linearly elastic, meaning the arches (not the soil) will rebound so long as stress does not exceed the yield limit. Steel is also easy to instrument. The process of matching deflection to determine the steel section will be described in

more detail later. Strength is a major issue for the steel arches; an HSS (hollow structural steel) or pipe section would be an efficient section for bending to an arch shape, but the required yield capacity dictates a prohibitively large section modulus of 25000 mm^3 for 290 MPa steel; any section with a capacity near this limit was too stiff. To correct this, additional steel was needed near the neutral axis, suggesting a steel plate, which is materially inefficient for bending, but does provide a high bending strength to bending stiffness ratio. Plates were sized for both grade 36 (250 MPa) and 50 (344 MPa) steel, but grade 50 steel will have a smaller section with a more reasonable width.

2.4.3. Decking

The decking in arch bridges built prior to the design of this testing program is 200 mm thick concrete (maximum thickness) with #5 bars at 200 mm on center in the transverse direction and #3 bars at 400 mm on center in the longitudinal direction. The concrete deck is supported during casting by a corrugated FRP deck. The decking is not symmetric. Figure 2.6 has a section view of the decking by Matthew Pellerin of AIT (Clapp and Davids, 2011). The transverse direction runs into and out of the page.

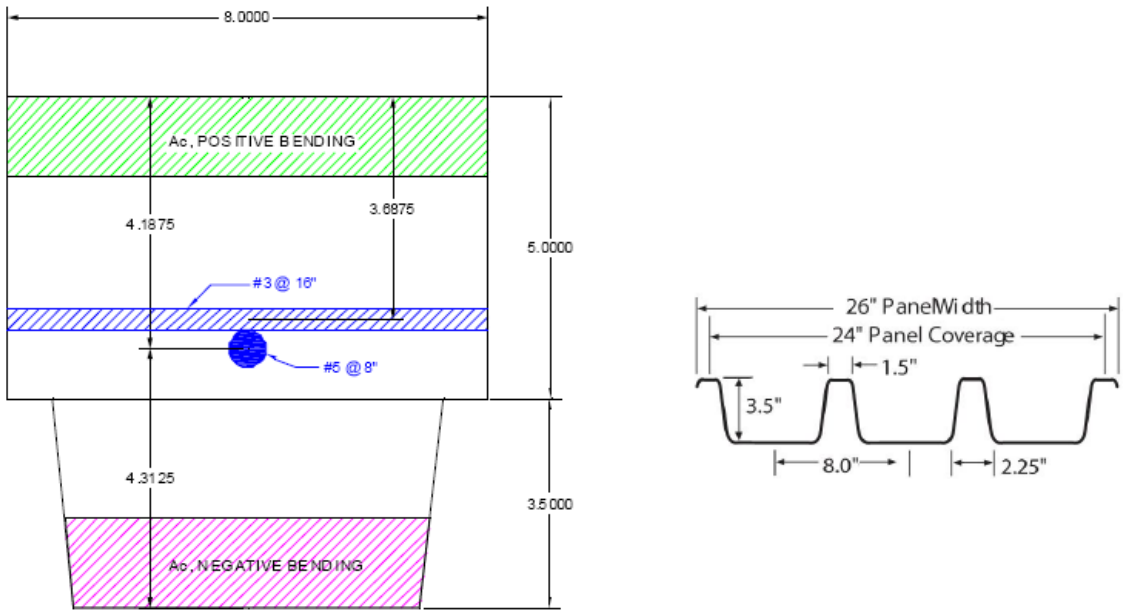

Figure 2.6. Decking Cross-Section (provided by AIT)

The transverse response of the decking was scaled, and no longitudinal effect of the deck was considered in the subscale model. Decking for central arches, those that carry truck and lane loads, is designed as an infinite continuous beam. With only three arches, and thus two inner spans, decking deflection is influenced by the response of the two cantilever spans outside the arches; to keep inner deflections consistent the outer decking cantilevers should generate the same moment as an additional decking span. To keep zero rotation in the decking above the arches, the moment at the cantilever edge must equal the moment in the continuous span. For simplicity, soil and traffic loads are treated as a uniform load. The moment at the fixed end of a uniform loaded cantilever is $wl^2/2$, while the moment at the end of a continuous span is $wl^2/12$. The scaled length for the continuous beam is 760 mm; to produce the same moment the cantilever span should be 310 mm.

Transverse deck stiffness must be represented in the subscale test. The concrete deck assumes transverse #5 bars at 200 mm on center slightly above the central height of the section. The top width per bar is 200 mm and the FRP decking corrugations make the bottom width per bar 155 mm. For a fully cracked section assuming the Whitney stress block and a maximum compressive strain of 0.003, both sections have a similar *I* which can be rounded to two significant figures to 52000 mm^4/mm. To get the same deck deflections with the subscale as with the full-scale the bending stiffness of the arches should be reduced by one-64^{th}, however width is already scaled by one half; scale factor was one-32^{nd}. *EI* for the full-scale arch deck is 2120 kN/mm; required *EI* is 66 kN/mm. This is too soft for a concrete deck, and FRP decks are expensive; a wooden deck, using a combination of flat-wise studs and sheathing, is inexpensive and can have the same bending stiffness. SPF-s (spruce, pine, fir – south) has average longitudinal elastic modulus 8.3 GPa, and flat-wise 2x lumber has *I* equal to 4600 mm^4/mm. *EI* for continuous lumber is 60 kN/mm and additional stiffness is required. Adding a ¾ in nominal plywood sheet adds 4.4 kN/mm (APA 1998) assuming a non-composite section, a composite section would be higher. This stiffness is adequate to mimic the decking behavior.

Two decking effects were not imitated in the subscale: the additional weight of the concrete deck and the longitudinal stiffness of the concrete deck. The surface area of the concrete deck is scaled with soil volume, but the 165 mm mean thickness and 2.4 Mg/m^3 density of reinforced concrete are not scaled by using 57 mm pine, with 0.36 Mg/m^3 density. The additional weight does not cause much deflection because it is uniform over the arch; it does not initiate soil springs because soil is not yet placed when the deck is cast. The additional stiffness is small because longitudinal reinforcing is a #3 bar spaced at 400 mm on center; it is also not symmetric, because the deck runs opposite the corrugations, and the concrete inside the troughs is neglected

for longitudinal analysis. The cracked positive longitudinal moment of inertia is nine times larger than the cracked negative moment of inertia. During analysis, this property is directly added to the arch stiffness, and while small compared to the arch stiffness, it is another difference between full scale and subscale analyses.

2.4.4. Load

There are two main sources of load: soil dead load and truck live load. Soil dead load was scaled with volume, and the magnitude of the live load is scaled by the same ratio: one to eight. Surface live loads are distributed through the soil using the Boussinesq assumption for a patch load (Holtz and Kovacs 1981), which requires a patch size and shape. AASHTO (2014) defines a truck tire patch (from a wheel load) as being a uniformly loaded rectangle of area 25 mm x 50 mm. For the subscale patch the dimensions are scaled by one-half, the same ratio as the span. For design, AASHTO requires both the HL-93 truck and tandem. Although the HL-93 design truck has higher wheel loads, the tandem has smaller spacing and often controls design for short span bridges, including buried concrete filled FRP bridges. In this program the tandem is the only truck considered, and further reference to a truck's load refers to the tandem's load. The tandem is a 224 kN vehicle with two axles spaced at 1200 mm with a 1800 mm axle width. The State of Maine also requires a 25% capacity increase on the HL-93 truck, which was included in the model (Maine Department of Transportation 2003). All models are run with the load of the tandem, plus the Maine 25% increase, plus an additional 20% increase to account for overloaded trucks, similar to the multiple presence factor. Impact is not included in this analysis because laboratory loading will not be dynamic and impact is reduced on buried structures. All models have service level loads; service loads will be applied to the lab experiment to find appropriate

deflection. In design, service loads are applied to the bridge to find deflections and handle nonlinear behavior; the loads are scaled with strength factors after to verify capacity.

For laboratory testing, it was deemed impractical to apply the four patch loads required for true AASHTO specified tandem loading. Models were made for the truck either as two line loads, one representing each axle, or a single combined line load that concentrated the full weight of the tandem. The line load uniformly spanned all three arches. For the full scale 300 mm arch, Figure 2.7 (tall arch) and Figure 2.8 (short arch) compare the model predicted moments for the center of three arches with the assumed loading from the four tandem patches, the two axle lines, or the concentrated line, all straddling the arch apex. The moments are very similar, indicating that there is little difference between the three loading cases. The single line load makes the moment more positive at the point of load, and the difference is more pronounced in the short arch.

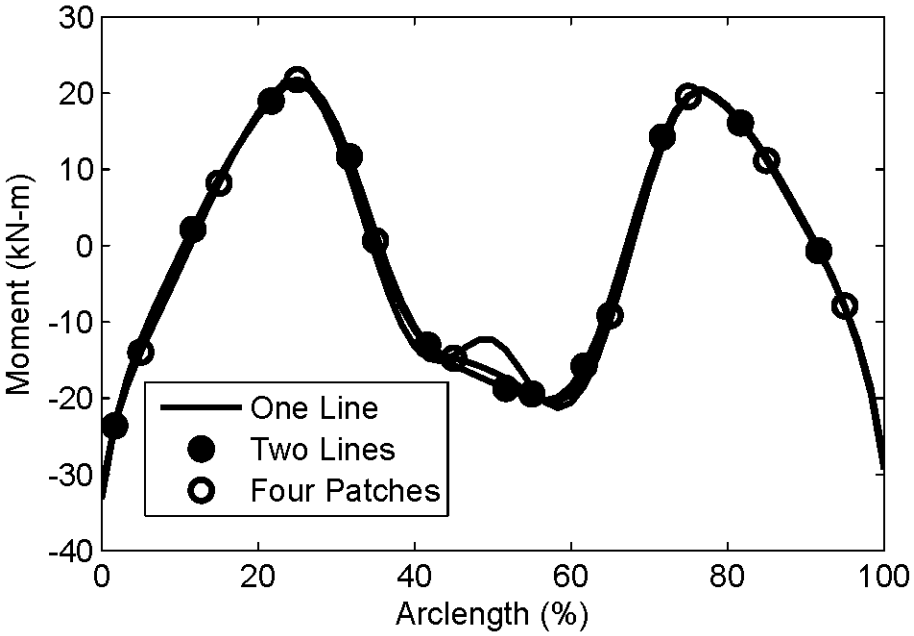

Figure 2.7. Tall Arch Moment from Different Truck Models

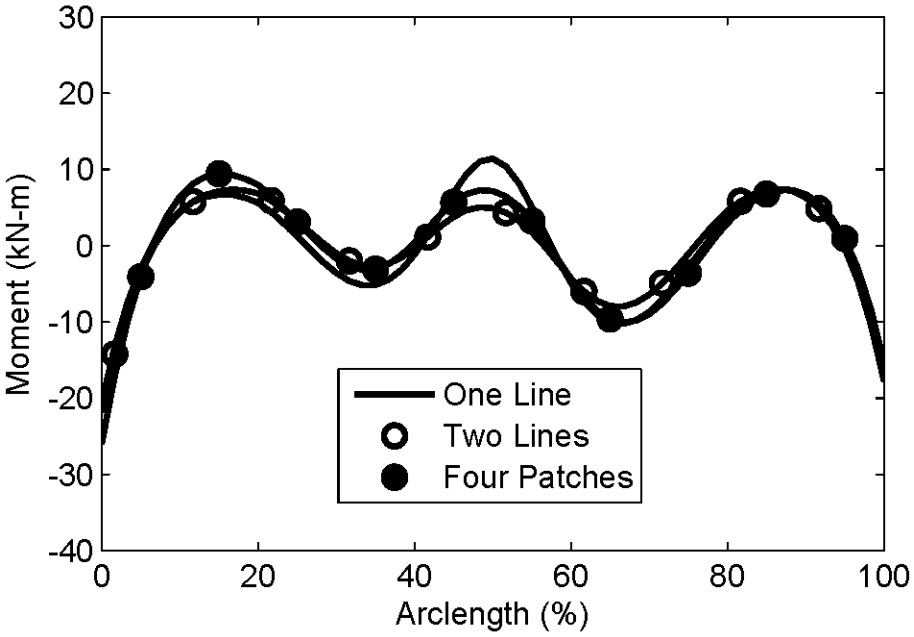

Figure 2.8. Short Arch Moment from Different Truck Models

The bridge will be loaded with the simulated tandem in multiple locations. Four different loading plans were proposed and the arch moment envelope for each plan was compared for both the two line loads and the single line load. Options included loading the arches over the entire span at 300 mm and 600 mm intervals, or loading the center 60% at 300 mm and 600 mm intervals. Testing time and logistics are important; each load position requires moving the actuator and possibly the reaction frame, not a trivial process, and the laboratory floor has holes at 600 mm intervals giving a strong bias to testing at that spacing interval. Figure 2.9 and Figure 2.10 contain the live load moments for subscale linear elastic steel arches applying two line loads. Notice that peak moments are still well represented by applying load at 600 mm intervals over the middle 60% of the span when compared to applying load at 300 mm intervals. The load over the outer 20% of span on either side appears insignificant; the moments in those regions are not strongly influenced by a direct vertical load and are smaller than live load moment above the

shoulders and the apex. Also notice that the peak moment is more consistent over the middle 60% using 300 mm loading interval, but there are still many locations where peak moment is the same for both loading conditions. This justifies that there will be opportunities to measure high live load using either load plan, which favors the substantially simpler 600 mm intervals over the middle 60% of the span.

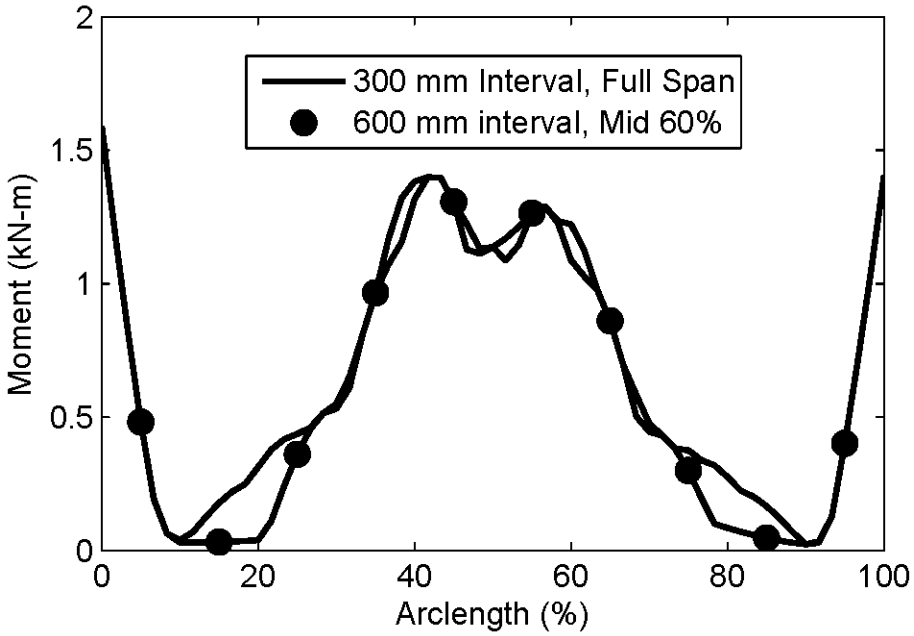

Figure 2.9. Tall Steel Arch, Maximum Positive Moment

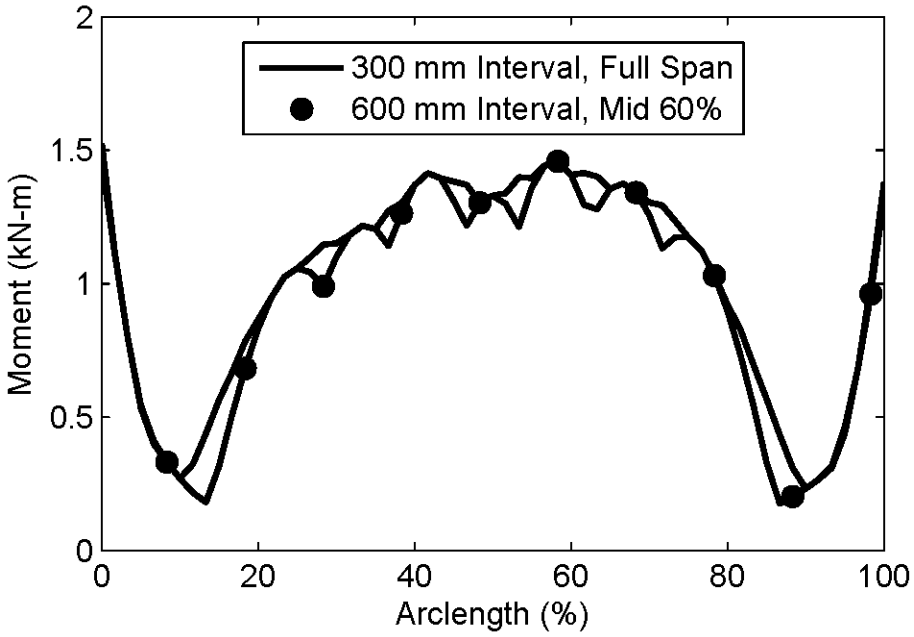

Figure 2.10. Short Steel Arch, Maximum Positive Moment

A second consideration is whether to apply load as a single concentrated load or as two line loads. Two line loads are more representative of bridge loading by a design tandem with two axles, but single line loading is preferable for testing logistics. Figure 2.11 and Figure 2.12 contain plots illustrating positive live load only moment envelopes for one and two line loading for both the tall and short linear elastic steel bridges. The load case depicted is middle 60% of span loading with 600 mm spacing. Notice that in both plots the one line loading envelope is higher for any location than the two line loading envelope, by as much as 40% in local maxima locations. Testing at a higher moment will give better resolution to gauges and improve model to laboratory experiment comparisons. Note: the envelopes are not symmetric because soil compaction occurs on one side at a time starting with the right side.

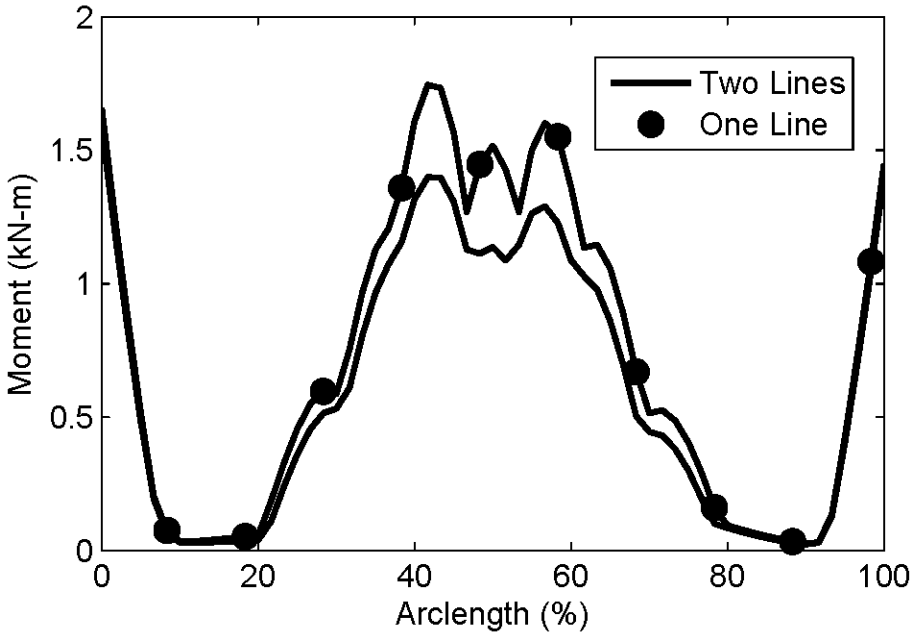

Figure 2.11. Tall Arch, Maximum Positive Moment, One and Two Line Loading

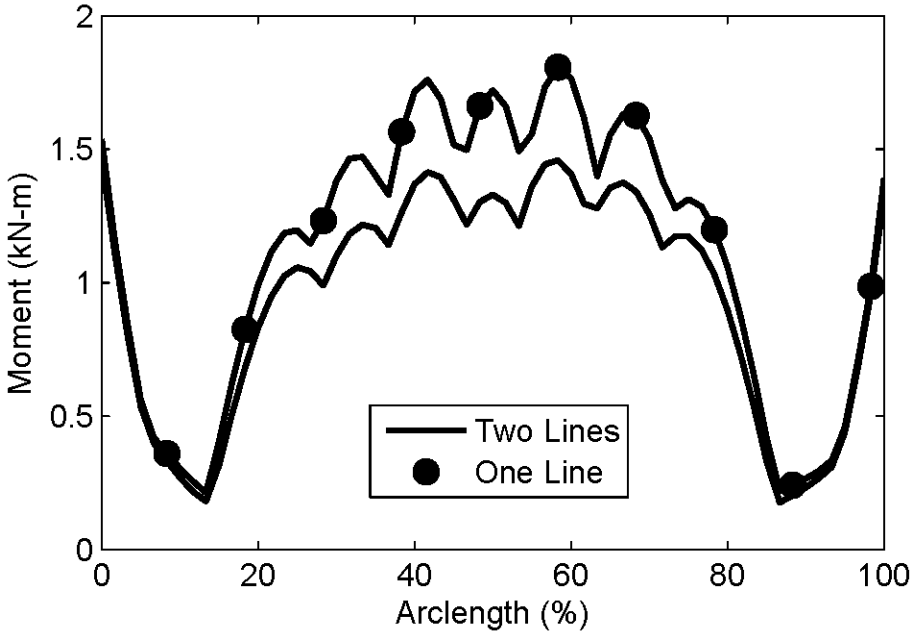

Figure 2.12. Short Arch, Maximum Positive Moment, One and Two Line Loading

2.4.5. Strength

The arches cannot fail during backfill or service loading, yet there must be enough actuator capacity to fail the arches during ultimate loading. For a concrete filled FRP arch the most likely failure mechanism is tensile fiber rupture. Because glass fiber is used for the longitudinal strength layer, and it typically has a higher strain to failure than carbon fiber, additional failure mode transverse fiber rupture (confining strength) is more likely than for a commercial arch. Longitudinal strain capacity was estimated as 1.85% based on prior testing of one-layer glass-only coupons by Demkowicz (2011). Notched tension coupon strength (Demkowicz 2011) was divided by elastic modulus from ASTM D3039 bar tests to get strain. Based on an appropriately high axial compressive load, the Burgueño model gives a failure moment of 9.6 kN-m; this value is dependent on axial load, but does not vary much in the critical axial range (130-200 kN). Coupon testing prior to full arch testing presented in Chapter 3 gives a better estimate of tensile rupture strain. Hoop strain failure was also estimated at 1.85%; for this failure, the Burgueño model predicts a failure moment of 15.8kN-m; the tensile failure is more likely, but these values are estimates and it is possible that the arch is stronger or weaker than anticipated. All loads calculated in this analysis are service level, not strength level; a factor of safety was calculated for each arch during backfill and live load. Figure 2.13 and Figure 2.14 show the moment envelopes for soil backfill the 600 mm interval mid 60%, single line live load envelope for the tall and short arch respectively. The soil backfill creates the largest moment in the load history of the tall arch; approximately 5 kN-m at the right footing. The subsequent live loading produces larger moments at the shoulders and the apex, positive 2.6 kN-m and negative 3.7 kN-m respectively. For the short arch the soil backfill moments are smaller; the largest moment is during live loading at the apex, near 4.5 kN-m. In all cases the moments are small compared to

the projected failure moment of between 9.6 kN-m and 15.8 kN-m, providing approximately a factor of safety of 2 for both arch geometries.

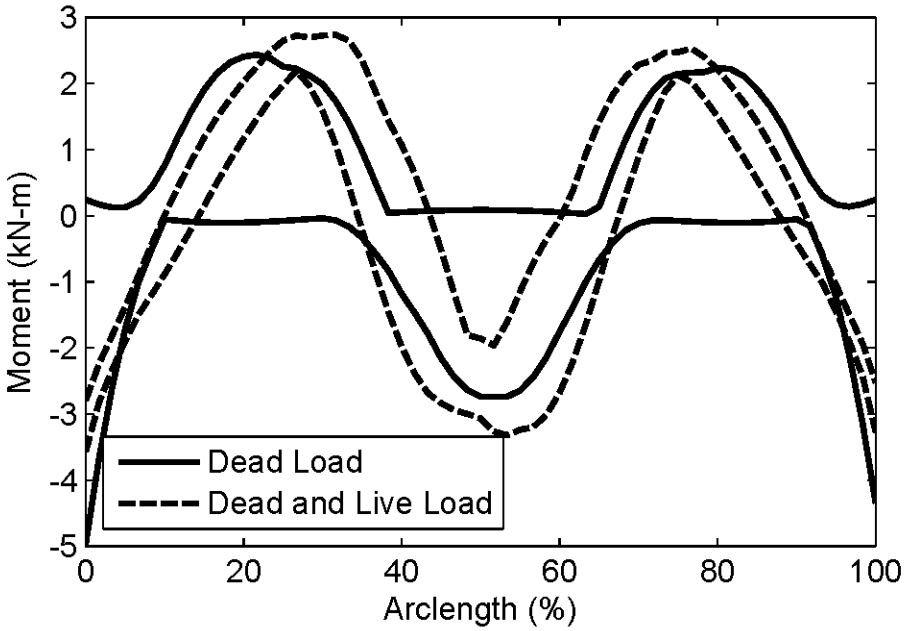

Figure 2.13. Dead Load and Dead Plus Live Load Envelopes, Tall CFFT Arch

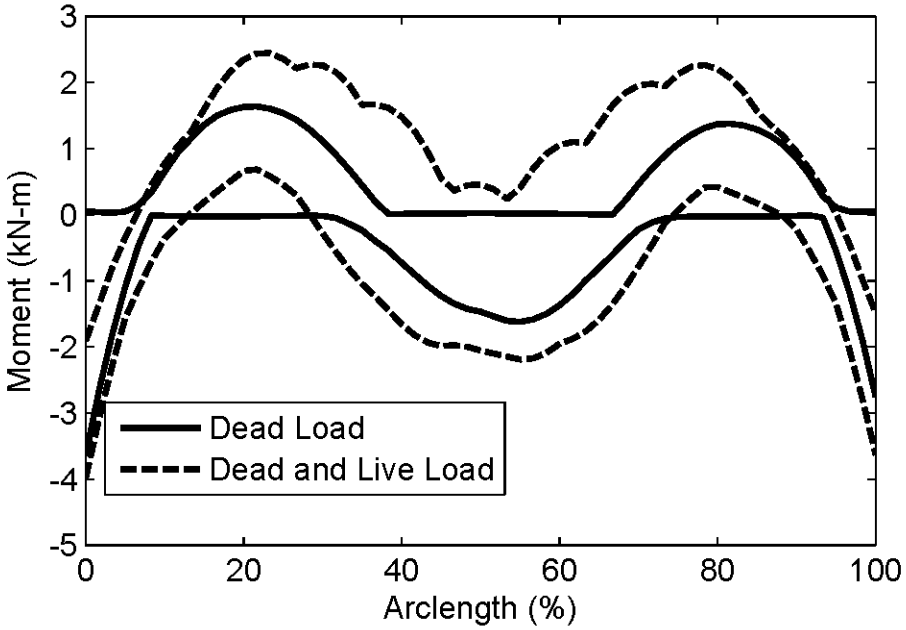

Figure 2.14. Dead Load and Dead Plus Live Load Envelopes, Short CFFT Arch

Soil pushing at the sides of the arches from partial soil depth causes the arches to rotate inward and generates negative moment on the footing (tension on the outside face). The peak footing moments are generated when the soil depth is level with the arch apex. Load applied to the arch apex deforms the arch into an ‘m’ shape, causing positive moment at the footings, reducing the effects of earlier backfill. Failure at the footing, generating a plastic hinge at the footing, would not necessarily fail the system, but would invalidate all following results because bridges in service retain a fixed footing to arch connection.

For steel arches, yielding at any point during the test would invalidate the assumption that the material is linear elastic. The steel arches are designed for appropriate stiffness and adequate strength with an appropriate factor of safety. Stiffness adequacy was determined by minimizing the difference in the scaled horizontal soil pressure between the full scale and the steel subscale. The optimal moment of inertia was approximately 460,000 mm^4 tall arch and 580,000 mm4 short arch. The steel arches have similar internal moments to the FRP subscale: maximum moments are 5 kN-m and 4.2 kN-m for the tall and short arch respectively. Arches are designed to have a safety factor of 1.5 against the start of yield. Axial load only uses 14 MPa or less of the steel’s capacity due to the large steel area and the relatively small axial loads. Assuming grade 50 steel (345 MPa) the required section modulus was 23,000 mm3 for the tall arch and 20,000 mm3 for the short arch; the best sections were a 1.5x4 (38 mm x 102 mm) bar stock for the tall arch and a 2x2 (51 mm x 51 mm) bar stock for the short arch (both dimensions are common manufactured bar sections). Hollow Structural Steel (HSS) is manufactured from 290 MPa steel (round) or 317 MPa steel (rectangular) and the axial arch stresses are higher because there is less area The tall arch cannot be manufactured from a hollow section, because the required section modulus is too

large relative to the moment of inertia, but the short arch could be manufactured from a rectangular section HSS 4x2x1/2 (102 mm x 51 mm x 26 mm) that uses the section's weak axis in the vertical direction. This option uses approximately half the steel of the 2x2 bar stock and may be economical, although the section may warp during arch shaping.

Arch failure for this research does not correspond to collapse of the arch but to inelastic behavior: the entire point of a steel arch is to find soil-structure interaction without material nonlinearity. After the onset of yield there is considerable reserve capacity before collapse. A plastic hinge forms at 50% greater moment for a rectangular section than the onset of yield, ignoring strain hardening, and even a single hinge does not cause collapse of the system: each arch is 3rd degree indeterminate, and can support two hinges before collapse. After initial arch yield the softer response of the yielded arch promotes load sharing between the arches. The soil also carries more load after initial arch yield due to decreased arch stiffness.

After completing the suite of live load tests it will also be important to find the ultimate system capacity. Load will be applied as a line across the apex until the arches fail. Ultimate load was estimated iteratively; load was applied to the apex until the moment exceeded the moment capacity for the arches; 9.6 kN-m to 15.8 kN-m for 115 mm concrete-filled FRP arches. The model predicted a failure load of 300 to 400 kN for the tall arch and 230 to 300 kN for the short arch. In both cases the capacity might exceed a single 250 kN actuator and it will be necessary to run two 250 kN actuators in tandem or a single 500 kN actuator, although this may not be possible due to space limitations. The failure analysis is also less accurate than other analyses; as load increases the soil plays a larger role and any error in soil behavior will be magnified. Despite loading a generous area, the 400 kN vertical load will apply 1200 kPa pressure under the

load beam and this pressure is likely to fail the soil, or at last cause excessive deformations that further concentrate the load.

Decking strength is a concern. Decking was evaluated based on the National Design Specification for Wood Construction (American Wood Council, 2005). This standard is based on allowable service loads; no load factors were required for analysis. In a very conservative assumption the plywood was ignored in analysis; this will under represent the total decking capacity. Two areas of concern are the dead load pressure near the footing and the live load pressure at the apex during ultimate load. The footing does not see much live load and the apex has little dead load. Allowable bending stress for #2 SPF-s is 5.3 MPa, but when flat use, repetitive member, shape, and load duration factors are considered the long-term capacity (month – dead load) is 11.6 MPa and the short-term capacity (10 min – ultimate load) is 16.2 MPa. Weak axis section modulus per unit width is 240 mm^3/mm; failure moment is 71 N-m. For compacted soil the horizontal pressure coefficient K can be taken as 1.0 at-rest (the footing does not move, soil is at-rest near the footing), the same as the vertical pressure. The stud will therefore have pressure equal to the weight of the soil above in the weak axis direction regardless of the orientation of the stud. Max moment is 70 N-m from 2.9 m of soil in the tall arch, below the allowable moment. Ultimate load decking force was taken as the point-applied gravity load at the apex node from analysis, 10 kN over a 0.10 m^2 tributary area. Also, the load is calculated assuming the soil does not deform; soil deformation will reduce the cover and reduce load propagation through the soil. The decking moment is 121 N-m, above the 70 N-m capacity of the lumber. Without the composite action the sheathing will still add some capacity, but for added safety an additional 2x4 above the sheathing bolted onto the 2x4 below will give enough

capacity, without composite action, to meet the load requirements. Away from the load source it is unlikely that the decking will fail, since vertical soil pressures drop rapidly.

2.4.6. Verification of Horizontal Pressure

The goal of this study is to determine soil structure interaction for a buried structure by mimicking the horizontal soil pressure for a scaled structure and testing it in the lab. As stated previously the most important horizontal soil pressure is the change, after considering the dead load pressures, caused by an apex live load. Horizontal soil load is calculated per node and is generated using tributary area assumptions. Nodes closer to the apex have smaller vertical areas and less vertical overburden and therefore have less potential to generate horizontal soil loads, while nodes closer to the footings have larger areas and more overburden, generating larger horizontal soil loads. In the transition from dead load only to dead plus live load, as shown in Figures 16-19, the nodes near the apex become more active, but the large increase in overburden pressure still causes a large pressure spike on the arches. Nodes closer to the shoulders deflect into the soil transitioning from active pressures to at-rest or even passive pressures, which generate a greater soil pressure. Near the footings the arches do not change horizontal soil pressure much, but the increase in horizontal load is still relatively high because of larger vertical tributary areas.

Change in pressure is compared at all points: error is calculated as the square root of the sum of the square of the difference between the target pressure and the subscale pressure (scaled by a factor of 2) divided by the sum of the target pressure. If this error term is zero, the numbers are identical and if error is greater than 1, the subscale model fits worse than zero pressure. The computed error can be deceptive; simulations that are divergent in only a couple of points can

show a large error even if many of the points are close. Small pressure changes, near zero, have little weight; good approximations of low values do not help the error estimate. For example, the computed error is 0.324 for the 115 mm subscale depicted in Figure 2.15, but 30% of the error comes near the far shoulder (5 nodes, 8% of the span) where the subscale's peak is higher and the secondary peak is off by a couple nodes. For the short arch in Figure 2.16 the fit is slightly better; the error was 0.281. Most of the error was at the shoulders as the full-scale model distributes pressure over a greater percentage of the arclength. This is ultimately still a reasonable fit.

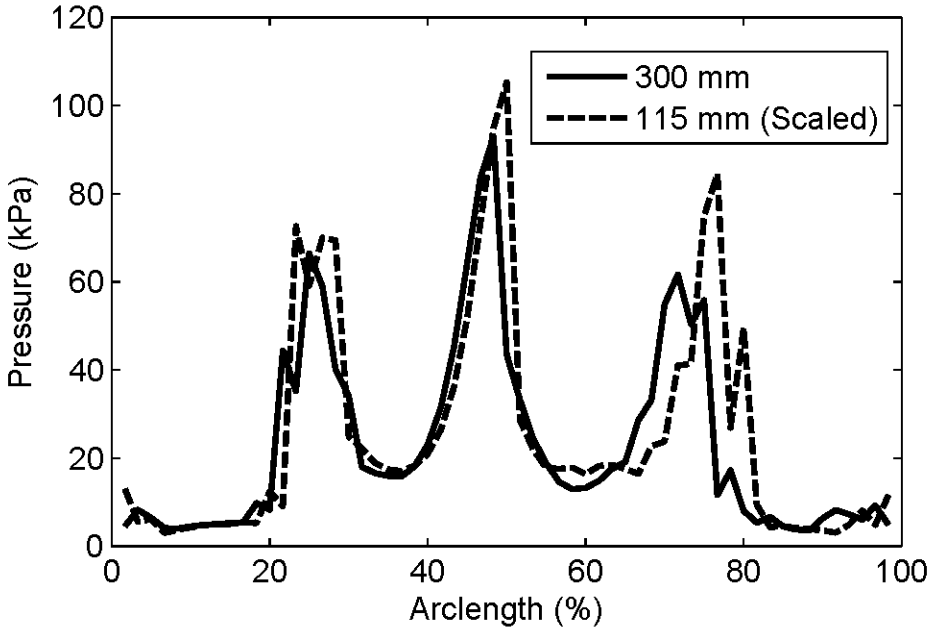

Figure 2.15. Scaled Change in Horizontal Pressure, Tall

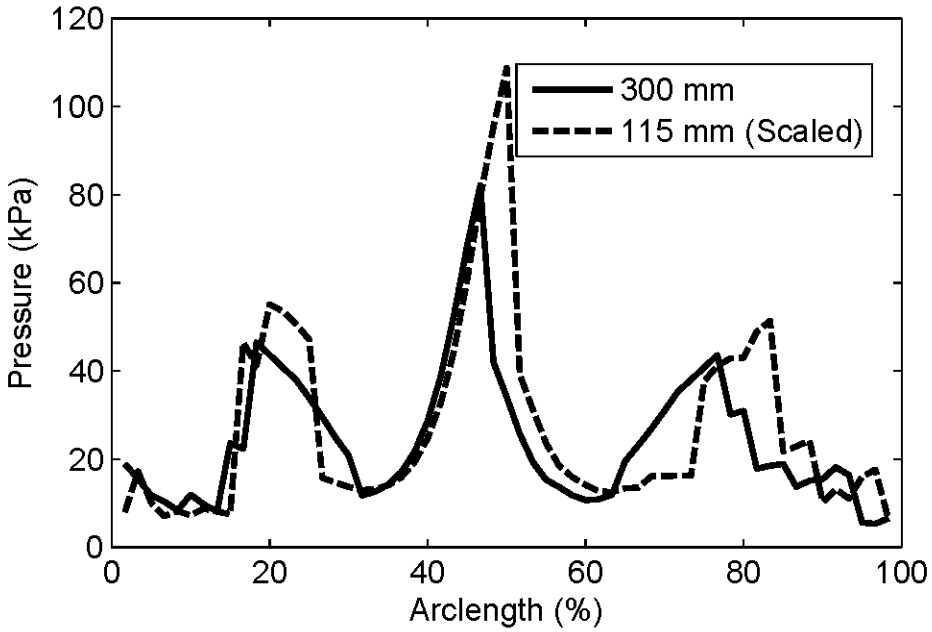

Figure 2.16. Scaled Change in Horizontal Pressure, Short

Overall, there was very little change to the horizontal soil pressure when the moment curvature relationship changed for the concrete arches. Changing the concrete strength has more effect on backfilling deflections, but minimal effects on deflections and horizontal pressures caused by apex load. Figure 2.17 shows the pressure difference for 34 MPa and a low strength 10 MPa concrete subscale tall arch. The lower strength concrete does behave more similarly to the full-scale, with an error of 0.255, but there are additional effects with changing the concrete mix, such as shrinkage and flowability, which outweigh the small improvement in replication.

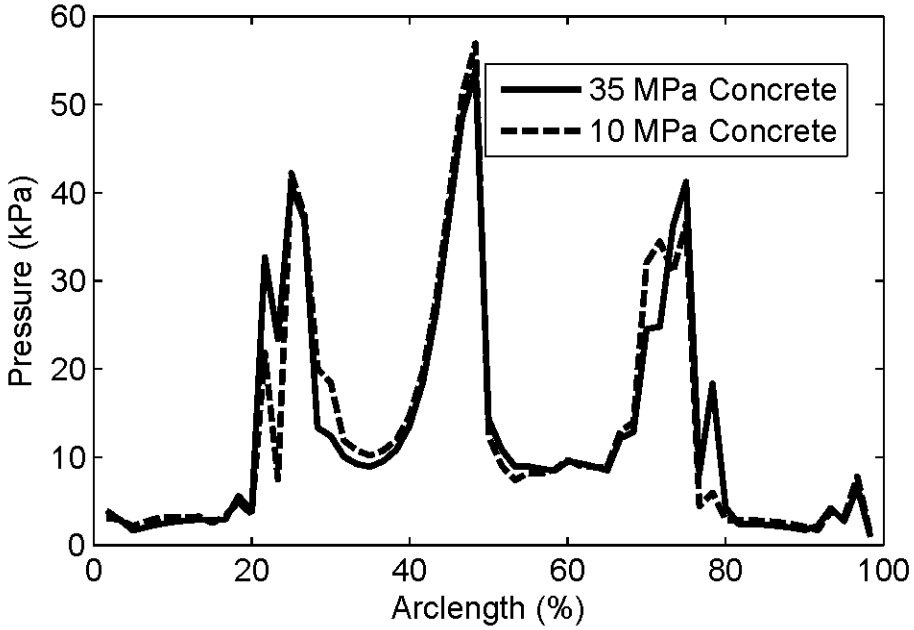

Figure 2.17. Horizontal Soil Pressure with Different Concrete Strengths

The steel arches were sized specifically to reproduce the horizontal soil pressures of the full-scale arches by varying the bending stiffness. No stiffness will be a good fit for all nodes; the selected section had the minimum value for any common bar stock section (in 50ksi). For the tall arch the fit is remarkably good; error was 0.075, and Figure 2.18 displays how close the values fit. For the short arch the fit was worse, error was 0.248, and Figure 2.19 displays this comparison. The fit could be improved by using a slightly higher moment of inertia, closer to 620,000 mm^3 instead of 550,000 mm^4, but there are no common bar stocks that are near that size, a 1.5x5.5 (38 mm x 140 mm) would give a better fit than the 2x2 (51 mm x 51 mm), but that is a custom section and requires double the steel area. The selected shape does have a similar error to the FRP subscale and is a reasonable solution. Alternatively, an HSS4x2x0.5 rectangular section, in weak access bending, also produces a better fit if it does not change shape during bending.

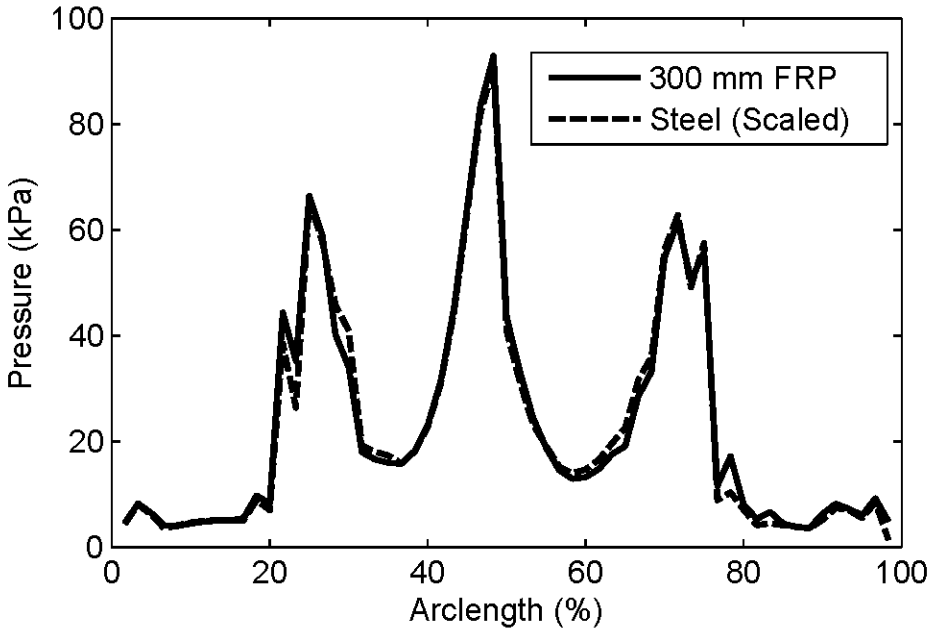

Figure 2.18. Tall Arch, Steel Comparison

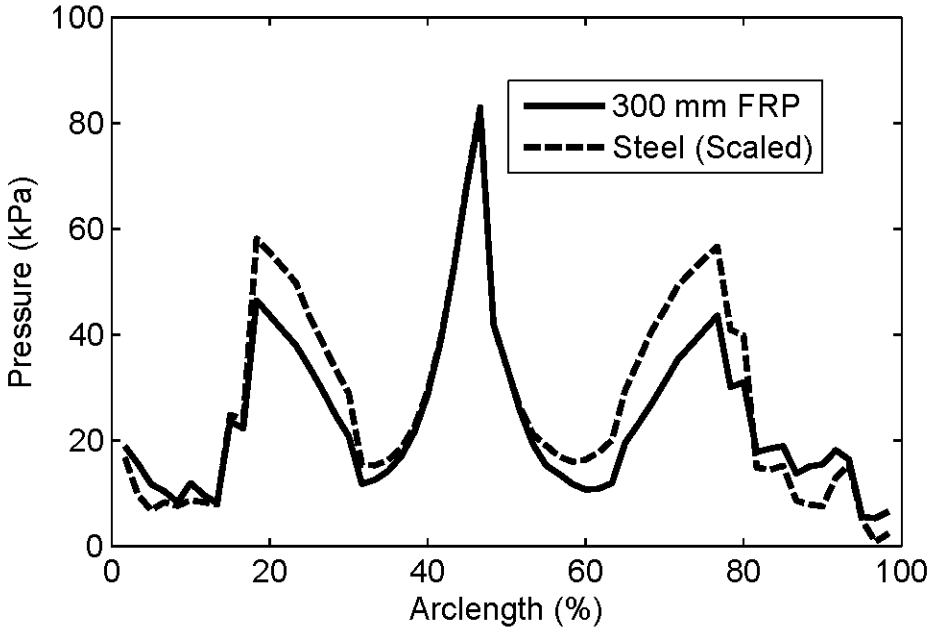

Figure 2.19. Short Arch, Steel Comparison

Horizontal soil pressure can be deceptive near the apex and footings. The model does not include soil springs at either the footings or the apex because the model footings are fixed against horizontal translation and any force corresponding to a fixed degree of freedom will be zeroed. The apex does not have a node because the apex has virtually no vertical tributary area; regardless of how large the horizontal pressure, it would not apply a horizontal force in the model. Similarly, the large spike in horizontal pressure at the apex of the model due to applied live load does not create a large spike in horizontal force. The horizontal forces of the nodes near the center remain modest compared to the forces near the footings and shoulders due to the relative vertical area.

2.5. Conclusions

By scaling the bending stiffness of the FRP arches there is a reasonable approximation of horizontal soil pressures. While further decreasing the arch stiffness produces a better fit to horizontal pressure, it comes at a price to manufacturability, structural similarity to the full-scale arch, and may compromise structural capacity needed in the testing program. A consequence of this scaling is a loss in deflection matching; the subscale arches must deflect less than the full scale arches to generate the same horizontal pressures, and this is unconditionally true if soil stiffness and load are dependent on the height of the arch.

Steel sections are limited primarily by strength and availability. For 345 MPa steel, sections were selected that are hot-rolled bar shapes, although they could be cut from plates. A 345 MPa 1.5x4 bar stock (38 mm by 102 mm) weak axis was used for the tall steel bridge and a 345 MPa 2x2 bar stock (51 mm square) was used for the short steel bridge.

CHAPTER 3. EXPERIMENTAL PROGRAM

3.1. Introduction

This chapter describes the laboratory testing effort for understanding soil-structure interaction for buried composite arch bridges. Laboratory testing is divided into three parts: soil box tests and construction, soil component tests, and structural component tests. Soil box testing was an extensive operation to find experimental response of buried arch bridges, and results are in Chapter 6 for steel arches and Chapter 7 for CFFT arches.

Prior testing on CFFT arches has focused on structural capacity as stand-alone components (Bannon 2009; Dagher et al. 2012), construction loading effects including local wall buckling during concrete filling (Davids et al. 2012; Walton 2011), and FRP material durability (Demkowicz 2011). Full-scale systems have been tested as part of load rating procedures (Goslin et al. 2015) and measured strains are small compared to predictions, with values typically under 20 microstrain. Long-term field monitoring was performed on a CFFT arch bridge constructed in Fitchburg, MA with live load capacity as the controlling design factor (Quinn et al. 2013). Results measured during bridge loading by two dump trucks indicated FRP extreme fiber strain was smaller than 50 microstrain, equivalent to approximately 0.3% of the fiber tensile strain capacity and 5% of the magnitude of seasonal temperature-induced strains (Quinn et al. 2013).

While the buried CFFT arch bridge system motivates the present study, there has been significant research conducted over the past 20 years examining other buried bridges, typically steel plate structures. Large-span steel culverts and box culverts are similar to CFFT arch structures. They often have shallow cover compared to span, making live load distribution important (Mak et al. 2009), but the high rise of the legs of the arch or culvert can result in

higher moments due to backfilling than due to service live load (Vaslestad et al. 2002). In contrast, small culverts are traditionally buried under sufficient soil such that live load can be effectively analyzed as a uniform pressure acting over a 1:1.15 (depth to spread) area where pressure from all wheel loads is applied uniformly over the spread area (AASHTO 2014).

Research has examined backfill loading (Manko and Beben 2005, Yeau et al. 2009, Mak et al. 2009, Bayoglu Flener 2010a, Vaselstad et al. 2002, Machelski et al. 2009), static live loading (Manko and Beben 2005, Yeau et al. 2009, Bayoglu Flener 2010b), and dynamic live loading (Beben 2013, Sezen et al. 2008). A field study including dynamic live load application has indicated that compressive strains are greater and tensile strains are smaller from dynamic loading than from static loading. This is likely due to lower moment and higher axial force from a dynamic load than a static load (Beben 2013). The effect of dynamic loading was not considered in the current study.

In a study of shallow buried box culverts experimental apex moments were lower than typical Swedish and Canadian design moments by a factor of 3 to 4 depending on cover depth (Bayoglu Flener 2010a), and typical design methods did not capture nonlinearity as applied load approached ultimate capacity (Bayoglu Flener, 2009). However, apex dead load moments compared well with the Swedish design method (Bayoglu Flener 2010b).

Structures with similar geometry (span, rise, cover depth, base angle of arch) and construction methods (superstructure cast in concrete foundations, soil compacted in lifts) exhibit similar behavior, traditional design methods can produce excessively conservative results when applied to long-span buried arches with shallow cover. These issues motivate the development and execution of the experimental program detailed in this chapter.

3.2. Scaled Arch Bridge Tests

This section describes particulars of scaled arch bridge testing. The Advanced Structures and Composites Center does not have a dedicated soil-structure testing facility, thus testing began by constructing a specialized temporary soil containment system hereafter referred to as the ‘soil box’ depicted in Figure 3.1. Steel and CFFT Arch bridge specimens were prepared. Groups of three arches were placed in the soil box and wooden decking was secured to the arches. Instrumentation was placed on and around the specimen to measure arch strains, arch deflections, foundation spreading forces, soil pressures, and applied live load. Arches were backfilled in progressive lifts mimicking field bridge construction. Arches were loaded with a series of distributed live loads as described in Chapter 2. After service loading the footings ties were released and live load testing sequence was repeated. After all service loading the arch bridge was loaded at the apex until failure. Compass directions are used to differentiate the orientation and position of parts of the test. The span of the bridge lies in the North-South direction and the span of the decking lies in the East-West direction.

Figure 3.1. West Side of Soil Box, During Backfilling

3.2.1. Soil Box Structural Design

The soil box enclosed a space 12.2 m long, 2.2 m wide, and 3.8 m tall and was designed to resist the soil assuming a lateral earth pressure coefficient (*K*) of 1. Bridges were 6.1 m span length, with a maximum of 6.6 m from outside of foundation to outside of foundation. This provided 2.8 m between end walls and the back of footing, which is 16 times larger than the combined decking thickness and arch diameter.

Consisting mainly of rough-sawn eastern hemlock timbers, the East-West (12.2 m) sides of the soil box were made from five 2.44 m long, 3.8 m tall wall panels per side. The panels used horizontal 4x4 (100 mm x 100 mm) timbers for the interior wall surface, which acted as sheathing. Sheathing timbers were fastened with 178 mm long, 9.5 mm diameter lag screws to

8x8 (200 mm x 200 mm) soldier beams spaced at 609 mm on center. Wall panels were supported by 10x10 (250 mm x 250 mm) walers, horizontal retaining wall members, positioned as shown in the schematic in Figure 3.2. The walers were connected with 19 mm through rods to make the walls self-reacting, and timber bracing was used before soil was placed to provide stability to the wall system. Rods were positioned as shown in Figure 3.2 such that rods not in the soil (below the bridge) were more than 150 mm away from arches to prevent contact during testing. Rods embedded in the soil (above the bridge) were greater than 760 mm away from arches to minimize their effect on soil movement for both bridge geometries. The center wall panel of the East and West walls had openings on of 1.63 m by 1.22 m to allow access to workers to install gauges after all soil box walls were erected.

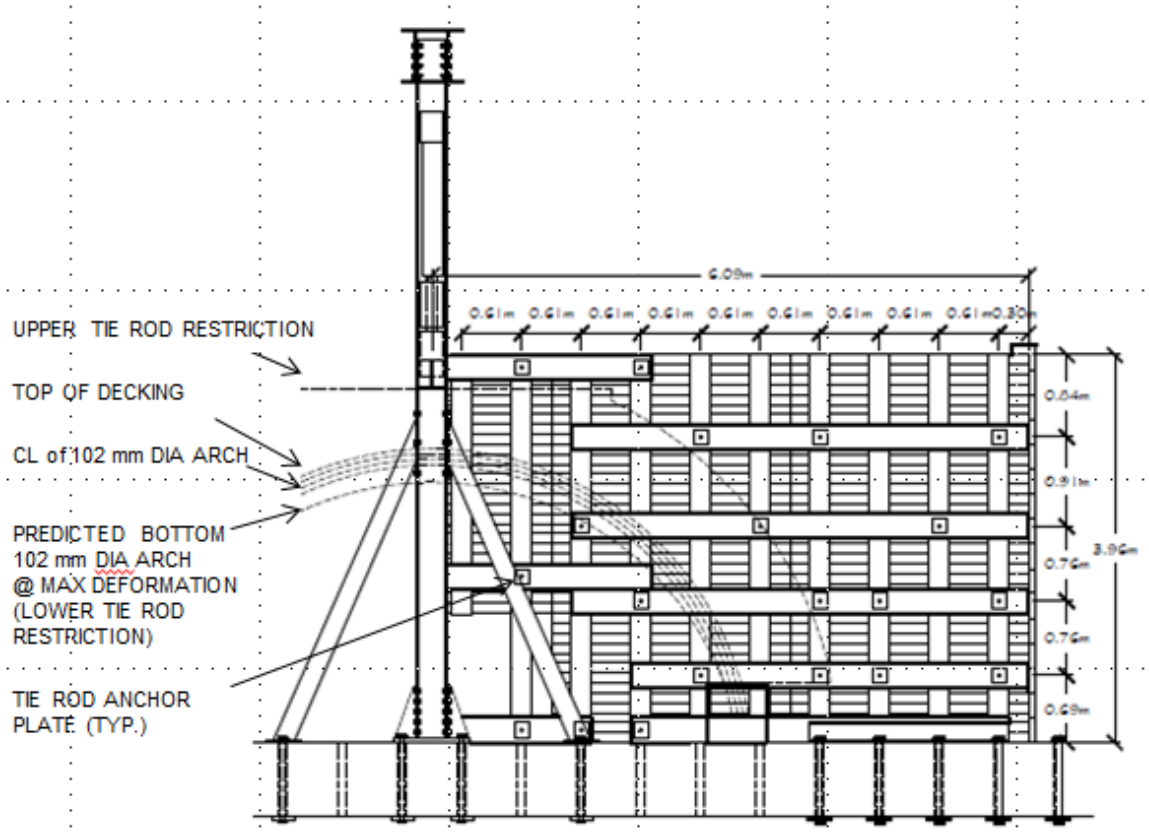

Figure 3.2. Schematic of the Side Walls with Tie Rod Locations and Arch Limits

The South wall, shown in Figure 3.3, was made of pre-cast concrete H-sections with flange width 3050 mm, flange thickness 460 mm, web height 1980 mm, and web thickness 460 mm. Existing laboratory infrastructure, this wall was post-tensioned through its 3.66 m height and through the 840 mm thick floor, making this wall rigid. The North wall, with a picture and schematic in Figure 3.4, was designed to resist the full footing thrust during ultimate load testing. This wall was hemlock 10x10 (250 mm by 250 mm) sheathing supported by (2) HP10x42 steel soldier beams (254 mm deep, 62 kg/m), supported by 2C10x25 double channel walers (254 mm deep, 37 kg/m). The North wall was not connected to the floor and was removable. The free-standing concrete wall and the mobile wood and steel wall were tied together with six, 19 mm diameter horizontal cables, making those walls self-reacting.

Figure 3.3. South End Wall Photograph

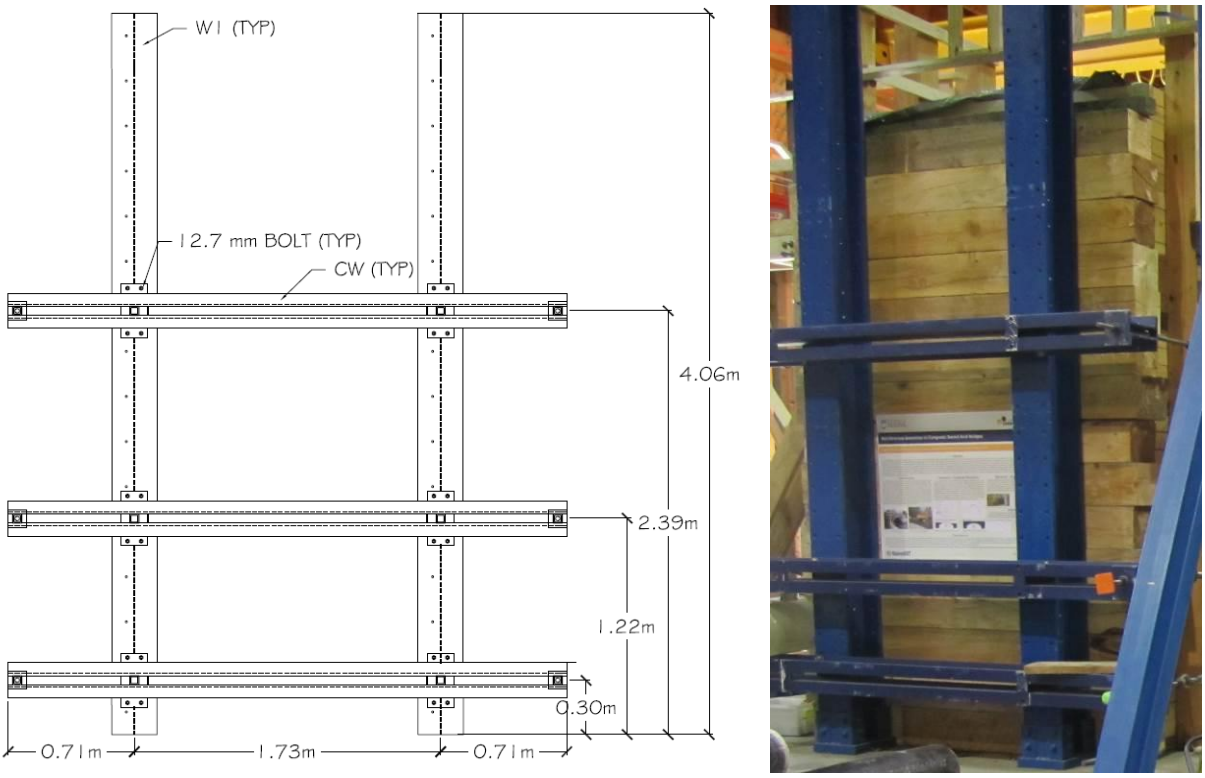

Figure 3.4. North End Wall Schematic and Photograph

Access to the top of the soil box was through a series of wooden stairs, platforms, and ladders specifically constructed for this project and designed to support a 2.2 kN point live load or a 2 kPa uniform live load in addition to self-weight. External access to the top of the soil box was provided along the East side of the soil box. A staircase gave access to the North side of a three platform system 3.66 m above the lab floor, which was level with the tallest bridge. Two 2.44 m by 2.44 m platforms allowed access to the North and South ends of the soil box, and a third 4.9 m x 0.6 m catwalk allowed access from the North platform to the South platform, as shown in Figure 3.5. The platforms were spaced such that there would be no interference during live loading with the steel reaction frame that holds the hydraulic actuators described later.

Figure 3.5. West Wall with Catwalk, Stairs, and Access Platform

Access to the floor inside of the soil box was provided by a series of descending platforms and ladders that were modified over the course of experimentation. Initially, a two platform system was used as shown in Figure 3.6. The upper platform was at elevation 3.66 m and was 1.22 m wide North-South and 0.76 m long East-West. This platform was bolted to two double wooden spruce-pine-fir, South (SPF-S) 2x6 (38 mm by 140 mm) lumber members, which ran across the soil box East-West and were supported on top of the 4x4 walls. A second platform at elevation 1.83 m directly underneath the first platform was 2.1 m long East-West by 1.22 m wide North-South and hung from the upper platform by SPF-S 2x4 (38 mm by 89 mm) tension members. This platform system used all bolted connections and allowed easy, stable access to the soil box. However, it was difficult and time consuming to raise while installing soil lifts. An improved solution was to use a single platform with four SPF-S 2x8 (38 mm by 184 mm) tension members that were nailed directly to the soil box with 16d duplex nails. All gaps between platforms were reached with wooden leaning ladders.

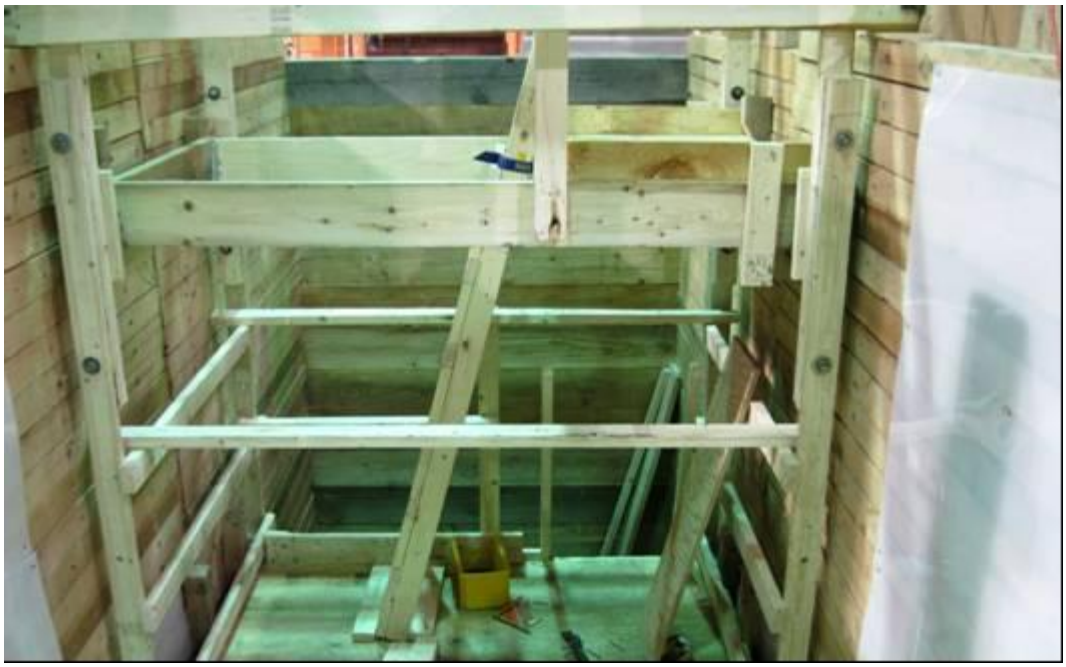

Figure 3.6. Internal Platforms for Soilbox Floor Access

3.2.2. Load Frame Modification

Typical tests in the Structural Testing Lab (STL) at the Advanced Structures and Composites Center use hydraulic actuators supported by steel load frames that transfer the load to the concrete floor. The reaction frame is comprised of two towers made from double W12x65 columns (305mm x 97 kg/m) and double W21x105 load beams (533 mm x 156 kg/m). The typical reaction frames were not wide enough or tall enough to accommodate this test. The large reaction frames are designed for fatigue loading with a 1500 kN actuator. For the first bridge tested (tall steel) a 250 kN actuator was used, shown in Figure 3.7, but this was pushed to its limit during ultimate load and all subsequent tests were with a 500 kN actuator. Because a smaller, 500 kN actuator was used in the test the full capacity of the frame was not needed. This allowed the reaction frame top beam to be extended with steel plates, shown in a schematic in Figure 3.8, and raised one hole above the top of the actuator and still provide adequate safety

against beam shear or bolt shear when loaded with the maximum actuator load. Expanding the width of the reaction frame also required a new H-frame to provide lateral support to the actuator.

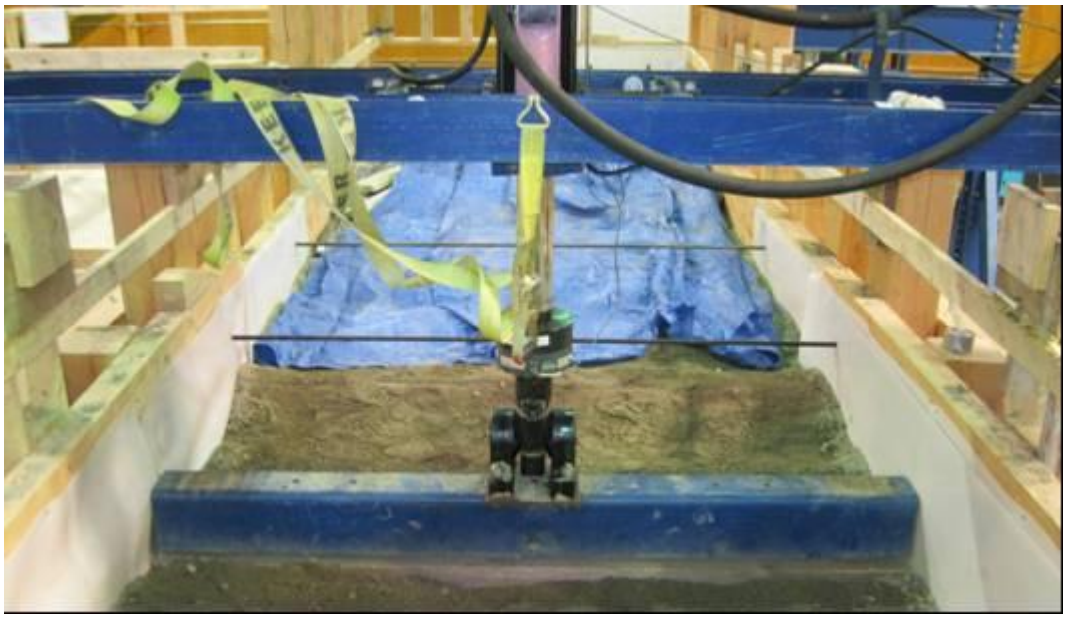

Figure 3.7. 250 kN Actuator, Ultimate Load, Tall Steel Bridge

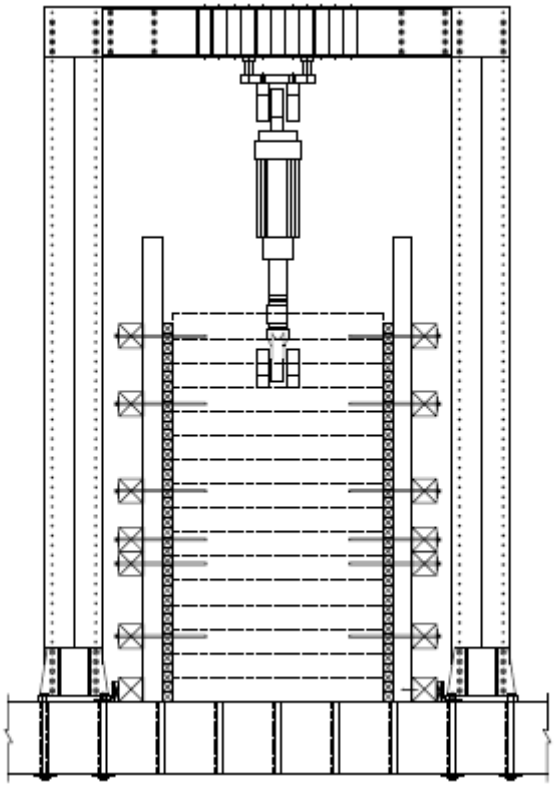

Figure 3.8. Load Frame and Soil Box Schematic with 500 kN actuator

The frame was moved between every live load test. Typically, the reaction frame is held to the floor with (16) 54 mm Grade B7 threaded rods, designed to provide adequate safety for fatigue loading with a 1500 kN actuator. These rods and nuts were prohibitively heavy and difficult to move, and given the number of times that the frame was moved would have greatly increased testing time. The large rods were replaced with 25 mm Grade B7 rods which had adequate strength given the capacity of the actuator.

A consequence of raising the center frame beam near or above the top of the reaction frame was that the 90 kN lab cranes were unable to lift the center load beam in a single crane pick, which is the typical method of moving the frames. To correct this, a lifting mechanism was built to lower the elevation of the pick point and to provide two pick points so that the frame could be

lifted with both cranes. The lifting adapter was made of two 5.5 m box beams HSS 10x10x1/2 (254 mm by 254 mm, 13 mm wall thickness) in the span of bridge direction, two 2.3 m box beams HSS 8x8x3/8 (203 mm by 203 mm, 9.5 mm wall thickness) in the bridge transverse direction, and is shown in Figure 3.9.

The smaller transverse box beams were bolted underneath the larger longitudinal box beams by single 25 mm B7 rods at the four intersections. The rods were torqued to 200 kN-M, creating greater clamping force in the four rods than the weight of the entire reaction frame, which prevented slipping while lifting the frame, causing racking or movement of the lifting mechanism. The longitudinal box beams were connected to the center load beam with four 19 mm B7 rods per box beam. Rods were connected to C4x7.2 (102 mm tall, 106 N/m) double channel sections above the center load beam and below the longitudinal box beams in the lifting mechanism.

3.2.3. Subscale Structures

Four different subscale arch bridges were constructed following the scaled specifications determined in Chapter 2. Each three-arch arch bridge system had a 6.1 m span and a 760 mm arch spacing. Two different rises were considered: a rise of 2.3 m, hereafter referred to as the 'tall arch', and a rise of 1.2 m, hereafter referred to as the 'short arch'. Both arch geometries had a steel arch system and a CFFT arch system scaled following the procedures in Chapter 2, thus there were no replicates and every test was of a unique system. All arches were cast into 610 mm by 610 mm by 2150 mm (in length) concrete spread footing foundations designed for bending strength and punching shear that were reinforced as shown in Figure 3.10. Foundation dimensions were not strength dependent or bearing dependent (as these bridges were built on a concrete floor). Foundations were dimensionally scaled to be half of the size of typical CFFT bridge footings. Also, footings needed to be large enough to provide 300 mm minimum embedment length to develop arch-foundation fixity. Tall arches joined the foundations at an angle of 73° measured from the horizontal with a between-foundation arclength of 8.19 m and a radius of 3.2 m. Short arches joined the foundation at an angle of 44° measured from the horizontal with a between foundation arclength of 6.73 m and a curvature of 4.42 m. The tall arch joined the footing at the middle of the top footing surface, 300 mm from the front edge, while the short arch joined the footing 150 mm from the front edge due to arch bottom angle and required embedment length.

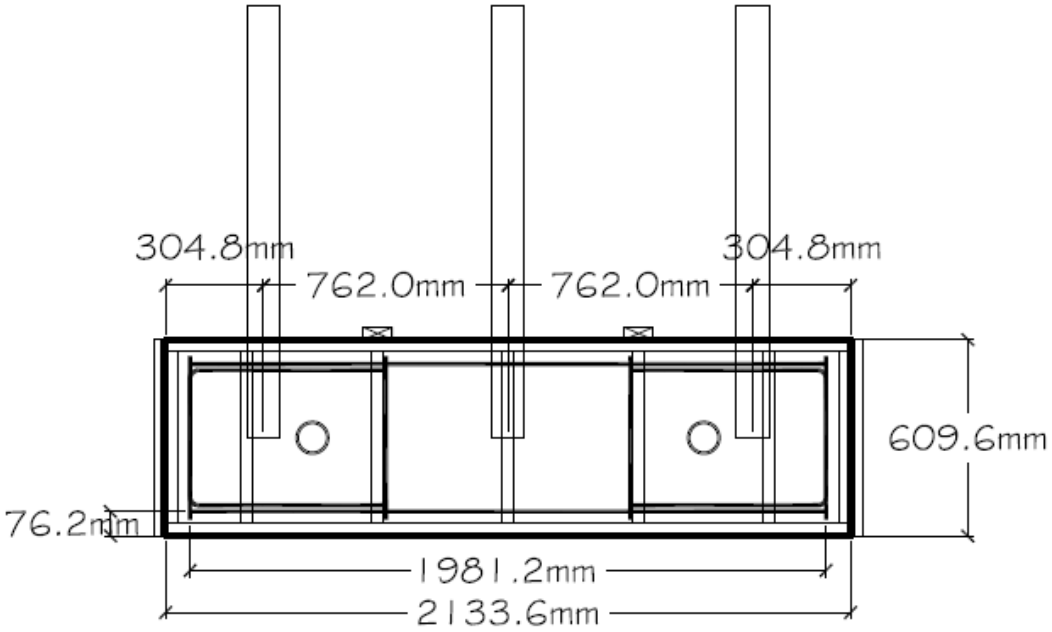

Figure 3.10. Plan View of Footing for Short Steel Arches

Tall steel arches were 1.5x4 (38 mm x 102 mm) 345 MPa bar stock and short steel arches were 2x2 (51 mm x 51 mm) 345 MPa bar stock. Steel arches were fabricated from 6.1 m long pieces that were hydraulically bent to the proper radius. Bent segments were butt welded to get the proper length. The tall arches needed an additional 2.8 m of material, which would place the weld in a local maximum moment. Therefore, 1.4 m of material was added to both ends of the arch positioning the weld in a lower moment region located between the foundation and the shoulder. The short bridge required only 1.4 m of additional material, naturally placing the weld in a low moment area with a single addition. Tall steel arches placed in the soil box are shown in Figure 3.11.

Figure 3.11. Tall Steel Arches in Soil Box

Arches were not manufactured to a perfect geometry. Difference in arch shape was primarily noticeable in reference to footing position, and was most noticeable in regards to the tall steel arches possibly due to greater arclength and two welded sections. Apex elevation for the center arch was 6 mm higher than apex elevation for the outer two arches, which had the same measured elevation. Arches were supported at the third points when the footings were cast and elevations were negligibly different at the third points and the quarter points for all three arches. The West tall steel arch span length was 60 mm longer than specified and the East tall steel arch was 19 mm longer than specified. This difference was split between the two footings to make the bridge as symmetric as possible North to South.

CFFT subscale arches used materials specified based on scaling given in Chapter 2. Arches were manufactured from two layers of braided E-glass fiber with inner layer thickness 1.2 mm and angle ± 81° and outer layer thickness 0.9 mm and angle ± 21°. Manufactured diameter was 110 mm, which is 5% smaller than the specified diameter of 115 mm. Arches were infused with Derakane 610C resin from two ports located at the apex. Four CFFT arches were made for both

the tall rise and the short rise: three arches of each rise were used in three-arch bridges, the additional arch for each rise was used in isolated arch tests described later in this chapter.

Typically arches are filled with concrete from a 76 mm hole at the apex after being cast in concrete foundations. However, this typical hole size is greater than 60% of the manufactured diameter of the subscale arches, and it was determined that cutting a hole that large and filling from the apex created an unacceptable risk of local buckling failure based on prior research on local buckling of CFFT arches during filling (Walton 2011). Therefore, arches were positioned upside down in custom wooden trusses as shown in Figure 3.12, which fully supported the arches while being filled from the arch ends in Figure 3.13. Tall arches and short arches were cast separately to reuse the truss formwork for both arch geometries. The truss formwork was also used to fully support the filled arches when they were flipped upright and cast into concrete foundations, identical to those used for steel arches. Due to the restrictive truss formwork the geometry was more uniform for CFFT arches than steel arches: rise and span for each arch was within 6 mm of specifications.

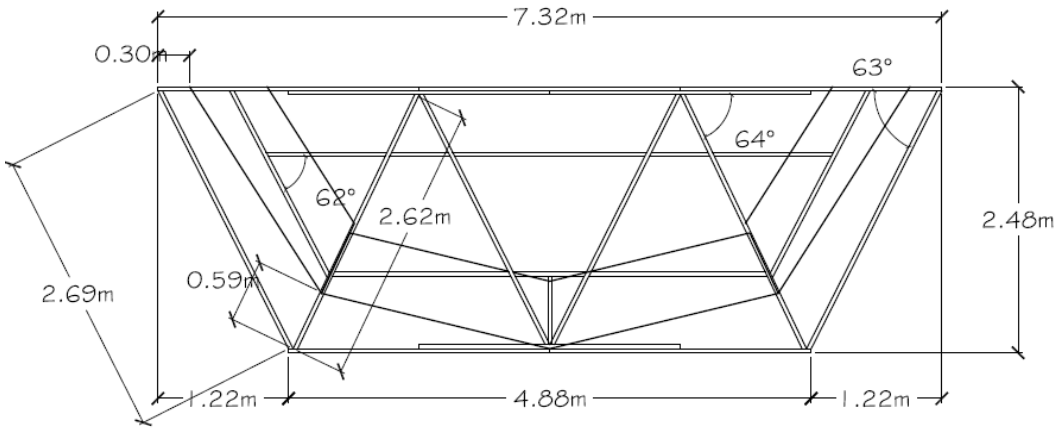

Figure 3.12. Schematic of Truss Formwork for Arch Filling

Figure 3.13. Tall CFFT Arches in Wooden Truss Forms Being Filled with Concrete

3.2.4. Decking

As explained in Chapter 2 decking was transverse stiffness-scaled for a typical (in 2012) cracked concrete deck section. A photograph of scaled decking is shown in Figure 3.14. The scaled decking was made from continuous 2.15 m long 2x4 (38 mm x 89 mm) weak-axis planks covered with ¾ inch nominal (17.5 mm) plywood. 2x4 planks were spaced from the arch with ¾ plywood strips with gaps at strain gauge locations, detailed in 3.2.6.1, to allow space for strain gauges on the top of the arches. Decking units were connected to each other with continuous strips of ½ inch nominal plywood (11 mm) and 41 mm wood screws. Decking was fastened to the arches with 290 mm long 2x4 boards connected to the decking with 127 mm long, 6.4 mm diameter lag screws for the steel arches and 178 mm long, 9.5 mm diameter lag screws for CFFT arches. Decking was smaller than the inner dimension of the soil box to allow room for

placement of low-friction plastic pads and an initial gap between decking and the wall to limit friction.

Figure 3.14. Underside of Decking During Installation

3.2.5. Boundaries

The inner sides of the soil box were rough-sawn 4x4 timbers. To reduce friction, the timbers were covered with 3.2 mm thick low-friction HDPE plastic panels in the area where load was applied and adjacent to the decking. A second layer of HDPE 1.6 mm thick was placed over the first layer to create a sliding surface. To limit the amount of soil to fall through the gap between the decking and the walls, plastic sheeting was placed over the final 150 mm at the edge of the decking and connected to the HDPE wall panels. Figure 3.15 is a picture of soil box walls with plastic.

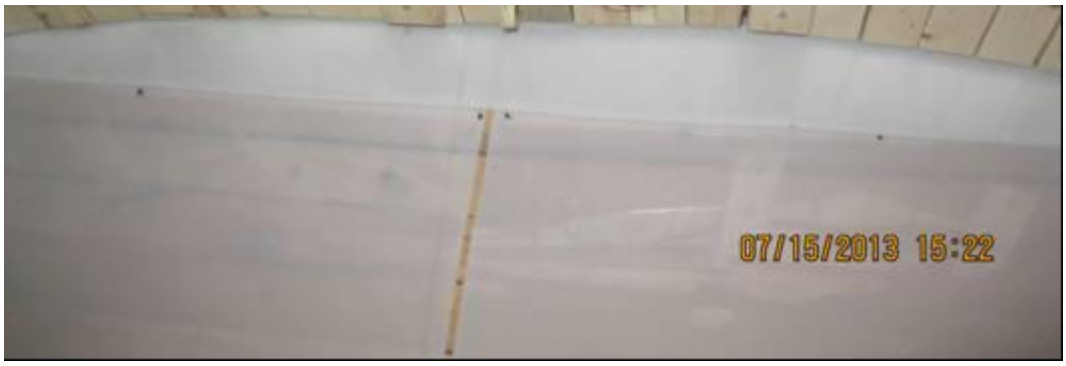

Figure 3.15. Plastic Attached to Soil Box Walls

A similar boundary was created under the footing. A 6.4 mm thick layer of OSB was placed on the concrete floor to deform into tie down divots spaced at 609 mm on center on the floor. A layer of 3.2 mm HDPE was placed atop the OSB and a layer of 1.6 mm thick HDPE was placed atop the lower layer of HDPE. The two slippery plastic surfaces were intended to create a reduced friction base so that tests with the footing ties released would represent a worst-case soil under a spread footing with very low soil-footing friction. Figure 3.16 shows an edge view of all three layers placed under a footing.

Figure 3.16. Edge View of Materials Under Arch Footings

During backfilling and during initial service live loading the footings were tied together (North-South direction) with steel rods to simulate a fixed foundation, shown in Figure 3.17. Tie rods were intended to limit deflection due to arch and decking self-weight, soil applied above the apex of the arches, and live loads. A four-rod two box beam connection described below was used on both the East and West sides of the foundations to make two independent tie rods that were easily removable during testing for two different foundation conditions. A simpler solution, two rods coupled in the middle, would have been more difficult or impossible to disconnect during testing because only one end of the rod in that system would be accessible in the space under the bridge.

Figure 3.17. Disconnected Tie Rod With Box Beam and Load Cell

The other end was buried under several meters of soil. 3.66 m long, 550 mm^2 area Dywidag steel rods were placed in two pass through ports per foundation spaced 1.22 m (East side and West side of foundation). This were a total of four rods: North-East, South-East, North-West, and South-West. The ends of the rods away from the foundations (near the center of the span) were connected to HSS 3x3x3/8 (76 mm by 76 mm by 9.5 mm thick) box beams through holes drilled in the center of the box beams. The two East side box beams were joined together and the two West side box beams were joined together to make two independent ties using two 610 mm long, 25 mm diameter Grade B7 rods per connection. 25 mm rods were spaced 100 mm away from the Dywidag rod. When footings were disconnected, both nuts fastened to the 25 mm diameter rods were directly accessible in the space under the bridge and were easily removed. The box beams were removed from the Dywidag rods, and the Dywidag rods remained under the bridge freely cantilevering from the foundations.

While soil elevation is below the apex of the arches during backfilling, horizontal soil pressure drives the foundations toward each other, and the tie rods and low-friction plastic pads would not accurately represent foundation conditions on a real bridge. Tie rods were designed as tension-only members, and were of no use in limiting inward foundation movement. To resist this deflection, foundations were blocked with timbers and wedges. Wedges were driven between the concrete foundation and two 460 mm long 10x10 (250 mm by 250 m) hemlock timbers placed in end bearing against the side of an 1830 mm 10x10 timber. The 1830 mm 10x10 timber was tied to the concrete reaction floor with two post-tensioned 25 mm diameter rods. When positioning the arches, the through rods were tensioned against the wooden blocking systems to resist self-weight and get the intended average footing position. Figure 3.18 shows the blocking system for the tall steel bridge.

Figure 3.18. Wooden Blocking and Footing Instrumentation, Tall Steel Bridge

3.2.6. Instrumentation

Most of the instrumentation was distributed evenly along the arch arc length to capture results for all loading conditions. Gauges were arranged at the eighth points of the arc length. The numbering scheme referred to throughout this report has gauge locations based on live load position and soil lift order. Each soil lift below the bridge apex was applied individually per side with the 'South' side receiving a soil lift first and the 'North' side receiving soil secondarily. Gauges start at '0' at the south foundation and end at '8' for the north foundation. Gauge positions are displayed in Figure 3.19 for the tall rise arch geometry. The arrangement of several

gauges relative to the arch geometry is shown for gauge position 6 for the tall steel arch in Figure 3.20.

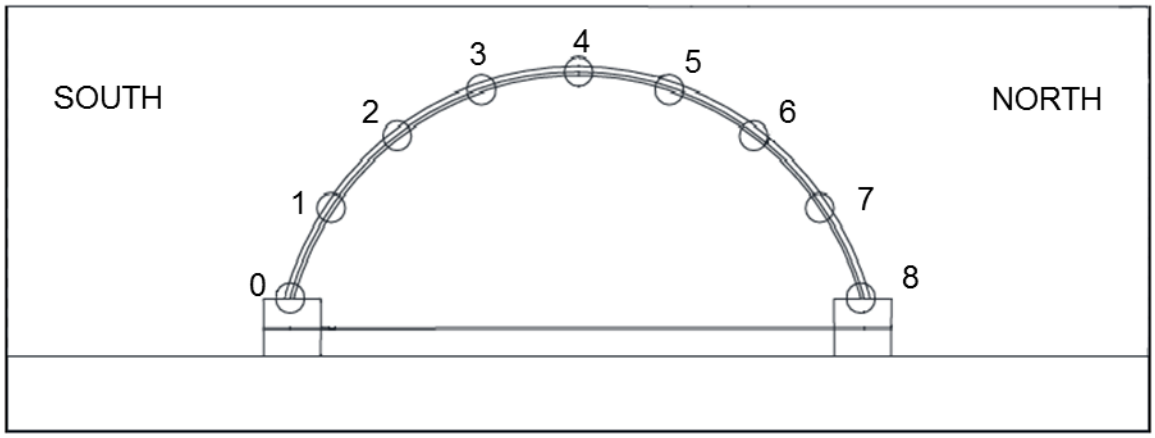

Figure 3.19. Gauge Positions Relative to Arch Span

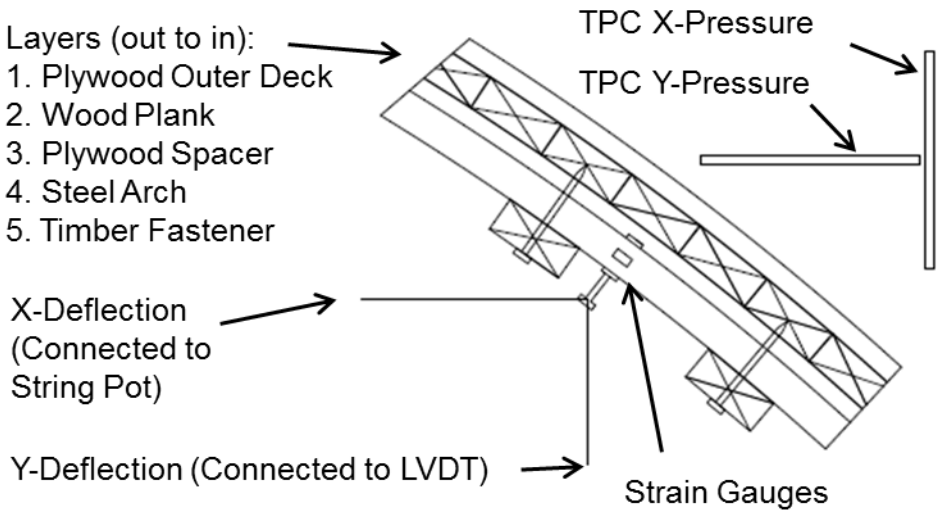

Figure 3.20. Detail of Gauges with Arch and Decking, Tall Steel Arch, Position 6

The zero point for pressure, deflection, tie rod load, and strain is assumed to be the start of backfilling, after arch placement. Data were collected at 1 Hz for all tests, except some backfilling stages for the tall bridge were collected at 0.1 Hz. Instrument noise for all gauges was

reduced using a nine-point moving weighted average during post processing. During backfilling, data were collected for the full working day. Backfilling was a multi-day process and the results of subsequent days are appended to the previous results, with the initial values at the start of a day assumed to be the final values of the prior day. Strains are stored during live loading so that total strains are known during ultimate loading when the arches yield.

3.2.6.1. Strain Gauges

Arch bending and axial strains were monitored with foil strain gauges located at points 0 through 8 of the center arch and at points 0, 4, and 8 for the two outer arches. Strain gauges were arranged in clusters of three per gauge location to measure strains at the top, bottom, and mid-depth of the arch section. The middle gauges were difficult to align accurately along the tangent of the arc, and data from them were not used due to questionable reliability, especially in steel sections with small thickness. The tall steel bridge used Vishay 3.2 mm strain gauges; all other bridges used Omega 13 mm strain gauges. Figure 3.21 shows foil strain gauges installed on a steel arch.

Figure 3.21. Foil Strain Gauge on Steel Arches

3.2.6.2. Displacement Gauges

Deflection was measured with 19 gauges for the tall steel arch and 21 gauges for all other arches except the ultimate load test on the short CFFT bridge where 25 gauges were used. Each arch had the same gauge configuration over the span. Point 4 (apex) vertical deflection was measured on each arch using 130 mm +/- LVDTs. Deflections 2, 3, 5, and 6 in the in-plane horizontal direction were measured using Celesco SP2, 640 mm string pots. Vertical deflection for those points was measured with 80 mm +/- LVDTs. Point 1 and 7 horizontal and vertical deflections were measured with 50 mm +/- LVDTs. The tall steel bridge had two 50 mm +/- LVDTs per foundation located at the mid height of the concrete foundation to measure horizontal foundation deflection. The other bridges had two 50 mm +/- LVDTs near the top of each concrete foundation and two 25 mm +/- LVDTs near the bottom to track foundation deflection and potential rotation. The ultimate load test for the short CFFT bridge also had four 25 mm +/- gauges to measure wall deflection.

All gauges except for footing gauges were lengthened with monofilament nylon line for a minimum gauge length of 1 m to limit interference from multidirectional arch movement. Deflection gauges were not directly connected to the arches: they were fastened to the wooden decking with lag screws. The lag screws were approximately 25 mm away from the arches so it is unlikely that decking flexure had any effect on the measured deflections. The decking was blocked from the arches with 19 mm of plywood in weak-axis bearing. Compressibility of this layer may have increased the negative deflection of the arches. influenced measured deflections more negative than arch movements. Figure 3.22 shows displacement gauges for half of the tall steel bridge.

Figure 3.22. Displacement Gauges Under Steel Bridge

3.2.6.3. Pressure Cells

Soil pressure was measured with Geokon 3500 total pressure cells (TPCs). TPCs were installed while placing the next full lift above the gauge elevation. (For example, a gauge located at an elevation of 900mm was installed with a 1000 mm – 1200 mm soil lift, not the previous lift of 800 mm – 1000 mm.) Horizontal and vertical gauge orientation refers to the direction of measured pressure, e.g. a horizontal gauge has a vertically positioned pressure pan to measure horizontal pressure. Eighteen TPCs were available for each test. After testing the tall steel arch, the TPC locations were modified for the other arches based on information quality. TPCs near the foundations and the apex had a range of 1 MPa, the other thirteen TPCs had a range of 250 kPa. Figure 3.23 is a pressure cell during installation.

Figure 3.23. TPC Being Installed to Measure Vertical Pressure

The tall steel bridge had two TPCs behind each foundation positioned at mid-height 455 mm from the centerline of the foundation to measure horizontal thrust. All other TPCs were in line with the center of the center arch. Each side of the bridge had a TPC midway between the soil box wall and the foundation measuring horizontal pressure. Positions 1, 2, and 3 had two TPCs to measure horizontal and vertical soil pressures. Positions 4, 5, 6, and 7 had TPCs measuring pressures normal to the arch (for position 4, normal is vertical). Additional TPCs were located in the soil mass mid-way between the arch and the soil box behind points 2 and 6 to measure horizontal pressure. The tall steel bridge was retested with under-compacted soil as defined later in this Chapter, and the gauge configuration was changed slightly: position 6 had a horizontal and vertical pressure TPC instead of a normal pressure and rear gauge. All other gauges for the under-compacted test were in the same positions described above for the compacted test.

The other bridges had a more symmetric TPC configuration. A TPC measured horizontal pressure behind the center of each foundation and a TPC measured vertical pressure from the centerline top of the foundation. A TPC was midway between the south foundation and the soil

box end wall behind the south foundation measuring horizontal pressure. All positions except 4 had a horizontal and vertical pressure TPC. Position 4 had only a vertical pressure TPC.

3.2.6.4. Load Cells

Omega LC8400 through-hole, washer-type load cells measured tie rod tension. Load cells were positioned between the North DYWIDAG rods and the North box beams for both tie rods. A load cell is shown in Figure 3.17 for an untied load cell. Measured tie rod tension was lower than anticipated because tie rods were anticipated to restrict all of the horizontal spread. Initially this was thought to be error in the gauge, and gauges of this type have been known to produce false readings with unsymmetric load. However, the tie rod tension was compared with load estimated from steel area and measured average footing spread, and it was determined that tie rod loads were close to expectation for the given spread, and poor understanding of the stiffness of soil behind the foundation led to undersized tie rods that were only a small percentage of the horizontal thrust force. In general, there was negligible difference in footing movement between loose and tied footing cases.

3.2.7. Backfilling Procedure

This section focuses on soil placement method and does not include information regarding soil properties, which are examined later in this chapter Soil backfilling was performed in lifts, and as is common during construction, lifts were not clearly demarcated. However, lifts were delineated TPC vibration data caused by the compactor. This allows data to be presented per lift instead of by time.

The number of backfill lifts differed for each bridge. The tall steel bridge initially was backfilled with compacted soil, installed in 150 mm lifts on alternating sides until Lift 14. Lift 1

was 450 mm on the South side and 300 mm on the North side. After Lift 14, soil was installed in 200 mm lifts. Soil lifts alternated until Lift 30, and the final three lifts were across both sides. For the tall bridge backfilled with under-compacted soil, Lift 1 was 600 mm on both the North and South side of the bridge. Lifts were constant soil volume, approximately 1.6 m^3, with average depth 200 mm and installed alternately on each side of the bridge. Soil lifts installed above the apex were also alternating for construction efficiency.

The other three bridges used the same lift schedule: consistent, approximately 200 mm thick lifts with lift 1 being 400 mm on the South side and 200 mm on the North side from the base of the foundation. Lifts alternated by adding 200 mm to each side of the bridge until level with the apex. The final three lifts were installed across both sides.

Soil was brought into the soil box using a 0.8 m^3 concrete dump bucket. The bucket was filled outside using a backhoe from a temporary soil storage area in the parking lot outside of the laboratory, Figure 3.24. The bucket was brought into the lab using a forklift and was moved into the soil box using an overhead gantry crane (Figure 3.25). Soil was dumped and hand spread with shovels to provide a level lift height Figure 3.26. Lift heights varied due to the size of the bucket and the amount of time to perform a lift: filling the bucket was quick compared to moving into the lab and moving it into the soil box. Initial lifts were two buckets of soil. It was inefficient to bring in smaller amounts of soil in a third bucket per lift to keep lift height uniform. The first 6 lifts per side were two buckets, the remaining lifts were three buckets. This meant that lift height dropped below 200 mm, and then afterward increased above 200 mm when a third bucket was used. Also, the bucket was not filled uniformly and some lifts were deeper or shallower based on the specific bucket fill level.

Figure 3.24. Bucket Being Filled with a Backhoe

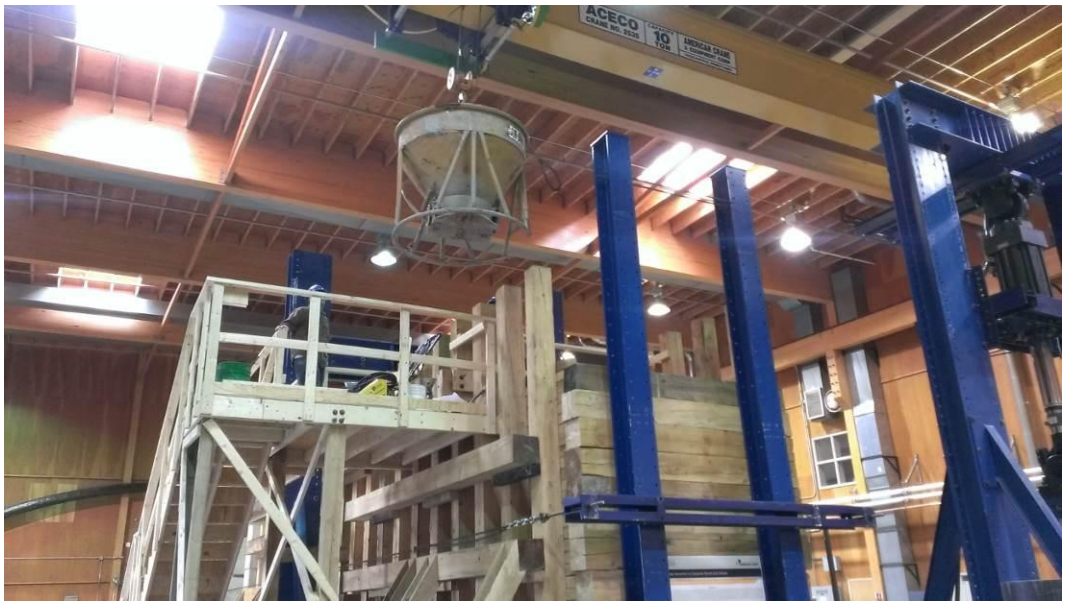

Figure 3.25. Soil Bucket Brought Into Soil Box with Overhead Crane

Figure 3.26. Soil Spread by Shovel Prior to Compaction

After soil was dumped a specimen was collected for moisture content testing. The soil was spread uniformly for the lift and was compacted with a 9800 N vibratory plate compactor, Figure 3.27. Two sand cone density tests were performed per lift. As soil depth increased steel through rods were installed through the soil mass. Rods were installed whenever the next compacted lift would be higher than the rod. Rod location is shown earlier in Figure 3.2. TPCs were installed during backfilling. The TPCs were installed when the next full lift above the gauge was placed to guarantee at least 150 mm of cover between the compactor and the gauge; on average there was 300 mm of cover over each gauge when installed.

Figure 3.27. Compacted Soil Lift

3.2.8. Live Load Procedure

To load each arch as equally as possible, live load was applied vertically using a hydraulic actuator with an HSS8x6x½ spreader beam having dimensions of 152 mm parallel to the bridge span and 2.1 m transverse to the bridge. Actuators in typical service have a hydraulic piston in line with a load, and in line with a clevis to allow rotation. When using a 250 kN actuator for the tall steel bridge the load beam was connected to the clevis on the actuator end by a 254 mm by 254 mm steel plate, 13 mm thick, welded to the box beam, shown previously in Figure 3.7.

For all other bridges a larger 500 kN actuator was used. The clevis was removed from the 500 kN actuator to allow more space under the actuator and to have no rotation at the base of the load cell. A short, 250 mm, HSS 8x6x1/2 (203 mm by 152 mm, 13 mm thick) box beam oriented

weak axis was directly connected to the load cell with six 19 mm bolts and with a centered hole on the opposite face large enough for a 19mm bolt. For the tall CFFT bridge a ball-socket fixture with a height of 250 mm and a ball diameter of 203 mm and a 19 mm tapped hole on the top center surface was fastened to the box beam adapter. Two L3x3x1/4 steel angles were used to connect to the 2.1 m long HSS 8x6x1/2 load beam. Figure 3.28 shows the load beam and actuator prior to ultimate load for the tall CFFT bridge.

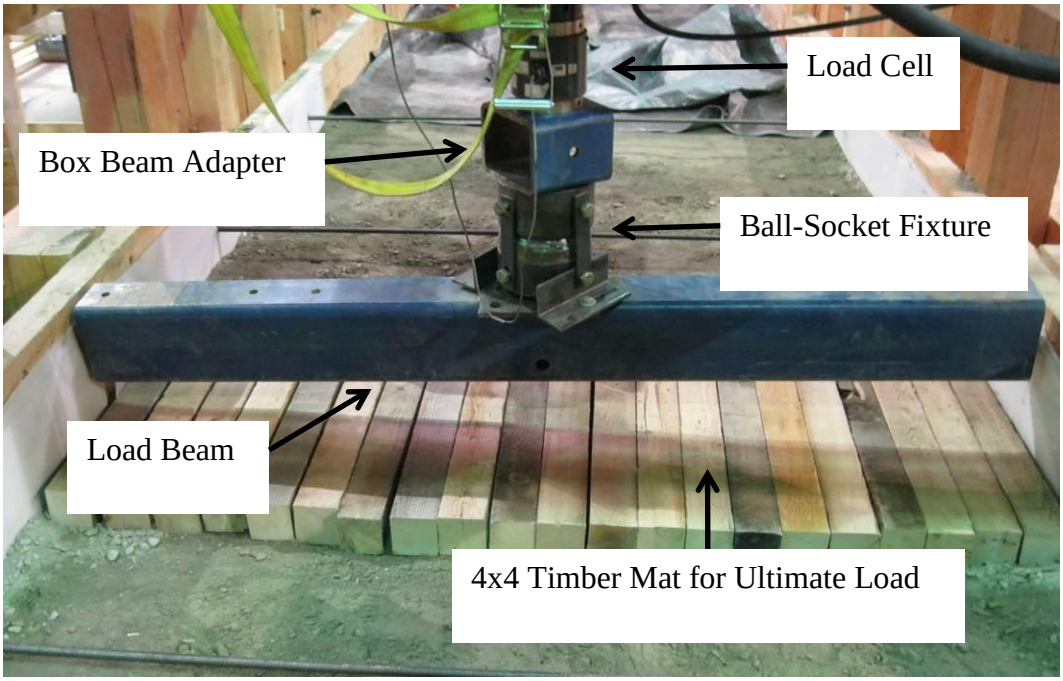

Figure 3.28. Tall CFFT Bridge Load Beam

For the short steel and short CFFT bridges the actuator could not be lowered without significant modification of the soil box. As such, a column was added in line with the actuator to provide the requisite load beam elevation. The utilized column was a 760 mm long, HSS 15x1 (381 mm diameter, 25 mm thickness) hollow round section with 460 mm by 460 mm 25 mm thick steel plates welded onto each end with a 25 mm diameter hole drilled through the center of

each face. To install the column under the actuator the load beam ball-socket fixture was removed from the actuator end. The small bolt on the end of the ball socket was replaced with an 860 mm long, 19 mm diameter threaded rod. Only 50 mm of the 19 mm diameter rod protruded from the top of the column and a plate was bolted on for transport. The column assembly was moved under the actuator with a pallet jack on top of the soil surface. The through rod in the column was fastened to the box beam adapter mounted to the actuator base. The rod is not strong enough to hold the actuator's capacity, but all testing was in compression, not tension, and the only load the rod needed to carry was the self-weight of the column, ball-socket fixture, and load beam, or about 3 kN.

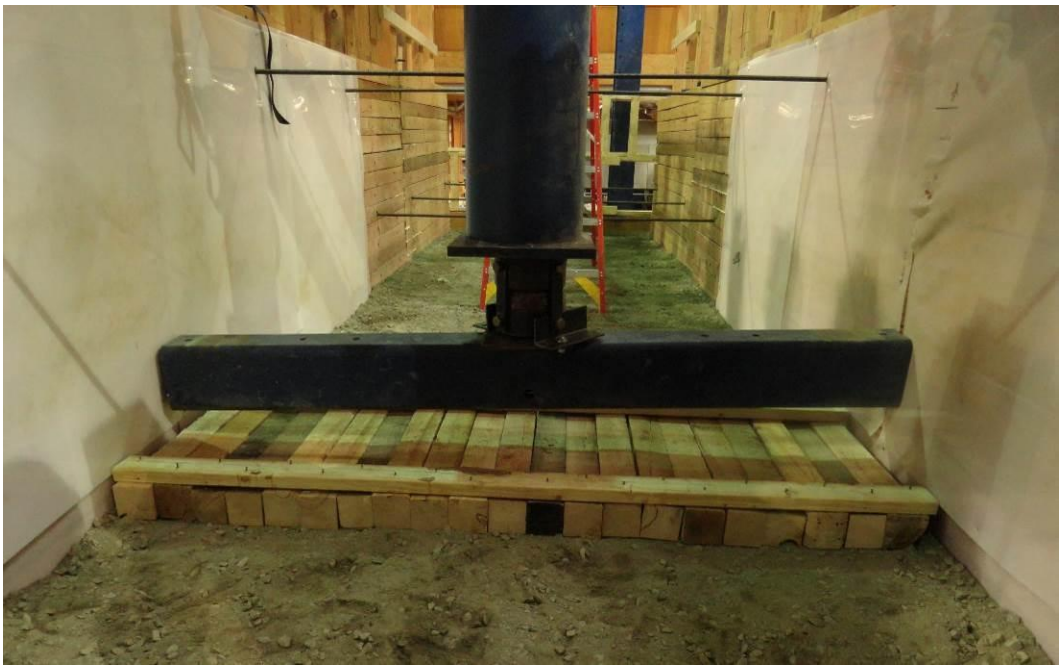

Figure 3.29. Short Steel Bridge, Ultimate Load, Load Beam

The initial service load was 42 kN, which preliminary FE models indicated produced scaled loads similar to an AASHTO (2014) HL-93 tandem with multiple presence and Maine state load

increase of 25% for vehicular strength loading (Strength I Limit State (Maine DOT, 2003)). Because of the small magnitude of pressures and deflections measured in the bridge system during initial loading, the service load was doubled to 84 kN. Also, strains were initially thought much smaller than actually measured due to a mistake in the analysis software which used 10^5 as a conversion factor from gauge recorded strain to display and file reported microstrain. All strains were corrected during post-processing.

For service tests, the load was ramped from a preload of 2.2 kN to the service load over 3 minutes. The 83.4 kN service load was held for 3 minutes, and then the load was ramped down to the 2.2 kN preload over 3 minutes. The load was held at 2.2 kN for typically 1 minute, and this process of loading and unloading was repeated 3 times. During each service live loading event, load effects including arch strains, deflections and soil pressures were locked into the system. Permanent changes due to each individual load application are included when determining total load effects during subsequent load applications. Any creep or relaxation that may have occurred between load steps was neglected because of gauge creep and difficulty reconciling physical changes in the structural system and measurement devices (e.g., zero shift of strain gauges).

All bridges were initially service loaded at the apex. Load was then applied to alternating sides of the bridge: 1830 mm North, 1830 mm South, 1220 mm North, 1220 mm South, 610 mm North, and 610 mm South, (North and South are relative to the apex; Figure 3.19). Following this sequence, the apex was then reloaded. Alternate side loading is not a realistic representation of bridge truck loading sequence, but was done to limit permanent side sway of the arches caused by off-apex loading. Loading was at even divisions along the middle 60% of the span, and since gauges were placed at even eighth points of the arc length, load and gauge locations do not correspond. The first sequence of service live loading at all locations was performed with the

pre-tensioned foundation tie rods in place. The entire service live load sequence was then repeated with the foundation tie rods removed. The tied and untied scenarios bounded both foundation lateral restraint and the horizontal soil resistance developed behind the foundations.

Lastly, the bridge was loaded to failure, defined as irrecoverable loss in carrying capacity, at the apex with the tie rods removed. For the tall steel bridge, ultimate load was performed by driving the 152 mm wide load beam into the soil until bridge failure. In this case, the load beam embedded 430 mm into the soil, or 70% of the initial cover, as in Figure 3.7 and Figure 3.30. For all subsequent tests, a pad made of timbers 100 mm thick, 760 mm in the longitudinal direction, and 2150 mm in the transverse direction was placed over the soil (Figure 3.28 and Figure 3.29) to mimic pavement on a real structure and prevent punching failure of the load beam above the bridge arch.

Figure 3.30. Removal of Dunnage from Ultimate Load Test of Tall Steel Arch

3.3. Soil Characterization Tests

3.3.1. Grain Size Distribution

Typical CFFT bridges built to date have used well-graded granular fill with less than 10% passing the #200 sieve (i.e., fines) and maximum particle size less than 75 mm. The smaller scale experimental bridges and scaled lift height of 200 mm required a smaller maximum soil size of 25 mm to ensure even spreading and compaction. Soil was classified as AASHTO A-1-a to A-1-b and USCS GP or SP and had an average of 38% gravel (6.4 mm and larger), 61% sand, and 1% fines (passing the #200 sieve). The soil was poorly graded due to a low curvature coefficient related to a smaller upper limit soil size and low percentage of fines. Grain size distribution was performed following ASTM D422. Grain size distribution was taken once per truck delivery and there was little variation in the performed tests. Figure 3.31 shows grain size distributions from several soil samples.

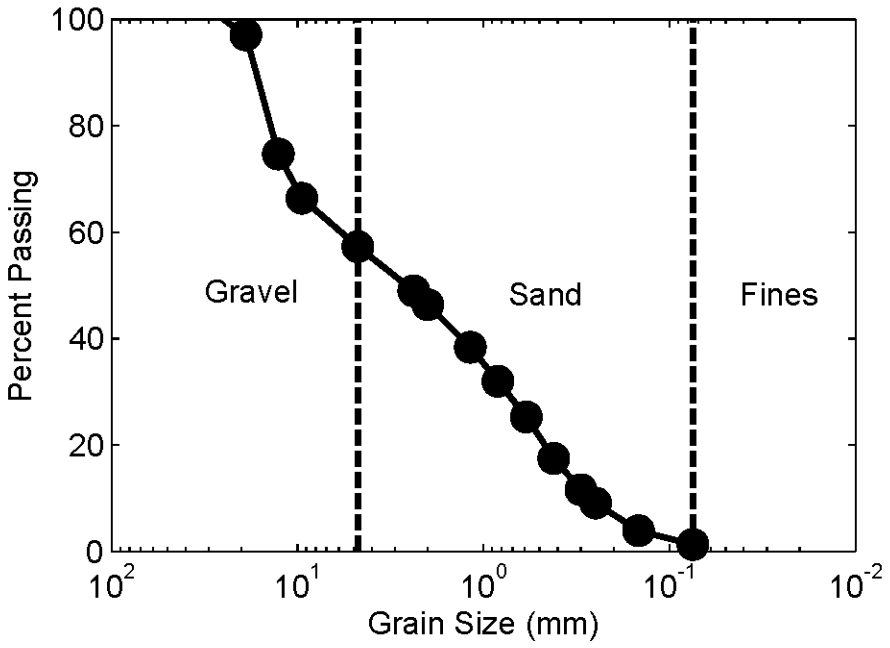

Figure 3.31. Average Grain Size Distribution

3.3.2. Standard and Modified Proctor Density, Optimum Water Content

Maximum dry density determined from the Standard Proctor test (ASTM D698) was 2.05 Mg/m^3 at an optimum moisture content of 8.5%. Maximum dry density determined from the Modified Proctor test (ASTM D1557) was 2.2 Mg/m^3 at an optimum moisture content of 7.5%. Because of the maximum grain size of 25 mm, the 152 mm diameter mold was used for both Standard Proctor and Modified Proctor tests. Typical CFFT bridges use a minimum of 95% relative compaction based on Standard Proctor maximum dry density. Research by Drnevich et al. (2007) indicates that low percentage of fines causes the Standard Proctor test to underestimate dry density of soils installed with vibratory compactors. Visual observation of Standard Proctor specimens indicated a soil that was noticeably looser than soil in the soil box.

3.3.3. Direct Shear

Mohr-friction angle (ϕ) was determined for the soil in accordance with ASTM D3080 *Standard Test Method for Direct Shear Test of Soils under Consolidated Drained Conditions*. Testing was conducted using a GeoTac Digi-Shear™ computer controlled loading system with displacement and load sensors and data acquisition system.

Regarding the material and specimen size, ASTM D3080 specifies:

- minimum specimen diameter for circular specimens [….] shall be 2.0 in. (50 mm), or not less than 10 times the maximum particle size diameter, whichever is larger;
- minimum initial specimen thickness shall be 0.5 in. (12 mm), but not less than six times the maximum particle diameter;
- minimum specimen diameter to thickness or width to thickness ratio shall be 2:1
-

Specimens were 2.5 inch diameter and 1 inch tall (2.5:1 diameter to thickness ratio) using the available equipment. The maximum particle size based on diameter is 6.35 mm, while the maximum particle size based on thickness is 4.3 mm. Therefore, the backfill material was screened to remove the 31.3% of particles larger than 4.75 mm, or the gravel component.

Specimens were prepared from bulk material at optimum water content, w_{opt}, compacted into the 63.5 mm diameter box in three layers by hand tamping using a 25.4 mm diameter wooden tool with the target unit weight of the corrected $\gamma_{d\text{-}max}$ of 1.82 MG/m^3. Trials were performed until a reliable method was developed to prepare the specimen at a consistent initial density. During the trials it was found that the highest density the specimen could be compacted to in the shear box was approximately 99% of $\gamma_{d\text{-}max}$ (i.e., RC = 99%). This density was used for all tests. This void ratio is likely higher than the void ratio resulting from vibratory compaction in the soil box testing. Higher density would likely lead to a higher friction angle for the soil.

Vertical consolidation of the specimens was performed prior to shear. Final consolidation stresses for the five specimens were 48 kPa, 120 kPa, 240 kPa, 360 kPa, and 480 kPa. Each specimen was sheared at a rate of 0.3175 mm/min (i.e., 0.5% of the diameter per minute) until 20% horizontal strain: 12.7 mm. Assuming an intercept of 0 (no cohesion), direct shear results gave a ϕ of 44.3° as shown in Figure 3.32.

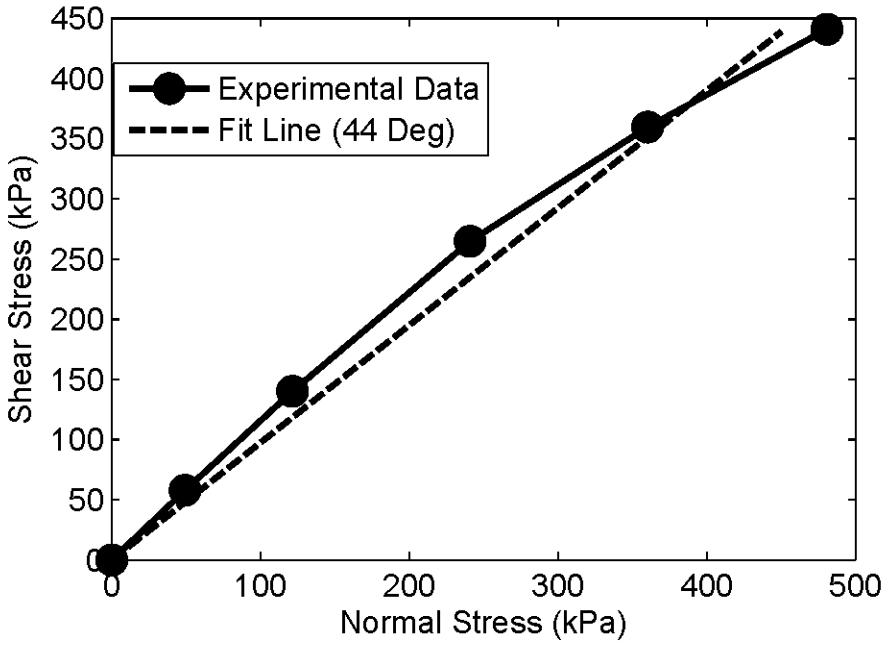

Figure 3.32. Stress Diagram from Direct Shear Tests to Determine Friction Angle

3.3.4. In-Situ Density and Water Content

The moisture content for all soil buckets was measured using the oven drying method (ASTM D2216) from specimens that massed between 0.3 kg and 1 kg. Moisture content varied between 2.5% and 7%, with over 80% of all specimens between 3.5% and 4.5%. The wettest specimens (greater than 5.5% moisture content) were collected while soil was brought in during heavy rainfall. Free water later drained through the granular soil mass. Figure 3.33 shows the soil with in-use moisture content and with desiccated soil.

Figure 3.33. Desiccated Soil and In-Use Moisture Soil

Soil density was measured using the sand cone density method (ASTM D1556). Two specimens were taken per side per 200 mm lift. The average dry density of the compacted material was 2.3 Mg/m^3 with a coefficient of variation (CoV) of 6%. Little variation was found between specimens taken from the center of the soil lift and near the arch sides. The tall bridge was tested a second time with under-compacted soil, since measured densities for compacted bridges were higher than indicated by Standard Proctor test. The loose soil was spread and walked on, but no vibration was applied to the soil. The average density for this soil was 2.04 Mg/m^3 with a CoV of 10%. There was more variation in loose soil density because areas that had been walked on and where soil had been dumped were noticeably denser than soil that was spread and not walked on. Table 3.1 shows average moisture content and dry density for each bridge. Both the compacted and under-compacted soils averaged above the 95% relative compaction requirement based on Standard Proctor density.

Table 3.1 Density and Moisture Content

	Tall Steel	Tall Steel-UC	Short Steel	Tall CFFT	Short CFFT
Dry Density (Mg/m^3)	2.3	2.1	2.4	2.4	2.4
CoV (%)	6	8.5	4.6	4.1	3.8
Moisture Content (%)	4	4.4	4.6	3.4	3.5
CoV (%)	35	28	21	18	27

3.4. Structural Tests

3.4.1. Steel Arch Properties

Coupons were cut from the region starting 150 mm from the foundation. The arch moments decrease rapidly a small arc length distance from the foundation according to the soil-spring model in Chapter 4, and no measured foundation strain was above yield for the steel arches. Four steel specimens were machined into tension dog bone specimens for both bridge geometries. Specimens had a 12.7 mm thickness and geometry per ASTM A370. Specimens were tested in tension on a 500 kN hydraulic actuator until tensile rupture of the steel specimen. A failed specimen is in shown in Figure 3.34. Stress was computed from measured cross sectional area. The average stress and measured strain are plotted for specimens cut from both bridge geometries in Figure 3.35.

Figure 3.34. Failed Steel Coupon

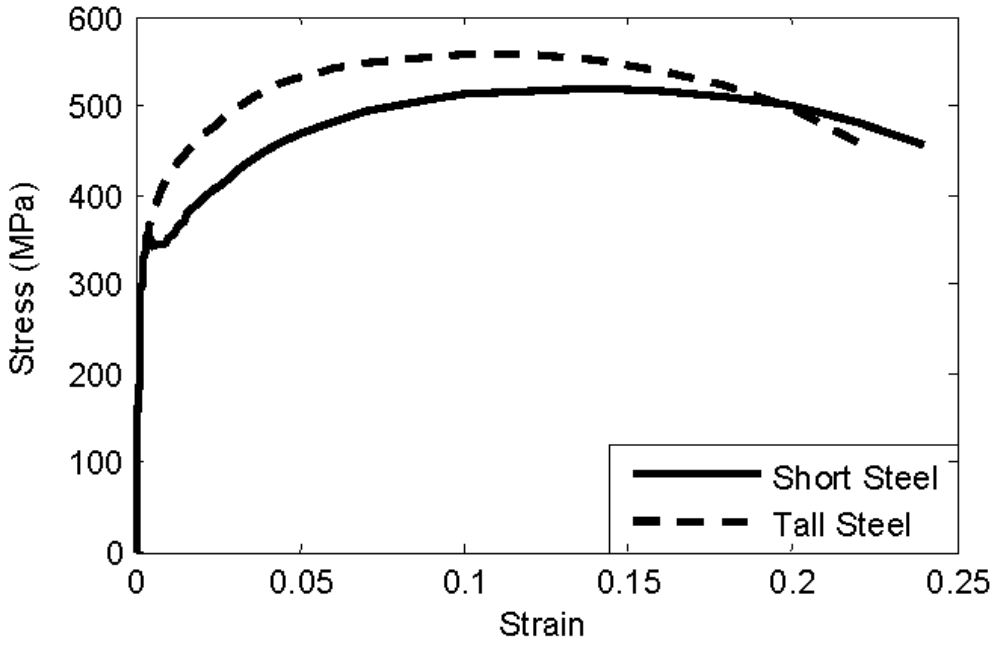

Figure 3.35. Stress-Strain Relationship from Tension Tests

3.4.2. Under Footing Compressibility

There are two layers of high-density polyethelene (HDPE) and a layer of oriented strand board (OSB) under the foundation of the arches during testing to promote a lower friction base. The materials under the footing are compressible compared to the concrete floor and the concrete footing. Also the layers have uneven surfaces: the plastic was damaged from repeated use, which created local unevenness. The OSB is made from discrete strands, which leads to a macroscopically rough surface. When a relatively-rigid level surface (bottom of concrete foundation) comes into contact with the strand board it will load unevenly and generate stress

concentrations. As the OSB compresses the surface will get more uniformly loaded and the stiffness (load versus deflection) of the layers under the foundation will increase. The average stress caused by self-weight is 17 kPa, which is small compared to the average stress caused by soil loading (155 kPa) and it is likely that the material under the foundations changes stiffness significantly during the loading process, and that the stiffness is considerably smaller than the elastic modulus of any of the materials. This means that foundation rotations are likely higher than would occur with rigid foundations.

The material under the foundations was tested in uniform compression to finds the stiffness of the materials. 150 mm by 150 mm square specimens were tested between two steel platens in uniform compression. Tests recorded load and cross head displacement. Four specimens were tested, and the results of the tests are shown in Figure 3.36. Notice that as expected there is a large difference in stiffness with load, and it occurs within the range of the expected average pressures. Aso notice that there is a large difference in response among the four specimens. These differences are most likely caused by defects in the plastic (HDPE) layers. More flexible layers had screw holes in the plastic, which lead to a thickened area and uneven loading. Notice that this is not atypical of materials placed under foundations: the plastic layers were damaged from soil particle embedment and from arch placement (sledge hammers and wedges were used to adjust the foundation positions). The results from this test were used to model the stiffness of springs under the foundation of the arches in the soil-spring model described in Chapter 4.

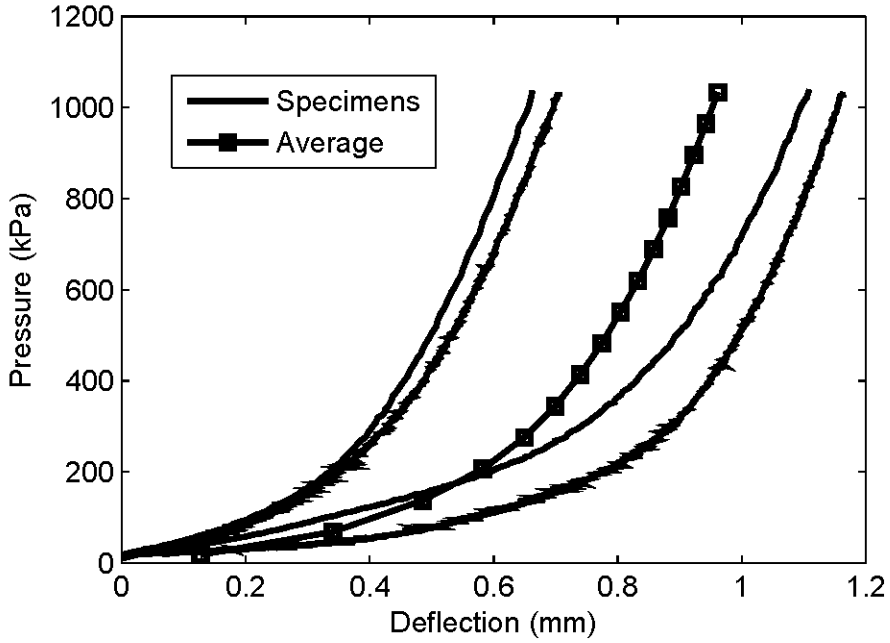

Figure 3.36. Pressure Versus Deflection of Base Material

3.4.3. FRP Strength and Stiffness

FRP strength and stiffness characterization follows procedures outlined by Bannon (2009) and Demkowicz (2011). Test specimens were manufactured as flat panels using fibers preset to the proper fiber angle per Demkowicz (2011). Specimens used the same resin as arch test specimens, Derakane 610C. Specimens were cut with a water jet to get coupons in both the longitudinal orientation (in the direction of span) and the transverse orientation (radial). Stiffness was found from tension testing of (12) 25.4 mm by 254 mm bar specimens of each fiber orientation according to ASTM D3039. Strength is found using a notched tension test. The notched tension specimen has a total length of 127 mm, a width of 50.8 mm, and at mid height has a 2 mm wide notch that extends 14.7 mm from each edge. The resulting shape behaves similarly to a bow tie specimen and is intended to have only continuous fibers through the center of the gauge length. This limits edge failures which are not characteristic for an arch, which has

no edges. Failed specimens for the 3039 coupons are shown in Figure 3.37 and failed notched specimens are shown in Figure 3.38. The average thickness for all specimens was measured to be 20 mm. Elastic modulus and strength results for both fiber orientations is in Table 3.2.

Figure 3.37. 3039 Bar Specimen

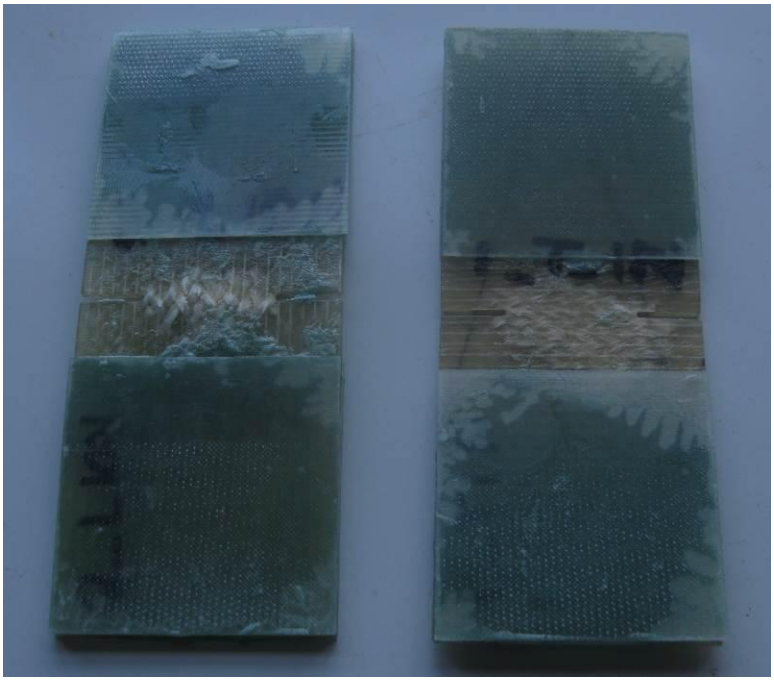

Figure 3.38. Notched Tension Specimen

Table 3.2. FRP Strength and Stiffness

	Stiffness (GPa)	CoV (%)	Strength (MPa)	CoV (%)
Longitudinal	13.8	10.7	313	5.7
Transverse	19.4	10.6	374	4.8

3.4.4. Isolated CFFT Arches

An isolated CFFT arch made with both arch geometries (1.22 m rise and 2.29 m rise) was tested to find the strength of a single arch for comparison with ultimate load testing of the buried structure and to verify the Burgueño moment-curvature relationship introduced in Chapter 2. Both arches were manufactured to be identical to arches in the three-arch buried system and were filled in the same process. Isolated arches were tested as fixed-fixed and required an excessively large (not strength dependent) footing to fit tie-down geometry. Both 110 mm diameter arches were cast into 1.52 m wide, 0.91 m long, and 0.46 m deep footings.

During testing arch footings were tied to the concrete floor with four 19 mm diameter rods. Arches were braced against out of plane movement during testing. The tall isolated arch was tested between testing the short steel bridge and testing the tall CFFT bridge, and the bridge displacement gauges were used in this test. The apex and shoulder vertical displacements were measured with +/-127 mm LVDTs and the horizontal displacements were measured with 635 mm string potentiometers. The short isolated arch was tested while the short bridge was being tested and the typical bridge gauges were in use. Instead, different Celesco SP2 string potentiometers were used for all five displacements. Arches were also instrumented with top, middle and bottom Omega 12.7 mm foil strain gauges at the apex, both footings and both shoulders (quarter points).

Arches were loaded in deflection control with a deflection rate of 12.7 mm/min. Arches were tested with an in-line load cell because expected capacity was very small compared to the load

cells typically connected to the actuators on the structural testing floor. For the tall steel bridge a 1500 kN actuator was used with a 100 kN load cell, shown in Figure 3.39. For the short bridge a 250 kN actuator was used with a 50 kN load cell, shown in Figure 3.40.

Figure 3.39. Tall Isolated Arch Test

Figure 3.40. Short Isolated Arch Test

The capacity of the tall arch was 12.1 kN and the capacity of the short arch was 15.5 kN. Arches failed at the apex at the peak load and then were able to reload up to approximately 70% of capacity before failing at the footing. The tension gauge at the apex of the tall arch went out of range (disconnected) prior to ultimate load and measured strain at failure was not available. The tensile strain at peak load for the short arch was 1.27%, which is lower than the predicted failure strain of 2.3% based on coupon testing computed by dividing the measured rupture strength from notched specimens by the measured elastic modulus from bar specimens in testing described earlier in this chapter.

Experimental results were compared to FE model results for an isolated CFFT arch. The model was run using a nonlinear moment curvature relationship following a similar procedure to Bannon (2009) and Dagher et al. (2012). The model used a nonlinear moment-curvature

relationship (Burgueño 1999) and the material properties (experimental longitudinal and transverse modulus) and geometric properties (arch diameter, wall thickness from coupon specimens, arch span and arch rise) were based on measured values. The isolated arches were modeled with fixed foundations because the foundations were tied to the floor and were unable to move during this test. This procedure is different from earlier isolated arch testing and modeling where a pinned on bottom foundation had been used. (Bannon 2009, Dagher et al. 2012).

The model predicted apex deflection versus load was compared to the experimentally determined apex deflection versus load as a method of determining the fitness of the nonlinear moment-curvature relationship for the CFFT arches used in this report. The isolated arch test was much simpler than soil box tests: there was no restraint from soil and loading was monotonic, therefore damage from repeated loading was not a factor in this test. The stiffness after cracking was close, based on the measured cross section and the testing validated FRP stiffness, but the experimental CFFT arches were initially stiffer than predicted by the FE model and the elastic region prior to concrete cracking was too short. This difference may be explained by the higher confining stiffness than is typically employed in a CFFT arch. As mentioned in Chapter 2, the confining stiffness, thickness times radial elastic modulus, is greater than 60% of that in a full scale arch yet the diameter is only 37% of a typical arch. As a result, the confining pressure is greater, which potentially explains why the arch is stiffer than anticipated. To account for this, the tall arch is corrected by adding 22 kN axial compression to the arch while the short arch is corrected by adding 11 kN of axial compression. The average value is 17 kN. Figure 3.41 and Figure 3.42 show the deflection of the tall and short arches as predicted by a beam model arch

with the as-built moment-curvature relationship and various additional axial force moment curvature relationships.

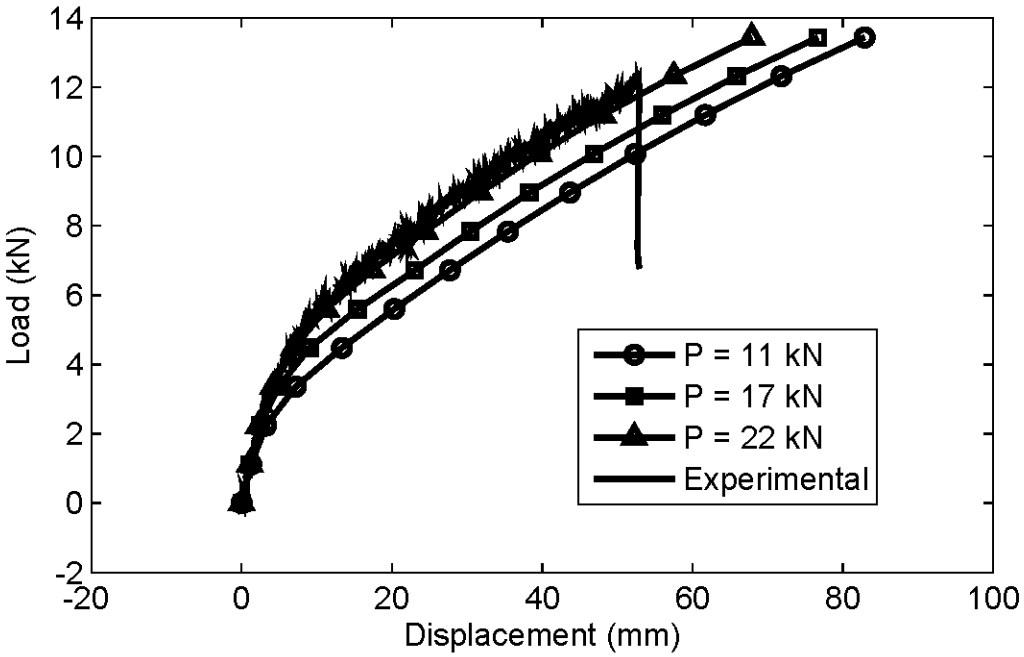

Figure 3.41. Tall isolated Arch Apex Displacement

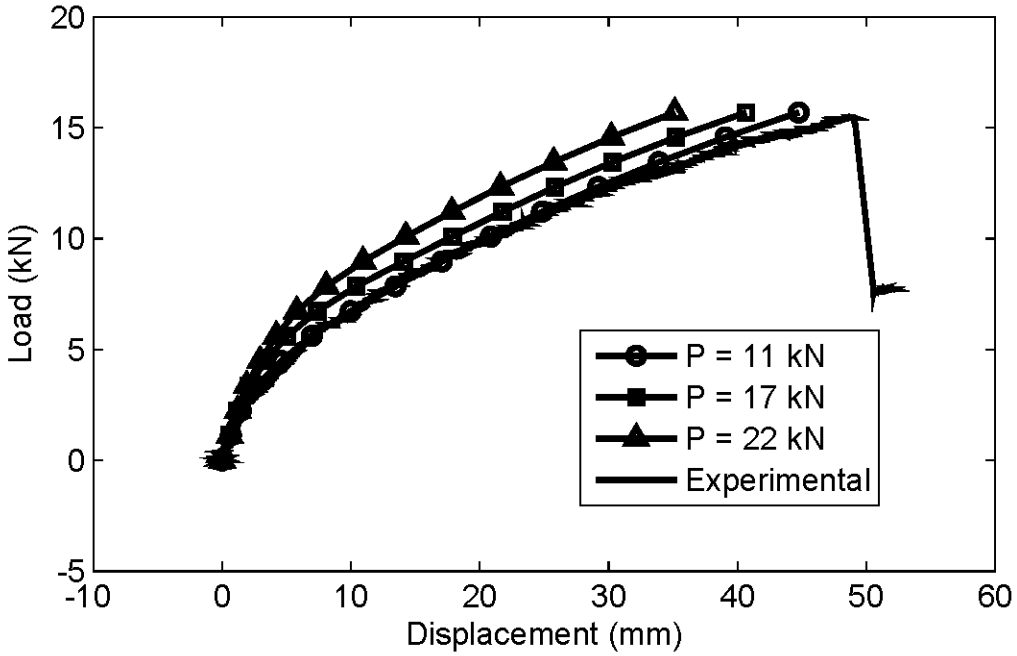

Figure 3.42. Short Isolated Arch Apex Displacement

3.5. Suggestions for Future Improvements

The testing program was successful, and the soil box performed as intended: soil was retained and the bridges were subjected to a series of live loads successfully. While it is unlikely that a test similar to this will ever be repeated, there are several recommended improvements to the testing procedure.

Soil box access was a constant issue during testing. The internal platform system originally designed and built proved very difficult to implement in practice. The platforms did not slide past each other well, it was nearly impossible to run a compactor with under 1.5 m of head space, meaning that platform movement occupied too much construction time and effort. The secondary system, platforms nailed to the soil box walls, was better, but is not an ideal solution. Platforms were too flexible and felt unsafe at times. Also, height was initially very close to violating OSHA construction height limitations. A better platform solution would have been to utilize the arches themselves as a structural unit. Two temporary suspended platforms (one outside and one inside

the soil box) and one temporary platform set on the apex of the arches could have provided access to the apex of the decking prior to closing the North end wall. Lumber nailed to the decking with easily removable duplex nails could have provided access along the decking itself to the whole soil box. This would have made spreading and compacting soil much easier because the temporary platforms would be central enough that direct access from the permanent platforms would be possible by the time that the temporary platforms became an obstacle.

Plastic wall panels to reduce friction were an annoyance during construction and probably provided little reduction in friction because gravel found its way between panels and ruined any claim to being low-friction. Also, plastic panels were warped and torn by soil and load beam loading, which further increased its friction. A better solution would have been a single stiffer sheeting material such as plywood that could have covered the wall and a roller system mounted under the decking. Little soil leaked through the sheeting plastic installed between the soil box walls and the outer edge of the decking, so rollers may not have been jammed by sand. Spring-loaded three-dimensional rollers that cantilevered from the decking and served as guides could have reduced some wall friction. However, there would always be an issue with soil bunching by the deck cantilevers and limiting motion.

Variable soil depth tests should have been performed on more bridges and in particular on the steel bridges with repeatable load history. The testing plan used was constricted by time. Testing the tall steel bridge with under-compacted soil eliminated several test options due to a need to install the final bridge before frost. The only possible solution would have been to have instrumentation ready earlier to allow backfilling sooner or to have had a better soil box platform plan for the first three bridges.

CHAPTER 4. SOIL-SPRING MODEL

4.1. Introduction

Soil-spring models, often referred to as P-y models, are used to approximate soil restraint in soil-structure applications such as piles (Reese and Wang 2006, Chung et al. 2015), integral abutment bridges (Lehane 1999, Greimann et al. 1986), and retaining walls (Chen et al. 2010, Wang and Arrellaga 2007). Soil-spring models, which often represent the structure with one-dimensional beam elements and idealize the soil with a series of one-dimensional axial-only springs, use far less computational time than soil-continuum models, and are simpler to develop. Soil-spring analysis is used in commercial software packages such as FB Multipier (Chung et al. 2015), Lateral Foundation V2.0 (SoilStructure.com 2013) and L-Pile (Reese and Wang 2006). However, soil-spring analysis may not provide accurate soil pressure at all locations, for it treats a soil mass as a series of independent springs dependent on individual spring deflection and does not address interaction between adjacent springs. Also, soil spring models do not account for surcharge dissipation and separate methods are necessary to assess the vertical effective stress.

Recent investigations using soil springs are typically related to dynamic models (Gerolymos and Gazetas 2005) or other repetitive models producing pressure-deflection curves for a series of sand properties (Jeong and Seo 2004) where fewer modeled degrees of freedom allows for shorter run time. Soil springs are used to represent pile behavior in stand-alone piles and in integral abutment bridges (e.g, Greimann et al 1986). Soil discretized as a single spring per abutment has produced comparable results to two-dimensional continuum models in integral abutment bridge thermal response (Lehane 1999). Other researchers have used multi-spring analysis where a soil continuum is represented by a series of springs (Ates and Canstantinou 2011). Soil springs used in buried pipe buckling analysis produce strengths that mimic findings

from the American Iron and Steel Institute (Kang et al. 2008). The variety of applications and geometries that soil springs have been used in indicates that they can be an effective means of discretizing a buried structure while limiting degrees of freedom.

4.2. Description of Model

To-date, design analysis of buried CFFT arch bridges has used simplified assumptions in place of better understanding of soil behavior prior to validation, taking the form of reduced soil stiffness. This research intends to validate the beam-spring technique as a solution for buried arch behavior and introduce improvements to the current analysis method. This section will refer to a 'design model' which is presently used in buried CFFT bridge analysis and design and a 'research model' which includes enhancements developed as part of this study. In the experiments discussed in Chapter 3, steel arches were tested in addition to CFFT arch bridges to serve as a linear-elastic material counterpart with justifiable moment and axial load extraction from measured strains. In this chapter, steel bridge arches will be used for mesh refinement studies and to explore mesh refinement and the effect of analysis parameters. Moment will typically be used as a comparison guideline for this structure because it controls the design of CFFT arch bridges. The CFFT arch section is more effective in axial compression, and shears are small. When comparing model results in this chapter the baseline bridge analysis is a large deformation, 80-element, short (1.22 m rise), 6.10 m span steel arch assuming plastic response above the yield strain, without decking elements, with footing elements and ties, and with dense granular soil with friction angle (ϕ) = 44 degrees, at-rest lateral earth pressure coefficient (K_0) = 1, and soil density = 2.4 Mg/m^3. The arch cross-section is 50.8 mm x 50.8 mm, and the steel

yield stress is taken as 345 MPa based on coupon-level tests described in Chapter 3. The sections below describe the use and relative importance of the above parameters.

A bridge system is represented as a single arch with a tributary width of soil equal to arch spacing. The arch system is modeled using beam elements, transverse beam elements that represent decking, horizontal axial spring elements that represent soil, and very stiff beam and spring elements that represent foundations. A graphical representation of the model is shown in Figure 4.1, where a very coarse mesh is displayed for clarity. The global *x*-direction runs in the span direction, the global *y*-direction is in the rise direction and the global *z*- direction is transverse to the plane of the arch. The arch structure is represented using 2-noded, 2D, Euler beam elements with curvatures defined by cubic shape functions. The elements are not shear deformable, but due to arch shears that are low compared to other loads, often 10% or less of the axial load, and the span to depth ratio of greater than 50:1, shear deformations are small for this structure. Arch material properties for steel and CFFT arches are based on material coupon tests described in Chapter 3 detailing test setup.

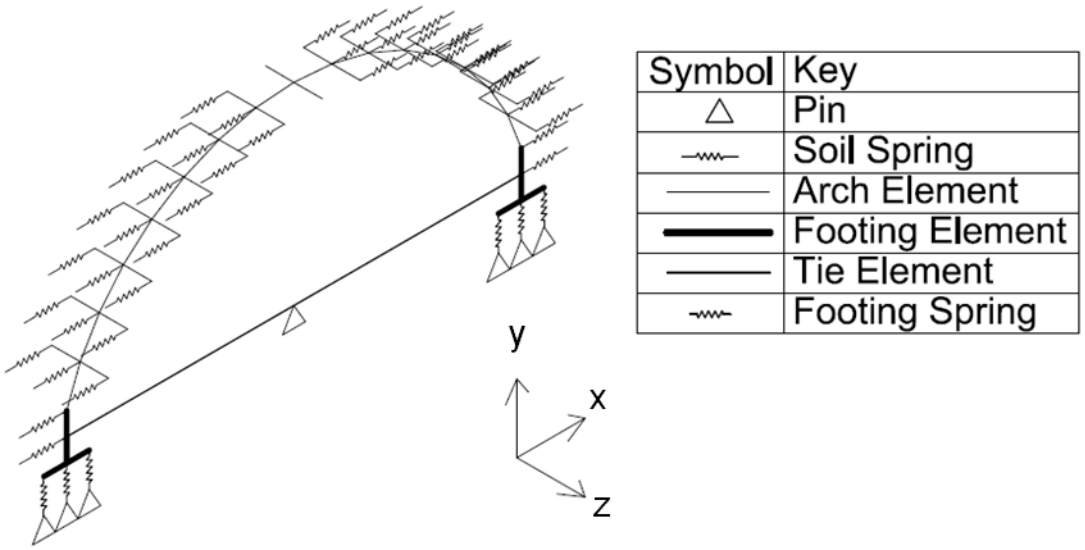

Figure 4.1. Spring Model Diagram

Small deformation analysis satisfies force equilibrium for the initial undeformed structure, while large deformation, small strain, geometrically nonlinear analysis satisfies force equilibrium for the final deformed position, and therefore requires an iterative solver that incorporates geometric stiffness terms and updates nodal position as loads are applied. For a typical point loaded or continuous loaded beam, considerable deflections are required before there is a significant difference between large- and small-deformation model results, so the simpler small deformation analysis is used in many cases. For beam-columns and arches with interaction between bending moment and axial compression, smaller deformations can produce a meaningful difference between large and small deformation analysis. In this case, axial load acts through the deformed shape generating moment, known as a P-delta effect, in the same manner that moment is generated in an eccentrically loaded column. This is relevant for a shallow arch because there are considerable bending moments and axial compressive forces in typical structures.

The design model uses small deformation analysis, which was initially assumed adequate because deflections are small compared to beams. A typical arch bridge has predicted service live load deflections of approximately 0.1% of the span length. But, axial loads are high enough that when acting through this small deflection they produce additional moment that may affect design of a bridge. Figure 4.2 is a plot comparing small deformation and large deformation analysis moments for a live load of 84 kN (2x service load) applied 40% of the span away from the apex (toward the footing) for the baseline structure outlined earlier in this chapter. Notice that the small deformation analysis is unconservative compared to large deformation analysis; the

footing negative moment and the peak positive moment are underpredicted by approximately 30% of the large deformation analysis' solution. For this reason, large deformation analyses will be used for all test data and model parameter comparisons beyond the pretest modeling, which was done with small deformation analysis. Large versus small deformation makes a smaller difference during backfilling, when axial loads are smaller, and during apex load, when the arch returns close to its original undeformed position.

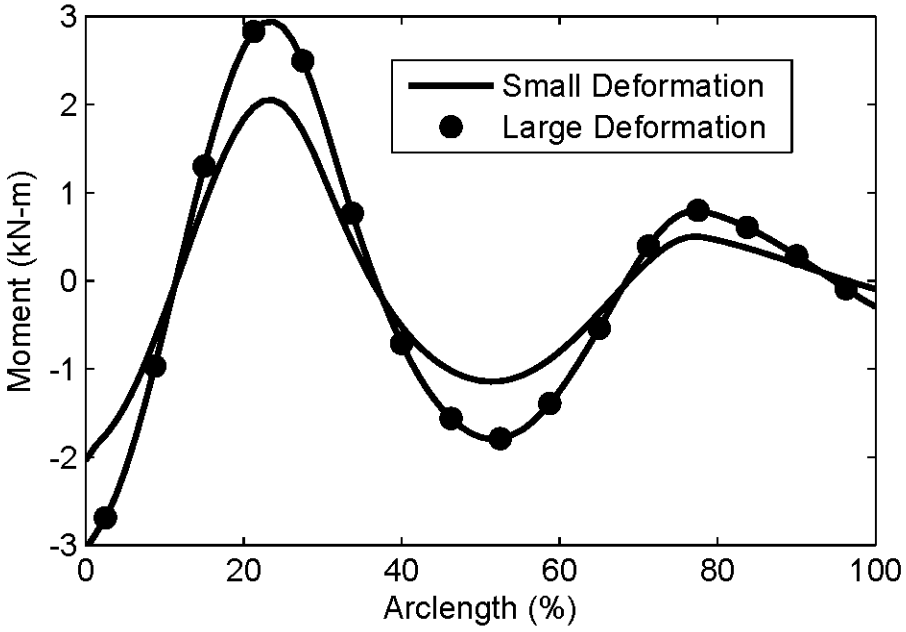

Figure 4.2. Moment Comparison for Small vs Large Deformation Analysis

4.3. Mesh Refinement

Small deformation linear elastic Euler beam elements produce exact answers for a range of simple load cases and minimal mesh refinement for a straight beam, but for the present case where large deformation and nonlinear material elements are used with a curved geometry, convergence must be studied. To determine an appropriate number of elements, the basic analysis model was run with 10, 20, 40, 60, 80, 120, and 160 arch elements. Since horizontal soil

springs are placed at each node, varying the number of elements in the arch automatically varies the level of soil-spring discretization. Three moment parameters were considered: apex end of backfill, apex due to apex live load, and shoulder due to shoulder point load. Table 4.1 includes the moments for the three cases in kN-m and the percent difference from the finest mesh for each number of elements. Notice that the 60 element case is within 1% of the 160 element case, and is an acceptably converged solution, but it does not have nodes that coincide with all gauge locations, so the 80 element mesh is used for all analyses.

Table 4.1 Mesh Refinement, Moment in kN-m and Difference in Percentage

	10	20	40	60	80	120	160
Backfill	-1.68	-1.66	-1.68	-1.69	-1.71	-1.72	-1.70
Difference	1.07	2.36	1.13	0.46	0.78	1.18	0.00
Live	4.48	3.48	3.29	3.29	3.27	3.22	3.25
Difference	37.5	6.87	1.11	0.97	0.49	1.02	0.00
Shoulder	3.00	3.02	2.90	2.88	2.87	2.85	2.85
Difference	5.20	6.02	1.82	0.87	0.82	0.11	0.00

4.4. Simulation of Staged Backfilling

A progressive multi-stage simulation was used to capture the effect of backfilling. This method was established by Clapp and Davids (2011) and is also used in the design model. In each step, soil depth increases in 200 mm lifts on alternating sides of the bridge apex to mimic construction. With each new lift, vertical loads increase on each arch node below new soil depth. Soil springs are initialized for nodes that are soil-covered during the new lift step. The position predicted for nodes buried during the new lift step defines their at-rest positions and they are given a horizontal earth pressure coefficient (K) higher than typical Rankine at-rest values, suitable for compacted soil (Clough and Duncan, 1990). Horizontal spring stiffnesses and K values for previously established soil springs are iteratively calculated depending on arch

displacement and the vertical soil pressure at each node elevation. Details of how soil spring properties were derived are discussed later in this chapter.

The end of backfilling establishes the baseline locked-in soil stress and soil spring stiffness and arch axial load, moment, and shear appropriate for subsequent live load application. One outcome of sequential backfilling simulations is that soil spring properties and internal arch stresses are not symmetric about the apex prior to live load application. Also, arch stresses are higher during, rather than at the end of, the backfilling sequence. Moments for the baseline structure in Figure 4.3 are compared for end of backfill, backfill envelope, and a theoretical 'wished in place' case where soil is placed around the arch assuming equivalent fluid pressure and a K_0 of 0.4 (Rankine K_0 for $\phi = 37°$). The wished in place case produces greater moments than even the highest moments during the backfill sequence at the shoulders, the apex, and the footings, by 50% at the peak shoulder moment. The end of backfilling case has lower negative footing moment and positive shoulder moments that the envelope results because the moments when soil is level with the apex produce the worst-case loads, and non-symmetric loads at that level force higher moments in the 0% of arclength footing (first side of backfill) than the 100% of arclength footing, which persist throughout the dead load and live load sequence.

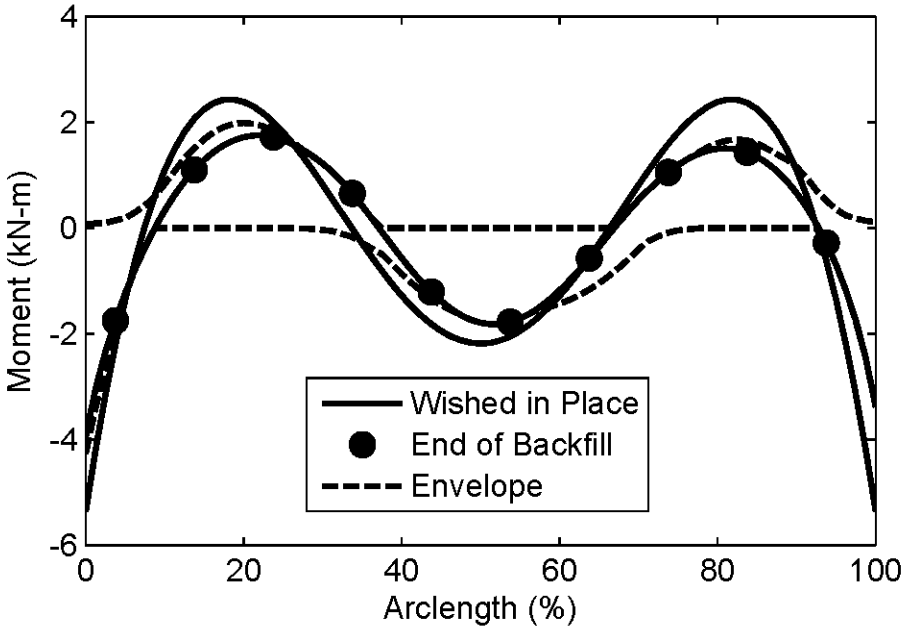

Figure 4.3. Backfill Moment Comparison, Short Steel Arch

4.5. Application of Live Loads

Following backfilling, loads are applied over the middle 60% of the span at tenth points, corresponding to load points from laboratory experiments detailed in Chapter 2 (scaling) and Chapter 3 (testing). Live load sequence does not matter for the soil-spring model, since all of the elements are elastic springs that return to the original backfill position when live load is removed. Live loads were applied as surface patch loads and distributed through the soil using the Boussinesq assumption (Holtz and Kovacs, 1981). The design model uses a Boussinesq assumption with surface point loads. The Boussinesq model assumes load distribution within an infinite half space (infinite length, width, and depth) for a homogeneous, linearly elastic material. Infinite half-space is a reasonable assumption in the span direction, since the experimental soil box is 12.2 m long or 80 times larger than the patch length. In the width direction, the load is applied on 98% of the soil width, appropriately modeled with an infinite strip. Soil is not a

homogenous, linear elastic material, however this assumption has traditionally been accepted in design for soil stress below a foundation. Live loading occurs in the model at the top of the soil elevation. This is justified using experimentally observed soil deflections, which were mainly 3% or less of the cover depth based on experimental actuator deflections. The one exception was ultimate loading of the tall bridge, where the load beam punched through 70% of the soil cover depth at failure during the experiment. When simulating this case in the model, live load was applied at 70% below the soil cover depth.

During ultimate load simulation an apex line load increases linearly using the standard Newton solver used for all other analyses. When the Newton solver no longer converges (i.e. when the arches begin to buckle) a Riks-Wepner arclength solver was used (Crisfield 1991). This method sets an additional force multiplying variable that balances additional deflection with a smaller increase in the load increment, finding a stable position with either a smaller increases in load or eventually a decrease in load. This solver does not predict a much higher load, only about 5% of ultimate load than that reached with the Newton solver. The Riks-Wepner solver illustrates that the arch experiences a geometric instability, that load peaks at a certain position, and when deflections are beyond peak load, less load is required to hold the new deformed position. The ultimate load analysis will be discussed in more detail in Chapters 6 and 7.

4.6. Decking Elements

A model discretization option is the addition of beam elements cantilevering transverse to the plane of the arch representing decking. Decking elements are rigidly connected to the arch nodes, and the ends of the deck are fixed against translation in the global *z*-direction and rotation in the global *x*- and *y*-directions, a symmetric boundary condition. All decking nodes are connected to

soil-spring elements, allowing for different soil stiffness depending on decking deflection, although decking boundary conditions do not affect arch in-plane stiffness.

Transverse decking is modeled with beams elements with the local 1-direction along the decking element length, element local 2-direction through the thickness of the deck, and element local 3-direction in the plane of the decking. Rotational stiffness about the 1-direction (torsion) and about the 2-direction (bending the deck in plane) are set arbitrarily high to limit motion in those directions. Rotation about the 2-direction (bending through the thickness) is based on material properties of the deck. The model can have multiple elements per section of decking. An infinitely rigid deck will produce the same deflections as the arch and will not affect any results in the model. An infinitely flexible deck will deform away from the soil and will have all active soil pressures, which will decrease backfilling moments (when soil pressure causes moment) and will increase live load pressure (when soil restraint strengthens the arch). Realistic decking produces an effect somewhere between these two cases.

Three models were created to test the effect of decking in the subscale arches: zero-deck, two-deck and four-deck, indicative of the number of decking elements per arch node. The zero-deck model produces end of backfill footing moments 3% lower and apex live moments 1% lower than the two-deck model, which does not justify the additional run time for decking elements considering the sensitivity to other modeling parameters. Additional decking elements produce less effect: a four-deck model was within 0.5% moment and deflection with the two-deck model for all important locations such as footings, shoulders, and apex under all load conditions. No deck elements are used in the baseline analysis.

4.7. Soil Spring Elements

Soil was modeled as a series of horizontal spring elements connected to arch nodes or decking nodes. The soil springs are elastic and are therefore unable to capture the hysteretic load-deformation response caused by soil-arch deformation and relaxation interaction. Soil spring force and stiffness are computed based on *K*, the total vertical pressure (soil and live load), and the tributary area of each spring. *K* depends on the relative deflection of the arch normalized by the height from the base of the foundation to the apex of the arch.

The NCHRP (Barker et al. 1991) approach for calculating the horizontal earth pressures on cantilever retaining walls was adopted. The NCHRP (Barker et al. 1991) deflection-*K* curve (Figure 4.4) uses the traditional Rankine earth pressure coefficients to define ultimate active and passive soil conditions and provides intermediate values based on deflection. Greater soil stiffness correlating to a higher friction angle (ϕ) decreases the deflection required to achieve full active and full passive pressure (Clough and Duncan 1990). For example, dense sand (ϕ = 44°) requires half as much deflection to achieve the full passive conditions as medium-dense sand (ϕ = 37°), and loose sands require more deflection than typical granular fills to reach the full passive condition (Figure 4.4). Compaction modifies the K_0. K_0 for a granular soil compacted against a non-moving wall is 1.0 (Clough and Duncan 1990). Following Clough and Duncan (1990), the *K*-displacement curve is shifted toward a more active state in Figure 4.4, ensuring a K_0 of 1.0 corresponds to zero deflection. K_0 is a user specified value in the analysis that influences moments; higher K_0 makes higher backfilling moments and lower live load moments, but for K_0, between 0.45 and 1.0 the total apex and foundation moments stay within 5% during apex live load.

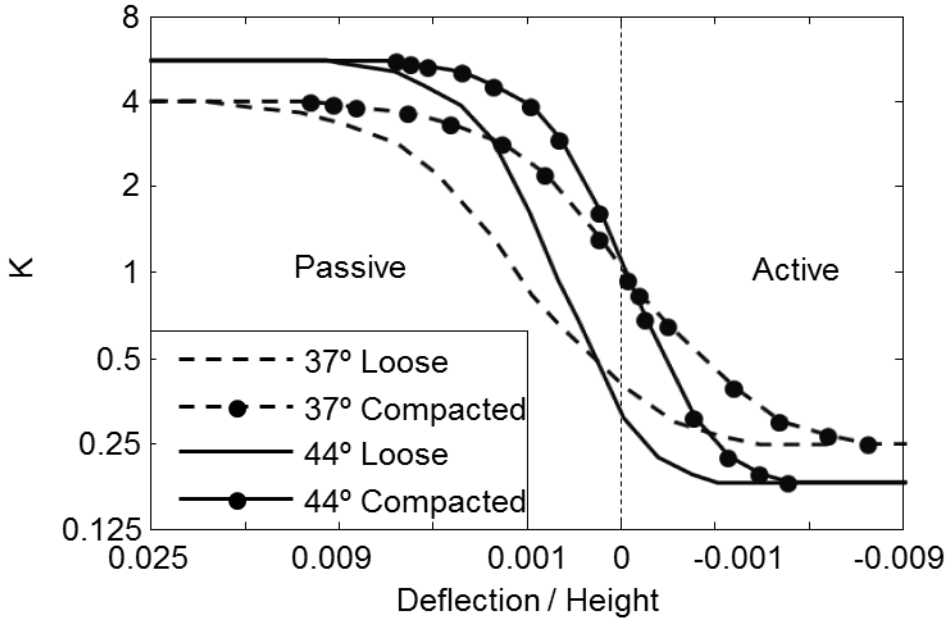

Figure 4.4. Deflection-*K* curve reproduced from NCHRP 1991

The *K*-deflection curve used for the model is based on soil properties from experimental laboratory testing described in Chapter 2, where friction angle is 44° and the total density of the moist soil is 2.4 Mg/m^3. When calculating overburden pressures, pore pressure is assumed to be zero (ignoring positive or suction pressures). Thus, effective stress is assumed to be equal to total stress.

The arch is flexible in a typical backfill simulation, which allows *K* to decrease from the initial compacted value of 1.0. As the arch moves away from the soil during the early stages of backfilling, many soil springs achieve lateral earth pressures that are nearly fully active, regardless of the spring starting point. As soil is added over the apex, its added weight causes the arch shoulders to press into the surrounding compacted soil. The soil springs then compress toward a more passive condition, approaching the K_0 condition. Applied live load causes the arches to sway away from the load. Soil in areas nearest the load experiences more active

conditions. As the arch in areas distant from the load is forced into the soil, conditions in the soil move towards the passive region, but remain below the fully passive condition under service-level loads. Only near ultimate load does soil around the arch approach a fully passive condition.

Soil property selection has an effect on analysis results. Figure 4.5 contains the live load moment from an 84 kN apex load, Figure 4.6 contains the live load moment from an 84 kN shoulder load, and Figure 4.7 contains the end of backfilling moments for the baseline steel bridge model. All three models use density 2.4 Mg/m^3 and K_0 = 1, but vary the friction angle and the assumed amount of compaction. Models include ϕ = 30° and loose soil (conservative design assumption), ϕ = 37° and medium dense soil (design model assumption), ϕ = 44° and dense soil (research model assumption, based on experimental friction angle and compaction). Densities are not realistic for the looser soils, but a consistent density was chosen for all models to get comparable baseline results. Decreasing the density to realistic values for looser soils lowers the backfilling moments when soil weight drives loading, but raises the live load moments because the higher vertical effective stress of heavier soil allows for higher horizontal soil-spring resistance. Response varies from model to model with the denser soil model having less moment under all loading conditions. During backfilling, footing moments are lowest for dense soils with 17% greater footing moment for medium-dense soil and 33% less footing moment for loose soil. During apex and offset live loading a similar trend emerges: arches with lower compaction soil have more moment. Footing moment from a shoulder load is 25% higher for medium density soil and 61% higher than loose soil for a dense soil, with the loose soil and medium soil both exceeding the yield moment of the arch. Peak positive response of the arch to an apex live load is 18% higher for a medium dense soil and 49% higher for a loose soil than a dense soil.

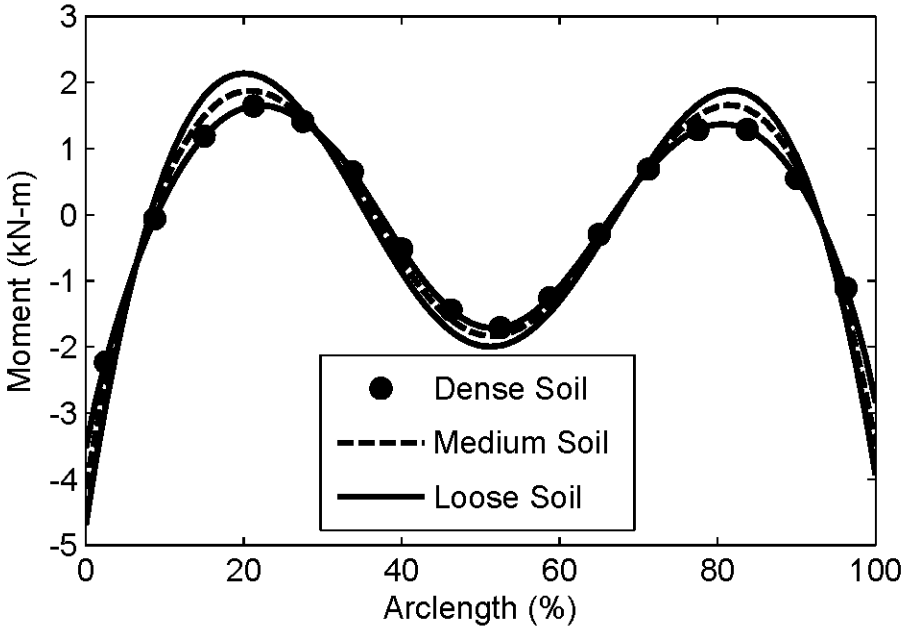

Figure 4.5. End of Backfilling Moment, Different Soil Properties

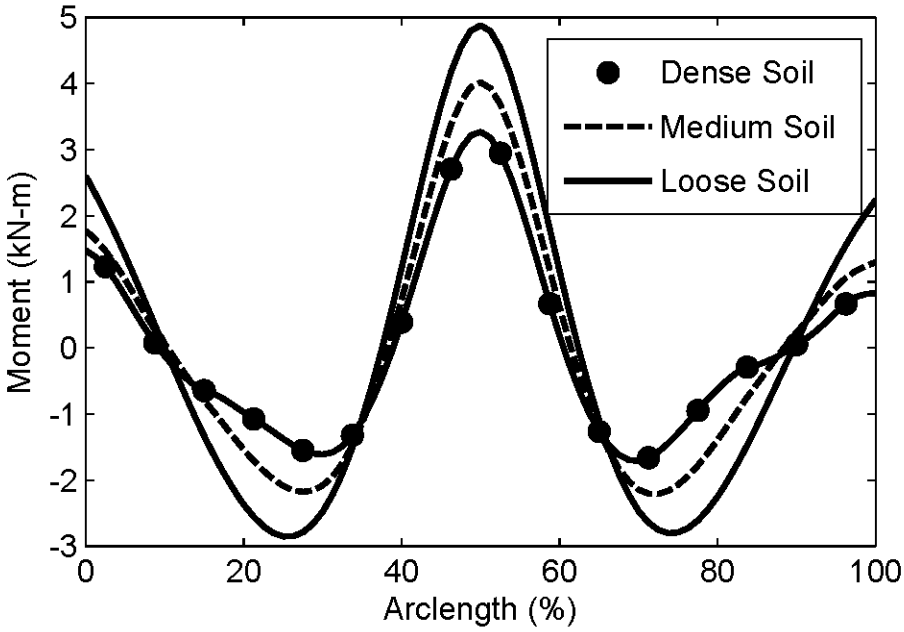

Figure 4.6. Apex Live Load, Live Load Moment Only, Different Soil Properties

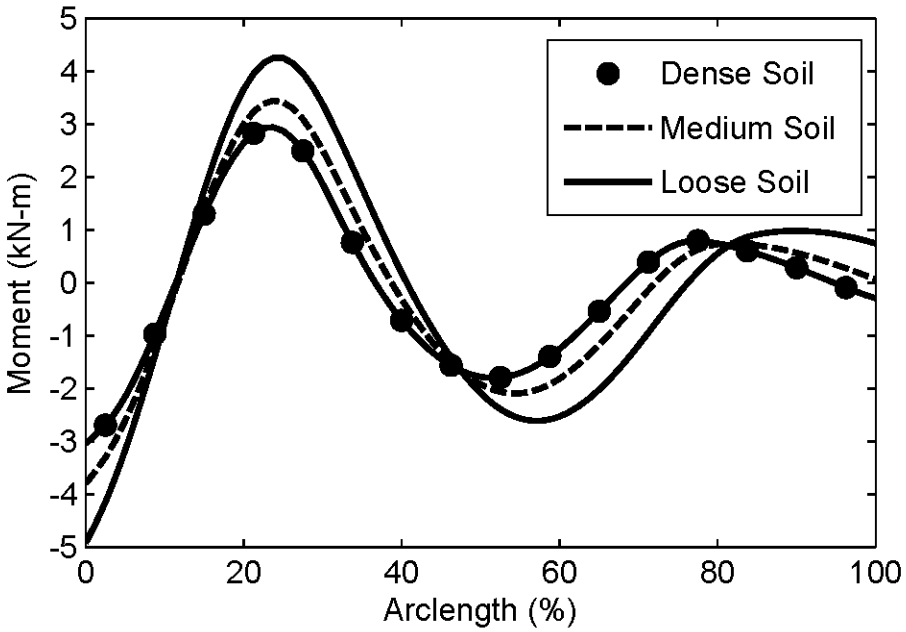

Figure 4.7. Shoulder Live Load, Live Load Moment, Different Soils

4.8. Foundation Elements

The design model for buried CFFT bridges assumes that the arch is fixed against rotation at the top of the foundation and that the foundation remains fixed in three dimensions, or that the foundation is pinned at the top of the foundation. However, a more realistic representation of foundation response may be required, as the toe of the foundation lifted off the floor causing foundation rotation during the testing described in Chapter 3, yet the arch itself is cast in concrete and there is little flexibility at the arch-foundation interface. A pinned base model does not replicate correct motion, as the FE modeled foundation rotates excessively toe downward during backfilling if footing weight is not incorporated in the analysis, resulting in an increase in live load moments at the arch-foundation interface.

To address foundation rotation, the FE model implemented in this study uses foundations shaped like upside-down tees (Figure 4.1). Vertical and horizontal foundation beam elements are

assigned an elastic modulus typical for concrete and a 610 mm by 760 mm section for a tributary arch, which ensures they are very stiff compared to the arches. Vertical foundation elements are connected to horizontal soil spring elements which are treated identically to soil springs connected to the arch. The foundation weight is distributed to horizontal foundation elements to resist overturning. The top of the foundation behind the arch is also assigned vertical pressure from the overburden soil. Base foundation elements are supported by vertical nonlinear springs, which have nearly zero stiffness in tension and are very stiff in compression, allowing the toe or heel of the foundation to rotate off the floor, but not penetrate it. Friction is included in the model. Friction force is the friction coefficient (μ) times the total vertical weight at the base of the footing. When the friction force is greater than base shear the footing is modeled with the sliding degree of freedom restrained. When the friction force is exceeded by the base shear the sliding degree of freedom is freed and the base node is given the applied friction force opposing the direction of motion.

System vertical restraint is entirely controlled by vertical foundation springs. The horizontal spread between the two foundations is initially limited by tie elements given an axial stiffness of 2280 kN/m based on the steel ties used in testing described in Chapter 2. The center of the ties is fixed in the FE model to provide horizontal stability and limit outward horizontal motion before sufficient backfill is applied to each side. Tie elements are assigned nearly zero stiffness during simulation of ultimate and untied service loading to reflect removal of the ties under these loading conditions. Ties were used experimentally to provide more horizontal rigidity, similar to a rock-grouted foundation, and would not be used in actual bridge construction.

Footing conditions do not greatly affect moments and the largest impact is in footing moment due to apex live load, which does not control design. Figure 4.8 shows the difference between

the fully modeled footings described above, fixed footings, and sliding only footings with no base rotation or sag. The fixed footing has on average 67% more live load positive footing moment than the fully modeled footing, however this moment opposes the backfill moment so it has limited effect in design. A tall bridge analysis was also compared and the fixed footing model predicted 17% higher footing moments at the end of backfilling than the full footing model, but this effect is minor in the load history of the bridge. Footings can justifiably be modeled as fixed at the base of the arch for design purposes. However, the research model used for comparison with experimental results presented later in this study will utilize the full foundation model.

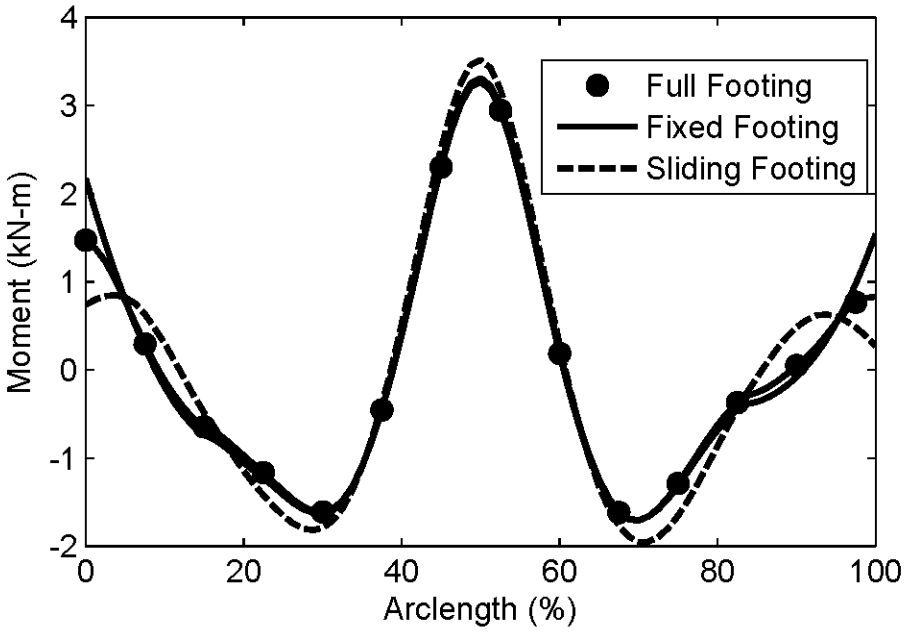

Figure 4.8. Different Footing Conditions, Apex Live Load

4.9. Pretest Model

The pretest model defined in Chapter 2 used the same analysis package as the research model, but without any of the advancements discussed in this chapter. To show the importance

of model improvement the 12.2 m span, 4.57 m rise, 300 mm diameter cross section FRP arch model that represents a typical in-service buried CFFT arch bridge was analyzed with updated properties. The moment envelope for backfilling and service line loads (same loads as experiments) are plotted in Figure 4.9. Notice that negative footing moment (the highest magnitude moment) is lower by 32% than the pretest model. The final model also predicts 18% higher peak positive moment (caused by live load at the 40% offset). This moment increase is predominantly the result of large deformation analysis during live loading, for the peak positive dead load moment is lower for the updated model analysis.

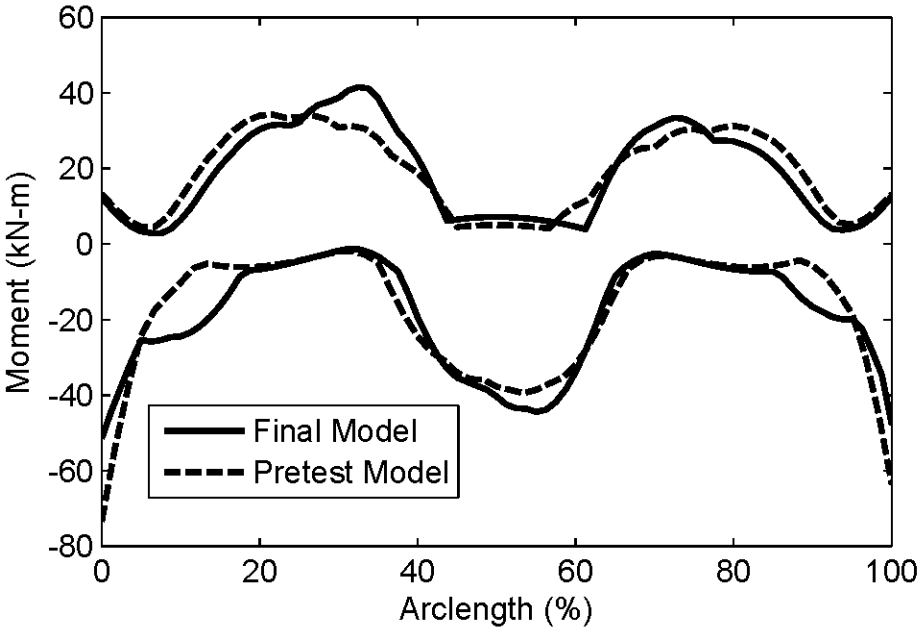

Figure 4.9. Final and Pretest Moment Envelopes for Full Scale Tall FRP Bridge

Large deformation analysis is a large portion of the difference between the pretest model and the final model. Large deformation analysis makes the greatest difference over small deformation for a 60% South offset live load, and is shown for a full-scale arch with a 337 kN patch load in Figure 4.10. The difference in peak positive moment is 21%. This is half as large as the difference for a subscale arch, but because small deformation analysis is unconservative, the

difference is large enough to justify the additional run time for the large deformation solver. Backfilling moments are larger than live load moments and have better agreement between the two solvers. There is only an 11% difference in total moment at the peak positive moment value.

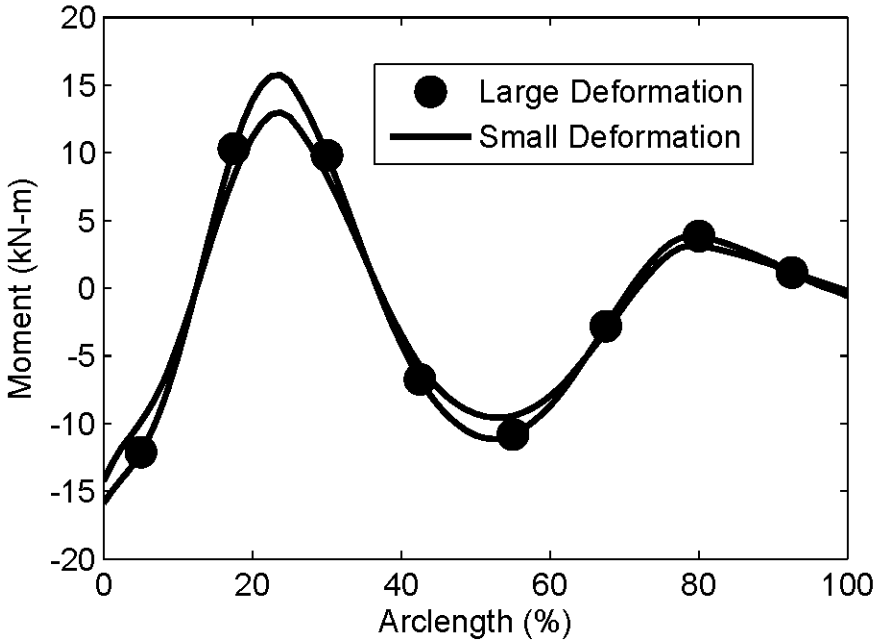

Figure 4.10. Full Scale Arch Large Versus Small Deformation Analysis

4.10. Conclusions

This chapter has discussed the formulation of a soil-spring model used in computing soil-structure interaction for buried composite arch bridges. The soil spring model uses several different elements to model decking, nonlinear arches, nonlinear soil springs, and various footing boundary conditions. Nonlinear soil springs are based on NCHRP (Barker et al. 1991) pressure – deflection relationships for retaining walls. The model uses a Boussinesq patch load distribution with vertical and horizontal stress propagation as a result of surface live load application.

This chapter has also discussed model modifications. Decking elements have traditionally been used in design, but were omitted in the present case because their inclusion only changes moments by 3% or less at critical locations such as the arch apex, footings, or shoulders. Footing elements were added that mimic the constraints of the experimental test with stiff linear-elastic elements representing the concrete footing, vertical springs allowing rotation, tie elements, and soil springs connected to footing nodes. The footing elements do not affect the analysis in a meaningful way for design purpose; they cause a large difference in footing moment due to apex live load, but this is not a critical design load case. For the critical design cases of positive moment at shoulders, negative footing moment during backfilling, and negative footing moment due to offset load, the footing elements have negligible effect and could be replaced by a fixed footing without significant loss of accuracy. In general, changing the footings from fixed to realistic behavior changes arch moments away from the footing by a negligible amount.

The role of different soil properties was examined in this chapter. Traditionally in the design of buried CFFT arch bridges, soil has been modeled as a medium-dense soil with ϕ = 37°, density = 2.0 Mg/m^3, and K_0 = 0.45. Laboratory soil tests explained in Chapter 2 for the specific soil used in this test indicate that these values are not correct and a more appropriate soil is dense, with ϕ = 44°, density = 2.4 Mg/m^3, and K_0 = 1.0. The stiffer soil reduces live load and backfilling moments compared to looser soils. Peak moments are reduced by 18% at the apex due to apex load and 25% at the footing due to shoulder load by using a dense soil model instead of a medium-dense soil model. Soil backfill used in the tests described in Chapter 3 had a high friction angle and density, which is controlled by a variety of factors including grain size distribution, soil angularity, and mineral composition. It would be necessary for an engineer to

have confidence in the backfill soil properties before specifying a higher friction angle and density.

A large deformation solver was implemented for this analysis. Large deformation has a critical effect on moments in the arch due to the interaction of axial compression and bending displacement. The small deformation solver underpredicts positive shoulder moment on the short steel bridge by 42%, which makes using the small deformation solution problematic, as this is the peak positive moment in the bridge. The research model using a large deformation solver also predicts higher positive live load moments in a full scale FRP arch than the pretest model, despite the research model having stiffer soil that provides better lateral restraint.

CHAPTER 5. CONTINUUM SOIL MODEL

5.1. Introduction

The soil-spring model discussed in Chapter 4 is intended as a design tool and is used to predict arch moments with relatively rapid analysis and easy transitions between different geometries and material properties. The soil-spring model does not attempt to accurately represent soil stresses; it separately catalogs vertical stress as load distribution and horizontal stress as restraint. In a real structure there is a complex stress state due to both oad distribution and soil restraint of the arches. A continuum-soil model using Abaqus (Abaqus 2011) uses a different approach: it models soil-structure interaction by attempting to accurately mimic soil plasticity to predict stress behavior and then use those stresses to load and restrain the arches.

To predict buried bridge response to live and dead loads, many researchers have adopted complex, two-dimensional (2D) (Taleb and Moore 1999) or three-dimensional (3D) (Moore and Taleb 1999, Petersen et al. 2010, Elshimi et al. 2014), continuum finite-element models that rely on simulating soil stress response and plasticity. The 2D models are effective for simulating backfilling loads which are comprised of uniform soil lifts, but cannot transmit patches accurately through a third dimension. CANDE (Katona 2015) is a commonly used 2D design tool for culverts and is considered conservative for buried structures by approximating a truck axle with an infinite strip load. 3D models expressly model load dissipation in all directions and are preferable to simulate load distribution. Continuum models are computationally expensive and may be of limited utility for design engineers who analyze many load combinations and load positions to find the most critical loading state for a bridge, but provide the best opportunity for understanding the behavior of a buried structure.

The accuracy of soil-continuum modeling depends on how well the soil material model imitates the physical behavior of the intended soil. The simplest material model is linear-elastic. Basic linear elastic models do not provide realistic modeling of soil behavior and are best used as a conservative design tool with a small soil elastic modulus, *E*, when little is known about the soil surrounding a bridge or culvert (Katona 2015). Improved soil models vary stiffness with depth, and depth-dependent elastic results have given good agreement with experimental data (Moore and Taleb 1999). Depth-dependent elastic models used in CANDE (Katona 2015) and in a parametric study by Petersen et al (2010) follow the Duncan elastic modulus model (Duncan 1980) or the Duncan-Selig bulk modulus model (Selig 1988), which were developed for culvert design. The elastic models may be combined with plasticity criteria to determine the effect of soil shearing failure, which tends to be more important for determining soil weight loading (Taleb and Moore 1999) and ultimate capacity (Katona 2015). The study by Petersen et al (2010) found a significant difference between plastic and elastic models under typical live load levels.

Soil plasticity models are divided into two groups: elastic-plastic models and hardening models. Elastic plastic models include the Mohr-Coulomb and Drucker-Prager models. Both models are elastic until shear stress exceeds allowable values, and then become perfectly plastic (i.e. no stiffness). The Mohr-Coulomb model is based on classic soil-mechanics and uses cohesion *c* (undrained shear strength for clay) and friction angle ϕ to determine shear limits (Abaqus 2011). The Drucker-Prager model uses different variables to represent similar behavior to the Mohr-Coulomb model. The Drucker-Prager model has an option for nonlinear (hyperbolic relationship) shear strength versus confining pressure and has a different flow rule for post-yield behavior than the Mohr-Coulomb model (Abaqus 2011).

Hardening models include the Drucker-Prager cap model and the cam-clay or limit state model (Abaqus 2011). The cap model and the limit state model incorporate plasticity without exceeding a yield strain to add further nonlinear behavior into the system. Both models attempt to replicate loss of voids and soil densification during loading and are intended to more accurately model hysteretic soil response than other plasticity models that are limited to failure (Oettl et al 1998). However, the cap model requires five additional variables to describe the shape of the yield surface in the principal stress / shear stress plane, and this data is difficult to predict from geotechnical tests.

5.2. Model Description

An explicit solver is used for the continuum FE analyses in this study because it allows zero stiffness tensile dilation in the granular backfill. Tensile stress develops during backfilling as the top surface of a soil lift bends under self-weight. The tensile stress magnitude is small, but the change in stiffness causes an irreconcilable difference in an implicit solver unless significant and uncharacteristic cohesion is added to the model. Other researchers have used explicit solvers with soil plasticity models (Taleb and Moore 1999, Petersen et al. 2010). Material model instability is exacerbated during live load when a small patch is applied to the surface of the soil.

The explicit solver creates many small time steps (10^{-5} to 10^{-6} seconds depending on element size, stiffness, and density). The explicit solver calculates the dynamic energy effects due to live load and operates under the assumption that the change in deflection and stress over a time step calculated with initial stiffness is close enough to the stress and deflection from the final stiffness that any error can be rectified by future steps. This allows stability during rapid change in stiffness. Explicit modeling is often used with contact problems and with rapid transitions in

stiffness (Abaqus 2011). Progressively installed backfill initializes large contact areas and granular soil dilation causes large transitions in stiffness.

The explicit solver is expressly dynamic and to be consistent with modeling efforts discussed in Chapter 4 it was necessary to limit the dynamic influence of the model by providing damping and by gradually applying load during dead load and live load steps to eliminate kinetic energy representative of impact forces. Realistic bridge soil loading is between impact and static: soil is dumped from an excavator or pushed by a bulldozer and is then compacted with a vibratory roller. However, a complete compacted soil lift is not dropped instantaneously on the bridge, and reducing kinetic energy is the most realistic way of representing construction loading. All loads are linearly ramped over 1 second of model time and held for one half second of model time in this analysis. Additional ramp time did not appreciably change results, but increased computation time.

Rayleigh mass-dependent damping primarily damps lower order (global displacement) arch vibration and is used in this analysis. The mass-dependent damping coefficient is set to 5% of critical damping for the lowest order frequency mode, which is an apex snap-through, and is based on Abaqus frequency analysis of an isolated apex loaded arch. Raleigh stiffness-dependent damping primarily damps smaller higher-order vibratory modes and is not used in this analysis as it substantially adds to solution time when used to provide more than 1% damping within the first 10 frequency modes.

5.2.1. Sequential Analysis

Progressive backfilling simulation requires separate sequential analyses. Jobs are run from input files that are created and batched using MATLAB (MATLAB 2011). The following paragraphs describe the process of implementing this solution.

The existing structural and soil states from prior analyses are loaded into the new analysis as a pre-state, with element stresses and deformed mesh geometries caused by the application of all prior lifts retained. The new soil lift mesh geometry is determined from the final nodal locations of the adjoining parts, the lower soil lift(s) and the arch, to limit the gap between the parts while insuring no initial overclosure. All communication between Abaqus and MATLAB is through Command Line prompts (DOS command) in MATLAB. MATLAB creates an Abaqus input text file (.inp), runs Abaqus through Command Line, creates an Abaqus output database (ODB) report in CSV format through Command Line, then reads the ODB report to get the final nodal coordinates after analysis. MATLAB automatically updates the stored mesh geometry and then adds the next lift or live load impactor. This process is repeated beginning with self-weight and continuing through backfilling and live load analysis. This allows plastic deformation of the backfill to reflect the full construction process.

5.2.2. Soil Element Mesh

Meshing is a critical part of this analysis: not only is the solution mesh size dependent, but initial overclosure (spatial overlap) or spacing between existing parts and the new soil lift causes large dynamic effects that ruin model accuracy. Abaqus adds a spring force equal to the overclosed area times the elastic modulus, and although the elastic modulus for soil is low compared to other structural materials, it is orders of magnitude higher than the density. Initial

overclosure greater than 10^{-5} mm is unacceptable and causes explosive rebound force changing the geometry of the new lift and adding impact that affects total arch stress. Initial gap between parts is 0.1 mm: small enough to have little dynamic effect when the soil lift descends into contact with existing parts, but large enough to be numerically distinct from prior lifts despite rounding error as results are loaded into MATLAB and exported to Abaqus via text file.

Soil above the footing is meshed using linear triangular elements to better match the curved arch geometry without distorted elements and with similar element size for all elements. New mesh geometry uses a characteristic element length that is user determined (typically 33 mm for the laboratory scale tests) and begins numbering perimeter nodes from the lower-outer corner such that the upper-outer (away from arch) surfaces and lower-inner (adjoining arch) surfaces have equal number of nodes and the last node (node *N*) adjoins the first node, as shown in Figure 5.1. The top surface uses ceiling rounding while the bottom surface uses floor rounding to ensure that there are fewer nodes along the bottom surface than the top, which guarantees a finer mesh near the arch where mesh refinement is most critical. The meshing routine also has a user-defined option to skew the mesh and place a finer mesh near the arch, but that was not used in reported analyses and had a minimal impact on solution time. Note that for visual clarity Figure 5.1 represents a 150 mm characteristic element length and 400 mm deep lift, and is therefore coarser and deeper than typical meshes used in analysis.

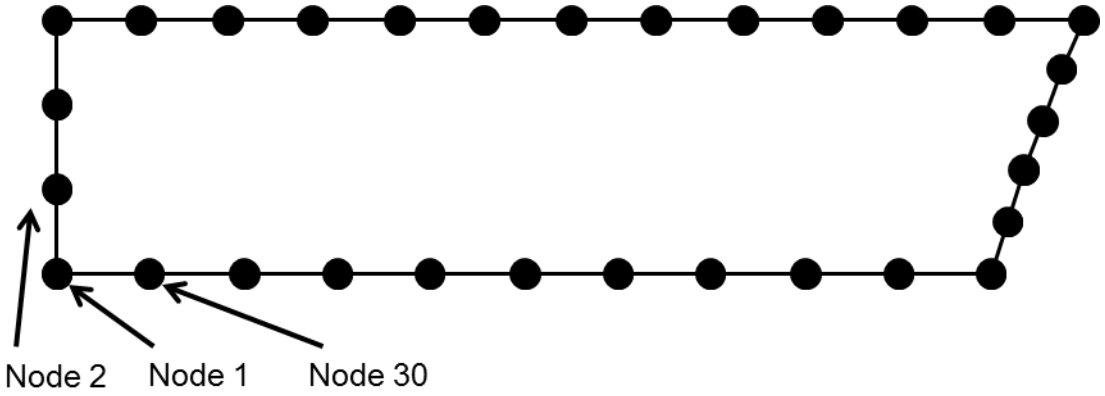

Figure 5.1. Perimeter Nodes

Interior nodes lie on vertices between opposite nodes along the perimeter; node 2 is connected to node *N*, node 3 is connected to node *N*-1, etc. Figure 5.2 shows perimeter nodes and interior lines, shown with dashed lines, upon which future nodes lie for a 30-node system.

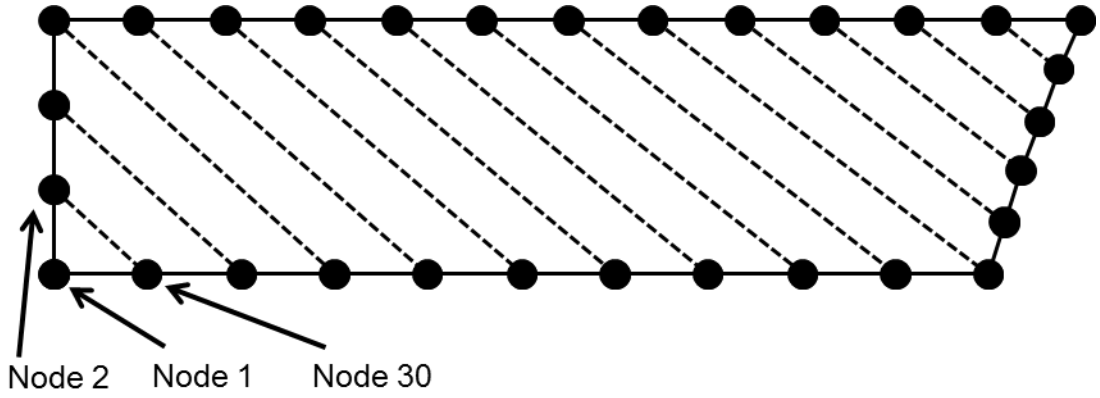

Figure 5.2. Perimeter Nodes and Lines for Constructing Future Nodes

If the adjoining line is longer than the characteristic element length, intermediate nodes are added along the dashed lines. Figure 5.3 contains a plot of seeded internal nodes for the same 30-node external mesh shown in Figure 5.1.

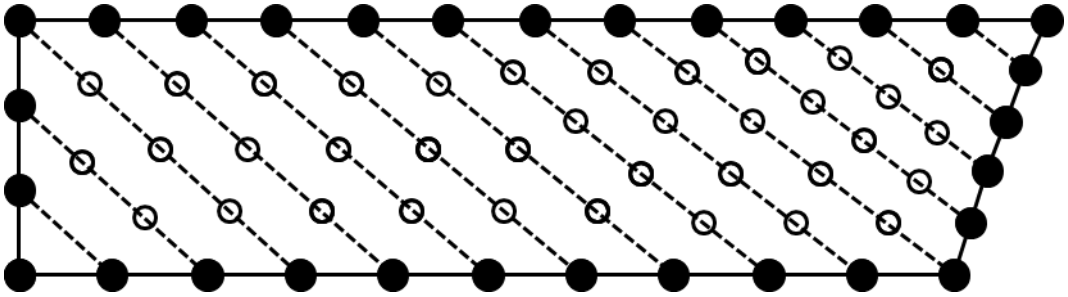

Figure 5.3. Internal Seeded Nodes for a Soil Lift

The MATLAB ‘Delaunay’ function finds the nodal connections that define the best triangular mesh for the given set of nodal locations. The Delaunay function also finds unintentional elements outside of the perimeter nodes, and this is illustrated in an inset in Figure 5.4.

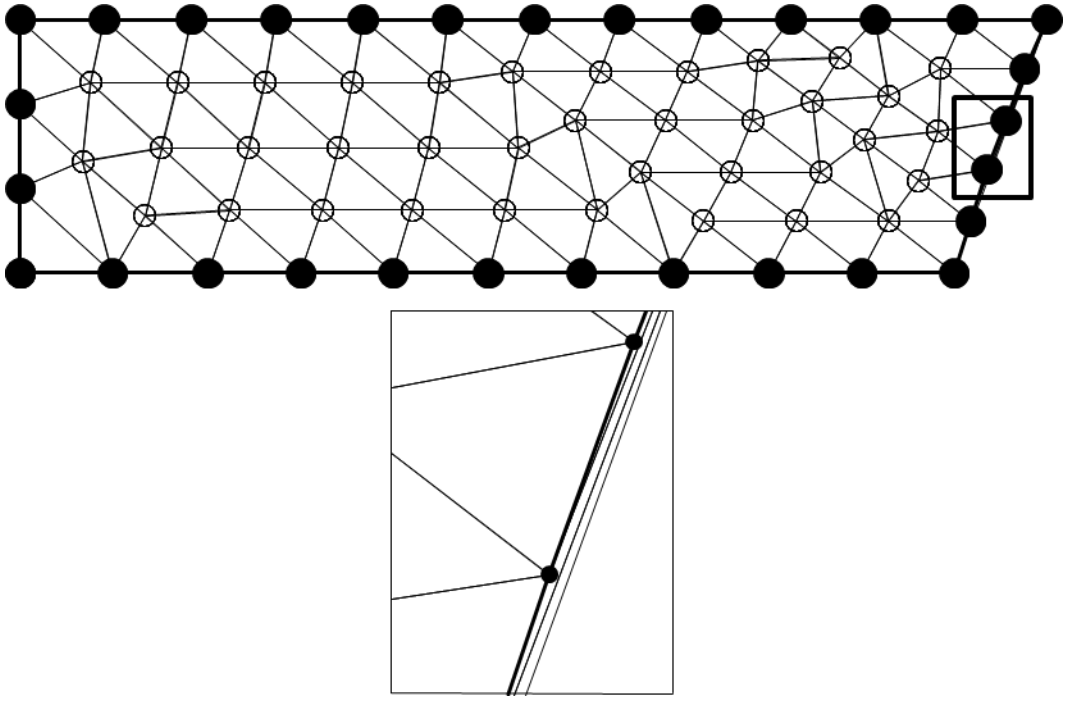

Figure 5.4. Delaunay Function Meshed Geometry, Close-up of Edge Elements

Elements that lie outside the perimeter are removed. All elements that include three border nodes are checked to make sure that they lie on two sides, which guarantees that they are internal to the perimeter defined by earlier analysis. The corrected mesh is shown in Figure 5.5.

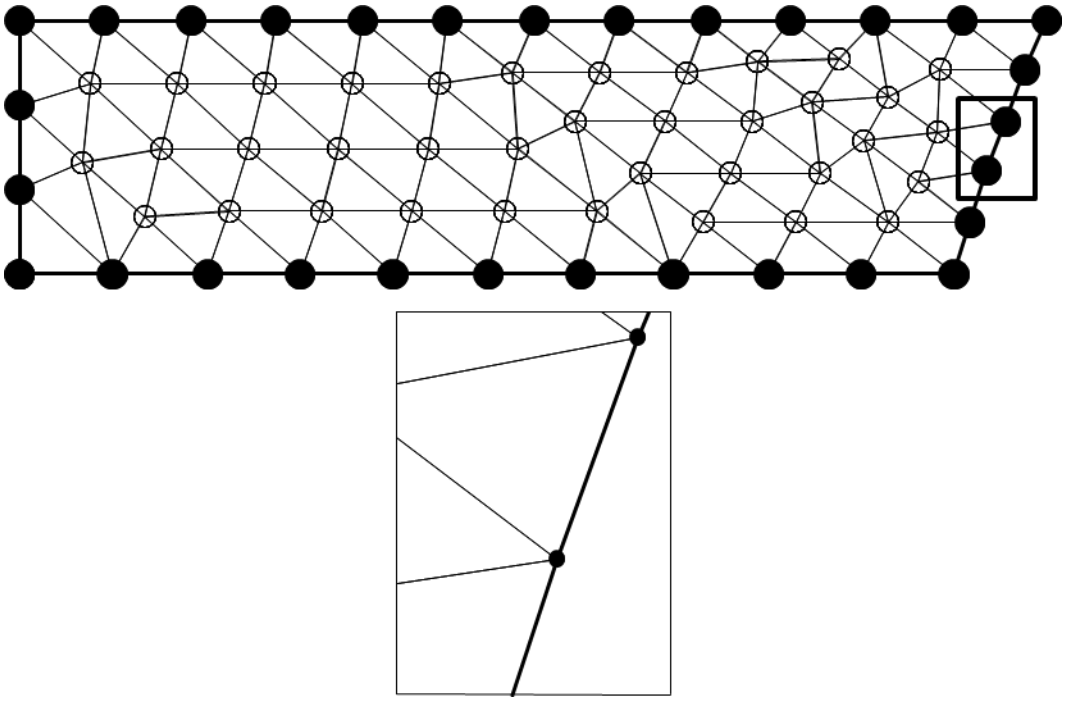

Figure 5.5. Corrected Mesh with External Elements Removed

The border elements (containing two border nodes) are listed for contact surfaces. Outer side nodes are used for boundary conditions. This meshing routine is typically used with fairly smooth meshes; lower soil meshes do not change shape much when the next soil is applied, but it is designed to handle more complicated surface in case distortion occurs in earlier lifts. Figure 5.6 contains an example of a new soil lift being applied over a mesh with large prior soil deformations.

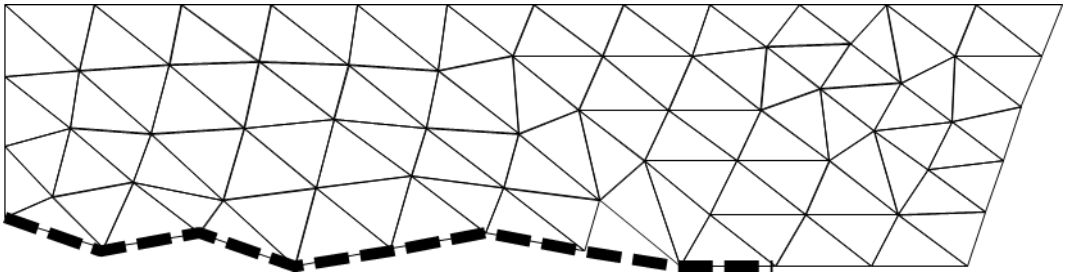

Figure 5.6. Next Lift Over a Distorted Mesh

5.2.3. Soil Stress

Geostatic stresses are applied as an initial condition for the new soil layer. Geostatic stress specifies a linear variation in vertical stress, based on soil weight, and a linear variation in horizontal stress based on a user-specified lateral earth pressure coefficient (K_0). K_0 has a small impact on model results. Changing K_0 from 1 to 3 decreases the footing moments caused by backfilling loads in the tall steel bridge by 6% and decreases the footing moments caused by backfilling loads in the short steel bridge by 10%. Away from the footing and during live loading the difference in moment is negligible.

At the start of a lift, the soil is confined on the bottom surface and the arch surface to prevent dissipation of the soil stresses. The bottom surface of the lift is loaded with the weight of the lift as a uniform pressure. The arch boundary of the lift is loaded with a combination of the vertical weight and the horizontal pressure, depending on the soil element angle. Horizontal and vertical loads along the curved mesh adjoining the arch surface are applied as concentrated nodal forces. A graphical representation of the mesh and loading is shown in Figure 5.7, with the concentrated forces drawn as a pressure. The confining forces are linearly reduced to zero over the first two-thirds of the next step to gradually initiate contact between the new lift and the existing elements. The remaining dynamic effects damp out over the last third of the step and the influence of

damping is shown in Figure 5.8 for apex moment of the short steel bridge. Notice that the model only outputs results at 0.05 second intervals to limit file size, which is inadequate to see the period of the moment oscillations. However, the final quarter second has nearly a constant moment indicating that dynamic effects have been damped at this point in the analysis.

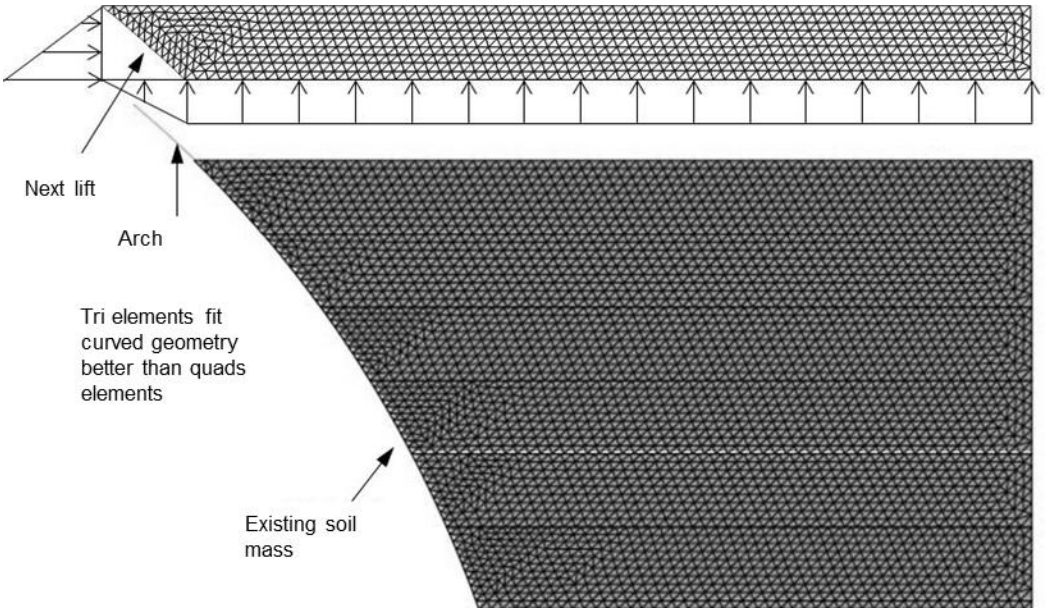

Figure 5.7. Soil Lift Placement, Continuum Model, Typical Mesh

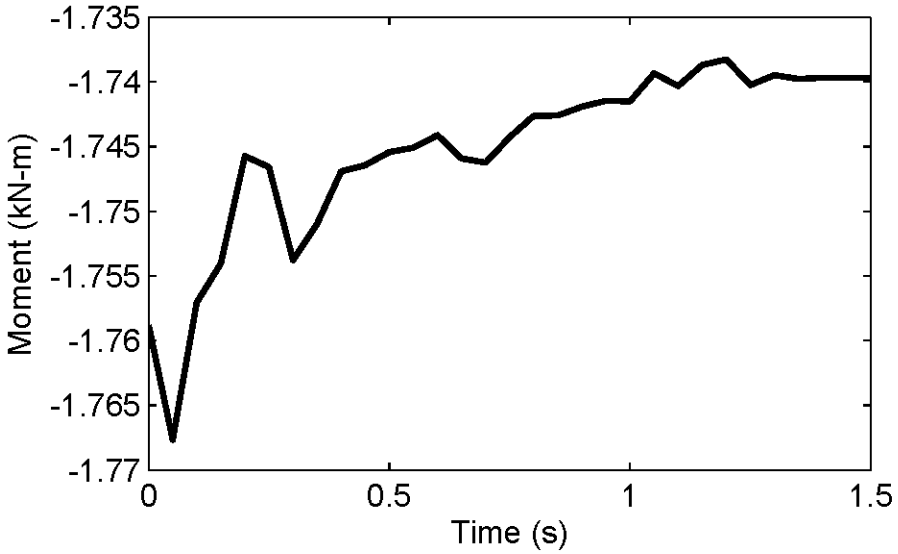

Figure 5.8. Apex Moment During Final Backfilling Step, Short Steel Bridge

5.3. Materials

Only the steel subscale arches are modeled using the soil-continuum model. The moment-curvature relationship used for CFFT arches does not easily translate into the Abaqus modeling software package and would require a user defined material. Thus continuum analyses of the CFFT arches that capture arch nonlinear material response are beyond the scope of the present research. Steel for the arches is modeled using classic metal plasticity with post-yield behavior determined from experimental stress-strain curves presented in Chapter 2.

Soil is modeled as elastic-perfectly plastic using the Mohr-Coulomb plasticity model. Soil elements have zero stiffness in tension or when the element fails in shear (dependent on stress state, friction angle, and cohesion). The volumetric strain is controlled by the dilation angle, (ψ). Petersen et al. (2010) indicates that there is a noticeable improvement in load distribution modeling results when using a Mohr-Coulomb model over an elastic model, but there is little value to using a more complicated plasticity model. The relationship Abaqus uses for principal and shear stresses is presented in Figure 5.9. Mohr-Coulomb plasticity is defined by three parameters: friction angle (ϕ), cohesion, and ψ. The soil model also has standard elastic properties and density.

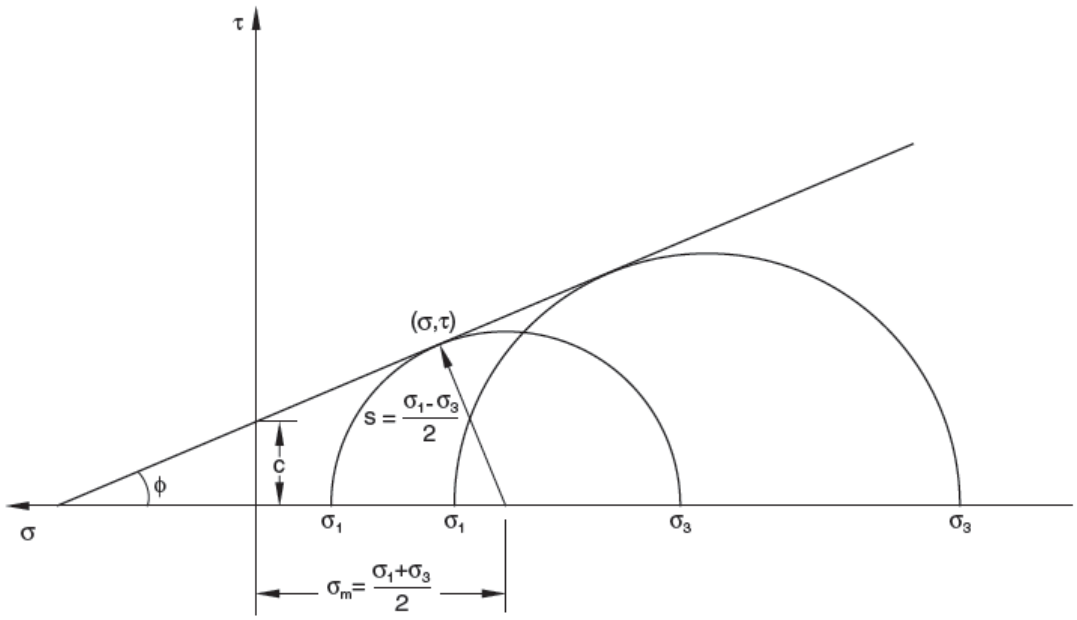

Figure 5.9. Mohr-Coulomb Failure Criterion, from Abaqus 2011

The soil used in experiments was described in Chapter 2. The following parameter values were used: friction angle of 44° (experimentally determined), a small cohesion of 50 Pa, dilation angle of 14° ($\phi - 30°$ taken from Petersen et al. (2010)), and total density for compacted granular fill of 2.4 Mg/m^3. An elastic modulus of 28 MPa (reasonable for well compacted granular soil at 1.2 m depth) and Poisson's ratio of 0.3 were assumed after Petersen et al. (2010). The elastic modulus of the soil is a parameter that is discussed in more detail later in this chapter, and varying elastic modulus with depth was considered.

Other structural components are added to the continuum analysis based on boundary conditions from experiments in Chapter 2. Experiment foundations were tied together and clamped against wooden restraint blocks with steel through ties. The foundations sat on low-friction HDPE pads over a concrete floor that prevented negative vertical deflection, allowed sliding, and did not restrain rotation. The steel ties are modeled with beam elements. All other

parts of the experimental foundation system are modeled using plane-stress elements and assumed elastic. Figure 5.10 shows a detail of the finite-element mesh around the foundation area for a typical model illustrating the range of element types and boundary conditions.

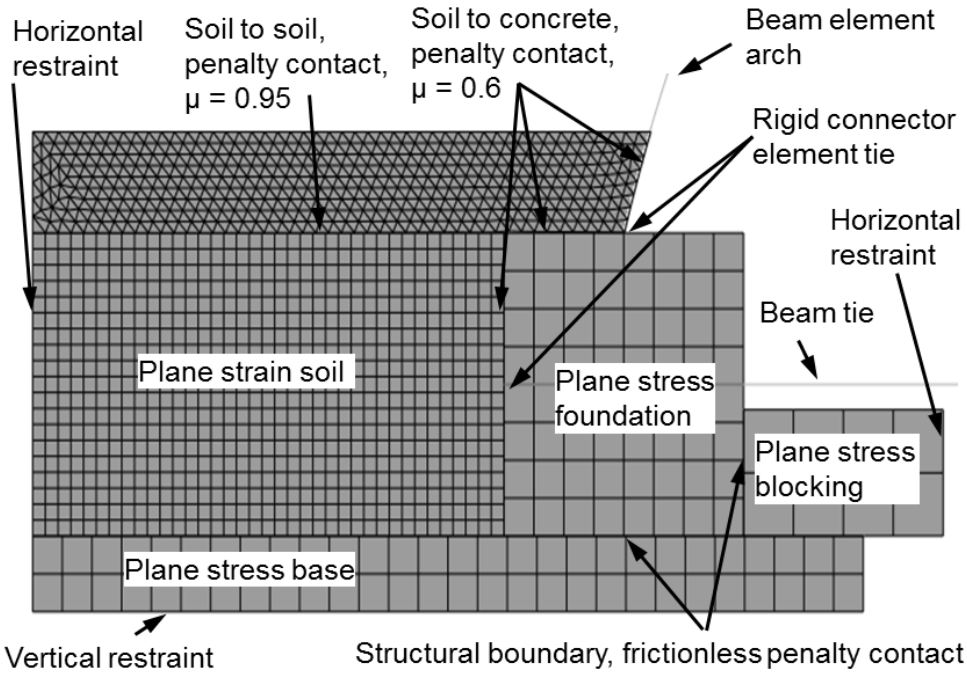

Figure 5.10. Detail of Arch Footing Model Interface with Contacts and Boundaries

5.4. Contact/Boundaries

The arch and foundation interface and tie and foundation interface are modeled with rigid connector elements to allow moment transfer between beam and continuum elements. The soil-soil interface between a newly placed lift and soil below is initially modeled as surface-to-surface contact with a rigid normal boundary and a transverse friction coefficient large enough to prevent slip of 0.95, although this parameter has no effect on analysis. Varying friction coefficient between 0.3 and 0.95 produced less than a 3% difference in moment for all backfilling load cases. Following placement of the lift, this boundary is subsequently changed to

a rigid tie so the in-place soil mass acts as one unit. The arch-soil interface is modeled using surface-to-surface contact with hard normal contact and a coefficient of friction of 0.6 (NAVFAC 1986) throughout the analysis.

The vertical soil boundary on the outside of each soil lift is fixed from horizontal movement, but is free to move vertically. Foundation restraint blocks are fixed on their inner edge from horizontal movement and fixed from vertical displacement along the bottom face. The base pads are fixed from horizontal motion along their outer vertical face and are fixed against vertical movement along their bottom face.

5.5. Live Load

Live load is applied to the model using a beam-element impactor designed to mimic the load beam in experiments. The soil-continuum model presented herein is expressly a 2-dimensional (2D) model, but it can represent experimental live loads which were applied as a uniform infinite strip, described in Chapter 3. The model presented in this chapter would not be accurate for true truck loading because the separate tire patches cannot be modeled using a 2D continuum. Figure 5.11 shows an Abaqus screen shot with the applied impactor element in a typical simulation.

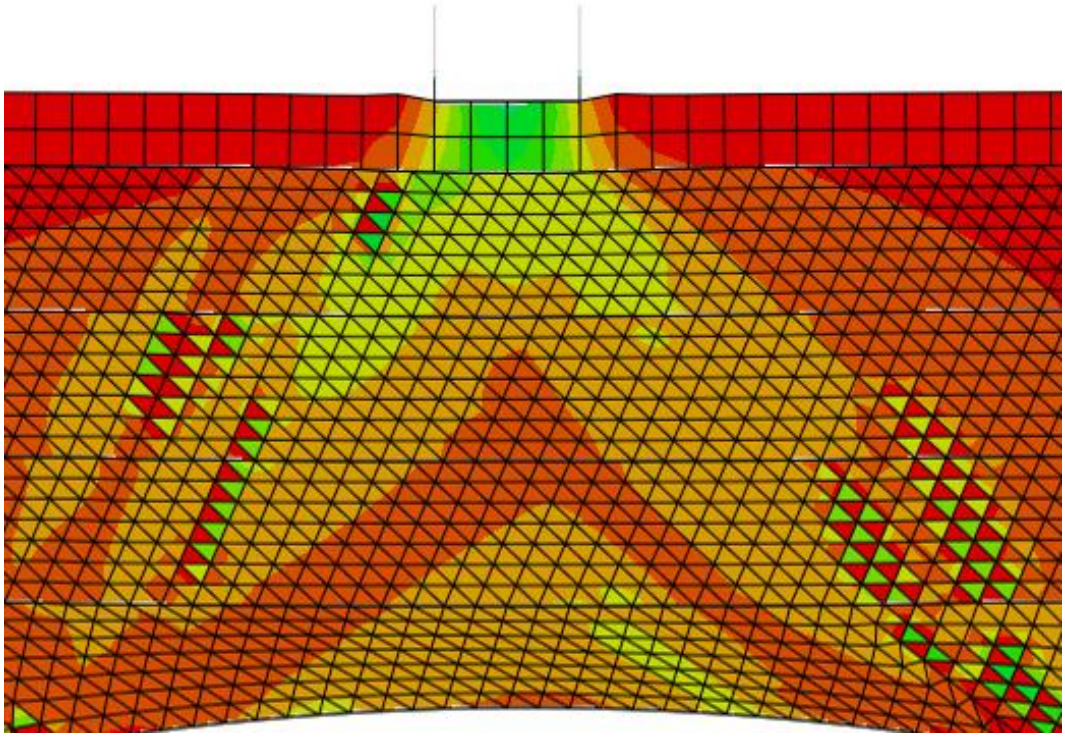

Figure 5.11. Impactor Contacting Apex Soil, Tall Bridge

5.6. Mesh Refinement

There were two different mesh refinement studies for this analysis: the mesh density for the arch and the mesh density for the soil. The arch mesh density was determined form the apex moment convergence in Table 5.1 for a uniform applied load (self-weight). Self weight of the arch produced small moments that are below yield. The arch uses B21 Abaqus beam elements which use constant moment in each element and are expected to exhibit poorer convergence than cubic shape function beam elements (Abaqus B23 elements), but are the only beam elements available in Abaqus Explicit analysis. The finest beam element tested was used in the typical converged model.

Table 5.1. Apex Moment Convergence Under Self Weight for an Isolated Arch

Element Size (mm)	Moment (kN-m)	Difference (%)
610	0.121	9.61
305	0.133	0.88
152	0.133	0.63
76	0.134	0.13
38	0.134	0

The soil mesh could not be refined independently in an isolated model, so it was refined using the full system analysis. Steel subscale bridges were backfilled using the progressive backfilling simulation and an apex live load was applied. Convergence is checked for the apex live load moment and the apex backfilling moment in Table 5.2. Due to the large contrast in solution time the second finest characteristic element length (33 mm) was used for all results and reported model information. Solution time for a live load is also reported.

Table 5.2. Model Soil Mesh Convergence

		End of Backfill		Live Load Only	
Element Length (mm)	Solution Time (S)	Moment (kn-m)	Difference (%)	Moment (kn-m)	Difference (%)
203	50	-1.76	4.30	2.56	4.44
152	215	-1.73	2.32	2.54	4.92
102	478	-1.72	1.60	2.61	2.43
51	906	-1.70	0.63	2.63	1.55
43	1278	-1.70	0.40	2.64	1.14
33	2112	-1.69	0.17	2.66	0.49
25	4018	-1.69	0	2.68	0

5.7. Effect of Soil Elastic Modulus

Soil stiffness is dependent on current stress and stress history. The best representation of soil is a pressure history dependent model. However, this requires a user defined material and additional soil parameters not found during laboratory tests in Chapter 3. It may offer only

limited model improvement (Petersen et al. 2010) with a substantial increase in work. Vertical stress in soil comes from compaction and overburden and it is common to model the soil stiffness as depth-dependent. During a progressive backfill analysis the soil depth is changing with each lift. Increasing the elastic modulus of existing soil elements based on the current depth causes uplift as the elements become stiffer, which is unrealistic and places forces in the arches that are not consistent with arch behavior. Defining a different soil elastic modulus for each soil element based on the elevation of the element is a viable solution discussed in more detail later.

During backfilling, the soil pressure is mostly dependent on active pressure and soil shear because the arch is moving away from the soil mass. This is controlled by friction angle and the plasticity model, not the elastic element stiffness. During live loading the arch reacts into the soil mass, which causes soil shear, but also causes elastic soil compression, meaning that elastic modulus may be important for live load moments in the arches.

To test the importance of soil elastic modulus assumptions three soil elastic modulus options were considered. The first was a depth-dependent elastic modulus model with linear-interpolated stiffness constant for each soil lift. Depth-dependent stiffness used in the model is displayed in Table 5.3 and is from densely compacted granular (well-graded sand, 95% relative compaction - SW95) used by Petersen et al. (2010). The other two models use constant stiffness based on a 1 m soil depth (average cover over the loaded area) and a 3 m soil depth (depth to the footings of the tall arch). Backfill moments for the tall bridge for both the low constant *E* case and the variable *E* case are plotted in Figure 5.12.

Table 5.3. Elastic Modulus vs Depth for Varying Stiffness Model

Depth (m)	Modulus (MPa)
0	11

1	28
2	41
3	59

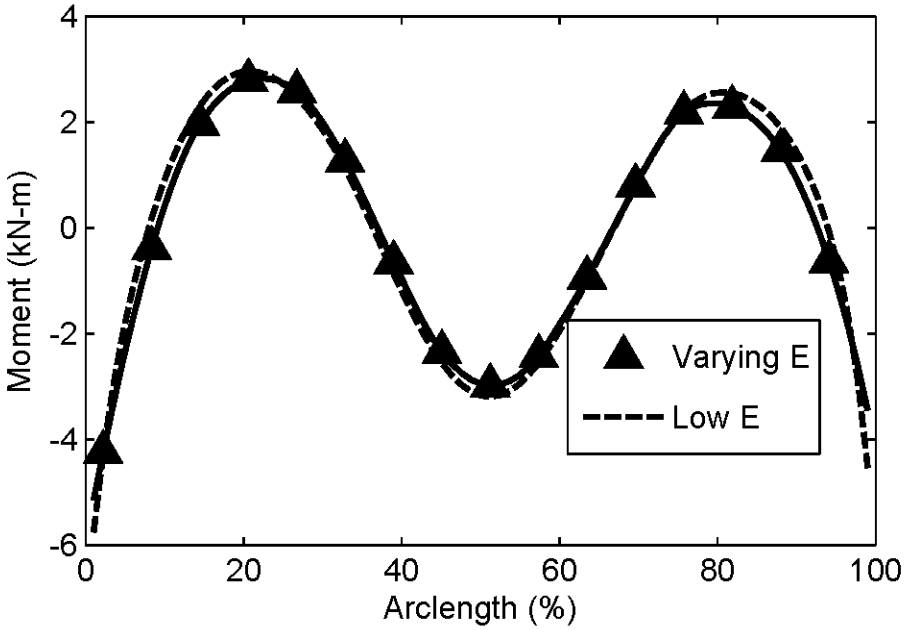

Figure 5.12. Comparison of Constant and Depth-Dependent Soil Elastic Modulus

The moment in Figure 5.12 is very similar for the variable *E* and low *E* cases. Moment for the models differs by less than 0.1 kN-m at all measured points except near the footings. The low *E* model predicts higher footing moments. A high *E* model was also created, but it is indistinguishable from the varying *E* model in all load locations except the footing. Apex live load response differs more and is shown in Figure 5.13. The high *E* plot is included in this model, and it shows that the two constant elastic modulus models bound the result of the variable soil stiffness model. The variable stiffness model should better represent the soil behavior for live load, and the similarity during backfilling justifies the assumption that dead load is driven by

soil plasticity, not stiffness, and installing high stiffness lifts does not appreciably change the dead load response.

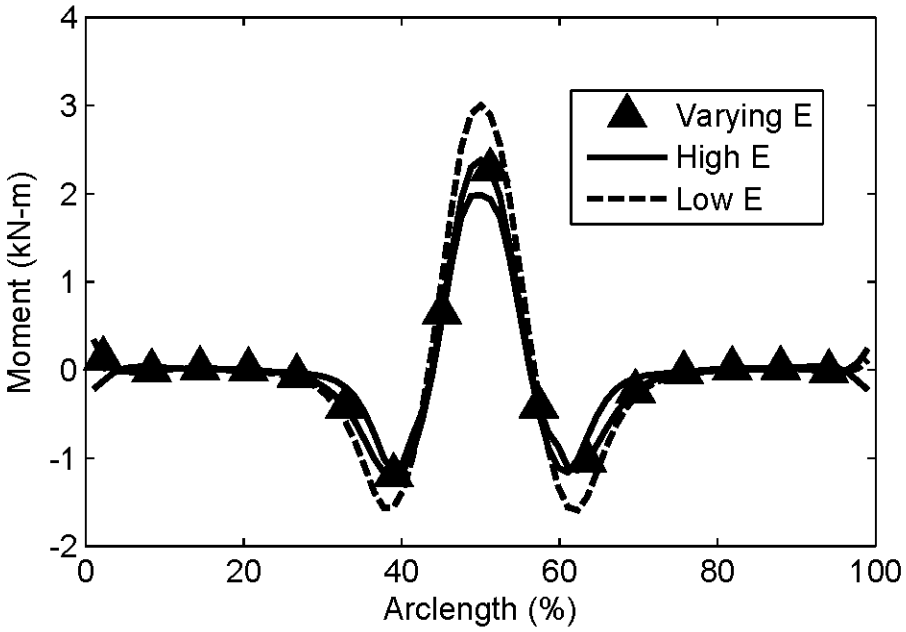

Figure 5.13. Moment Due to Apex Live Load, Different Soil Elastic Modulus

5.8. Soil Pressure

The primary motivation for continuum modeling in this situation was to more accurately mimic soil stresses than with the spring model. It is worth looking at soil pressures during analysis. The following six figures are screen shots from Abaqus showing soil stress gradient for the short steel bridge. In the plots the color white is 0 kPa and the color black is 140 kPa, with grayscale in between. Figure 5.14 is vertical stress at the end of backfilling, Figure 5.15 is vertical stress during 60% South offset load, and Figure 5.16 is vertical stress during apex load.

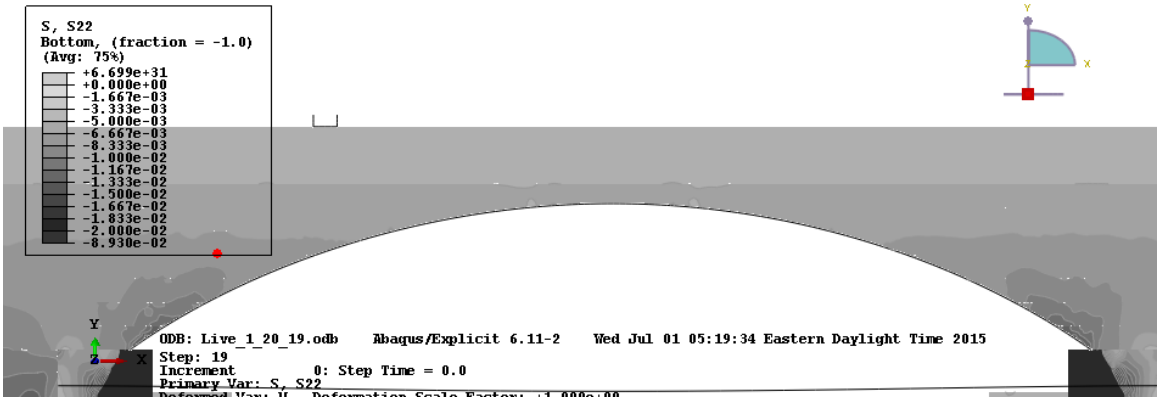

Figure 5.14. Vertical Stress, End of Backfilling Short Arch

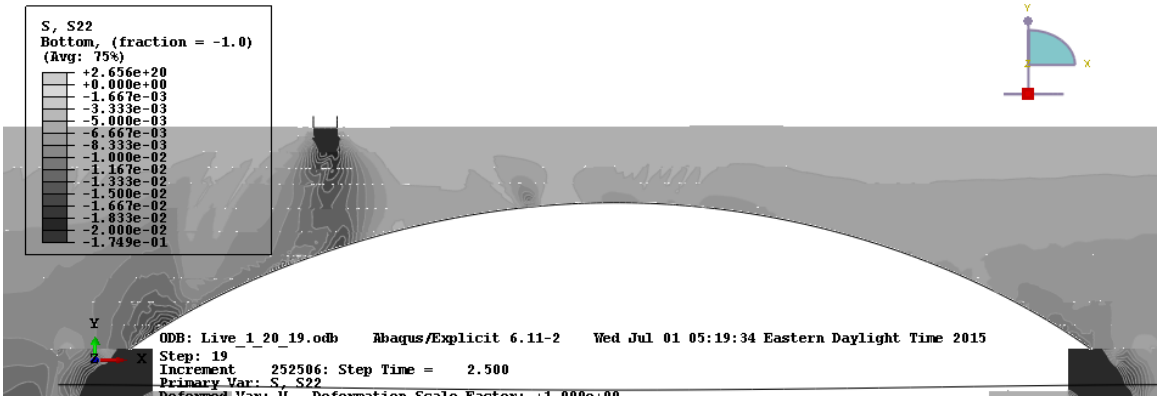

Figure 5.15. Vertical Stress, 60% South Offset Live Load, Short Arch

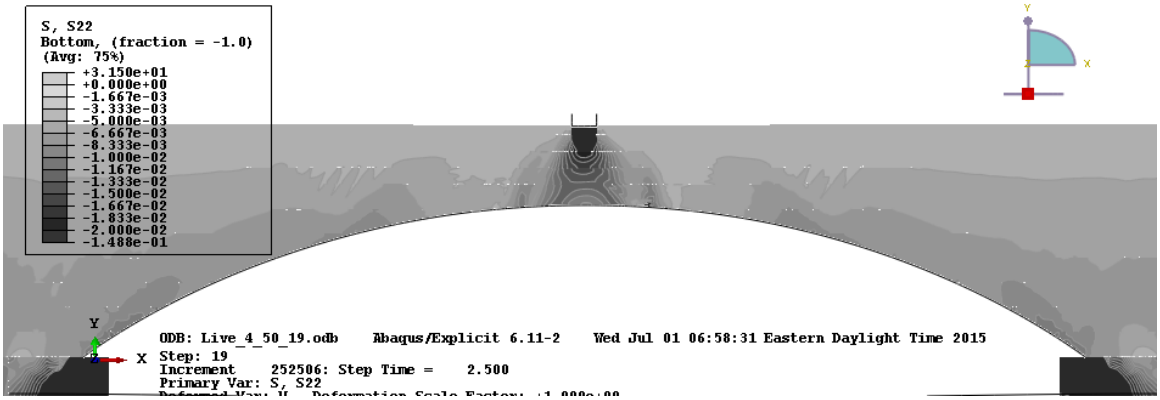

Figure 5.16. Vertical Stress, Apex Load, Short Arch

The apex and backfilling load behavior is close to expectations. Backfilling stresses have a nearly uniform depth-dependent gradation, although there is a soil stress concentration next to the arch about 1 m from the top of foundation. Apex load vertical pressures are nearly symmetric, and there is a slight pressure void at the apex where soil arching distributes the load over a greater area. The South 60% offset results are more unexpected. The vertical pressure at the apex is double the vertical pressure due to soil alone, and this is due to the arch apex being driven into the soil, not due to load distribution. Also, the pressure spike above the footing goes from 60 kPa at the end of backfilling to 130 kPa due to live load. For perspective, assuming soil self-weight and a Boussinesq soil distribution, pressure in the same region would theoretically be 35 kPa at the end of backfilling and 50 kPa during 60% offset load.

Figure 5.17 is horizontal stress at the end of backfilling, Figure 5.18 is vertical stress during 60% South offset load, and Figure 5.19 is vertical stress during apex load. Horizontal stresses are smaller than vertical stresses, and keeping the same color scale results in poorer differentiation of pressure. Pressure distribution at the end of backfilling and during apex load is close to symmetric, although North side horizontal pressures are slightly higher than South side pressures due to unbalanced load sequence. Offset loads are more interesting than the nearly symmetric cases. Under the point of load application and in the rest of the shoulder region the horizontal pressure is smaller than during backfilling, an example of active soil loading. Horizontal pressures are higher on the passive side of the arch, which is expected. One unexpected result is the high magnitude of horizontal soil pressures on the South side (loaded) of the arch above the point of load and trending toward the apex. The arch is moving away from applied load in this region, so conventional theory suggests that these pressures are active. Based on local soil depth this would be pressures from 5 kPa to 15 kPa. But, the continuum model indicates that the

pressures are much larger and vary from 20 kPa to 70 kPa in this region. The vertical stresses are small, close to the theoretical value of 10 to 20 kPa, and a 70 kPa horizontal pressure with a 10 kPa vertical pressure would exceed the Mohr-Coulomb shear capacity, which would help explain the variation in pressure throughout the region.

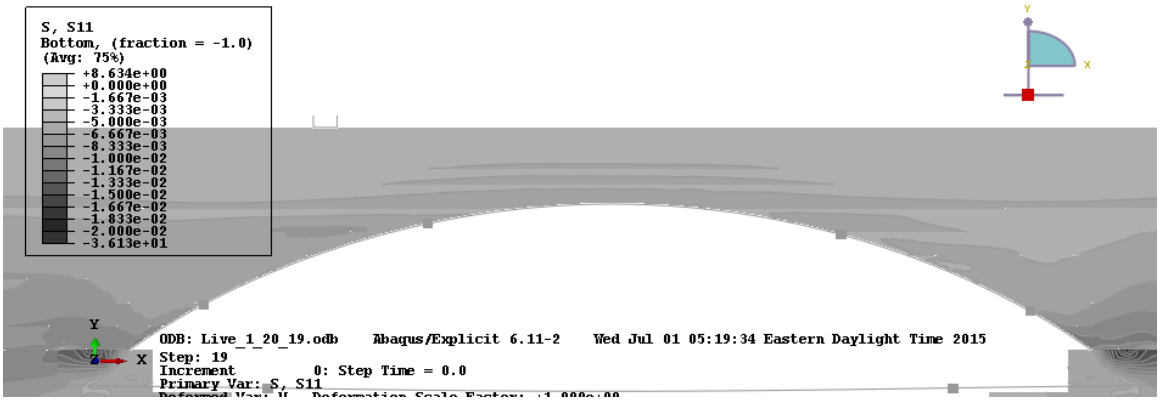

Figure 5.17. Horizontal Stress, End of Backfilling, Short Arch

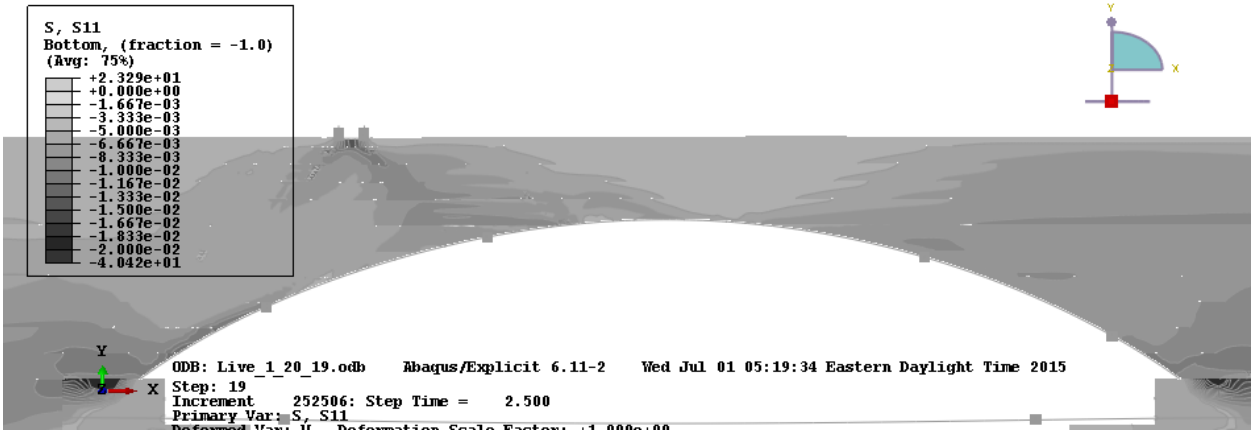

Figure 5.18. Horizontal Stress, 60% South Offset Load, Short Arch

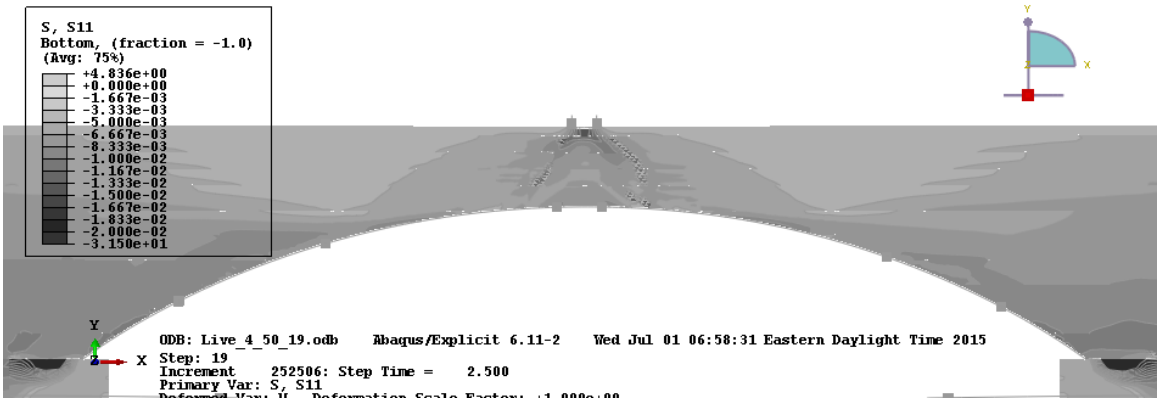

Figure 5.19. Horizontal Stress, Apex Load, Short Arch

5.9. Conclusions

The chapter discussed a soil-continuum model that was developed in Abaqus using an explicit solver to implement true tensionless granular soil plasticity. This approach is intended as a physics-based model that uses a consistent assumption for load distribution and arch restraint, as opposed to the soil-spring model which uses a Boussinsq load distribution to distribute vertical load and soil springs to provide horizontal restraint.

The soil-continuum model is intended to mimic the steel bridge laboratory tests and was modeled in Abaqus using a classic metal plasticity model. Results are compared with steel bridge experimental data in Chapter 6. This research did not include soil-continuum CFFT arch bridges because the CFFT arches are complicated nonlinear components that would require a separate user-defined material. The arches are modeled in the soil-spring simulation following Burgueño (1999) and assuming linear-elastic fiber behavior and nonlinear confined concrete behavior based on a Mander (1988) model. This is handled in the beam-spring model with a moment-curvature relationship, but it cannot be translated simply into Abaqus, which uses stress-strain material relationships and integrates over the beam depth to find bending stiffness.

The soil-continuum model simulates the progressive backfilling sequence and live loads following soil installation. The progressive backfilling simulation uses a custom meshing routine that generates triangular elements to closely follow the deformed shape of the arch and the underlying soil. Live loads are applied using a beam element impactor part that replicates experimental live loads. The soil-continuum model is also used to replicate ultimate load.

Varying the stiffness of soil with depth is considered an acceptable practice and is used in design software and in the literature. Implementing this option has an effect on solution values and so will be used in comparisons. The initial horizontal soil stress has a small effect on footing moment but does not change moment away from the footing. Changing the friction coefficient for soil lift placement has no measureable effect on solution values.

CHAPTER 6. STEEL ARCH RESULTS

6.1. Introduction

Arch spacing, diameter and/or composite shell fiber architecture in buried composite (CFFT) arch bridge designs are typically controlled by moment capacity. Arch moments depend on soil dead load and the effect of added vehicular live load. Soil dead loads are applied in progressive backfilling where compaction produces elevated horizontal stresses and imparts permanent displacements. After soil is placed it provides restraint for all future soil lifts and for vehicular loads, supplementing arch stiffness. Soil also distributes vehicular loads. These three effects produce complicated load profiles and are not well-represented by prior research, which has focused on highly idealized load cases: isolated, without soil, CFFT arches subject to an apex load (Dagher et al. 2012, Bannon 2009), or straight CFFT members under 3-point bend (Parry 2013) and 4-point bend (Dagher et al. 2012, Bannon 2009). CFFT arches have a nonlinear moment response with regard to curvature and axial load because their stiffness is largely governed by concrete, which cracks in tension and exhibits a nonlinear stress-strain response at high compressive stresses that is influenced by the confinement provided by the FRP shell. Soil also has a nonlinear response with regard to arch deflection; as soil is loaded it compresses and becomes denser and stiffer until it begins shearing, in which case it dilates and loses stiffness. Both nonlinear material phenomena are present in CFFT arch bridges, but it becomes hard to distinguish the role of soil on arch restraint and load distribution when the arch itself has large variations in stiffness.

There was a need to assess the response of CFFT arch bridges to realistic loads. To this end a scaled testing program was initiated. The scaling procedure is explained in Chapter 2 and the scaled test method and design is explained in Chapter 3. This chapter focuses on the response of

subscale steel arches, which are stiffness-matched to CFFT subscale arches and are designed to be linear elastic under service level loads, decreasing the nonlinearity in the system. Steel also lends itself to moment and axial load extraction from measured strains. Experimental data from subscale steel arches is compared to model predicted response from both a soil-spring model presented in Chapter 4, which is a modified version of the design software for current CFFT bridges, and results of the soil-continuum finite-element model presented in Chapter 5, which uses soil plasticity and frictional contact to produce a more physically accurate approach for arch-soil behavior.

Experimental results include moment and axial load, which are inferred from measured strains. Strain gauges were mounted on the top face, bottom face and the neutral axis for each measured location. Due to the small thickness of the arches and the curvature neutral axis gauges were not positioned perfectly and the strains they record are neglected in all calculations. To compute axial force and moment the cross section is divided into 100 equal thickness sections (with equal areas due to a uniform rectangular cross section for both steel bridge arch cross sections). Each section is assigned an average strain and based on the measured extreme fiber strains and the assumption that strain varies linearly over the depth of the member (plane sections remain plane). Stresses for each portion of the cross section are inferred from strains based on experimental results of coupon tests reported in Chapter 3, with different response for both thickness arches. Note that stress-strain response was linear-elastic until strains exceeded 80% of the yield stress (275 MPa) which was the onset of softening prior to plastic straining. Force is computed by multiplying stress and area for each cross section division. Axial load is the sum all 100 of the computed forces over the depth. Moment is the sum of each cross sectional force times the cross sectional height of the local force, and because axial force is

assumed to act at the center of gravity of the cross-section, moment is corrected by subtracting the produce of the axial force times half of the depth.

Cross sections were chosen to provide a scaled stiffness in in-plane bending with adequate capacity to remain elastic throughout backfilling and live load sequence. A consequence was that the chosen sections are axially stiff while being flexurally soft for the given loads. The bending strain is commonly 90% of the total member strain, which reduces the reliability in computed axial force. Slight gauge misalignment or gauge error that only changes the moment response by 3% may change the computed axial response by 30% or more. This error is particularly prevalent near the foundations: strain gauges were aligned to be on a transverse cross section, but the arch foundation interface occurs at an angle. For short rise steel arches this means that the bottom face gauge was centered 65 mm from the concrete foundation, but the outer face gauge was centered 115 mm from the concrete foundation. This may have led to a systematic mismatch in strains as the foundation is an area with potentially rapid transition in moment. Selected results are shown and discussed in this chapter.

6.2. Backfilling Response

Soil backfilling was performed in lifts, and as is common during construction, lifts were not clearly demarcated. Lifts were delineated while post-processing total pressure cell data (TPC) to identify TPC vibration caused by the compactor. This allowed data to be presented per lift instead of by time.

The number of backfill lifts differed for each bridge. The short bridge consistently used approximately 200 mm thick lifts with lift 1 being 400 mm on the South side and 200 mm on the North side from the base of the foundation. Lifts alternated by adding 200 mm to each side of the

bridge until lift 16. The final three lifts were installed across both sides. The tall bridge initially was backfilled with compacted soil, installed in 150 mm lifts on alternating sides until Lift 14. Lift 1 was 450 mm on the South side and 300 mm on the North side. After Lift 14, soil was installed in 200 mm lifts. Soil lifts alternated until Lift 30, and the final three lifts were across both sides. For the tall bridge backfilled with under-compacted soil, Lift 1 was 600 mm on both the North and South side of the bridge. Lifts were constant soil volume, approximately 1.6 m^3, with average depth 200 mm and installed alternately on each side of the bridge. Soil lifts installed above the apex were also alternating for construction efficiency.

6.2.1. Backfilling Soil Pressure and Axial Load

Figure 6.1 illustrates North foundation soil pressures for the short bridge. Figure 6.2 illustrates North foundation soil pressures for the tall bridge with under-compacted soil (abbreviated UC soil). The tall bridge with compacted soil had soil pressures measured using horizontal TPCs only (not vertical and horizontal TPCs as with the other bridges) and soil pressures are not presented for this structure. Figure 6.1 and Figure 6.2 indicate that changes in vertical pressure alternate between large gains, when soil is placed over the given side, and small gains, when soil is placed on the opposite side and the foundation under the gauge rotates. They also indicate that horizontal pressure behind the mid-height of the foundation does not increase uniformly with the addition of each lift. Horizontal pressure increases modestly for the short bridge during the early stages of backfilling, and increases more rapidly during final backfilling stages. This is a sign of horizontal foundation thrust and movement, which can be significant for a short arch structure. Early in backfilling, the soil drives the foundations together. When soil elevation increases, more axial load is carried by the arches. Figure 6.3 illustrates axial loads computed from measured short arch strains at the North foundation, highlighting this increase in

arch compression with increased soil elevation. While some of the horizontal foundation thrust caused by arch axial load is carried by the steel tie rods, some of it also results in higher horizontal soil pressures behind the foundations.

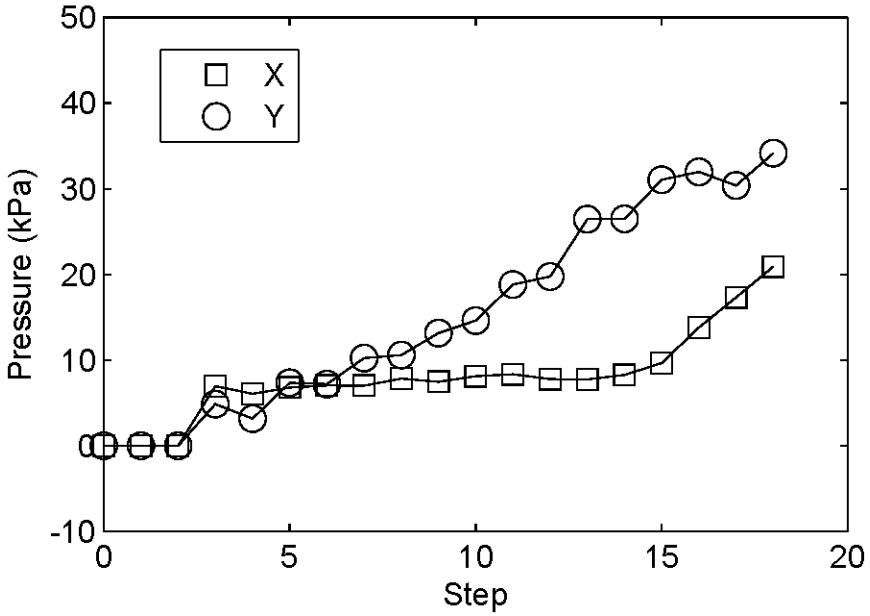

Figure 6.1. North Foundation Pressure During Backfilling, Short Bridge

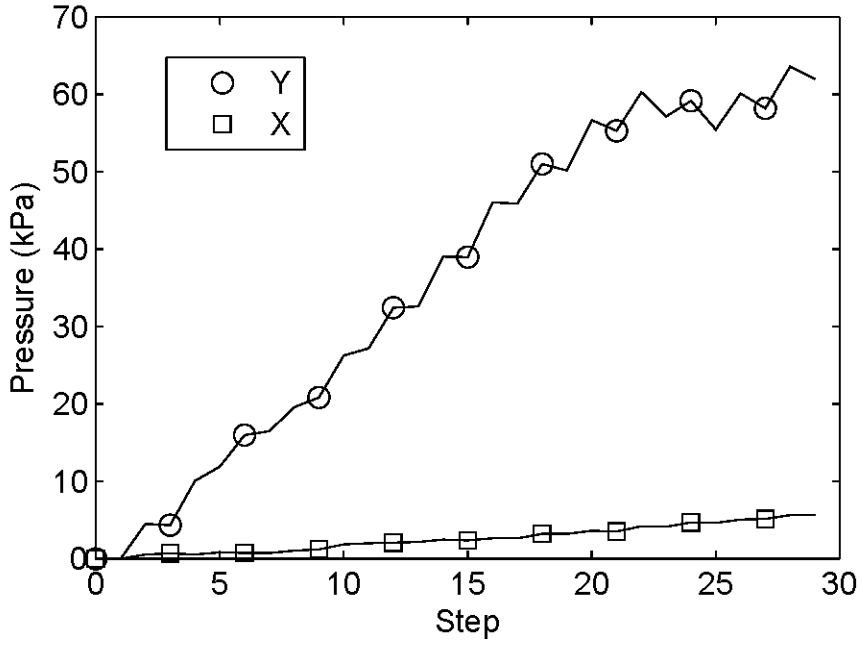

Figure 6.2. North Foundation Backfilling Pressure, Tall Bridge, UC Soil

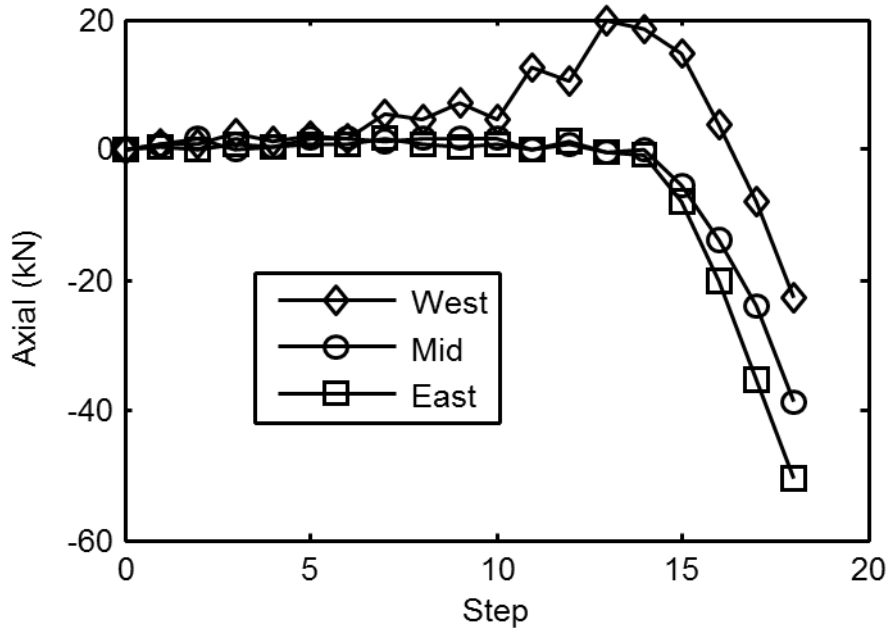

Figure 6.3. Arch Axial Load, North Foundation During Backfilling, Short Bridge

The change in vertical foundation pressure added per lift decreases as backfilling progresses for the short bridge. Early lift pressures increase by an amount equal to or greater than the weight of overburden soil, while later lifts have pressure changes less than the weight of overburden soil. This suggests that foundation rotation during soil placement and high axial loads cause the heel of the foundation (buried in the soil) to dip down while the toe of the foundation rotates upward. In contrast, tall bridge vertical pressure increases remain nearly uniform per lift and closely reflect the weight of overburden soil, indicating little foundation rotation.

Also notable in Figure 6.3 is that the axial loads in the arches near the foundation are in net tension for the first half of loading. Horizontal force from soil pressure along the arch creates tension in the section while vertical soil force creates compression in the section. Early stages of backfilling have larger horizontal force from compaction than vertical force due to the steep arch angle near the foundation. Soil forces applied above the shoulder are mostly vertical due to arch shape, which results in predominantly compressive axial load. At the same time the horizontal soil forces closer to the foundation become more active as the arch is driven by the soil. The inconsistency in axial load between arches is likely a result of arch geometric irregularity near the footing produced during manufacturing. Arches were welded to length from pre-bent sections, and when cast in footings, the apex and shoulders of all three arches were aligned. However, this caused the arch-foundation position to vary slightly and resulted in uneven loading in the bottom eighth of the arc length.

6.2.2. Backfilling Displacement

Figure 6.4, Figure 6.5, and Figure 6.6 illustrate apex displacements (positive upward) during the backfilling process for the short bridge, the tall bridge with compacted backfill, and the tall bridge with under-compacted backfill, respectively. The short bridge has good agreement

between each of the three arches, with a peak displacement near 10 mm and final displacement near 6 mm. The tall bridge has greater apex displacements than the short bridge, with compacted soil peak displacements between 12 mm and 18 mm, and under-compacted soil peak displacements between 24 mm and 30 mm, approximately 0.5% of the height for both compacted bridges and 1% of the height for the under-compacted bridge. Peak displacements for the tall bridge were larger for the under-compacted soil, indicating that denser soil in the compacted bridge provides more restraint to bridge movement, as expected.

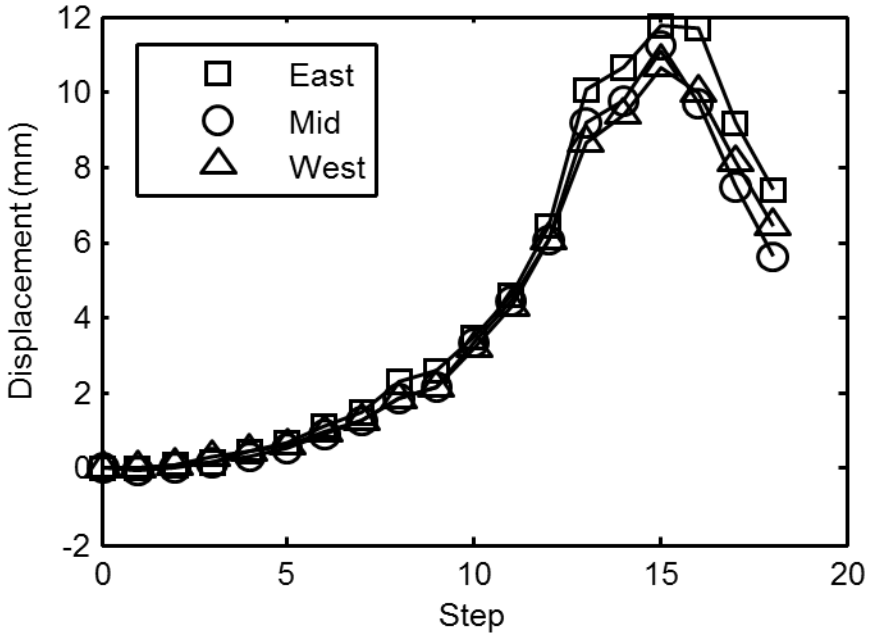

Figure 6.4. Apex Displacement During Backfilling, Short Bridge

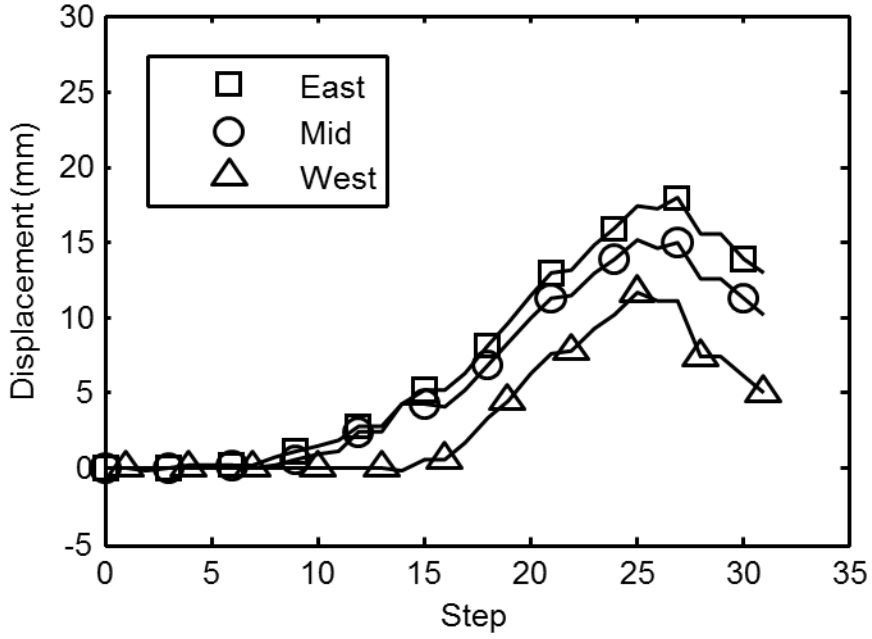

Figure 6.5. Apex Displacement During Backfilling, Tall Bridge

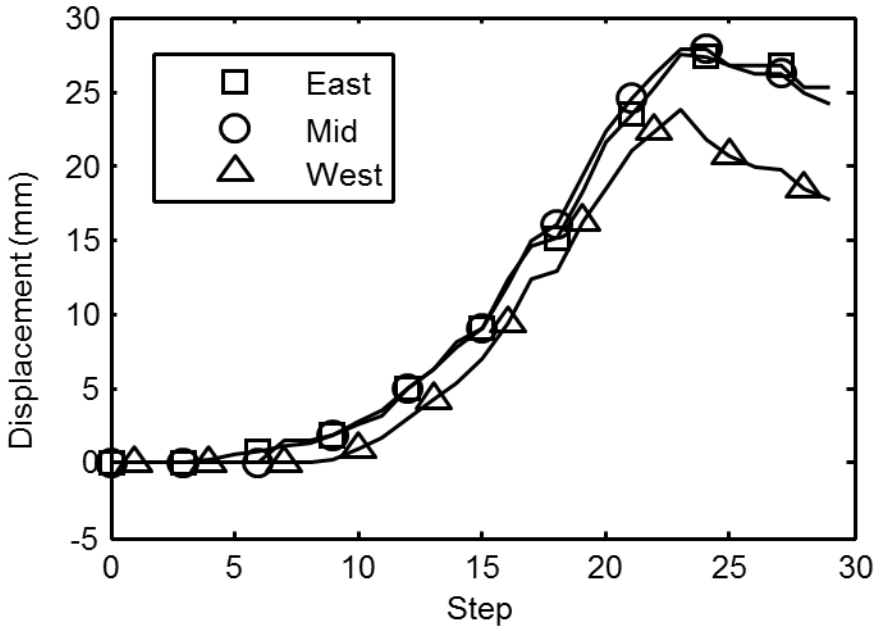

Figure 6.6. Apex Displacement During Backfilling, Tall Bridge, UC Soil

6.2.3. Backfilling Flexure

The same trend also holds true for arch bending moments inferred from measured strain during backfilling. Figure 6.7, Figure 6.8, and Figure 6.9 contain the moment for the center arch at the foundation, apex, and shoulder throughout backfilling for the short compacted bridge, tall compacted bridge, and tall under-compacted bridge, respectively. There are negative moments at the foundation and apex locations and positive moment at the shoulder for all bridges (positive moment produces compression on the outside face of the arch). The apex moment follows the same shape as the apex deflection and at the end of backfilling becomes less negative. The moments for the tall compacted bridge are lower than for the tall under-compacted bridge. Compacted soil is stiffer due to higher friction angle and lower void ratio and develops greater passive resistance and smaller active loading than under-compacted soil. Despite the greater compaction energy required to achieve a higher as-placed density, the compacted bridge has smaller moment and deflection during backfilling due to soil restraint.

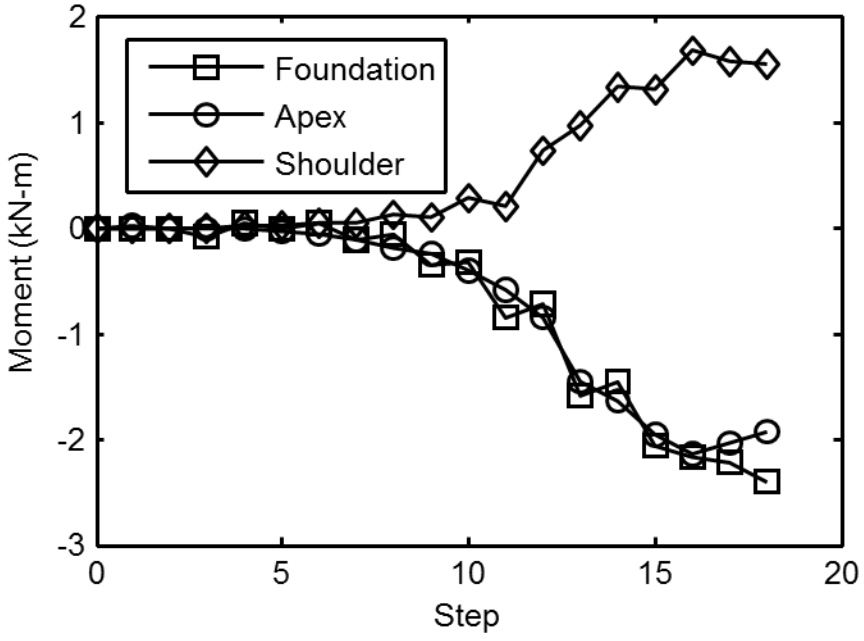

Figure 6.7. North Side Moments, Middle Arch, Short Bridge

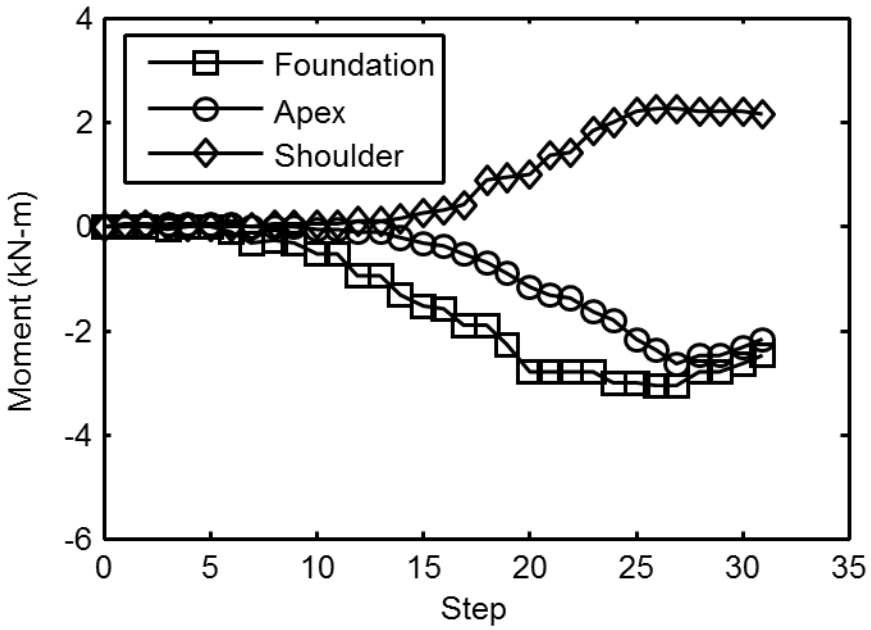

Figure 6.8. North Side Moments, Middle Arch, Tall Bridge

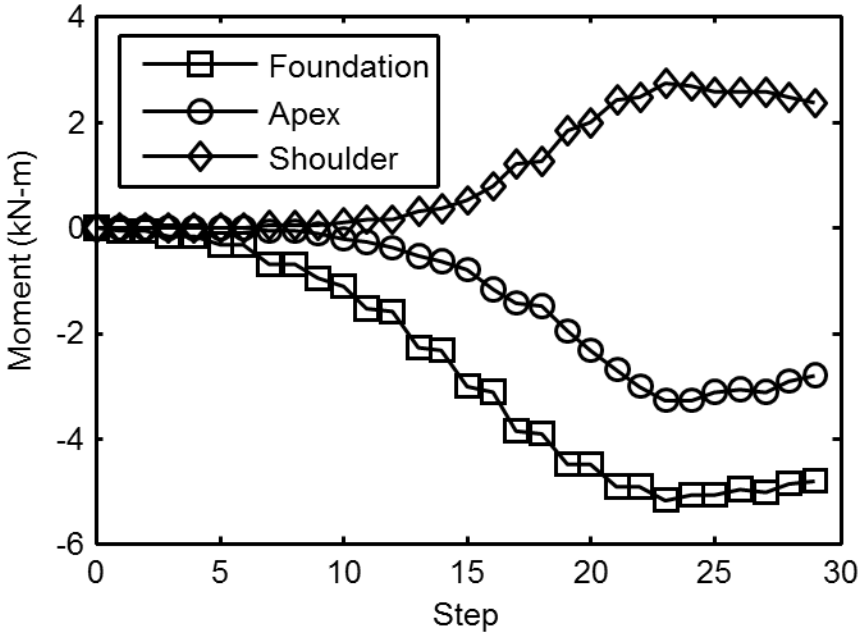

Figure 6.9. North Side Moments, Middle Arch, Tall Bridge, UC Soil

Arch moments at the foundation of the tall bridges are higher than either shoulder or apex moments and deserve design consideration. Also, the peak moment occurs prior to the end of backfilling, which indicates that an analysis that ignores the backfilling progress will not find this potential worst-case loading. This finding is consistent with model results of plate steel arches where peak moment occurs when the soil is at or just above the apex (Morrison, 2000). However, the approximate 50% difference in backfilling footing and apex moment between under-compacted and compacted soil disagrees with results for steel plate arches presented by Webb et al. (1999), which indicated that compaction had little effect on backfill moment.

6.2.4. Comparison to Backfilling Predictions

Figure 6.10 and Figure 6.11 show apex moment during backfilling for the tall and short bridges with comparisons to both models. Notice that for the tall bridge, both models have nearly identical results and the experimental peak moment is well predicted by both models. The models have a smaller moment reduction from peak than experimental results. The short bridge apex moment is not as well represented by either model, and both models are unconservative. The soil-spring model final moment is closer to the experimental results than the soil-continuum model, but the soil-continuum model better follows the trend indicated by experimental results; soil loads above the apex produce positive moment experimentally and in the soil-continuum model, reducing the negative moment from prior loading. The soil-continuum model suggests that the final two lifts approaching the apex, one per side, produce positive apex moment.

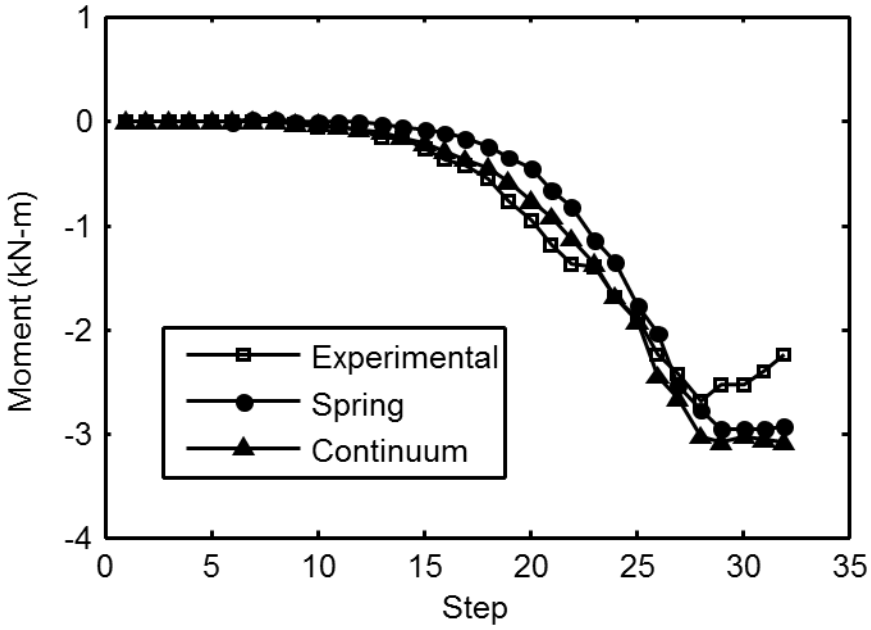

Figure 6.10. Tall Arch Apex Moment During Backfilling

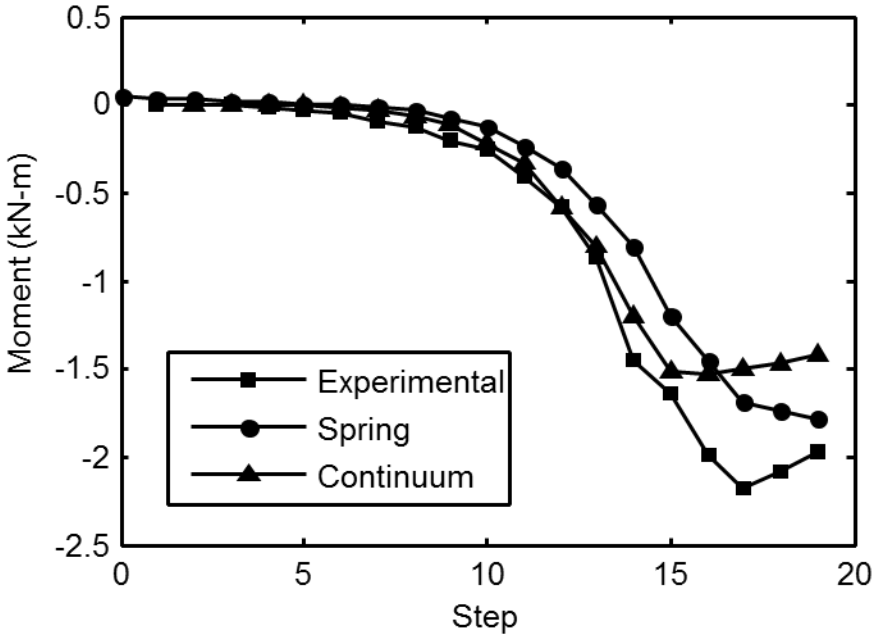

Figure 6.11. Short Arch Apex Moment During Backfilling

Figure 6.12 shows arch moments near the North footing of the tall bridge during backfilling. The soil-continuum model and soil-spring model assuming concrete under the arch footing both do a poor job of predicting moment after step 22. The soil-continuum model continues to predict larger negative moment with each step instead of reducing negative moment as shown by experimental data, overpredicting final footing moment by 200%. The soil-continuum model better predicts final moment, only over-predicting by 15%, but it over-predicts negative moment by a maximum of 65% at step 27. Using realistic spring stiffness based on experimental compression tests of the layered OSB and plastic sheets under the footing described in Chapter 3 overpredicts the moment by only 32% at the peak case and overpredicts the final moment by less than 5%, indicating that footing rotation can significantly affect backfilling footing moments. Due to the high computational cost of small elements in the explicit continuum model a realistic foundation stiffness could not be simulated within the restrictions of the current model.

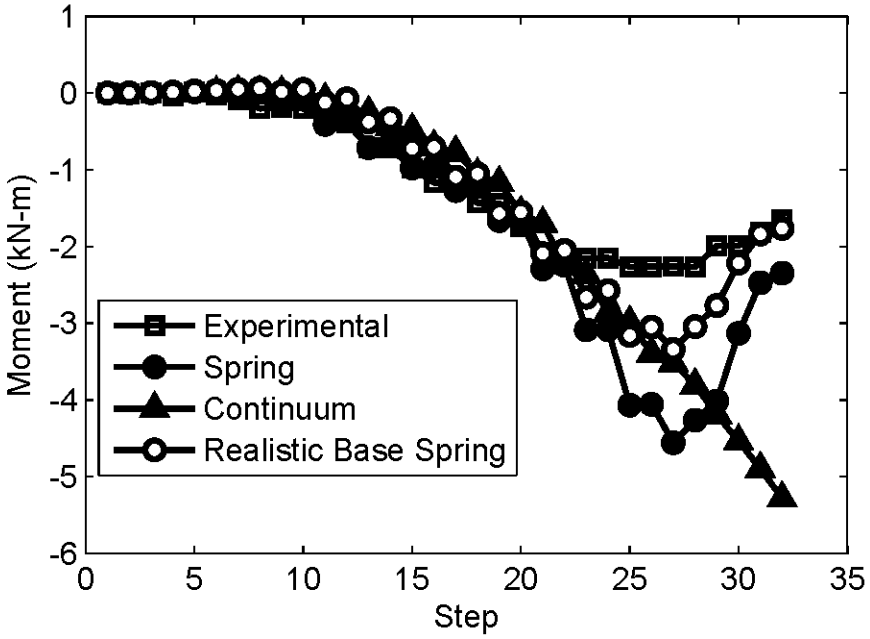

Figure 6.12. Tall Arch Foundation Moment During Backfilling

Figure 6.13 and Figure 6.14 show post-backfilling moments along the arch arc length for both the soil-spring and soil-continuum models and experimental results for the two bridge geometries with compacted soil. Generally, moments predicted by both models follow a similar trend as the experimental moments, however apex moment magnitude is overpredicted by the soil-spring model by 27% for the tall bridge and 7% for the short bridge, while the soil-continuum model over-predicts the apex moment by 28% for the tall bridge and 27% for the short bridge. The models indicate peak positive moment appears near the span quarter points for the tall bridge and one-eighth of the span away from foundations for the short bridge. The soil-spring model predicts a more symmetric response than was experimentally observed, as illustrated by the overprediction of peak positive moment in the tall bridge by only 13% on the South side and 70% on the North side. The soil-continuum model also reports a smaller side to side difference than experimental results. The short bridge soil-spring model underpredicts the peak positive moment by 17% and predicts that the peak moment is closer to the quarter point. Foundation moments are well represented by the soil-spring model with a difference of 20% or less compared to average experimental results, and the model properly predicts asymmetric foundation moment response, but underpredicts the difference in magnitude. The soil-continuum model overpredicts foundation moments by as much as 220% and shows a need for further model refinement near the foundation.

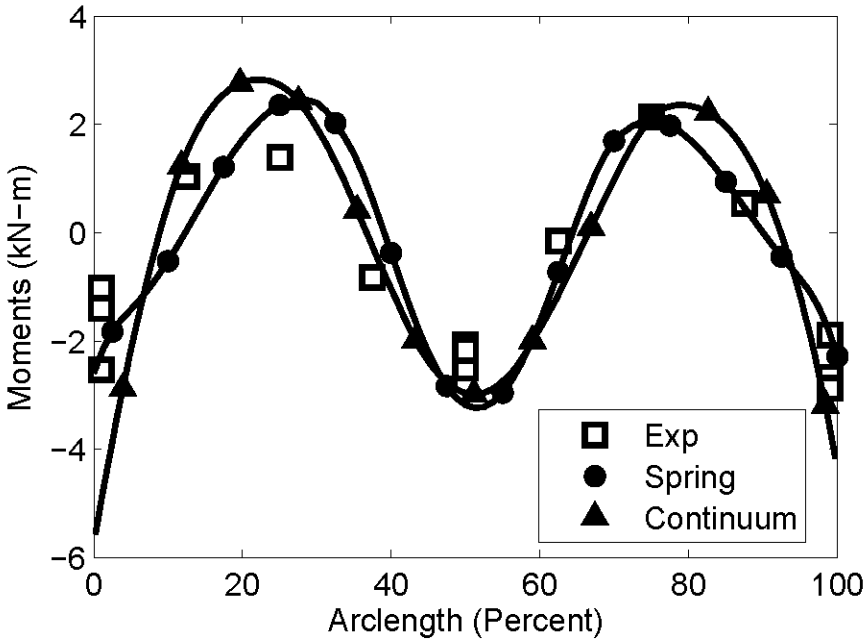

Figure 6.13. Moment at the End of Backfilling, Tall Bridge

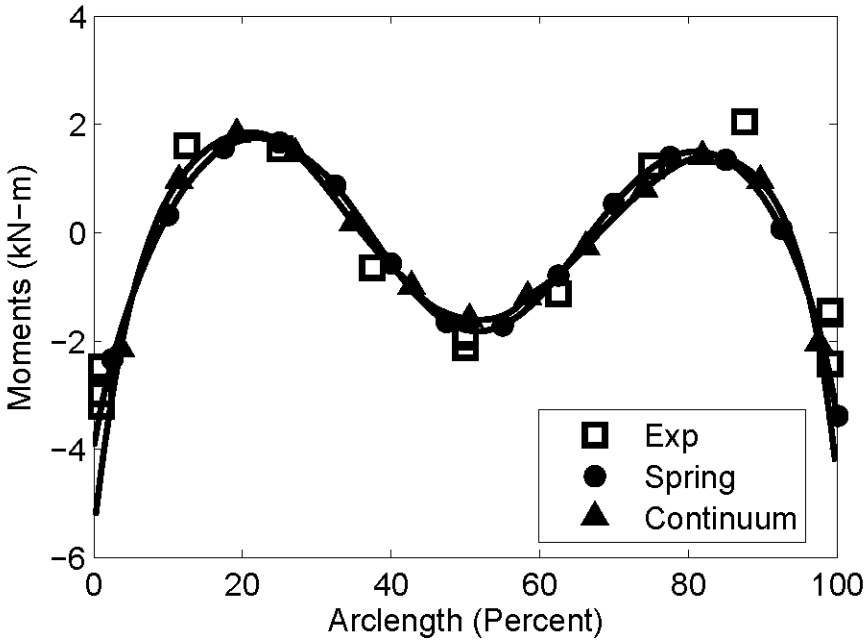

Figure 6.14. Moment at the End of Backfilling, Short Bridge

Figure 6.15 shows the moment response at the end of backfilling for the tall bridge with under compacted soil and the tall bridge with compacted soil conditions. No models are included with this data. Notice that the backfilling moment response is greater for the loose soil case, with increases in negative moments at the footing and apex as well as increases in positive moments at the shoulders. This indicates that soil with better compaction (stiffer and denser) is preferable for design. The added stiffness of compacted soil more than compensates for the added soil weight of compacted soil.

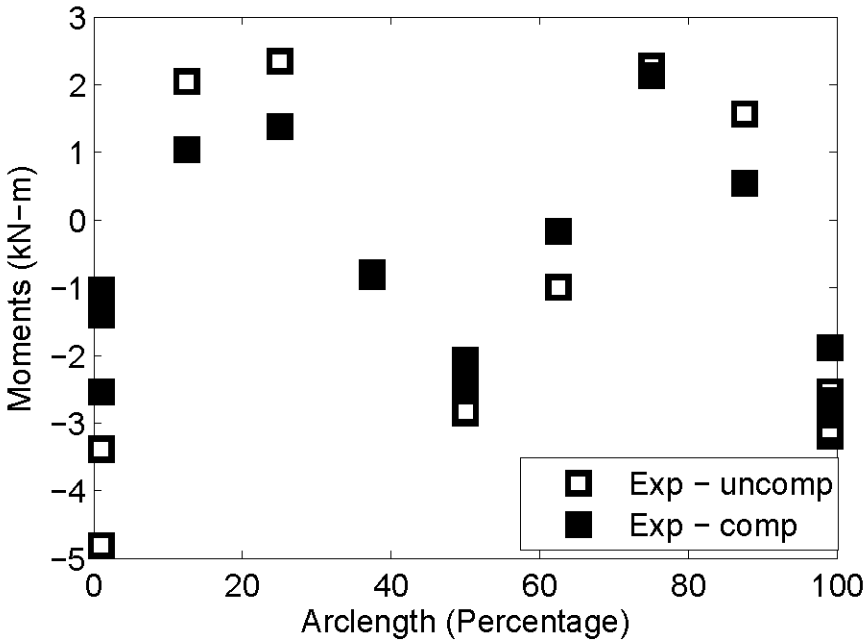

Figure 6.15. End of Backfilling Moment, Compacted and UC Soil

A simpler alternative to nonlinear soil-spring elements is to assume a constant lateral earth pressure coefficient *K* for all elements for all analyses. However, simulating backfilling with a constant *K* model proves challenging. This is particularly true for the tall bridge, where any *K* greater than 0.3 causes the arch to buckle as soil is applied up to the height of the arch apex. Apex moments in the tall arch exceed 11 kN-m, which are greater than experimentally-

determined backfilling moments from Figure 6.13. In contrast, the soil-spring model having nonlinear soil springs allows *K* to drop to as low as 0.2 (nearly full-active) along more vertical elements between the apex and the foundation and also to exceed 2.0 at more horizontal elements between arch shoulders and the apex when the soil elevation is above the apex. The horizontal forces above the shoulder create positive moments and the horizontal forces below the shoulder produce negative moments, bringing the predicted arch moments closer to the measured experimental data. This indicates the importance of accurately capturing soil pressures during the simulation of staged backfilling.

6.3. Service Live Load Response

The arches were loaded at intervals of 10% of the span between mid-span to 60% of the distance between the apex and the foundations. The steel arches remained elastic, with maximum measured total steel strains below 0.0013, or 75% of the yield strain. Peak displacements were 22 mm and 15 mm for the tall and short arches, respectively. Arch moments inferred from measured strains for the 84 kN service load are reported for each load position in the following sections. Sections are divided by load case, and relevant pressure and displacement data are included to explain moment results.

Each plot contains the first cycle load response with tied foundations, the first cycle load response with loose footings, the spring model predicted response and the continuum model predicted response. Note that the models predict nearly identical moment response with tied and untied foundations, thus only the tied models are reported for clarity. Total arch moment is inferred from measured strains including the strains in the current load test and the final strains from all previous live load and backfilling tests. Creep or relaxation between tests was not

accounted for, and figures show live load moment, which is the total moment less the moment at the end of backfilling.

6.3.1. Apex Load Response

Figure 6.16 and Figure 6.17 illustrate apex load moment response for the tall and short bridge. Apex moments are well captured by the soil-spring model, differing by 5% or less for both the tall and short bridge from the average of the three measured moments. The soil-continuum model predicts a very similar response for the tall bridge, but underpredicts the apex moment response by 25% for the short bridge. Moments distant from the apex also follow the predicted trend; however reporting percent differences would be deceptive due to the low magnitude of the experimental moments. Foundation moment magnitudes are over-predicted by the soil-spring model for both bridge geometries for every loading case. Soil-spring predicted live load moments are more positive than measured live load moments, but the total moment due to backfilling and live loading is within 10% of experimental moment because the model overpredicted negative moment during backfilling and positive moment during apex load, and the differences offset.

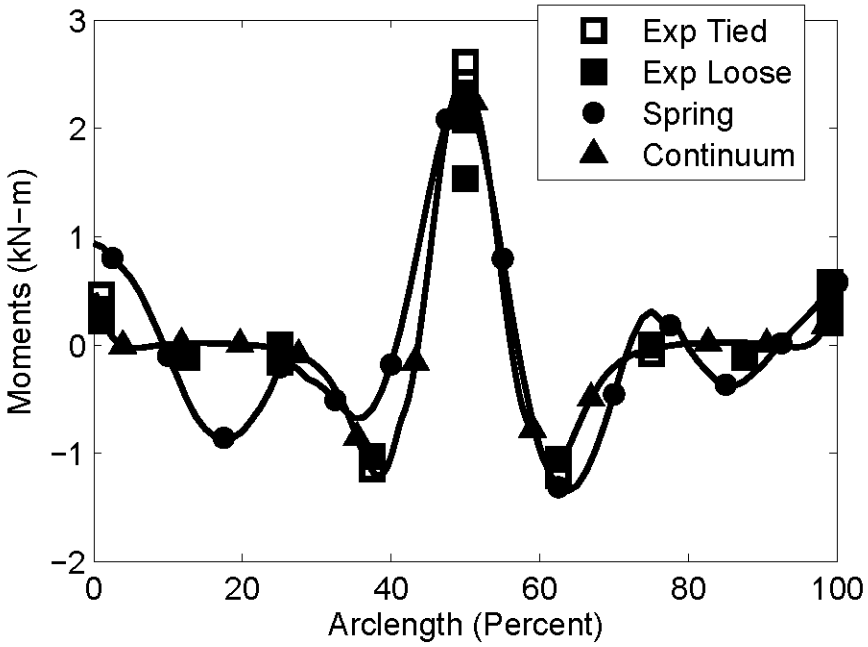

Figure 6.16. Tall Arch Apex Live Load Moment Response

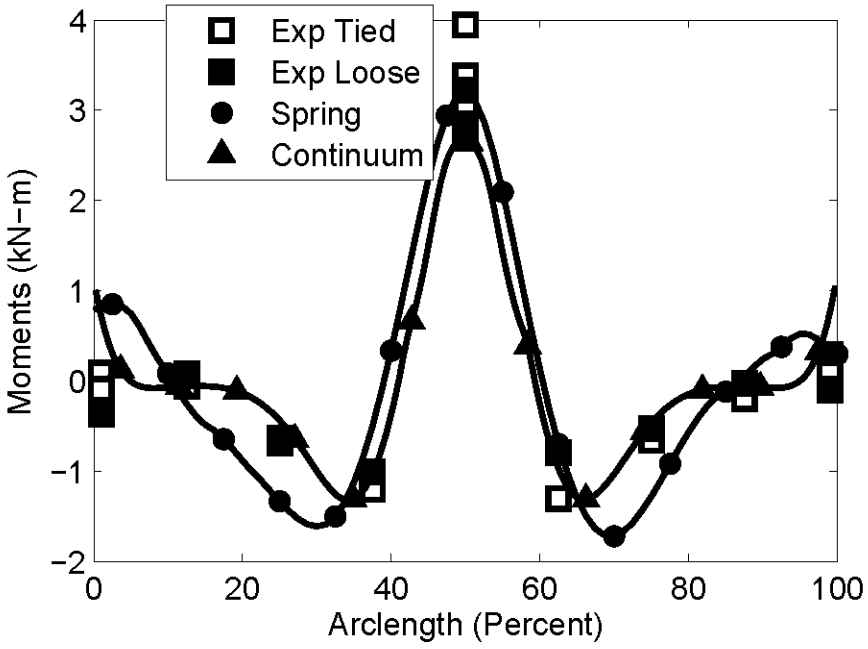

Figure 6.17. Short Arch Apex Live Load Moment Response

Vertical deflection response for the short bridge due to apex load in Figure 6.18 is underpredicted by the soil-spring model by 25% and underpredicted by the soil-continuum model by 50%. Experimental results may be more negative than model results because displacements are measured from the wooden decking, not the steel arches, and the weak-axis plywood layer between the decking and the arches compresses during loading. Under load the wooden decking compresses, particularly the 19 mm spacing between the decking planks and the arches. Pressure near the apex is between 80 and 90 kPa for the short bridge. But, this is distributed across the full width of the decking (2.15 m), while the contact width between the decking and the arch is only 152 mm for the three arches. This means that pressure between the decking and the arches is approximately 1200 kPa.

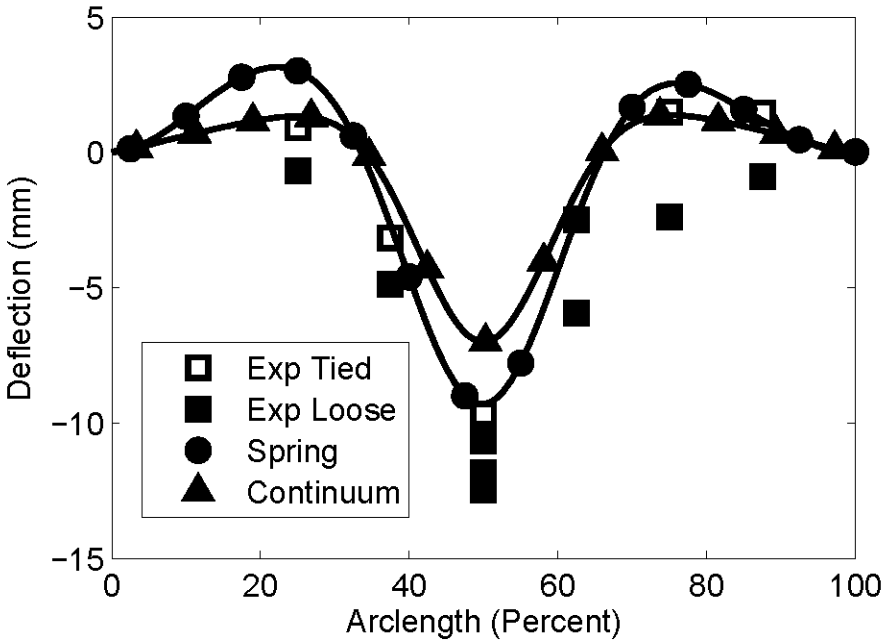

Figure 6.18. Short Arch Apex Load Vertical Deflection Response

Horizontal deflections due to apex load are presented in Figure 6.19. The North side experimental response with untied foundations is substantially different for the measured North

side response and the measured South side response. This is likely due to load history: the bridge was backfilled in progressive lifts on alternating sides. This causes a locked-in offset position and makes the response of each side different. The North side was filled after the South side, which shifted the arch toward the North side throughout backfilling. Also, this was the first load test after the foundation ties were removed, and it appears that enough thrust was caused by the applied load to make the foundation begin to slide.

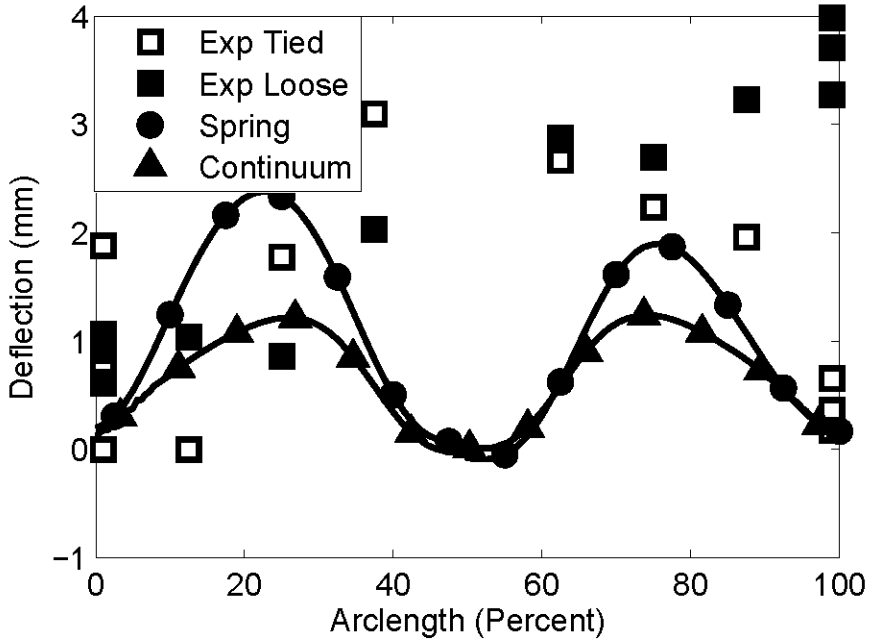

Figure 6.19. Short Arch Apex Load Horizontal Deflection Response

Horizontal deflection response was poorly predicted by both models. According to experimental results the tall arch basically did not move horizontally, as shown in Figure 6.20. This result illustrates the difference that additional soil depth can have on arch restraint. Also notice that the models disagree with each other: the continuum model was nearly symmetric but the spring model predicted greater positive movement on the South side of the arch. This is due to more asymmetry predicted by the spring model during backfilling.

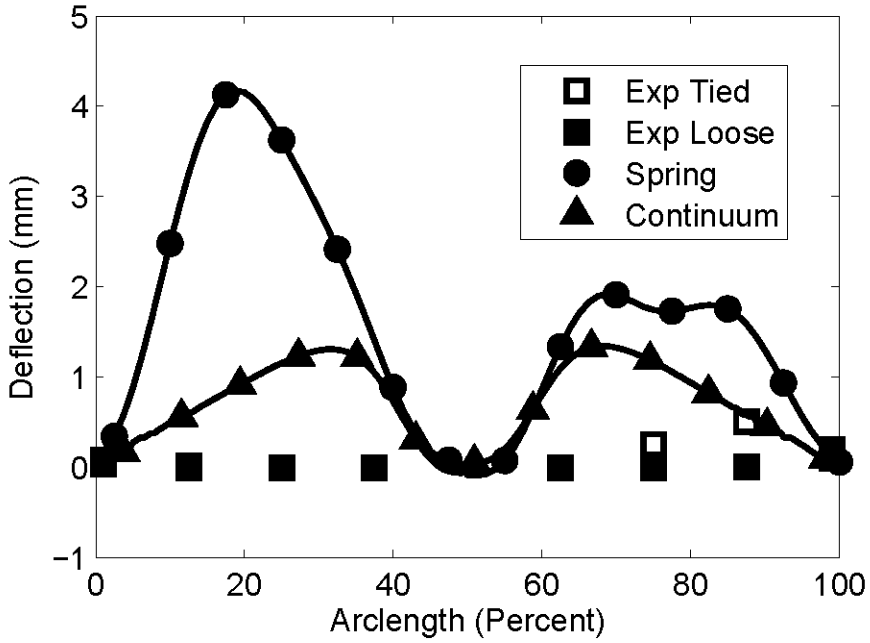

Figure 6.20. Tall Arch Apex Load Horizontal Deflection Response

Axial load is poorly predicted by both models, but this may be an artifact of the test. Axial load is computed from measured strains, but the sections in question have high axial stiffness compared to bending stiffness as a consequence of adequate scaling. This makes axial load response prone to error because small misalignment or gauge error can cause a larger percentage difference in measured axial load. For example, a 2.2 kN-m moment, which is a typical peak service moment response, corresponds to a bending strain of 520 to 460 microstrain for the short and tall bridge. This same strain, if axially applied, corresponds to a force of 270 kN to 360 kN for the short arch and tall arch respectively, which is much larger than any measured or anticipated axial force. Figure 6.21 shows the axial load response for the tall bridge to an apex load. Notice that in regions where the moments are small, below 25% of span and above 75% of arclength, model predictions are better than in the high moment region in the middle 50% of the arclength. Also notice that the spring model does not anticipate a drop in axial load at the apex

while the continuum model does anticipate this response. There is not enough evidence to conclude that this phenomenon is real, but it also does not greatly affect the design of arches.

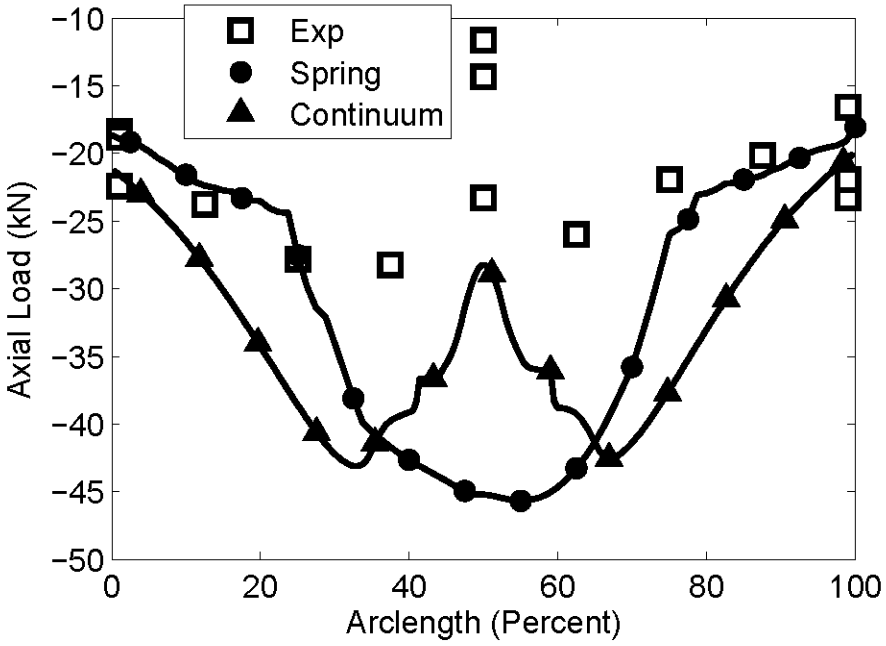

Figure 6.21. Tall Arch Apex Load Axial Response

6.3.2. 60% Offset Load

The tall arch apex moment for a 60% offset is well predicted for South loading (Figure 6.22) by both models and is unconservatively predicted for North loading (Figure 6.23). This is a case where results can be misleading: the large negative moment for North loading is directly caused by the prior load cycle, which was apex live load, and which stored a 0.7 kN-m final average apex moment. Removing this value from the subsequent response produces total negative moments that are very close to predictions. The peak positive moment predicted by the soil-continuum model is 30% higher than the peak positive moment predicted by the soil-spring model for a 60% offset load. However, no gauge was present at the location of peak positive moment, thus it is impossible to tell which model more accurately predicts peak moment.

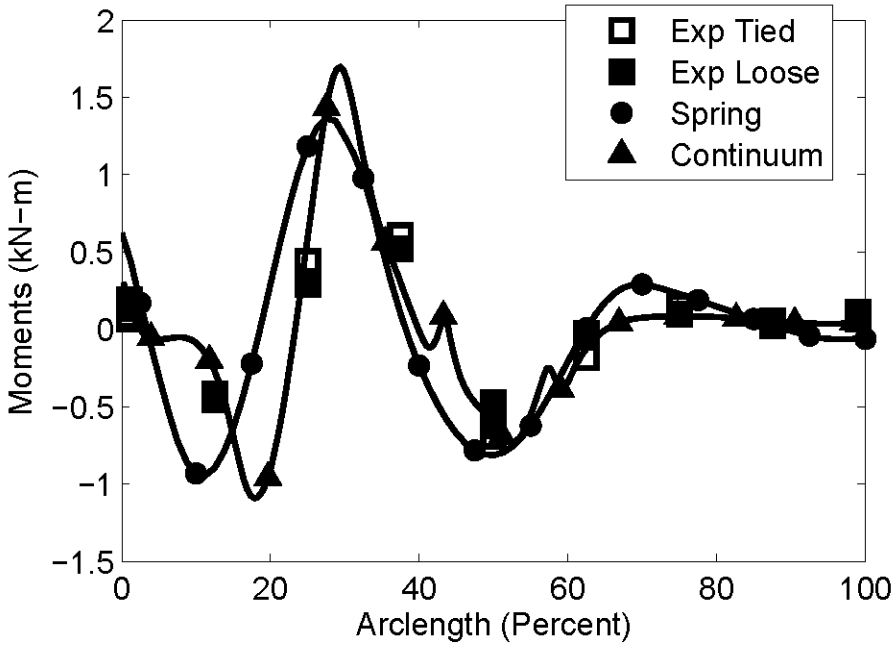

Figure 6.22. Tall Arch 60% South Offset Live Load Moment Response

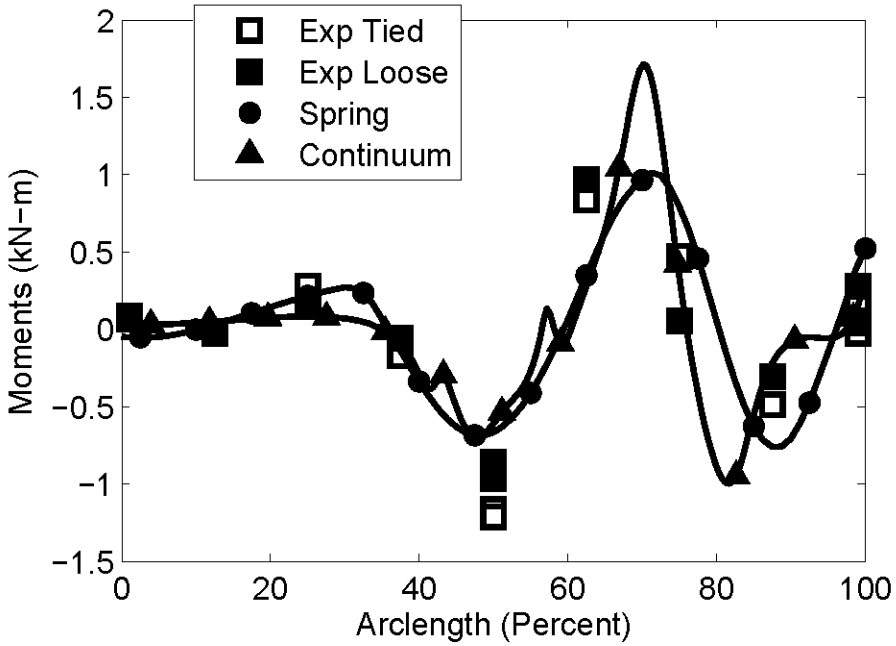

Figure 6.23. Tall Arch 60% North Offset Live Load Moment Response

A likely controlling load case according to the soil-spring model for a short rise arch is negative moment at the foundation under the 60% offset load (Figure 6.24, Figure 6.25). In this case, the continuum model agrees well with experimental results that the foundation moment is small due to live load, but the spring model shows a large negative moment (-3 kN-m). This moment is likely an artifact of the soil-spring model and shows a need to improve the existing design analysis beyond the scope of this report. Likely, it is due to inadequate soil restraint near the apex of the shallow arch, which could be addressed by adding horizontal friction or vertical soil restraint, both of which are currently neglected in the model. Near the apex of the arch the tributary area of the spring elements becomes very small because the vertical rise of each element becomes small. As a result, the model cannot generate enough soil resistance in this region without uncharacteristic deflections and very large assumed horizontal pressures.

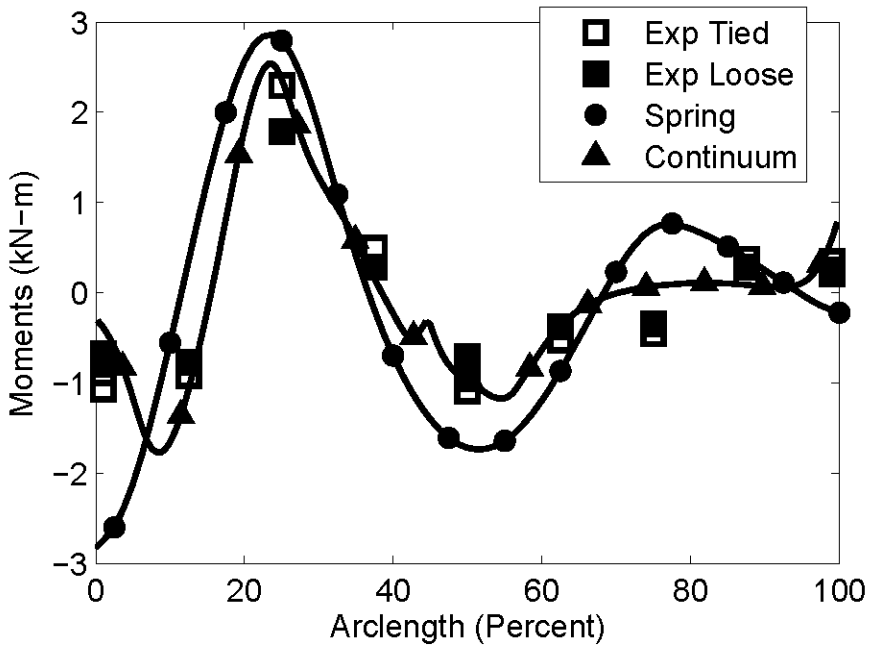

Figure 6.24. Short Arch 60% South Offset Live Load Moment Response

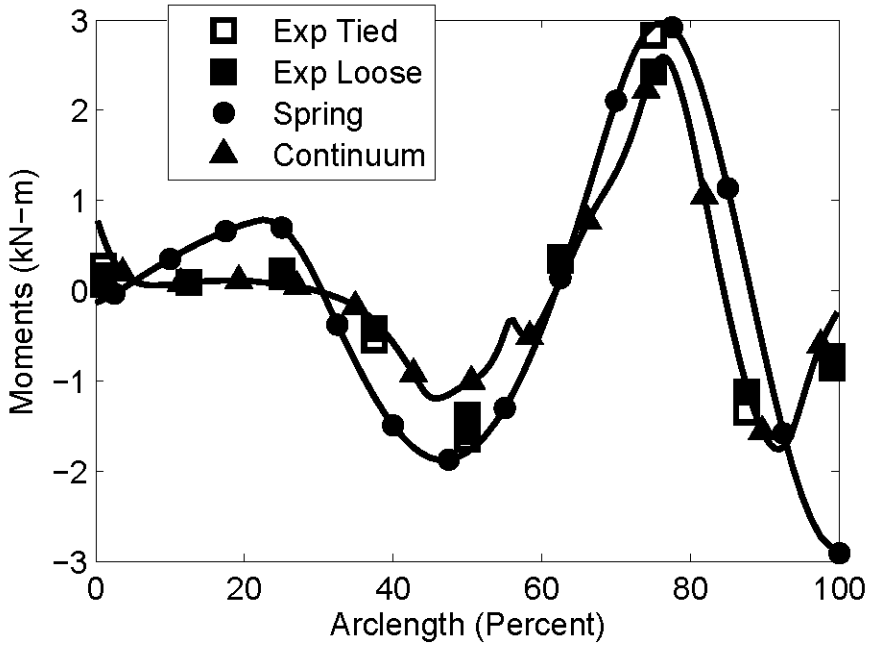

Figure 6.25. Short Arch 60% North Offset Live Load Moment Response

According to this theory, the deflection response near the apex for an offset load should be overpredicted by the soil-spring model, while the soil-continuum model which has friction and vertical soil restraint should better predict the deflection response. Figure 6.26 shows the vertical deflection response of the short steel bridge for a 60% South offset load. The measured apex deflection is 2.3 mm to 2.4 mm for the three arches, while the spring model predicted apex deflection is 6.7 mm. Notice also that one gauge position to the North is also overpredicted by the soil-spring model. In contrast, the soil-continuum model more accurately predicts deflection response.

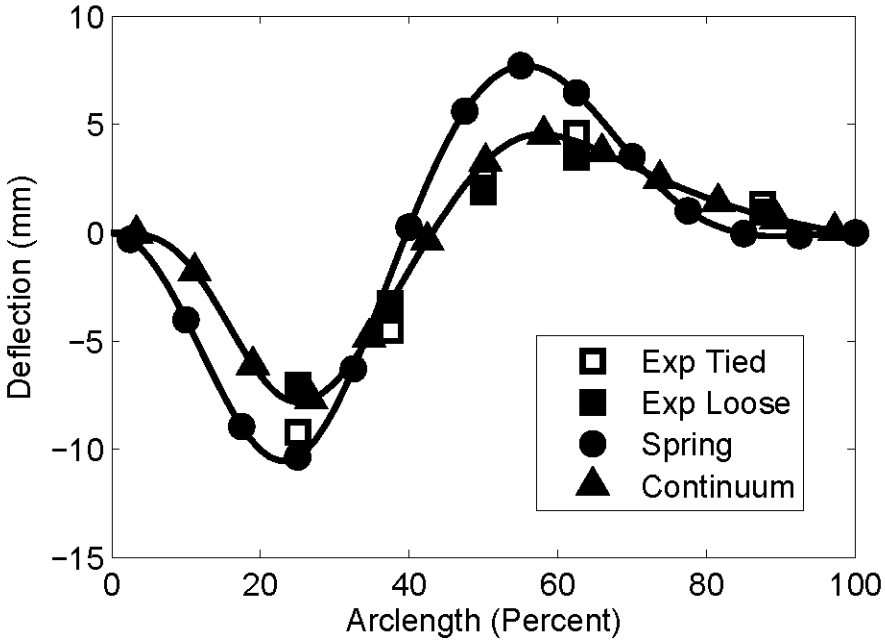

Figure 6.26. Short Arch 60% South Offset Load Vertical Deflection Response

The soil-spring model is not systematically inaccurate at predicting deflections. A figure presented earlier, Figure 6.18, showed vertical deflection for an apex load applied to the short rise arch. Agreement is better for the soil-spring model for an apex load than an offset load. Likely, the better response of an apex load is because the primary outward movement is in the shoulder regions, where the arch elements in the passive pressure regions (arch moving into the soil) have greater vertical tributary area. Consequently, the apex load model had stiffer soil springs in the passive region of the arches, and the stiffer soil springs were more restrictive of arch movement and representative of arch behavior than the springs near the apex for the offset load case.

Similarly, the deflection response for a tall arch with a 60% offset load (Figure 6.27) is better predicted by the soil-spring model than the defection response for a short arch with 60% offset load. The soil near the apex of the tall rise arch may still be too compliant, but the difference

between measured and predicted deflections was only 2 mm at the apex. The tall rise arch has greater geometric curvature and each element has more vertical depth than a corresponding element in the short arch model. The greater depth allows for greater passive restraint near the apex which in turn gives a more accurate representation of arch behavior.

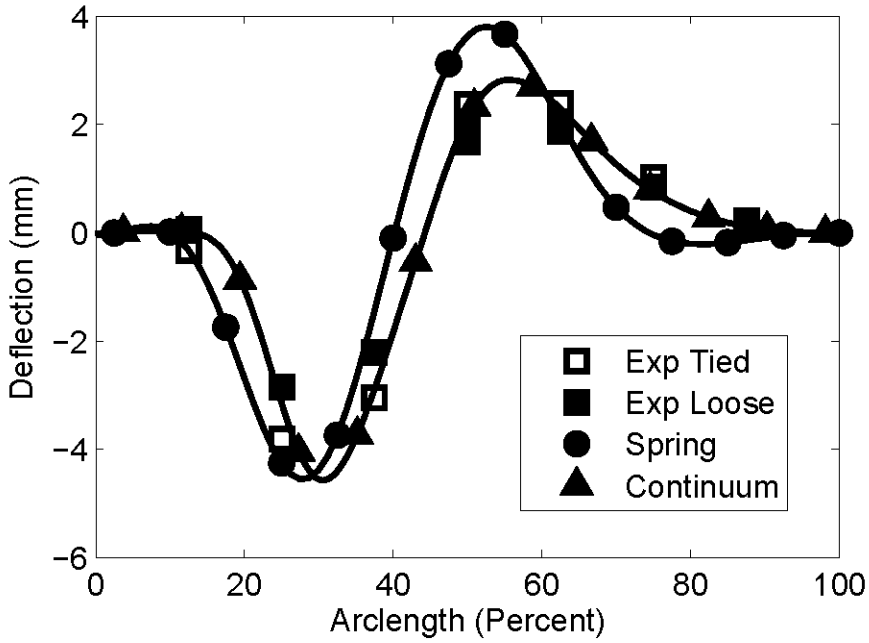

Figure 6.27. Tall Arch 60% South Offset Load Vertical Deflection Response

The spring model is meant to be phenomenological and was not meant to accurately represent soil stresses. For the low rise arch the model assumptions may be the primary culprit for overprediction of negative foundation moment. The deflection at the apex and North side near the apex are overpredicted, and this is likely caused by insufficient modeled vertical soil stress in this region. Figure 6.28 shows pressures for the short arch subject to a 60% South offset load. Notice that the spring-model assumes a Boussinesq distribution for vertical stresses and calculated nearly zero change in stress over the region from 50% to 100% of the span. Measured

stresses indicate an increase in stress in the region equal to about 7 kPa, or an increase in pressure equal to about half of the cover depth in the region. The stress increase is likely not caused by active soil arching, or the applied live load spreading over a larger region due to arch deflection away from the load, because the pressure under the point of load is greater than predicted with the Boussinesq distribution. The increase in pressure at the apex and in the North region near the apex appears to be caused by passive soil arching, by additional soil being carried by the apex due to soil shear interlock as the apex tries to lift upward. Instead of only supporting the soil directly overhead, the middle region is carrying soil that extends over the North shoulder and further into the North side of the soil box.

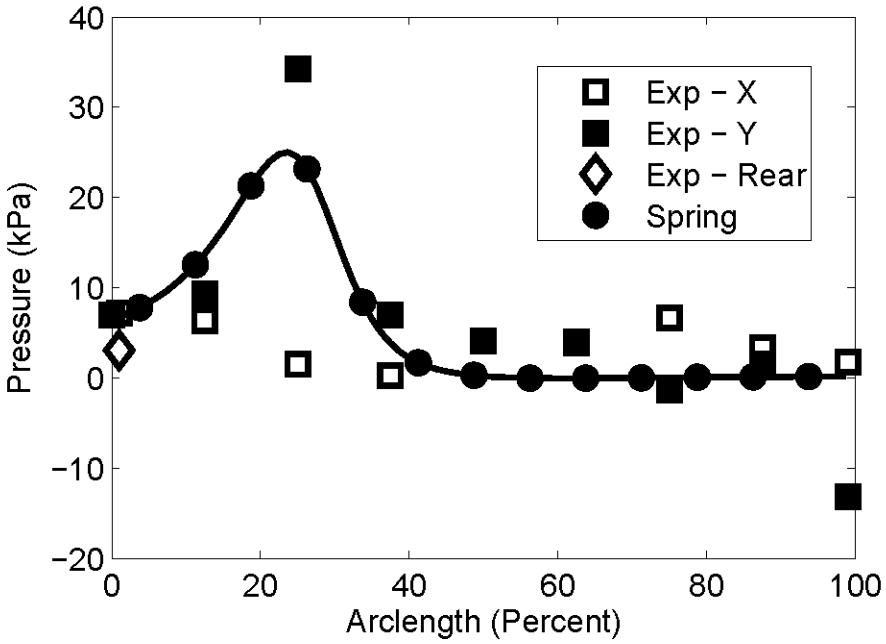

Figure 6.28. Short Arch, 60% South Offset Load Pressure Response

The horizontal deflection in the short bridge due to a 60% offset load (Figure 6.29) was well-represented by both models, which is inconsistent with the theory that arch restraint near the apex was inadequate for an offset load. Horizontal deflection for a 60% offset load was

overpredicted by the tall arch models (Figure 6.30), which more accurately predicted arch moment than the short arch model. It is worth noting that the short arch model reasonably predicts moment near the apex due to a 60% offset load, but fails to predict moment at the foundation. It is possible that deflections and curvatures can be right in one region of the arch with the wrong combination of loads applied to the arch, which results in poor moment prediction in other regions. Also note how much smaller passive deflections (North side) were for the tall bridge than the short bridge: this is not an isolated load case. In nearly every service load test horizontal deflection at position 1 and 7 is zero relative to the accuracy of the gauge and the deflection of other gauges.

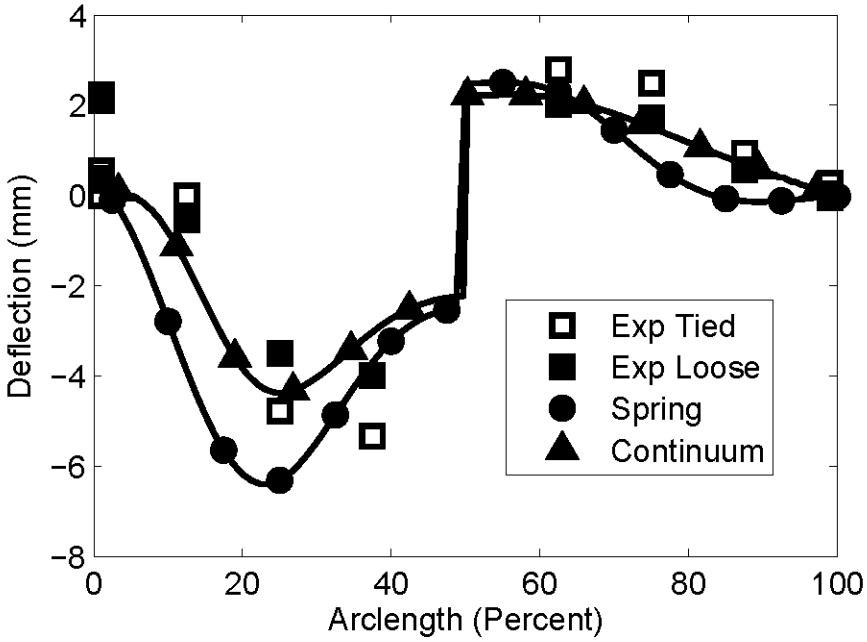

Figure 6.29. Short Arch 60% South Offset Load Horizontal Deflection Response

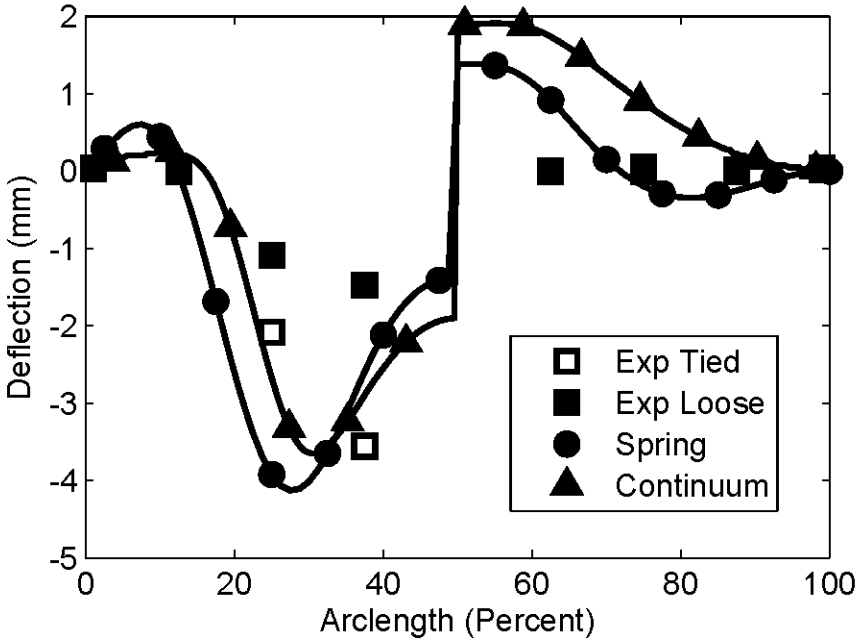

Figure 6.30. Tall Arch 60% South Offset Load Horizontal Deflection Response

6.3.3. 40% Offset Load

Under 40% offset loading (Figure 6.31 and Figure 6.32), gauges on the tall bridge coincide with the location of predicted peak positive moment. Experimental data and soil-spring model predictions differ by less than 3% for North side loading and South side loading. The soil-continuum model predicts a lower moment for North side loading that is unconservative. It is worth noting that a constant stiffness soil model with soil elastic modulus, *E*, of 27 kPa (corresponding to a soil depth of 1 m) predicts the same moment at the gauge location as the spring model, however it predicts a 32% higher moment 5% of the arc length closer to the footing where there were no gauges. There is a large difference in tall arch continuum-soil model response relative to *E*, and increasing *E* with depth produces a better fit to experimental response, but is a less conservative model.

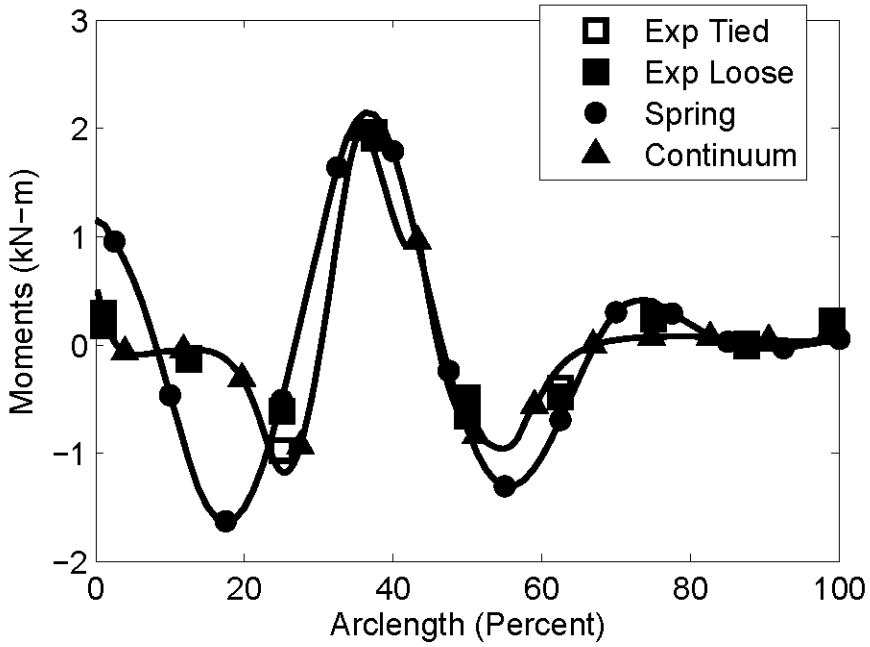

Figure 6.31. Tall Arch 40% South Offset Live Load Moment Response

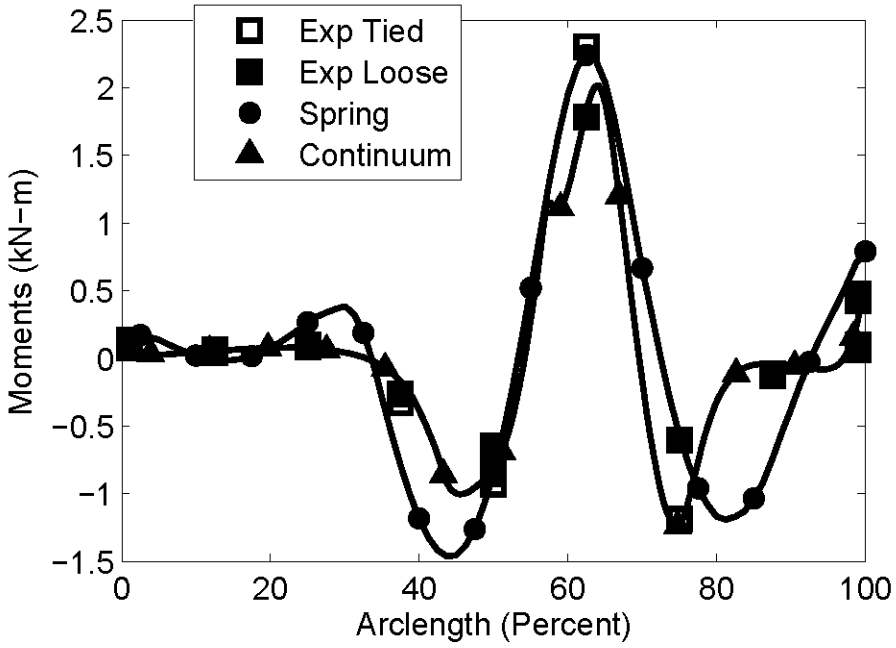

Figure 6.32. Tall Arch 40% North Offset Live Load Moment Response

As anticipated with the accuracy of the moment fit, vertical deflection is also well represented with a 40% offset load. Shown in Figure 6.33, both models follow the proper shape, although the spring model tends to overpredict deflection while the continuum model underpredicts deflection for tied foundation loading. The untied loading case has smaller peak negative deflection (where load is applied). The untied foundation structure should be slightly more flexible if the stress state for the tied and untied tests being the same. However, the soil state for both tests is not the same. Additional load cycles over multiple locations along the span densify the soil and change the stress state within the soil and the arch, resulting in a stiffer structure.

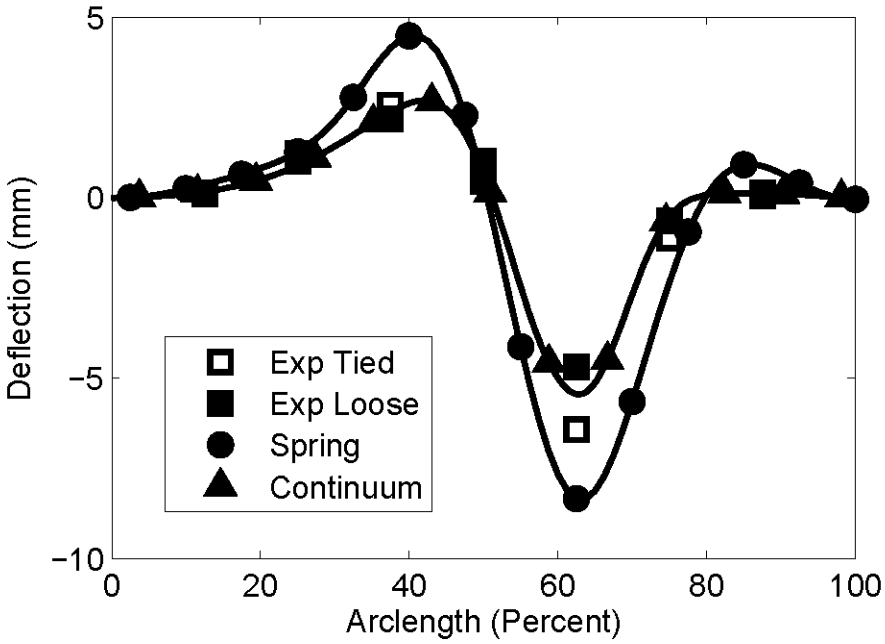

Figure 6.33. Tall Arch 40% North Offset Load Vertical Deflection Response

Moments in the short bridge due to 40% offset loads, shown in Figure 6.34 and Figure 6.35 were the largest peak positive predicted moments for the short bridge for both the soil-spring and soil-continuum model. Gauges were not present at the peak positive moment for this load, thus it

is impossible to verify that the peak moment predicted by either model is correct. However, the measured moment closest to peak loading, at gauge position 3 for South side loading and 5 for North side loading, is well predicted by the soil-spring model. However, the gauge reading on the other side of peak moment, gauge position 2 for South side loading and gauge position 6 for North side loading, was considerably overpredicted by the soil-spring model. Therefore, it is reasonable to expect that the model is close to accurate, but is generally conservative for peak moment due to this load. The soil-continuum model was better at predicting the moment at the outer positions, position 2 for South loading and position 6 for North loading, but underpredicted the peak measured moment at position 5 for North side loading, therefore the soil-continuum model may be unconservative.

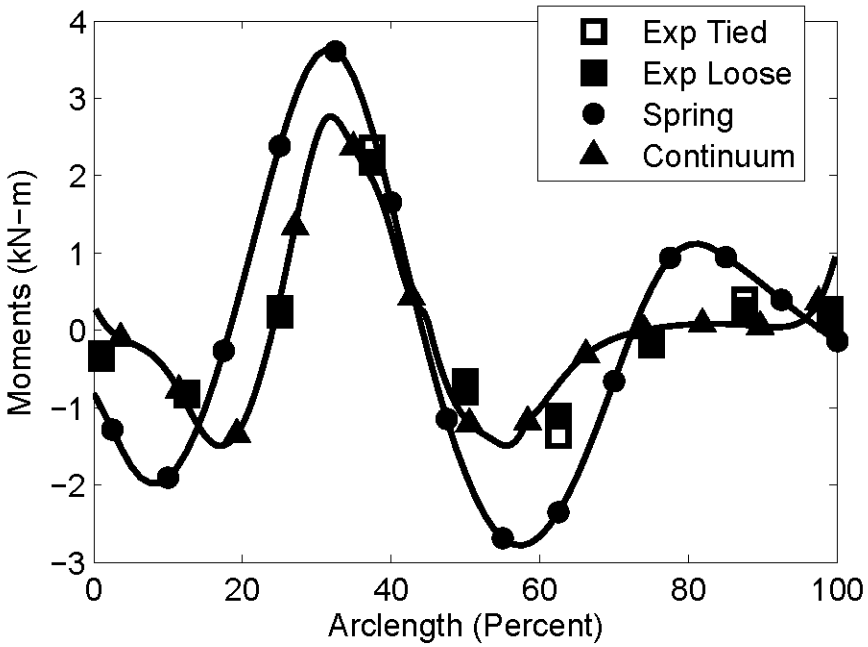

Figure 6.34. Short Arch 40% South Offset Live Load Moment Response

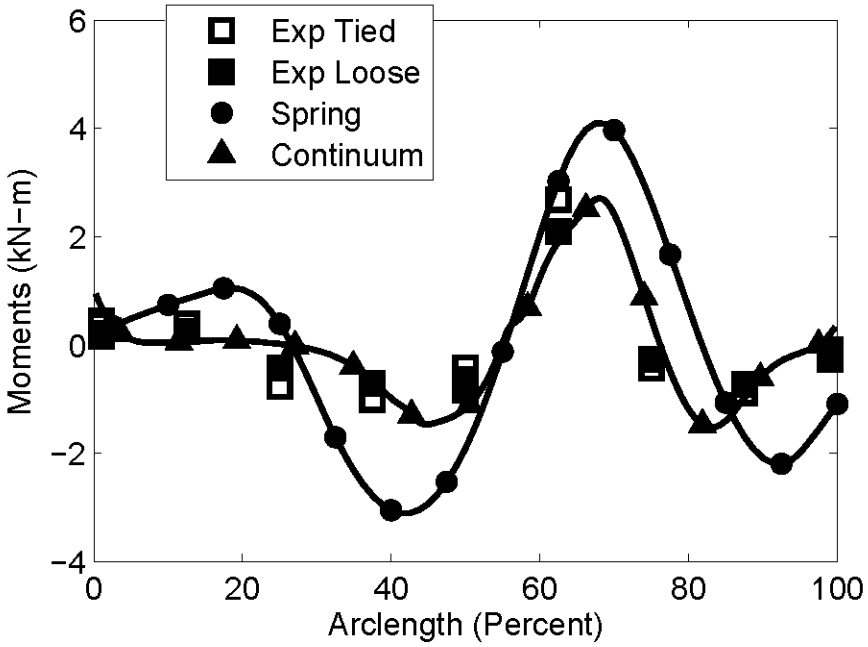

Figure 6.35. Short Arch 40% North Offset Live Load Moment Response

Despite the large magnitude of live load at positions 3 and 5 due to 40% offset live loads, 40% offset loads were not the controlling load case for this bridge. The dead load moments are at a maximum between position 1 and 2 for the short rise bridge, therefore the 60% offset load case produced more total moment. When using either the measured or predicted response to produce a bridge design or load rating factor the 60% offset loading case is still expected to control moment. Live loads are given a higher load factor than dead loads per AASHTO (2014), but the experimental tests use a scaled dead load and double a scaled live load. Doubling the live load is close to the load factors applied to a design bridge. The AASHTO Strength I live load factor is 1.75 and the impact factor for a structure with 1.2 m of soil (the scaled apex soil depth) is 1.167, giving a combined load factor of 2.04 (multiple presence factor and Maine modified HL-93 load factor were included in the test load magnitude). The normal design procedure for designing buried CFFT bridges is to perform a service load analysis and scale the live load response, and

due to the nonlinear soil stiffness applying a larger load produces greater effects than applying a smaller load and scaling the response afterward. This is demonstrated in Figure 6.36 for 60% North live load response for the short bridge. Notice that for both the spring model response and the experiment the moment increases more rapidly as the load gets higher. In the model this is attributable to P-delta effects and increased soil-spring stiffness.

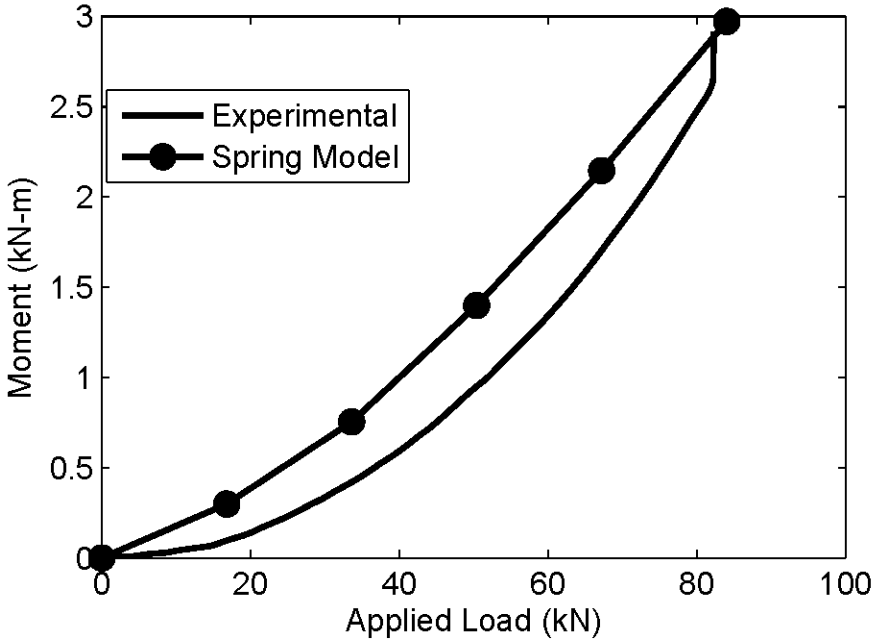

Figure 6.36. Short Bridge Position 6 Moment Versus 60% North Load

6.3.4. 20% Offset Load

The 20% offset load case has fewer design implications for the tall rise arch than the 40% offset load case because strain was not measured near the peak moment during this test. Peak moment was predicted to be nearly midway between the apex and the first gauge position on the loaded side. This is nearly directly below the point of load application. The predicted and measured response for a 20% South offset load and a 20% North offset load are in Figure 6.37

and Figure 6.38 respectively. Notice that the locations where moment was measured are well represented by both models. North side loading has larger peak negative and peak positive measured moments, which is generally consistent with other experimental behavior. The spring model predicts high positive moment on the loaded side, but this is a trivial result because the dead load moments are negative and are larger.

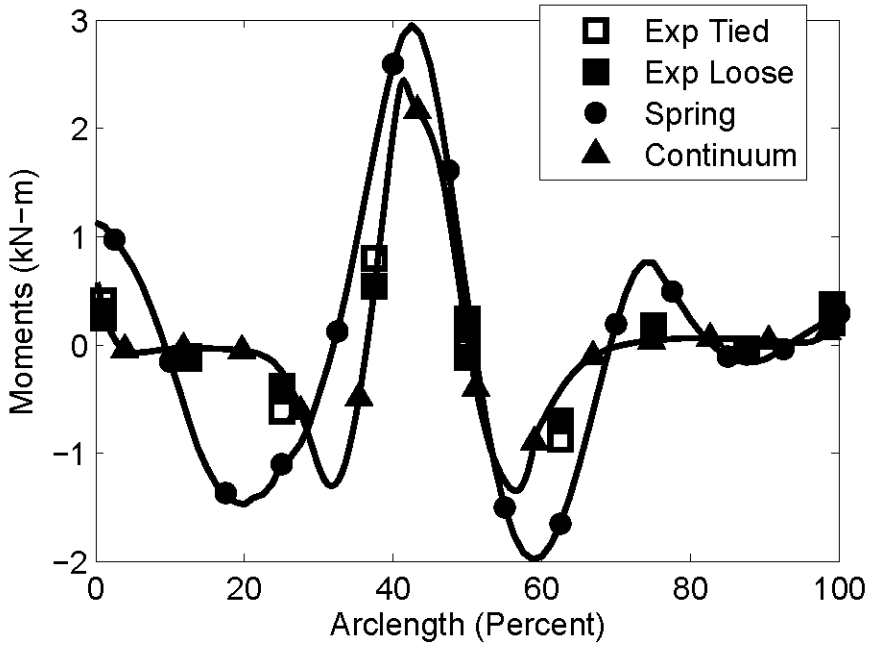

Figure 6.37. Tall Arch 20% South Offset Live Load Moment Response

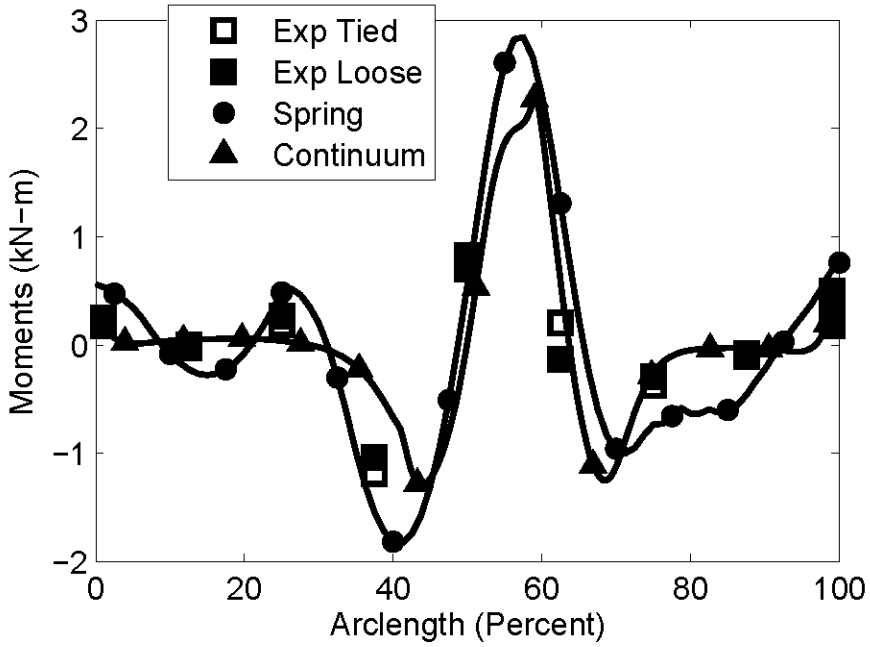

Figure 6.38. Tall Arch 20% North Offset Live Load Moment Response

The expectation is that good moment approximation coincides with good deflection approximation, that appropriate restraint is being considered by the model. Vertical deflection in Figure 6.39 appears to be well modeled by both the soil-spring and soil-continuum model, although the continuum model gives a more accurate prediction of experimental results. Both models predict uplift on the South side of the arch between the apex and the shoulder, and both models do a good job of predicting displacement at the apex. Unfortunately, no gauges were located at the peak predicted deflection for this load case. The spring model predicts approximately 60% more deflection at the peak value than the continuum model, which is similar to the difference in predicted moment for the two models at the same location.

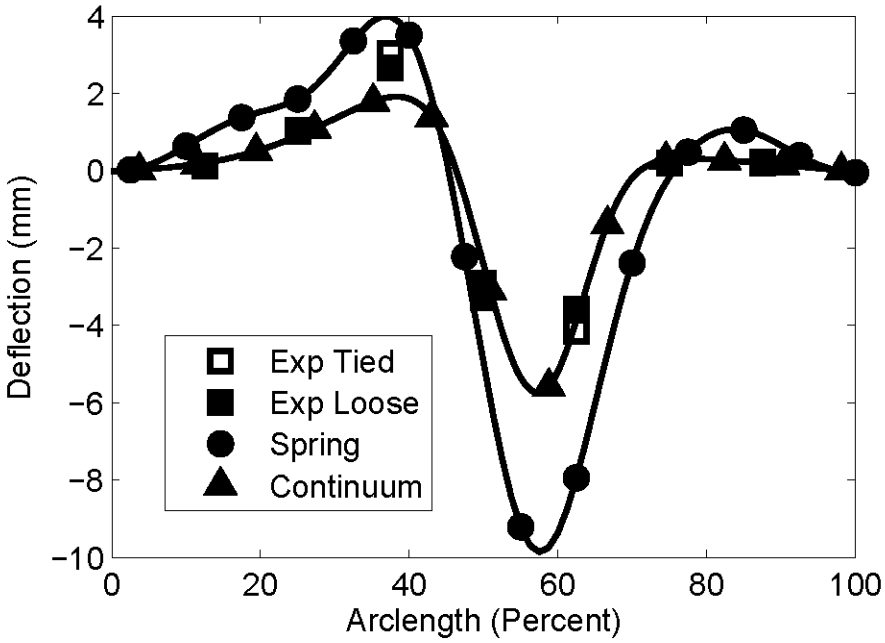

Figure 6.39. Tall Arch 20% North Offset Live Load Vertical Deflection Response

The moment response of the short bridge is more relevant for the present load position because a gauge was positioned closer to the expected location of peak moment. The moment response for the short bridge due to 20% offset load is shown in Figure 6.40 for South loading and Figure 6.41 for North loading. The continuum model appears to better predict the moment and is within 5% of the peak moment for the tied foundation case. However, the continuum model is unconservative at the location of peak measured moment for the South side loose foundation test. The soil-spring model predicts nearly 50% greater moment at this location than the soil-continuum model and it is conservative for measured values.

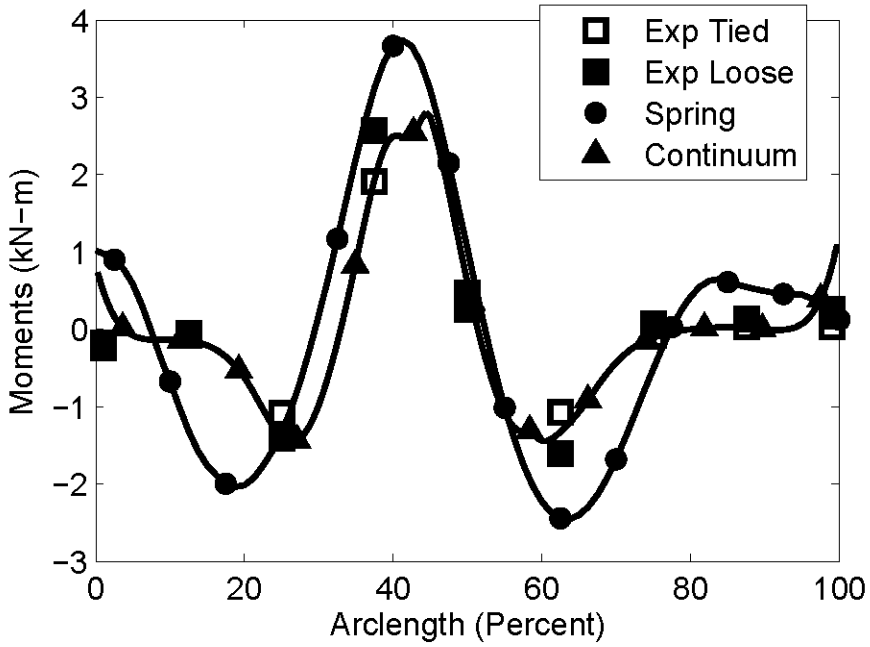

Figure 6.40. Short Arch 20% South Offset Live Load Moment Response

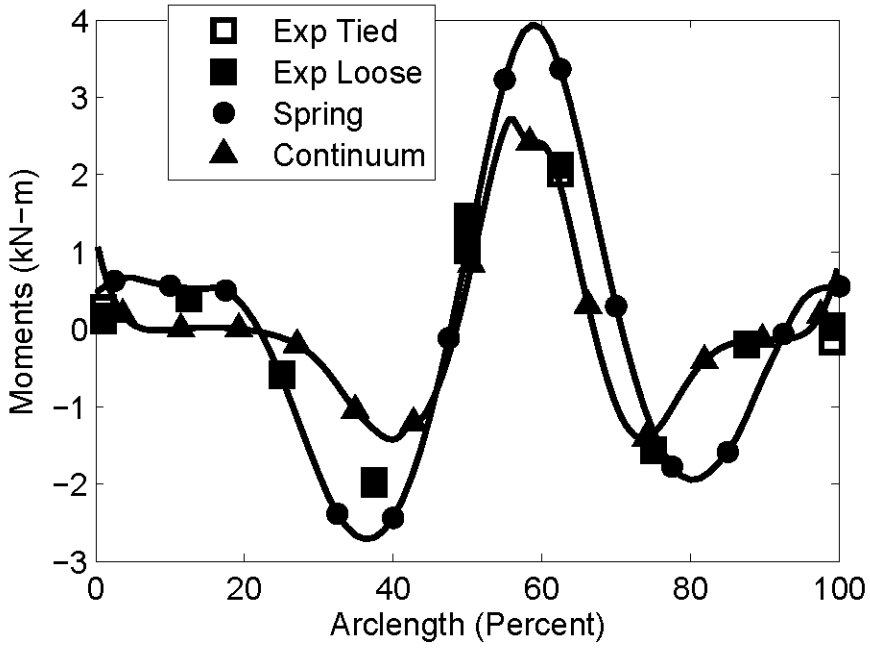

Figure 6.41. Short Arch 20% North Offset Live Load Moment Response

One atypical result from this test was that the loose foundation moments were definitively larger than the tied foundation moments for the South side load. The tied tests occur earlier in the test sequence and generally the moment response becomes smaller as the soil becomes denser from repeated loading. A potential cause is different foundation spread. The horizontal deflection along the span of the arch is shown in Figure 6.42. Notice that the tied foundation case has lower and higher foundation movement on the South side of the arch than the loose case. Therefore it is unlikely that the difference in moment is directly attributable to foundation spread. Also notice that the deflections were larger for the loose foundation test, particularly on the passive side (North). This confirms the results displayed for moments for this test.

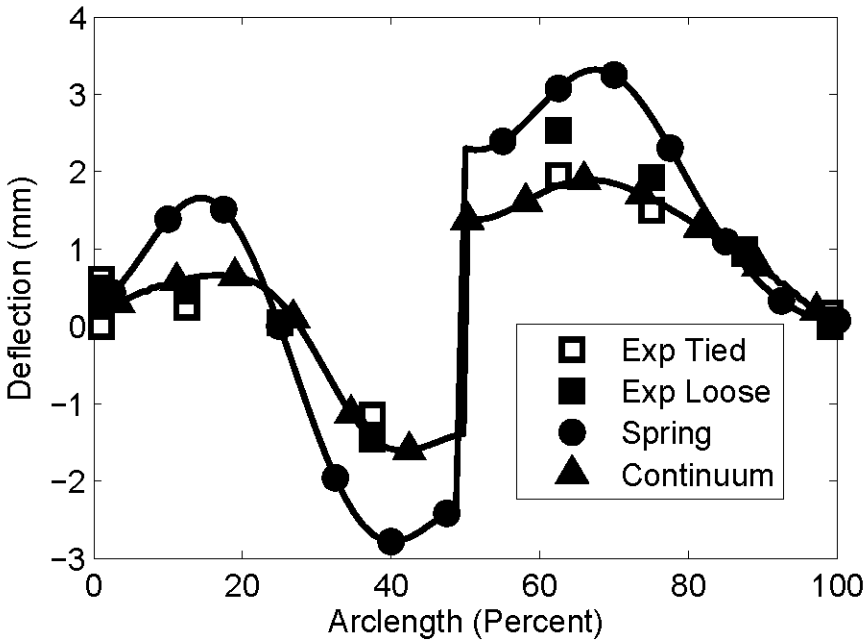

Figure 6.42. Short Arch 20% South Offset Live Load Hor. Deflection Response

6.3.5. Summary of Offset Loading Response

The soil-spring and soil-continuum models both produce reasonably accurate moments in many cases for peak positive moment. Using depth-dependent stiffness soil in the continuum model (as in these plots) produces moments that tend to be unconservative versus tied initial response for the short arch apex load (Figure 6.17), short arch 60% North offset (Figure 6.25), and the tall arch 40% North offset (Figure 6.32). The spring model is conservative for all positive peak moments except for apex live load, and the average of the three arch apex moments is within 5% of the spring model response for both bridges, although the central arch tends to record higher moments. Experimental North offset moments tend to be higher than South offset moments and this is likely due to load history: North offset loading occurred prior to South offset loading, thus there was more soil densification prior to South loading. Similarly, loose foundation moments are in most cases smaller than the tied foundation moments. This is also attributable to hysteretic soil response: the tied footings were tested first. Not shown in the results, repeated loading with the same foundation conditions tends to produce smaller moment response due to surcharge with each successive test, but the same or higher total moment due to surcharge plus backfilling. This is explained in further detail for the apex loading case later in this Chapter.

The soil-continuum model consistently tracked experimental moments away from the point of load application better than the soil-spring model. Practically, however, this does not affect the design of an arch bridge in most cases, because these moments do not control. The two exceptions where negative moment away from load application may control design are negative moment at the arch apex for a tall rise bridge with a 60% offset load and negative footing moment for a short rise bridge with a 60% offset load, as these two responses produce sizeable

negative moments that add to the negative moments during backfilling. The negative apex moment due to 60% offset load on the tall bridge was reasonably predicted by both models. The negative foundation moment caused by a 60% offset load was poorly predicted by the soil-spring model. This might be improved by the use of other spring configurations to better capture the passive resistance and arch-soil friction near the apex.

Spring model overprediction of offset negative footing moment potentially caused by underprediction of passive soil arching for a short rise bridge is not inconsistent with modeling assumptions. The soil-spring model assumes that all soil resistance takes the form of horizontal restraint. Therefore, vertical pressure is not affected by soil restraint. For a low rise arch this matters because of the shape of the structure. The model demonstrates a good ability to predict moments when outward motion is primarily at the shoulders and below, which is where elements have larger tributary area, allowing larger horizontal soil force. Near the apex elements are nearly horizontal, meaning that the tributary area for horizontal springs is nearly zero. The spring model predicts very high horizontal pressures, with earth pressure coefficients near 5 at the apex, but because of arch shape these very large pressures correspond to small forces that do not compensate for the lack of vertical restraint. Furthermore, there is no horizontal friction between the soil and the arch, which would also increase force over the larger horizontal tributary area.

For a taller arch the horizontal soil forces near the apex are larger, which gives a better fit for soil behavior than a short arch. Also, with greater soil depth above the applied load location more of the load is directed away from the bridge making the theoretical response smaller, which was observed with the 60% offset moment response for the tall and short bridge.

Apex live load produces positive foundation and apex moments, which oppose the negative backfilling moments. Therefore, apex loading may not be the worst case loading scenario for

design. Combining total moment caused by dead load and live load indicates that total positive moment is highest near the shoulders at positions 2 or 6 for a 60% offset load for both the tall and short bridge

Predicted live load pressure under the load application point is generally higher than estimated by the Boussinesq assumption in the soil-spring model which does not match expectations. The Boussinesq distribution does not include soil arching, which led to a theory that pressures would be overpredicted by Bousinesq load distribution. Pressure theoretically should diminish in areas near deformation away from the load source, causing greater load spread.

One area that behaved as expected was apex load for the tall arches, where the measured pressure at the apex was 28 kPa. This is 25% less than the model expected pressure. During untied foundation tests and during retest the measured apex pressure was 106 kPa and 88 kPa respectively, which suggests that the original value was an anomaly. During testing the apex TPC needed to be excavated and verified after backfilling and prior to live load testing due to suspected damage. The soil immediately surrounding this gauge may have been looser than other soil at the arch apex, which would have directed the load away from the cell. After testing the apex with an 84 kN load the apex was tested to 168 kN, which caused soil bearing failure and densified the soil immediately surrounding the gauge. Subsequent gauge pressures are higher than anticipated, which was common for all other gauges directly under the point of load application. The Boussinesq soil distribution was not conservative for measured vertical pressure as supposed. Simpler trapezoidal distributions would be less conservative for vertical pressure than the Boussinesq distribution because they give no increased pressure at the center of applied

load. Similarly, the Westergaard theoretical pressures (assuming a layered soil) also would produce less concentrated pressure than the Boussinesq.

6.3.6. Repeated Loading

The response of bridges changes as a result of load history: soil densifies and plastically deforms under service level loading. The current soil-spring model is elastic-plastic and does not have any change from prior live load. The continuum model is a Mohr-Coulomb plasticity model, which allows plastic deformation during shear failure, but because it is not a cap model there are no plastic densification effects from confined loading. Both models are unable to represent experimental behavior due to repeated loading, and all experimental data compared to experimental results in preceding sections was with virgin loading results, as this was the most representative data set. Experimental data includes several load iterations, and results for different bridges are compared in this section.

Figure 6.43, Figure 6.44, and Figure 6.45 include the experimental moments due to an apex live load for the short bridge, the tall bridge with compacted soil, and the tall bridge with under-compacted soil, respectively. The figures contain diagrams for virgin apex loading, the moment due to a third cycle of load (hysteretic), retesting with tied foundations after completing the seven load positions, and with unrestrained foundations after removal of the tie-rods. The tall bridge was not retested to 84 kN with tied foundations, and that data set is omitted from Figure 48. There are four apex load tests for each bridge: virgin tied foundation load, tied foundation retest, initial untied foundation test, and untied foundation retest. Also, each test has three load cycles. Out of twelve apex loads only four are plotted because there is no discernable difference

between the tied foundation retest and the untied foundation retest, and the third load moment (hysteretic effect) for any of the four apex tests is nearly identical.

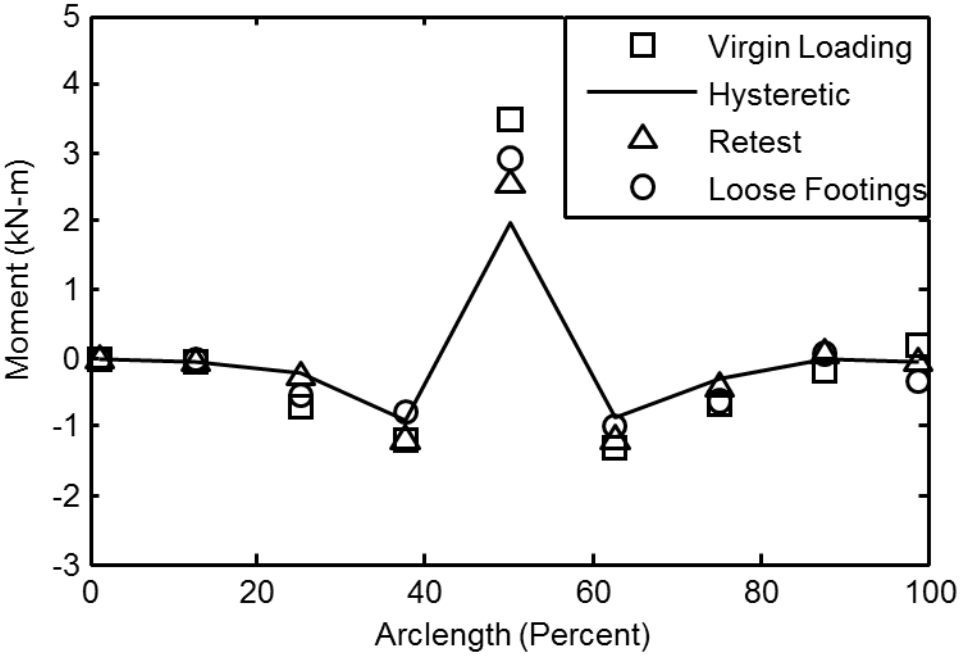

Figure 6.43. Moment Diagram, Apex Live Load, Short Bridge

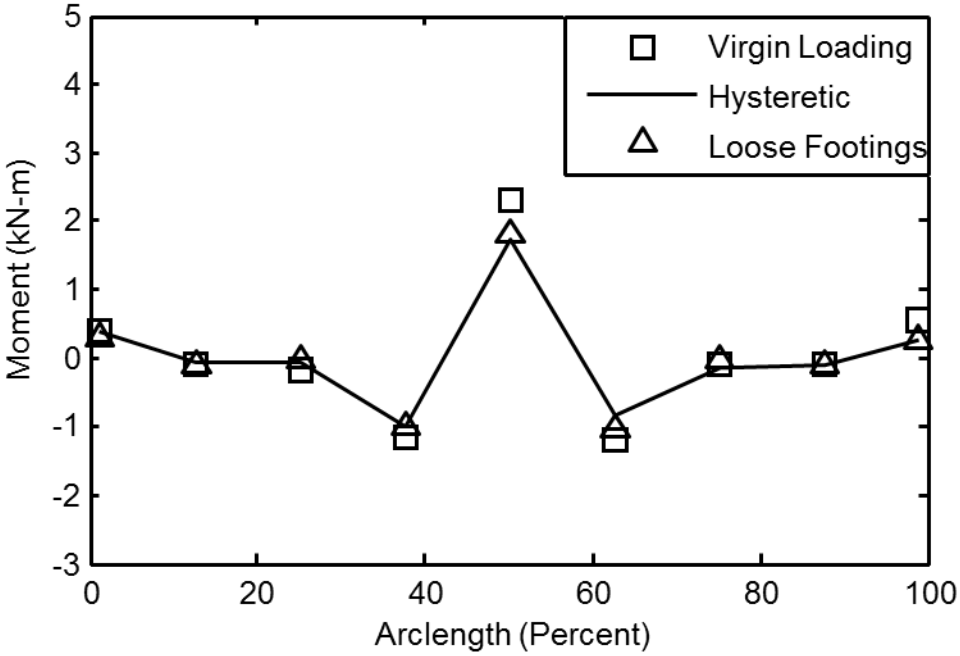

Figure 6.44. Moment Diagram, Apex Live Load, Tall Bridge, Compacted Soil

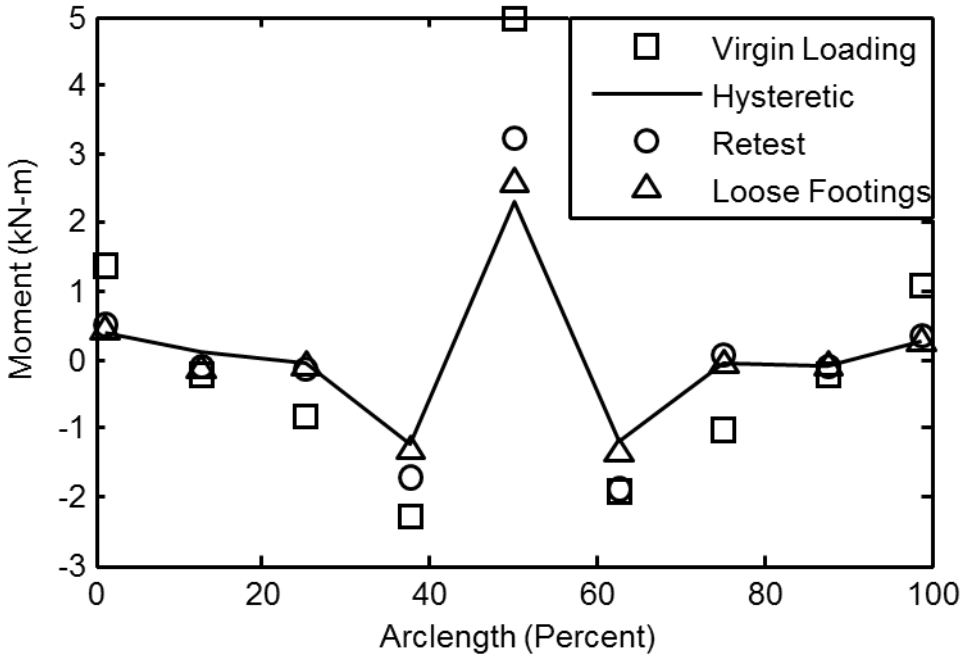

Figure 6.45. Moment Diagram, Apex Live Load, Tall Bridge, UC Soil

In all cases, the peak positive moment occurs directly under the point of load and the peak negative moment occurs one station to the North or South, not at the quarter points. The virgin moment response (negative or positive) is in all cases the largest moment, or indiscernible from other tests. As the arch deforms under live load it deforms into the soil, which results in locked-in stresses and deformations after load is removed from the structure. This effect diminishes with load cycling. Figure 6.46 includes the apex moment response for the short bridge for all three load cycles, which illustrates that there is less than 10% difference in the final moment between the first and third load iteration, and that the baseline moment changes by more than 40% of the total moment. Ultimately, the moment change due to live load in the third cycle is only about 50% of the change in moment due to the initial live load.

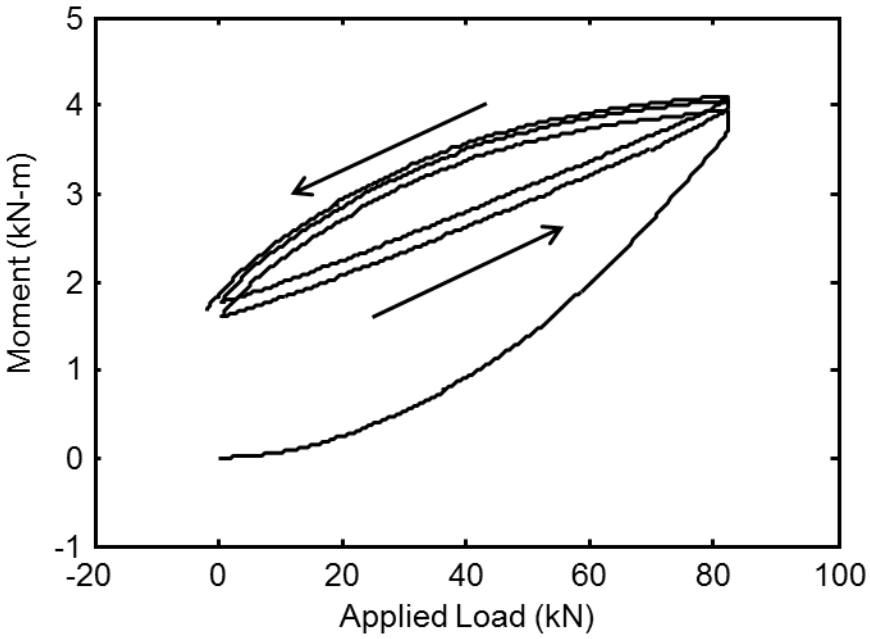

Figure 6.46. Mid Arch Apex Moment for Three Apex Load Cycles, Short Bridge

The effect of compaction is pronounced, especially for the virgin load. The peak apex moment for the virgin load is 115% greater for the under-compacted tall bridge than the compacted tall bridge. Repeated loading has a smaller effect, likely because the soil densifies from live loading and better confines the arches and distributes subsequent live loadings. The under-compacted bridge third load apex moment is only 32% higher than the compacted bridge. This effect is also observed at the foundation, where the virgin South foundation moment is 150% higher and the virgin North foundation moment is 180% higher for the under-compacted bridge versus the compacted bridge. This is consistent with prior research; for example, McCavour et al. (1998) tested buried plate arch bridges with backfill at 95% relative compaction and at 85% relative compaction bridge, and found a 50% difference in maximum apex moment due to vehicular live load. However, the tests performed here indicated that this difference

quickly goes away under load cycling: the third load cycle response is the same at the foundations for the compacted and under-compacted cases. Compaction during construction helps confine the bridge reducing the initial live load moment and reducing the total measured moment in the bridge, allowing for a more efficient structure.

6.3.7. Foundation Thrust Analysis

In addition to moment the foundation horizontal thrust forces are a design concern for typical CFFT bridges. To investigate this issue bridges were tested with low friction plastic pads between the concrete lab floor and the concrete arch foundations to minimize foundation resistance and create a lower bound for foundation horizontal restraint. For tall rise steel bridges the foundation thrust is generally minimal. Pressure during backfilling is 15 kPa on the North side and 10 kPa on the South side. Service live load pressures are smaller; for the tall bridge these pressures are below 2 kPa, and this pressure is below at-rest soil pressure, meaning that small deformations are associated with this pressure. During ultimate load there are larger horizontal footing movements (about 8 mm) and pressures (about 15 kPa), but for the tall bridge this is non-representative because the tall bridge ultimate test was for the under-compacted backfill, and thus the soil behind the foundation was more yielding than is typical for a bridge. The measured pressures were small and indicate a total horizontal earth pressure coefficient below 1.0. In contrast, the tall CFFT bridge with fully compacted backfill (results presented in Chapter 7) deflected less than 0.3 mm at the base of the foundation, and had similar recorded horizontal foundation pressure.

For a short rise bridge, foundation thrusts may be a design concern. Measured foundation movement and soil stress are higher during all loading cases, and this is directly attributable to the base angle of the arch. Higher base angle arches (tall rise arches) resolve to a greater vertical

foundation force than horizontal foundation force, and realistic friction prohibits foundation movement of these structures. For a 5:1 span to rise structure the base angle is 43.6^{o}, and arch axial force is more horizontal than vertical. The vertical force does increase base friction, but this increases less rapidly than thrust because a realistic foundation friction coefficient for design is 0.6 (NAVFAC 1986) for concrete on soil.

During backfilling on the short steel bridge horizontal pressure behind each foundation reaches a maximum of 20 kPa, which is similar to the tall bridge. In the first live load test after foundations are untied, an apex load test, the North footing moved horizontally outward (away from the center of span) almost 4 mm, which was the largest movement out of all service load tests. Generally, the movement is around 0.3 mm at the foundations for service load cases. One observation is that movements are permanent: even though movement in each stage is small, much of the movement is still in place after load is removed, indicating that the foundations are continuously spreading further outward throughout testing. This effect does not become smaller, and Figure 6.47 displays the final apex service load retest foundation movements, where it is clear that movements still do not recede with load removal.

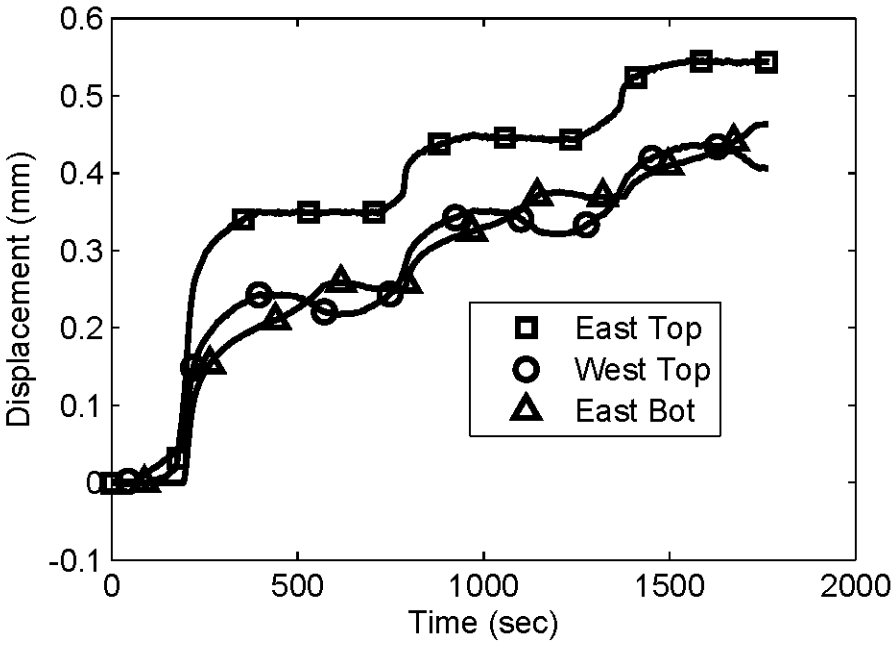

Figure 6.47. Short Arch Apex Load Untied North Foundation Deformation Retest

The measured pressure behind the North foundation during apex service load retest (corresponding to the foundation movement in Figure 6.47) was 7 kPa. Both the movement and the pressure are small relative to the scale of the pressure versus deflection chart presented in Chapter 4 for the spring model. Field installed bridge foundations not founded on bedrock are cast in-place on compacted soil and typically have a friction coefficient near 0.6 (NAVFAC 1986), which is higher than the expected coefficient of friction with plastic pads (0.2). The actual laboratory friction coefficient is likely higher than assumed for plastic because sand grains were embedded into the plastic and the plastic became damaged by repeated use. The minimum friction coefficient for a test can be back calculated by satisfying equilibrium for the foundation, and the actual friction coefficient can be back calculated during ultimate load when foundations begin to significantly slip.

Axial force at the base of the arch (F_{aa}) is the driving force and outward (away from the center of the arch) horizontal (X) forces are considered negative. Resisting horizontal forces, directed toward the center of the arch, include tie rods (F_t), soil pressure behind the foundation (F_{sh}), arch shear (F_{av}), and base friction (F_{bv}). These forces are considered positive. Vertical forces include the weight of the foundation (F_{wf}), the weight of the soil above the heel of the foundation (F_{ws}) and the vertical component of the arch shear and axial forces. All forces are displayed in a free body diagram of a foundation under load in Figure 6.48.

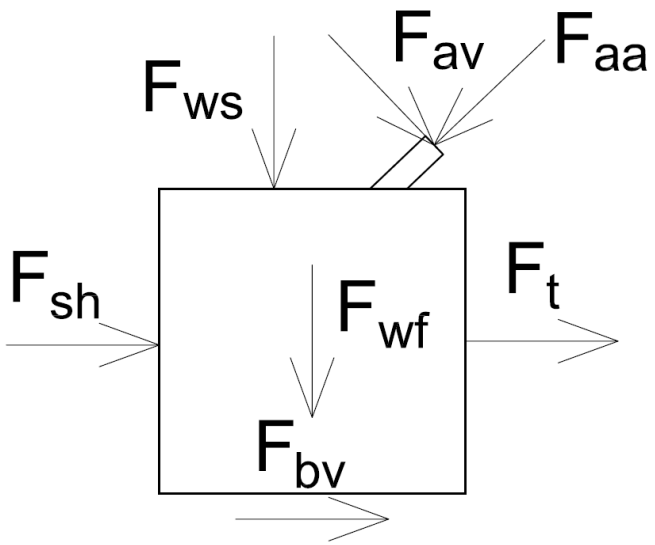

Figure 6.48. Free Body Diagram of Foundation Forces, Short Arch

It is theoretically possible that arch shear is directed outward, but soil-spring model results indicate that the shear at the arch-foundation interface caused by soil dead load is much higher than the shear at the arch-foundation interface caused by live load. The dead load shears are akin to the internal stresses near the base of a retaining wall, and are directed away from the soil mass due to the horizontal pressure of the soil. Future live load has smaller influence on base shear

because arch deflection is effectively restrained by the soil in the legs of the arch. The relatively high axial stiffness of the arch maintains large axial forces as a result of live load.

Numerical comparisons are made for three cases: tied end of backfilling, tied apex live load, and ultimate load when foundations begin to slide. The end of backfilling and apex live load cases are used in this comparison because they have the largest measured foundation pressures for any service tests, and the ultimate load test is used to establish a measured friction coefficient. For all three of these tests total arch shear is directed down and inward (positive per this sign convention). Total axial load for three arches, force in soil based on measured soil pressure behind the footings, and tie rod forces are reported for all cases in Table 6.1. Arch shear is taken from the spring model as it was not measured during testing. This analysis is for all three arches in the system.

Table 6.1. Foundation Force Analysis for Short Steel Arches

Forces (kN)	N Fill	S Fill	N Apex	S Apex	N Ult	S Ult
Foundation Wt [F_{wf}]	18.8	18.8	18.8	18.8	18.8	18.8
Soil Tail Wt [F_{ws}]	42.3	42.3	42.3	42.3	42.3	42.3
Arch Axial [F_{aa}]	113	110	224	207	234	229
Axial X	-81.8	-79.8	-162	-150	-169	-166
Axial Y	77.9	76	154	143	161	158
Arch Shear* [F_{av}]	32.7	32.7	33.4	33.4	35.5	35.5
Shear X*	22.5	22.5	23	23	24.4	24.4
Shear Y*	23.6	23.6	24.2	24.2	25.6	25.6
X-Press Force [F_{sh}]	27.4	22.1	29.3	27.6	74.8	51.9
Tie Rod [F_t]	7.7	7.7	28.6	28.6	-	-
Total Y	163	161	240	228	248	245
Total X [F_{bv}]	24	28	81	71	70	90
Friction**	0.15	0.17	0.34	0.31	0.28	0.37

*: Shear forces are from the soil-spring model and are not measured values

**: Friction is the required coefficient for force equilibrium, and at ultimate it is the value corresponding to the onset of sliding.

The soil heel weight is calculated as the weight of the soil column from the center point of the arches to the end of the heel of the foundation and neglects any added force or diminished force from soil arching. The horizontal pressure force is the measured soil pressure at the center of the foundation times the area of the foundation. During ultimate load it includes the pressure from all prior tests. The tie rod force is measured directly with in-line load cells. Friction along the sides of the soil box is neglected in this analysis. The side boundaries of the foundation use the same plastic layers as the base, except the outer edge of the gap between the soil box and the foundation was initially filed with spray foam to limit soil intrusion during backfilling. There should be very small horizontal force form the foundation into the soil box walls unless the bridge racks during testing.

Friction is assumed to be the horizontal force required to achieve foundation equilibrium. All other forces were measured during the test except the arch shear, which is assumed from model results. Because the foundation does not substantially slide during service tests the friction coefficient computed is a lower bound on the friction coefficient. The actual friction coefficient is computed during the ultimate load test, but this value is more dubious as it depends on the response of all prior tests for horizontal pressure while the axial force is the sum of the ultimate load axial forces and the dead load axial forces.

Notice that the friction reported in Table 6.1 is higher than anticipated for plastic, (0.2), and the reported friction values are the minimum friction required to achieve force equilibrium for backfilling and apex service load, but ultimate load is a measurement of the friction coefficient.

Foundation base horizontal movements were well below a millimeter during initial tied apex live load, thus the 0.34 friction coefficient is a lower bound for static friction coefficient. However, with the same calculation procedure the friction coefficient during ultimate load when sliding is initiated is lower. Likely this is a reflection on the inaccuracy of extrapolated axial forces from measured strains. For example, over the course of live load testing the total experimental axial force at the North West arch base reduces to 3 kN, or 10% of the dead load axial force. This is most likely a sign of the inherent inaccuracy of axial measurements at the foundation caused by arch base angle (the outside gauge is twice as far from the concrete as the inside gauge to keep the gauges on an arch cross section) and the small magnitude of axial strain (the steel sections are much stiffer axially than in flexure and error in the flexural strain measurement can produce inaccurate axial forces).

The soil-spring model predicts greater force from horizontal soil pressure behind the footing (-60 kN during backfill, -80 kN during apex live load) and anticipates a friction coefficient of 0.3 is adequate to prevent sliding during apex loading. The continuum model predicts nearly zero deformation at the foundation because base friction is sufficient to restrain movement. Soil-continuum predicted, pressure-induced average forces on the foundations from horizontal soil pressure are -47 kN during backfill and -54 to -58 kN during apex live load. Soil-continuum predicted soil force is closer to the soil-spring model than the measured values.

The foundation pressure and deformation become much higher at ultimate load because the tie rods were removed reducing the restraining horizontal forces, the axial load is greater, and the shear change remains small at the footing during ultimate load. Also, once the foundations begin moving the friction coefficient may drop from a static to a dynamic value. Figure 6.49 is the live load pressure behind both footings during ultimate load and Figure 6.50 is the live load

movement in each foundation due to ultimate load. Note that while the displacements and pressures are significant for this load case, this load case is not realistic for a bridge under service load or even AASHTO Strength I live load. The load factor for live load is 1.75 and the impact factor for a bridge with 2.4 m of soil cover (scaled to full size from the laboratory cover depth) is 1.167. These two factors give a total factored response of 2.038 times greater than service, (nearly identical to the scaled service tandem, 42 kN, compared to the actual applied load, 84 kN, performed in this report). The applied load corresponding to foundation spread was approximately 3 times greater than scaled service loading, an additional 50% more load than the factored AASHTO load case.

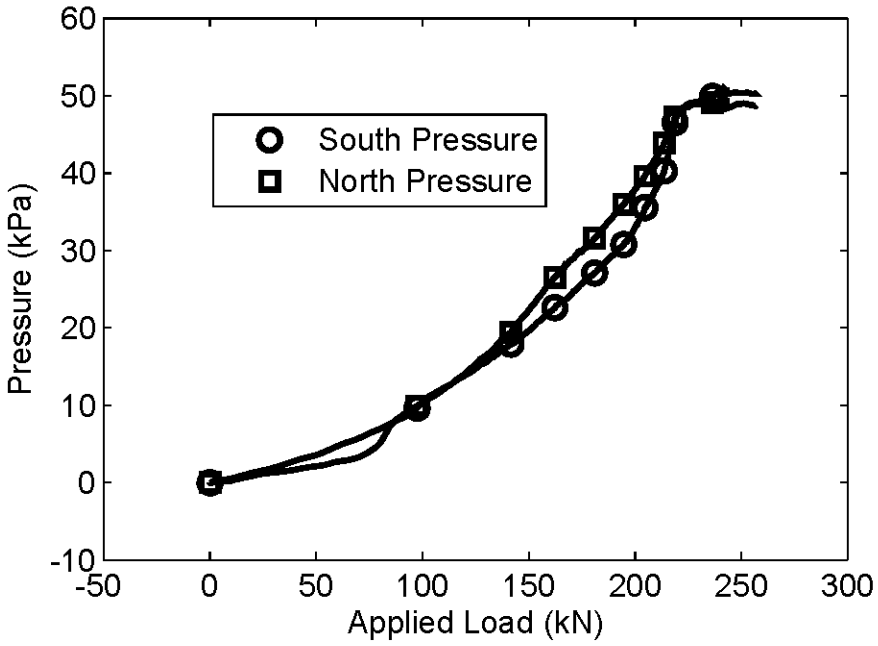

Figure 6.49. Short Arch Ultimate Load Foundation Pressure

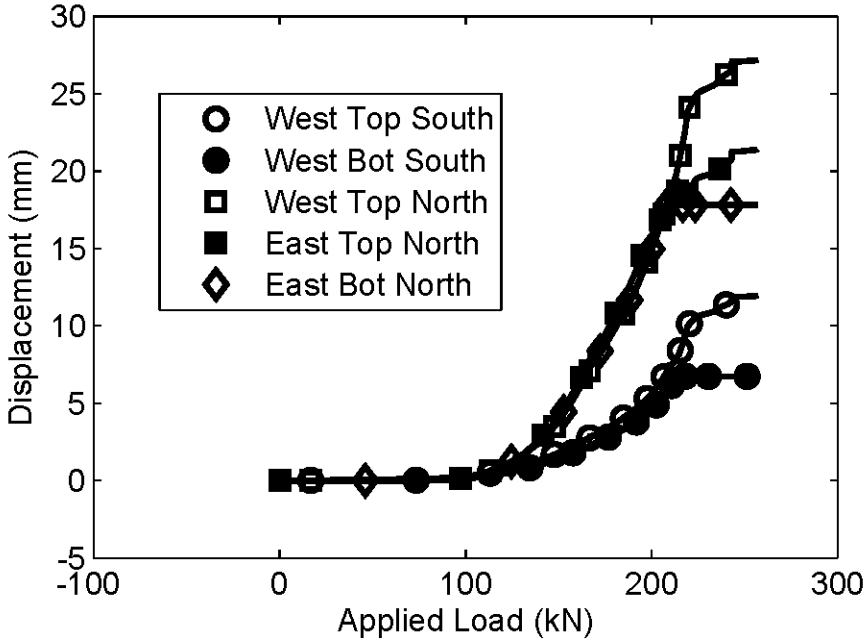

Figure 6.50. Short Arch Ultimate Load Foundation Movement

Buried arch bridge modeled response is designed with service load-deflection response, and then load effects (axial load, moment, and shear) are scaled by AASHTO load factors. The initial arch failure force is substantial: about 5.5 times a true scaled service live load (42 kN), and even at 3 times a scaled service live load (126 kN) the footings have only moved 1 mm on average, which suggests that a non-sliding footing analysis is acceptable for service loads. As force increases and deflections and pressures get larger the North foundation moves more than the South foundation, likely a result of the stiffer end wall on the South side. During service load there is minimal difference between the sides. Using the soil-spring model with a friction coefficient of 0.6, typical for cast in-place concrete on grade, the soil-spring model predicts no foundation spread at ultimate load: this further supports the theory that the foundation geometry used is adequate to eliminate horizontal footing movement even for a 5:1 span to rise arch.

6.4. Arch Response and Soil Pressures during Ultimate Loading

Figure 6.51 through Figure 6.59 include results from ultimate load tests. Experimental, soil-spring model, and short bridge soil-continuum model system failure was in-plane symmetric buckling ("snap-through") for the steel arches. As observed experimentally, the tall bridge soil-continuum model predicts a soil bearing failure under the load application point, but the soil-continuum model is incapable of converging beyond this event. As mentioned previously, there was considerable soil bearing failure (430 mm) in the tall bridge with an actuator displacement of 590 mm. Measured apex final deflections are 130 mm for the tall bridge and 180 mm for the short bridge, although this is based on one gauge, as two of three gauges exceeded the maximum measureable deflection. Soil-spring predicted apex deflection exceeded 130 mm for the tall bridge and 160 mm for the short bridge, showing good agreement with experimental results. Deflections are smaller for the soil-continuum model because it does not track post-buckled response. While arch apex moments are below the full plastic moment determined from coupon tension test data (17 to 19 kN-m), predicted and measured moments are both significantly above the moment at first yield, 8 to 9 kN-m. Experimental arch strains exceeded 0.06 at the apex of the tall bridge and 0.04 at the apex of the short bridge, which are much greater than the yield strain of 0.0018.

Figure 6.51 and Figure 6.52 illustrate the ultimate load total average (of the three arches) apex moment response for the tall and short bridges respectively. Experimental data include backfilling and hysteretic locked-in strains resulting from all prior loads. Notice the considerable difference in initial experimental apex moment for both plots compared to the apex moment at the end of backfilling (Figure 6.13 and Figure 6.14). The models only include backfilling, and match the previously presented model values. Live load sequence changes the moments locked

in the arches, and future loads thus cause different response than initial loads. However, once the load exceeds the maximum previously applied load of 84 kN, the soil-spring model-predicted and experimentally-determined moments agree up to soil-spring model predicted arch failure.

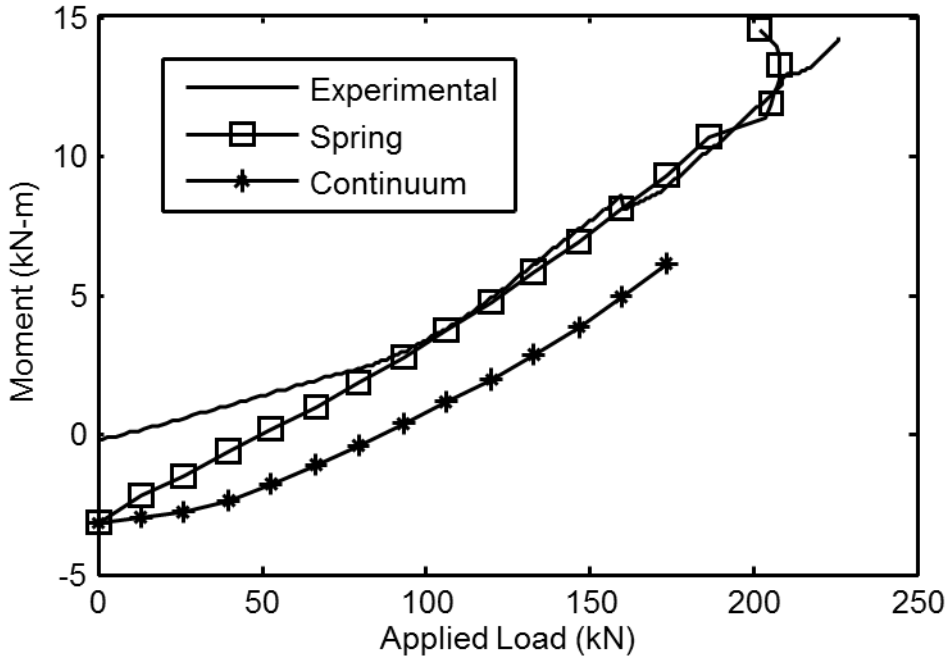

Figure 6.51. Ultimate Total Moment, Apex Load, Tall Bridge

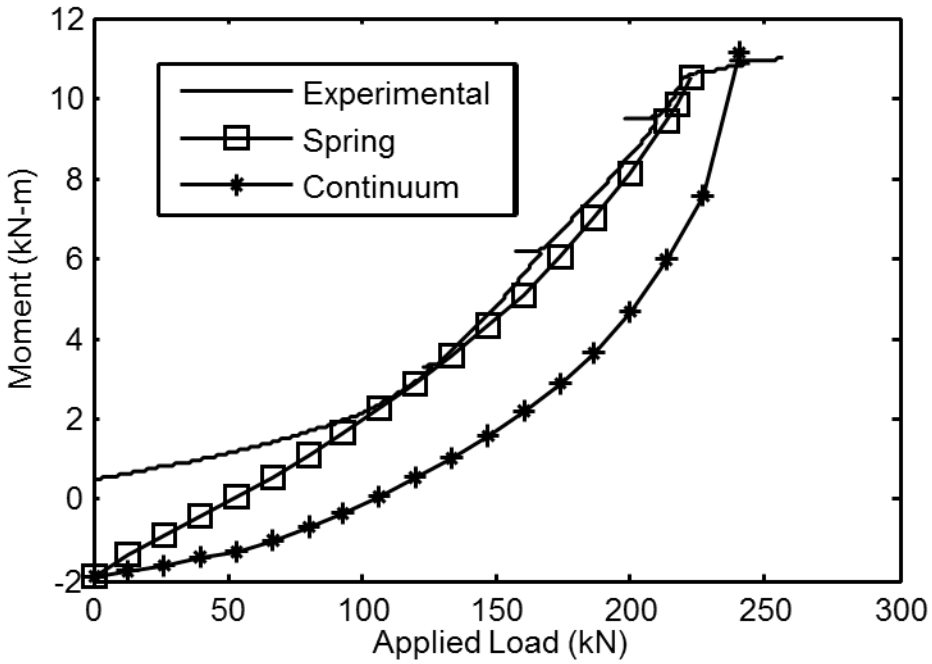

Figure 6.52. Ultimate Total Moment, Apex Load, Short Bridge

Soil arching action and load redistribution do not play a large role for much of ultimate loading given that the load is applied near the apex of the arch where soil cover is small. Near the end of ultimate loading apex deflections become large allowing soil arching despite the shallow cover. Experimental pressure for the short bridge diminished prior to ultimate load and for the tall bridge plateaued. This may explain the approximate 15% difference in capacity between experimental results and the soil-spring model, which does not redistribute live loads. The soil-continuum model predictions differ from the soil-spring model predictions, in that they do not approach the experimental results near the previously applied maximum load of 84 kN. The short bridge soil-continuum model predicts the experimentally observed buckling load within 6%, but this appears to be fortuitous as the model does not track moment response until it nears ultimate load.

The experimental moment agrees for all three arches in the system, thus an average experimental moment is used for clarity. During ultimate loading the arches yield at the apex and ultimate capacity is reached beyond the yield moment of the arches. The final deformed shape of the arches corresponded to a snap-through buckling of the arch, where the original downward apex curvature was inverted. The nearly constant moment for the final 40 kN of applied apex load shown in Figure 6.52 occurs after the short arches have yielded substantially. At this point there is only a small increase in moment with regard to strain, and the load distribution pad shown in Figure 3.29 allows load to spread away from the apex. The tall bridge apex moment (Figure 6.51) is also beyond yield, but because no distribution pad was used in this test the arches continue to strain and the moment continues to increase in the middle rather than being spread over a larger area.

As shown previously in Figure 6.50, foundation displacements are large during ultimate load, over 25 mm on the North side. Despite the large spread, foundation displacements do not create large moments at the foundation. Figure 6.53 is the North side foundation moments for all three arches, and these moments are not close to yield and are substantially lower than apex and shoulder moments. This further indicates that thrust is not critical for an arch: when the foundation slides a large amount local moments still do not control and moments between the arch shoulders are only minimally affected by footing spread.

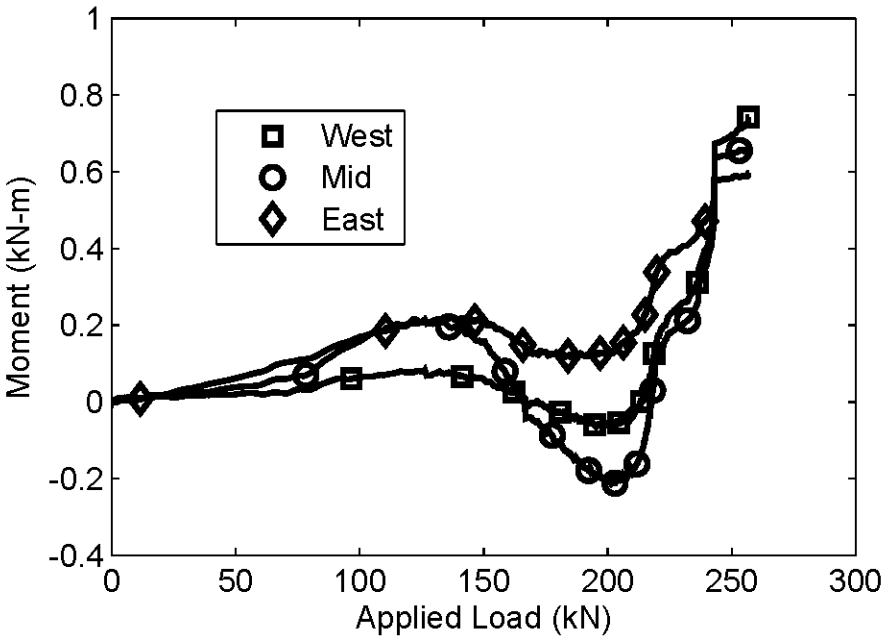

Figure 6.53. Short Arch Ultimate Load North Foundation Moment

Apex soil pressure and displacement results for the tall and short bridges are given in Figure 6.54 and Figure 6.55. The large pressure difference between the tall and short bridges is a function of load application – the tall bridge is loaded over a 152 mm long strip, full width, which embeds 430 mm into the soil, while the short bridge is loaded over a larger 760 mm long strip, full width, which embedded less than 50 mm into the soil. The tall bridge apex TPC measures over 60% of the actuator applied surface pressure. The short bridge apex TPC at failure measures a sharp decrease in vertical apex soil pressure after about 140 kN of applied load, with a total pressure below pressure at the start of the step. The larger distribution pad allows the load to spread away from the apex when the arch deforms and the soil-arch contact pressure is higher away from the apex.

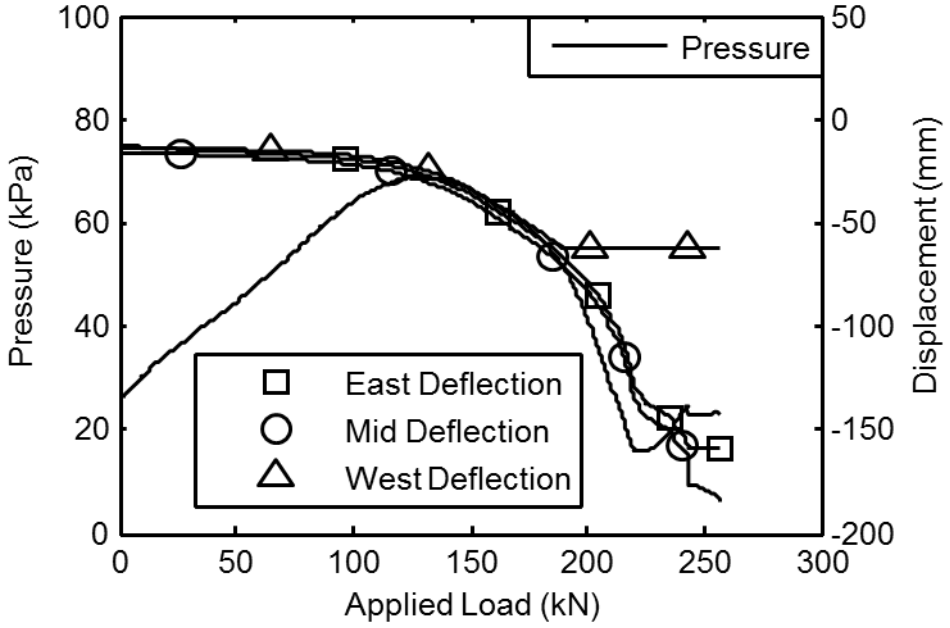

Figure 6.54. Ultimate load apex pressure and deflection, short bridge

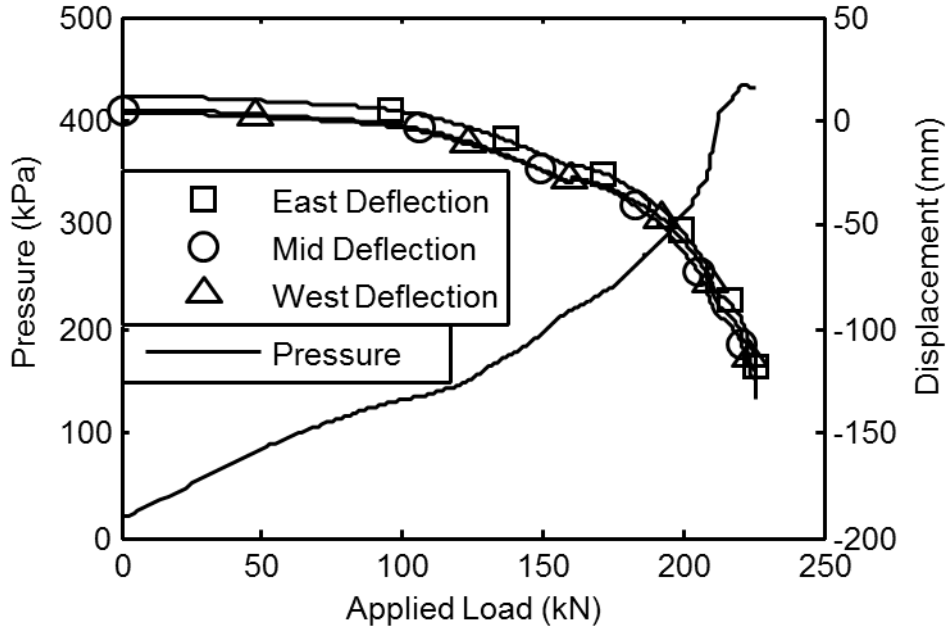

Figure 6.55. Ultimate load apex pressure and deflection, tall bridge

This is consistent with the soil pressures measured at the arch shoulders. Measured vertical pressure in the tall bridge at the shoulder (Figure 6.56 and Figure 6.57) is small compared to the horizontal pressure despite vertical displacements into the soil that are nearly 75% of the magnitude of horizontal displacements. In contrast, the short bridge (Figure 6.58 and Figure 6.59) sees higher vertical pressures than horizontal pressures at the shoulder despite negative (away from the soil) vertical displacements, indicating that vertical pressure response is influenced by load distribution, not vertical passive soil resistance.

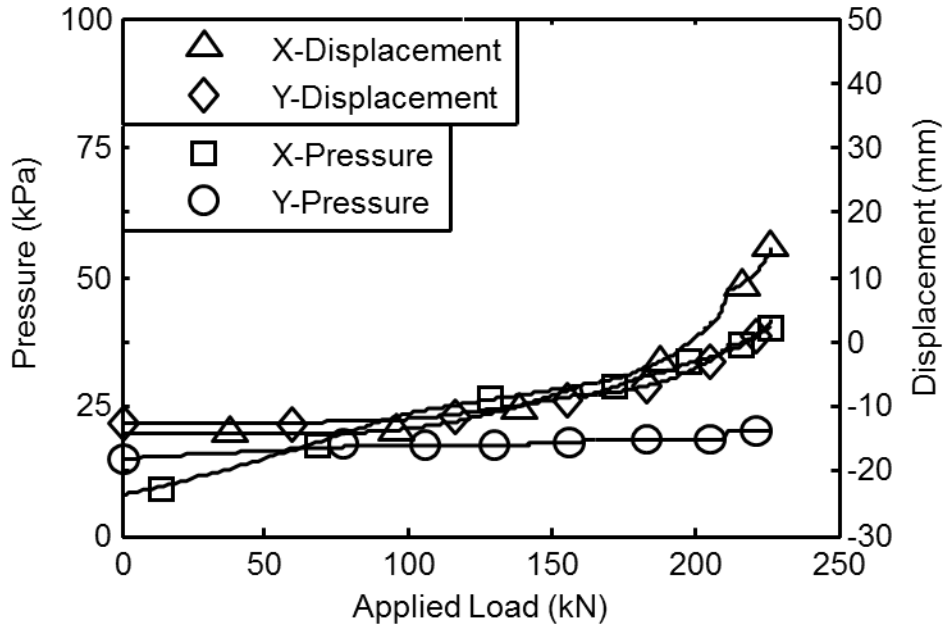

Figure 6.56. Ultimate Load South Shoulder Pressure and Deflection, Tall Bridge

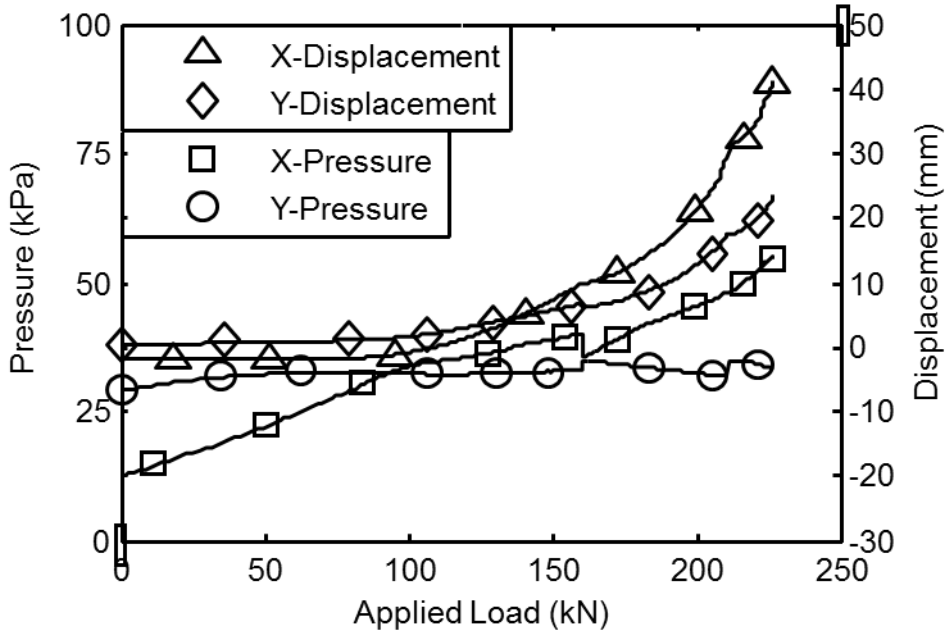

Figure 6.57. Ultimate Load North Shoulder Pressure and Deflection, Tall Bridge

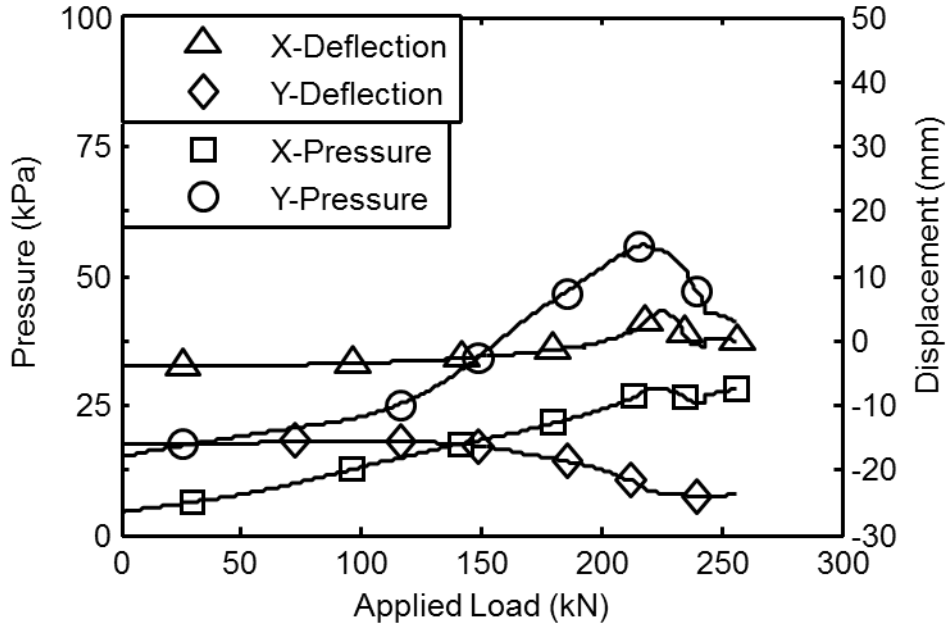

Figure 6.58. Ultimate Load South Shoulder Pressure and Deflection, Short Bridge

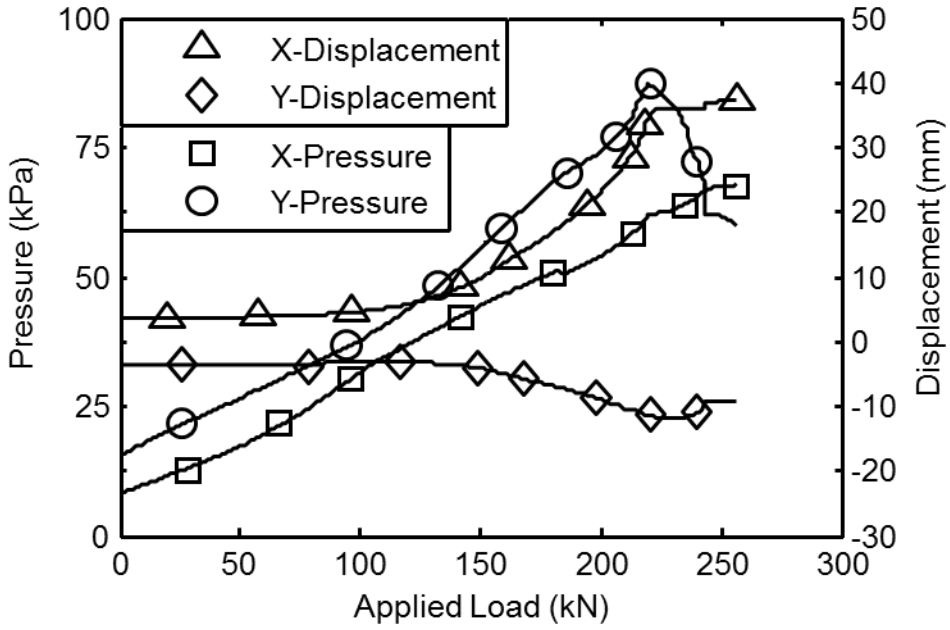

Figure 6.59. Ultimate Load North Shoulder Pressure and Deflection, Short Bridge

6.5. Soil-Spring Model Ultimate Capacity Prediction

The soil-spring model underpredicts the experimental ultimate load by about 15% for both the tall and short bridge, but remains an effective analysis tool compared to those with simpler soil assumptions. To demonstrate this, three simpler 2D models were created and used to predict ultimate capacity, presented in Table 6.2: a point loaded arch without soil, a point loaded arch with wished-in-place soil, and an arch with wished-in-place soil and assumed Boussinesq load distribution for an apex point load at the soil surface. The wished-in-place soil treated lateral soil loading assuming a deformation-independent fluid pressure with a horizontal earth pressure coefficient of 0.5. For all three models, arch capacity was limited by in-plane symmetric buckling of the arch, which corresponded to the actual failure mode.

Table 6.2. Buckling Load per Arch

Bridge	Tall (kN)	Short (kN)
Point Load, No Soil	33	37
Point Load, Dead Soil (K=0.5)	34	32
Boussinesq, Dead Soil (K=0.5)	35	45
Boussinesq, Springs	69	73
Experimental	78	86

Predicted capacities are given in Table 6.2. They indicate that, for both bridges, the soil-spring model does a better job of predicting the buckling load than simpler models that incorporate constant lateral earth pressure assumptions. The closest result of any model with wished-in-place soil has a predicted capacity of at most 52% of the measured capacity. Results in Table 6.2 indicate that models assuming a lateral earth pressure coefficient of 0.5 and ignoring lateral restraint provided by the soil predict only a small increase, or in one case a decrease, in arch ultimate capacity compared to a free-standing arch with no soil. Buried arches have greater capacity than free-standing arches due to soil restraint, which is neglected in analyses using constant stiffness soil. Varying earth pressure coefficient with deflection allows an arch to go from the active and at-rest pressures typical at the end of backfilling to the passive pressures at ultimate load, which magnify the arch capacity and allow the model to predict a more realistic buckling load response, differing by 15% from experimental results rather than 50% or greater.

6.6. Conclusions

Two buried steel arch bridges were instrumented and tested during backfilling and under live loading. This Chapter compares experimental data from subscale steel arch tests and model results from a soil-spring model and a soil-continuum model. The soil-spring model incorporates large-deformation analysis, horizontal non-linear elastic soil springs, and a Boussinesq

distribution for surface loads. The soil-continuum model uses Mohr-Coulomb plasticity and frictional contact to distribute load from the soil mass to a beam element arch. Significant conclusions given below:

- Poor arch confinement resulting from under-compacted soil conditions produces higher moments in the arches during backfilling despite lower soil density.
- Tall rise arches have smaller footing thrusts, smaller live load moments, and live load moments are more accurately modeled by the currently used soil-spring software than short rise arches.
- During initial live loading, bridges with under-compacted soil experience nearly twice the live load moments of bridges with compacted soil. This difference decreased with load cycling.
- Repeated loading does not substantially change the total arch moment due to a given live load due to the tendency of some moment caused by initial loads to be locked into the arch. Measured changes are within 15% for three load cycles for peak positive moment.
- The arch moment generated from a load is influenced by prior loading; soil is densified and sheared and rearranged during loading and locks the arches into a new configuration when load is removed.
- Peak backfilling moments for a tall arch do not occur at the end of backfilling, but occur when soil is near the arch apex. Additional soil causes positive moment at the foundations and apex reducing the peak values. In contrast, the short bridge experienced peak foundation moments at the end of backfilling.

- The critical location for arch design can be near the shoulder, not the apex, because backfilling moments are positive at the shoulder and live loads also produce positive moments for a surface load near the shoulder. In contrast, total moment at the apex is relatively small due to service live load since the apex moment due to backfilling is negative while the maximum live load apex moment response is positive. Short rise bridge design is controlled by negative foundation moment, which is inaccurately predicted by the soil-spring model. Future work is required to properly model soil confinement and improve this design location.
- The soil-spring model predicts backfilling moments well. Foundation moments are predicted within 20% and apex moments are over predicted by the model by 32% and 10% for the tall and short bridge respectively.
- The soil-spring model predicts the apex moment from an apex live load well, generally to within xx% of the experimentally inferred values.
- The soil-spring model is conservative in predicting peak positive moment for offset loads. The predicted moments for the tall bridge are better than the short bridge, but the model is either conservative or within 5% of measured moments for all service live loads.
- Foundation live load moments are overpredicted by the soil-spring model, but backfilling foundation moments are acceptably predicted by the model. This is most likely caused by a lack of vertical soil restraint in the soil-spring model.
- Ultimate load capacity is better predicted by the soil-spring model than by simple models that neglect soil springs. The soil-spring model predicts arch buckling before full plastic moment, as experimentally determined.

- During ultimate loading the soil-spring model acceptably predicts the moment from the maximum previously applied load until the model predicted buckling load. This shows that the model is capable of predicting response due to an overload vehicle.
- While the soil-continuum model better tracks moments away from the point of loading due to its ability to capture soil arching action and better predict the live load stress distribution, these moments typically do not control arch design.
- The soil-continuum model overpredicts final backfilling foundation moments and does not follow the same trend as experimental data and soil-spring model results for backfilling moments.

There are several improvements that could further enhance soil-spring model performance and reduce conservatism. These are outlined below:

- **Optimize Soil Spring Direction.** The soil-spring model uses horizontal soil springs, which may not be realistic near the shoulders and apex where the arch tangent becomes nearly horizontal itself. Because the spring tributary area is small in these regions, the model may underestimate the confining properties of the soil on top of the arch. Further study considering radial or friction angle springs (with limits when the soil cover is too shallow) may provide more realistic pressure response near the shoulders of the arch.
- **Improved Live Load Distribution.** The Boussinesq load distribution assumption is adequate when load is applied at the apex, but is not as the load is applied closer to the foundations. The load distribution model is not arch deflection dependent. A coupled continuum-spring model could solve this problem or potentially an analytical

expression for vertical pressure magnification as a function of relative arch movement.

- **Soil Hysteresis.** While the soil-spring model as presented uses elastic soil springs and is therefore unable to store the effects of soil compaction from live loads, load history changes the response of the real structure. Including the ability of the soil springs to store load history would likely improve model predictions, although it may have limited value for routine design. It would improve prediction of fatigue loading if that were a controlling load case.

CHAPTER 7. CFFT ARCH RESULTS

7.1. Introduction

Buried composite (CFFT) arch bridge designs are typically controlled by moment capacity. Ultimate moment capacity of CFFT arches is based on tensile FRP shell strain capacity. CFFT arches are nonlinear: their response to loading depends on the local internal stress state. In tension concrete cracks at a low stress level, and the stiffness is reduced considerably. Typical loading of a buried bridge is a combination of axial compression and bending, a tension and compression loading phenomenon. The soil spring model introduced in Chapter 4 uses a nonlinear axial load dependent moment curvature relationship for CFFT arches based on a model by Burgueño (1999) that uses a Mander (1988) nonlinear confined concrete stress-strain relationship.

Prior testing of CFFT arches has focused on highly idealized loading cases that do not represent realistic loading scenarios for a bridge: CFFT arches subject to an apex load (Dagher et al. 2012, Bannon 2009), or straight CFFT members under 3-point bend (Parry 2013) and 4-point bend (Dagher et al. 2012, Bannon 2009). The Burgueño moment curvature relationship accurately predicted curvature versus load for an apex loaded arch with a 300 mm diameter (Dagher et al. 2012). The arches used in this study are considerably different: diameter is only 110 mm and FRP shell longitudinal elastic modulus is approximately 40% of the shell elastic modulus used by Dagher (2012) due to scaling detailed in Chapter 2. This chapter compares experimental results with soil-spring model responses for CFFT 3 arch bridge systems made with 2.67:1 (tall) span-to-rise arches and 5:1 (short) span-to-rise arches to backfilling, distributed line load, and ultimate load applied over the apex of the arches.

Arch model response was not satisfactory using alternating backfilling lifts, as presented for the steel bridges in Chapter 6. The live load response of the CFFT bridges was close to symmetric, i.e. a 40% North offset load produced North strains and North deflections similar to the South side strains and deflections for a 40% South offset load. The model with alternating lifts disagrees with this finding for both bridge geometries. Because of this, a uniform loading model was developed. All figures in this chapter include both uniform and alternate backfilling simulation responses.

Likely, the Burgueño nonlinear moment curvature relationship is the primary culprit for the discrepancy between uniform and alternate backfilling results. The Burgueño model had only been verified for monotonic loading with CFFT arches. The present problem includes reloading, moments that are below previous peak values, and even moments that reverse sign. An elastic model like that used in the CFFT model does not accurately represent these scenarios. This issue was foreseen prior to testing, and hence steel arches with a linear elastic material response were also tested as described in Chapter 6. Specifically there are several potential issues during reloading and with response at service level testing:

- Tensile cracking strength of concrete is often underpredicted. Previous testing of CFFT arches indicates an average cracking stress of 8 MPa (Bannon 2009) which is 150% higher than the ACI predicted cracking strength of 3.2 MPa. The present arches provide higher concrete confinement due to a smaller diameter, which may further increase the cracking stress.
- Tensile cracking stress is variable. In Bannon (2009), Figure 4.20 shows curvature versus applied load for an apex loaded 300 mm diameter arch. Cracking occurs when load remains constant while curvature increases. For the five tested arches this

occurred at loads ranging from 31 kN to 94 kN, which illustrates how widely concrete tensile strength may vary from arch to arch.

- Assuming cracked section usually over-predicts stiffness loss because cracking is a non-uniform phenomenon. When peak strain is close to the cracking strain and cracks begin to form they occur in localized bands and the concrete between cracks retains stiffness, giving the arch higher bending stiffness than attributed by the model.
- When tension decreases (load is removed and moment diminishes), cracks may not close uniformly. This allows the concrete to carry compression deeper in the section than assumed by the model, which increases the bending stiffness.
- During moment reversal the compressive stiffness of previously cracked concrete may be lower than modeled. The cracked faces may not align properly as the cracks close. This will result in localized higher compressive stress but smaller effective area. As an extreme example, the elastic modulus of sand (which could represent highly crushed concrete) is less than 1% of the elastic modulus of concrete. This will also trigger a difference in strain between the shell and the concrete.

The net result of these potential issues is that the elastic range of arch response may be larger than modeled, the cracked bending stiffness with high moment is likely stiffer than modeled, and areas with moment reversal and low moment for the current load case are like more flexible than modeled. As a result, areas with high moment and low axial force, which is the prevailing case during backfilling, will give erroneous predictions. Cracking and load reversal are more extensive when alternative soil lifts are assumed. Uniform soil lifts prevent the arch from deforming as much during backfilling and reduce the locked-in strains at the end of backfilling,

giving a more realistic behavior for the structure and a better zero point for future live load modeling.

7.2. Backfilling Results

The discrepancy between model-assumed stiffness and actual material stiffness may be most evident during the backfilling process for the tall CFFT bridge, in particular in regard to top fiber arch strain near the foundation. Figure 7.1 and Figure 7.2 are the maximum and end of backfilling top surface strain diagrams for the tall CFFT bridge. The peak model and experimental South foundation predicted strain (1% of span) occurs when the South soil elevation is equal to the apex elevation and the North side elevation is 200 mm below the apex. The model predicted moment at 1% of span is 4.76 kN-m, axial load is 31.4 kN, and this corresponds to a top strain of 8420 microstrain with uneven loading. For even loading the maximum moment is 3.82 kN-m, axial load is 33.1 kN, and the corresponding strain is 7420 microstrain. At the end of backfilling the alternating side loading case moment is 28% lower (3.43 kN-m), the corresponding axial load is 113% higher (66.8 kN), and this corresponds to a 79% lower top strain (1790 microstrain). At the end of backfilling the uniform loading case moment is 27% lower (2.78 kN-m), the corresponding axial load is 102% higher (67.0 kN), and this corresponds to a 82% lower top strain (1350 microstrain). Conversely, experimental top strain results do not vary as much: the peak top strain was measured to be 2550 microstrain (mid arch), 3230 microstrain (west arch), and 2800 (east arch) while the end of backfill strains were 0% different (mid arch), 1.2% lower (west arch), and 5.7% lower (east arch). This means that the maximum strains were overpredicted by an average of 195% for alternating lifts, 160% for

uniform lifts, but the end of backfill strains were underpredicted by an average of 36% for alternating lifts and 45% for uniform lifts.

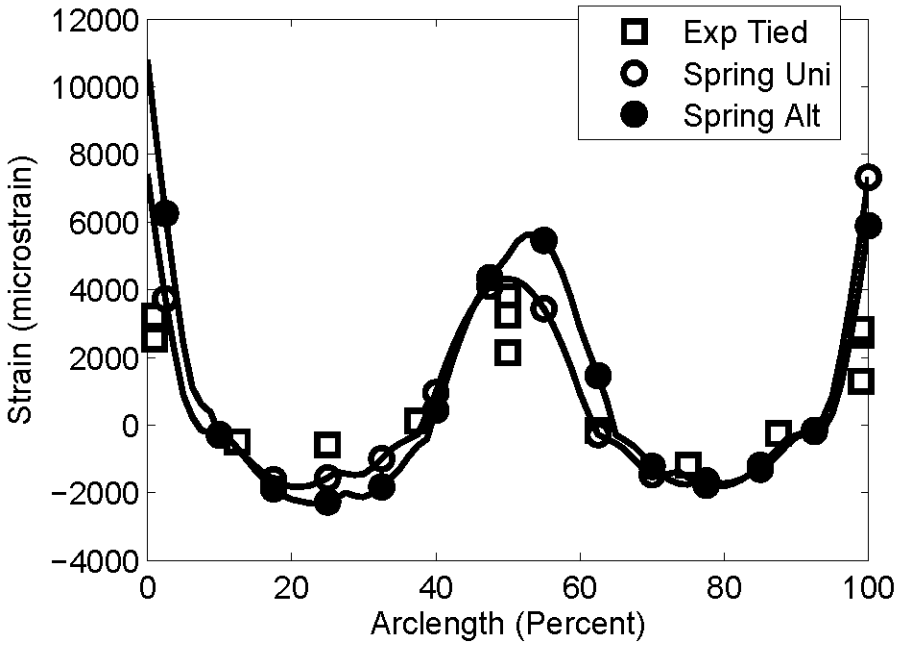

Figure 7.1. Tall CFFT Arch, Maximum Top Strain During Backfilling

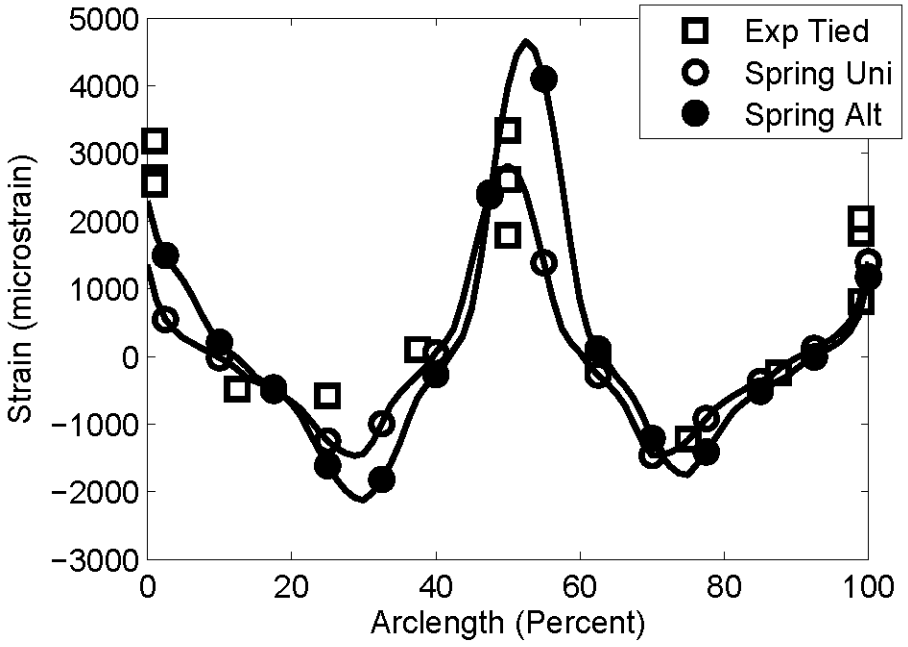

Figure 7.2. Tall CFFT Arch, Top Strain, End of Backfilling

The model substantially overestimates the peak tensile strain. A part of this is likely due to overprediction of the moment, as the model overestimated the peak foundation moment in the tall steel bridge by 32%. Reducing the moment by 32% gives a strain of approximately 5000 microstrain per the moment curvature relationship which is a 75% overprediction of strain. The measured strains are well above the rupture strain for concrete, so it is likely that the concrete cracked during testing, but it is possible that it is less cracked than the model assumes. When load is reduced the measured strains are higher than predicted. This is because the cracked concrete surfaces are rough. Reducing the moment and increasing axial load will attempt to close the cracks, but spalled concrete can wedge the cracks open, preventing as much loss in tensile strain as supposed by the model. Effectively, this is a hysteretic effect: the unloading stiffness for cracked concrete is not identical to the loading stiffness. Note that compression increased considerably for the tall steel bridge after soil was applied over the apex, thus the assumption that axial load more than doubles with the final 4 lifts is based on experimentation, not just model results.

Apex top strain (tensile face) response was on average 40% lower than predicted by the alternating lift model for the tall CFFT arches, but is still approximately 15 times higher than the tensile cracking strain based on the CFFT design equation used in the Burgueño model. Therefore it is likely the concrete at and near the apex is cracked, although the depth of cracking and frequency of cracking may be poorly represented by the model, which could explain part of the model discrepancy. The apex strain discrepancy between the model and the experiment could be an overprediciton of moment response by the soil-spring model, (the tall steel bridge apex

moment was overpredicted by 27%). For the model-predicted axial load a 27% smaller moment has corresponding strains that are within 5% of measured values. The uniform lift model is 5% above the average strain, which is remarkable agreement considering a range greater than 50% of mean apex top fiber strain with only three measured values.

As in the foundation, the apex is also likely subject to a combination of reduced moment and increased axial load as additional soil is placed over the apex. Unlike the foundation moments, the change in apex moment from peak value to end of backfilling is well represented by the model. The model predicts 20% smaller apex strain at the end of backfilling than the peak value, and experimental values agree, differing by 19% form the peak value to the end value. This is the same relative transition for the uniform soil lift model. This good transition may be coincidental and may reflect a combination of poor model-predicted moment response with a poor assumed moment-curvature relationship: the steel bridge experimentally had a 25% moment decrease over the final 3 lifts (as soil was placed over the apex), while the soil-spring model indicated an increase in moment (about 5%) over the same loading regime. Both the uniform lift and alternating lift soil-spring models predict a large increase in moment for the CFFT bridge over the final 3 lifts, 13%, and attribute the loss in tensile strain to a 30% increase in axial compression. This however does not agree with experimental results which indicated a small (about 3%) decrease in compressive strain, indicating a net loss in moment accompanied by a smaller net rise in axial compressive strain.

Smaller than anticipated apex curvature was accompanied by smaller than anticipated apex deflection with alternating lifts. The model predicted peak deflection, shown in Figure 7.3, was 44 mm while experimental peak deflection was an average of 29 mm. (Deflection was not measured for the middle arch during backfilling due to gauge failure, but both outer arches were

instrumented.) This is about a 50% increase in deflection above the experimental value, which is larger than the difference found in the steel bridge which was about 20%. The apex deflection at the end of backfilling was measured as 21 mm and predicted to be 27 mm, an overprediction of 25%. The end of backfilling deflection is characteristic with the model error found in steel bridge testing. Experimental deflection measurements are taken from the decking, an average of 35 mm from the arches, not the arches themselves, so that mechanical fasteners could be used that would not compromise arch integrity and would be ridged during a month of testing. This may partially explain consistently lower measured deflections than assumed by the model. The final deflection with uniform lifts was 17 mm, which is 20% lower than measured values. Both models predict peak positive deflection at the same step (one lift below the apex elevation), which disagrees with the measured maximum deflection (soil level with apex).

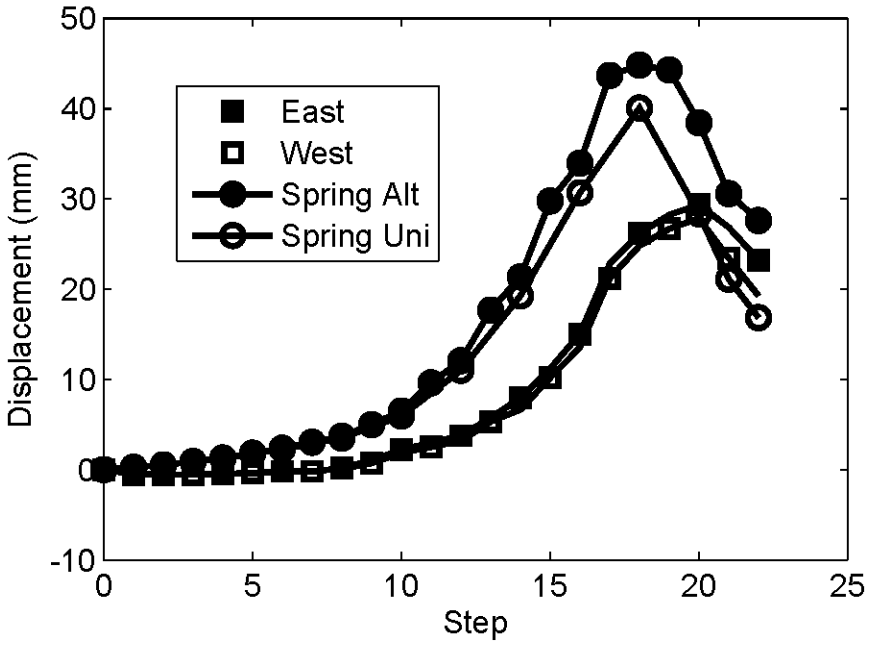

Figure 7.3. Tall CFFT Arch, Apex Deflection During Backfilling,

Applied loads were likely close to expected values. Soil pressures at the end of backfilling are plotted in Figure 7.4. Notice that the South side has higher than predicted pressure, while the North shoulder has lower than predicted pressure, but vertical pressures are generally close to weight of overburden soil (model predicted). Notice that both models predict nearly identical pressure: this is because pressure is based only on current elevation and the deflection difference between the two models is not large enough to have a significant impact on pressure. Observe that the horizontal pressures are also smaller than the vertical pressures at all gauge locations. This is not consistent with the model which magnifies horizontal pressure near the apex while neglecting the additional vertical pressure carried by soil arching near the arch apex and on the South side of the arches. Model predicted horizontal pressures are omitted for clarity.

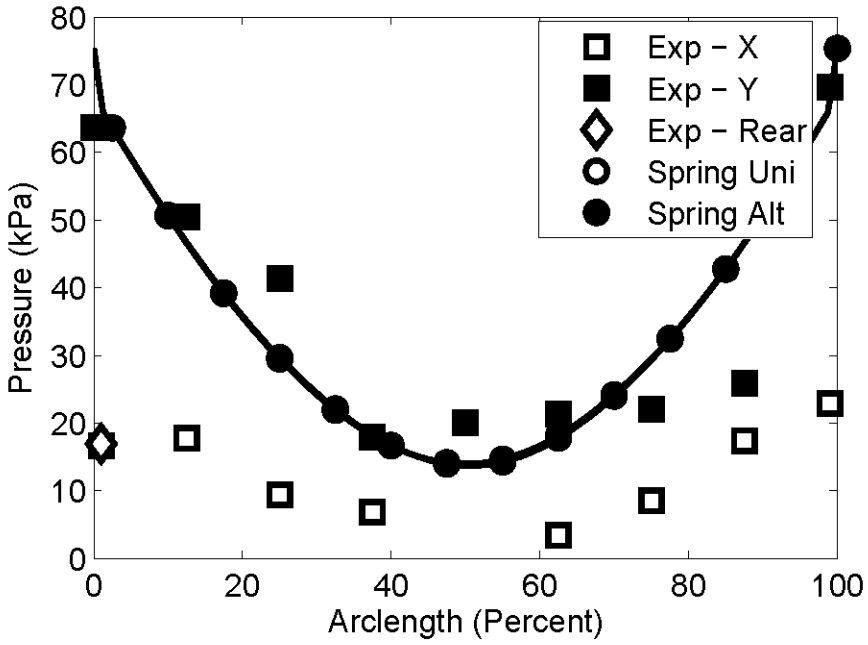

Figure 7.4. Tall CFFT Arch, End of Backfill, Vertical Pressure

The short rise CFFT arches had better strain agreement with the model, although they had a larger spread at the foundations (where gauges were in common across multiple arches). The short rise arch sees smaller moment during the backfilling sequence, although moments are similar for both arch geometries at the end of backfilling. Less moment corresponds to less cracking, both experimentally and predicted, for the short rise arch, which improves agreement between the model and the experimental results. The end of backfilling strains in Figure 7.5 include South foundation strains, which varied from 800 microstrain to 4200 microstrain, with the central arch reporting the lowest strain. The difference in magnitude is likely due to local concrete cracking and the proximity of the gauge to the foundation. The peak foundation strains occur during the last lift before the apex, where the alternating model predicts a strain of 5000 microstrain 1% of the span away from the foundation. This is higher than all measured foundation strains and more than doubles the average strain of the three foundations. The uniform model predicts smaller apex and shoulder strains, which agree better at the shoulders and are under-conservative at the apex.

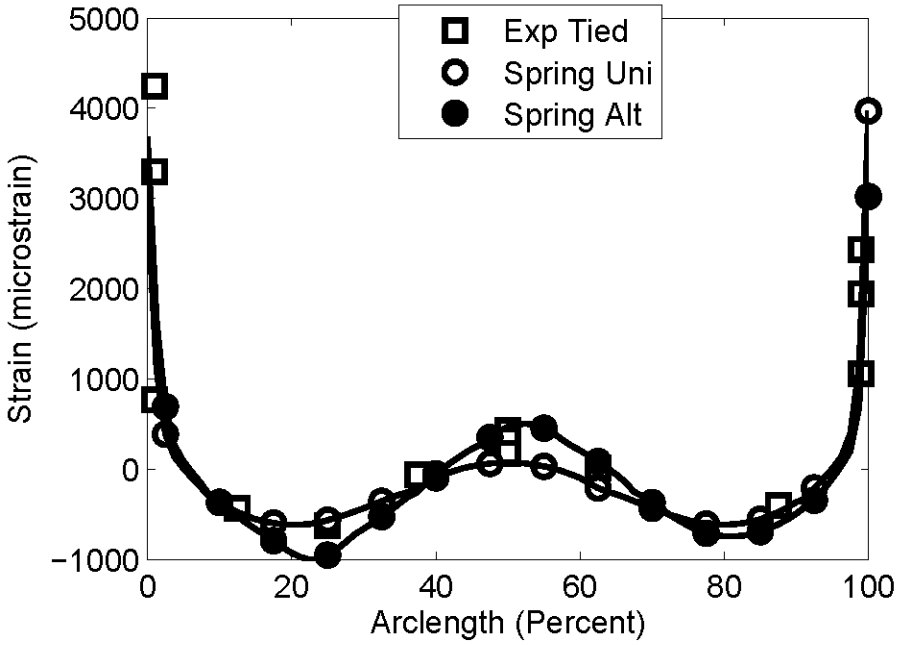

Figure 7.5. Short CFFT Arch, End of Backfill, Top Strain

Vertical deflection for the short CFFT bridge, Figure 7.6, consistently is under-predicted by approximately 5 mm at all gauge locations with an alternating lift model. This is a common occurrence: this is a similar magnitude to the discrepancy between model and experimental results for all of the other three bridges (steel and CFFT). The trend of deflected shape is very similar if a 5 mm offset were imposed at the foundations, however, there is limited justification for this process. This result, taken with the other three bridges, suggests that there is a lack of understanding about what happens in the foundations and in the lower reaches arches instead of a lack of understanding between gauge positions 1 to 7. The uniform model accurately predicts the deflections at the apex and at the North shoulder, but the South shoulder deflection is underpredicted because the model response is asymmetric.

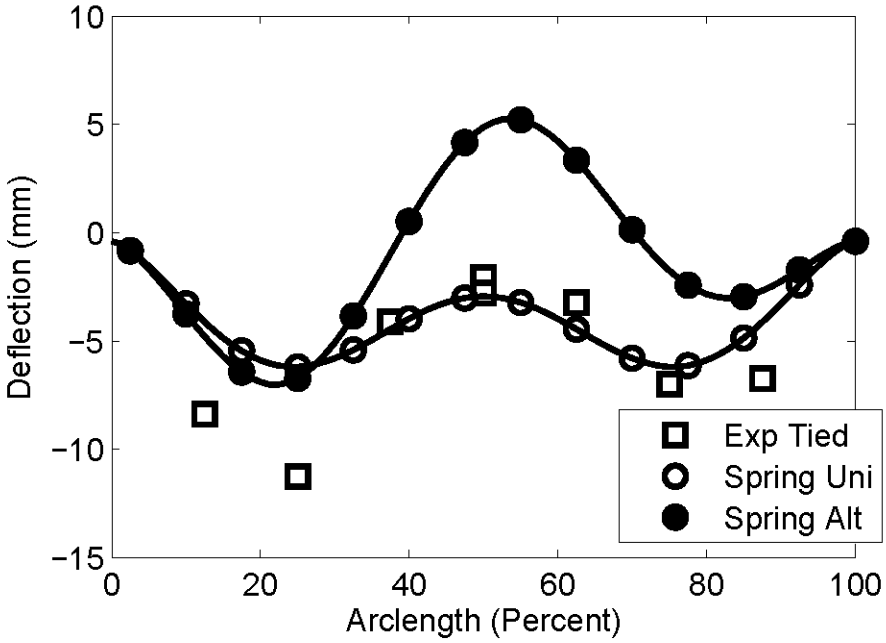

Figure 7.6. Short CFFT arch, End of Backfill, Vertical Deflection

The horizontal backfilling deflections in Figure 7.7 are not well modeled by the alternating side model because the experimental results suggest that the North side deflected further than the South side, which is inconsistent with the lift order. This further supports the use of a uniform lift model: the primary motivation of alternate side modeling is to establish the proper backfilling deformed shape for horizontal soil spring initiation, yet the alternating side model more poorly predicts the final horizontal backfilling deflections. Also, footing deformations are larger than model predicted. These deflections are at the top of foundation and reflect outward rotation. The model predicts an initially stiffer soil behind the foundation which overpredicts restraint: this indicates that the model-assumed K_0 of 1.0 may be higher than appropriate.

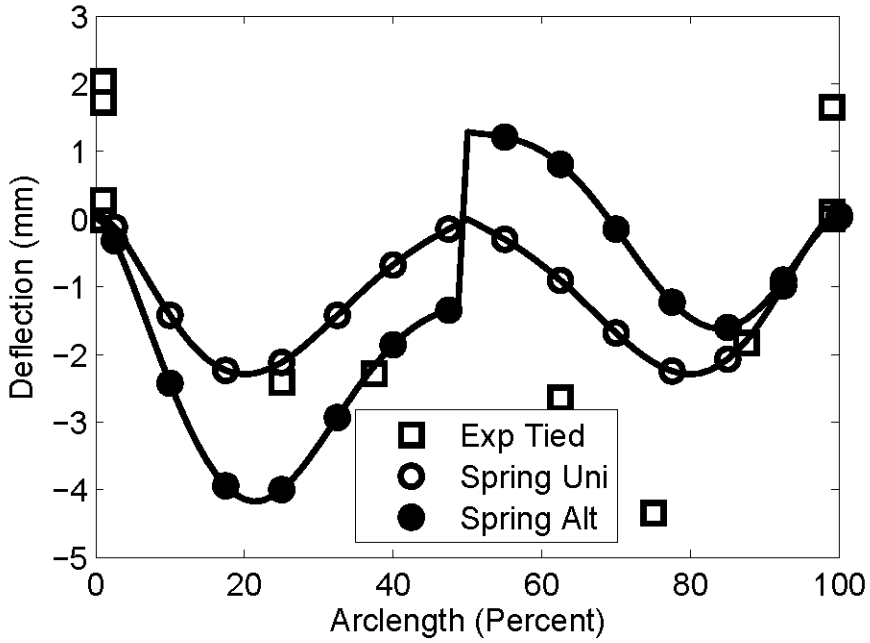

Figure 7.7. Short CFFT Bridge, End of Backfill, Horizontal Deflection

7.3. Live Load Results

Both CFFT arch bridge systems were tested over the middle 60% of the span at 10% of span intervals, in the same manner as the steel bridges. Both bridges were loaded with an 84 kN load that spanned the full width of the bridge, and were tested with tied (initially) and untied foundations (after). The short CFFT arch bridge system was also tested with variable soil cover while the foundations were tied. The top 300 mm of soil cover (half of the cover depth) was removed and the soil surface was recompacted. This process was done with hand labor and was relatively slow, thus instrumentation was not used while removing soil because gauge error due to temperature change and creep were considered significant over the long duration of adjusting soil elevation. All load positions were tested with the shallow soil depth at a load of only 42 kN, this was to prevent failure of the bridge system under a more concentrated load. 150 mm of soil was added back into the soil box and compacted, followed by retesting with the full double-

service load of 84 kN. The final 150 mm of soil was returned to the soil box, compacted, and the apex load was retested. Foundations were untied and the loose foundation and ultimate load tests were completed as normal.

7.3.1. Apex Live Load

The apex loading for the CFFT arch bridges with alternating lift models was predicted by the soil-spring model to have an oddly asymmetric effect based on current stress state within the cross section and asymmetric backfilling stresses. This effect seems to be overstated, or at least inaccurately predicted. Figure 7.8 shows top axis strains for the tall CFFT arches under apex loading. Notice that the peak tensile spike is at position 3, not position 5, indicating that the analysis was unable to find asymmetric backfilling effects. Also notice that apex strain is over-predicted by the model by an average of 46%. This may be an effect of the moment curvature relationship: the experimental results indicate an apex live load strain 2% higher and opposite sign from the backfilling strain. The model predicts a 3% lower apex strain due to live load than backfilling, with opposite sign. The experimental results and the alternating lift model predictions indicate that apex strain due to a double apex service load (84 kN) produces a total strain within 5% of zero, thus it is likely that the model accurately predicts the combination of the load effects, but fails to predict the relationship between moment, curvature, and strain required to get the proper strain prediction. In contrast, the uniform lift model accurately predicts the compressive strain response at the apex due to an apex load, likely this is due to better strain prediction during backfilling. The uniform lift model does not predict the tension spike at gauge 3.

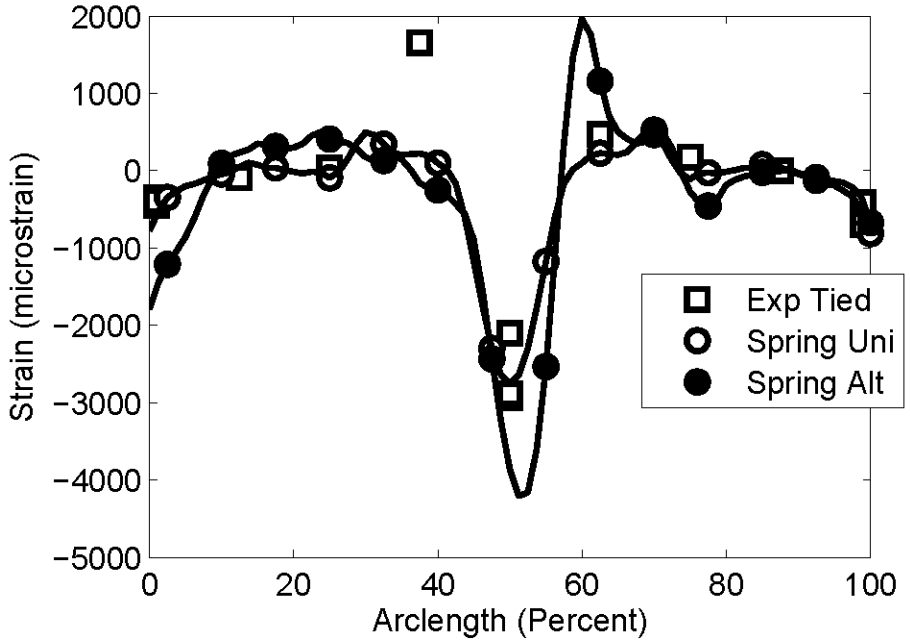

Figure 7.8. Tall CFFT Arch, Apex Live Load, Top Strain

In Figure 7.9, both models predict negative strain spikes in the shoulder regions (where extensive cracking was predicted during backfilling) that seem excessive based on experimental results: this is a symptom of lack of hysteresitic model response for the CFFT arches and follows the same trend as the transition in foundation strains from max backfill to end of backfill for tall CFFT arches. The recompression of previously cracked concrete was stiffer than predicted, and because the actual location of cracking is not well predicted by the model the strain response at discrete gauge locations can be poorly represented by either model.

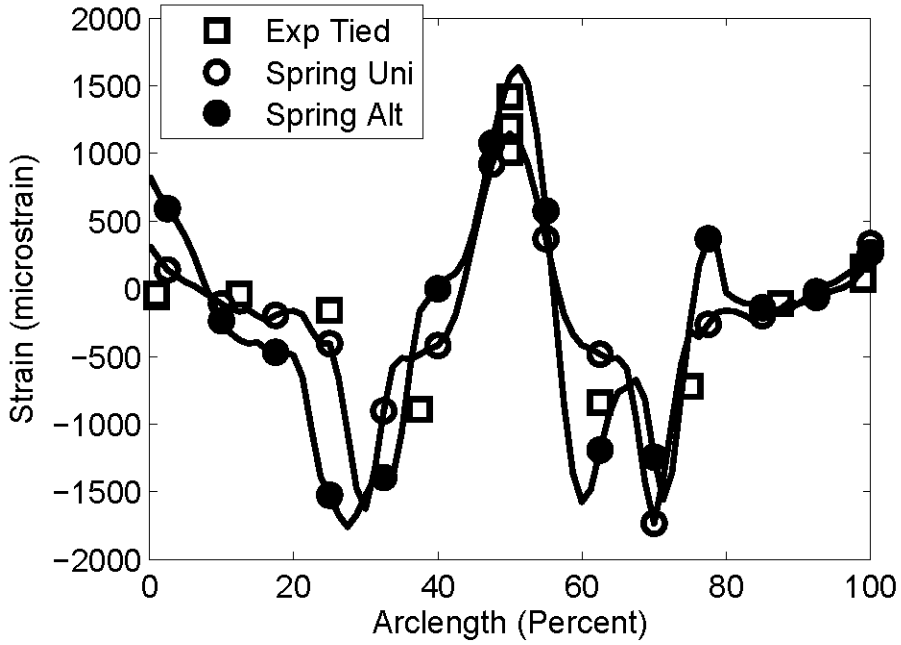

Figure 7.9. Tall CFFT Arch, Apex Live Load, Bottom Strain

Vertical pressure results for the tall CFFT arches are in Figure 7.10. The apex pressure is similar to steel bridge results and does not match pretest speculation: the predicted apex vertical pressure (41 kPa) is 40% lower than the experimental measured value (69 kPa). This is contrary to typical behavior of active soil arching situations. The apex deflection is away from load and, as shown in Figure 7.11, is an average of 13 mm. This is large enough that the apex pressure should be reduced from a traditional Boussinesq elastic pressure distribution. A layered soil (which typically employs a Westergaard distribution) should make this effect more noticeable. Yet, the measured apex pressure is higher than expected values.

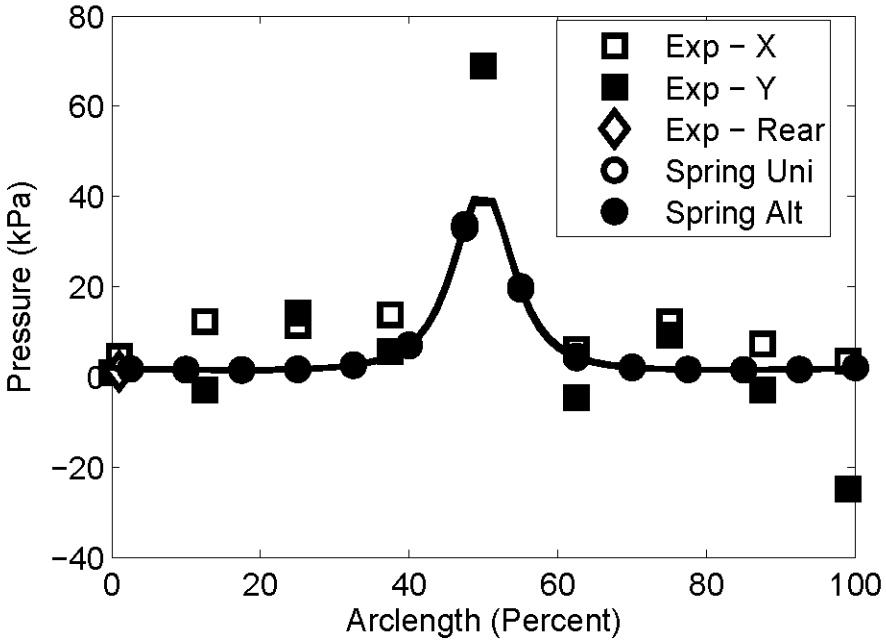

Figure 7.10. Tall CFFT Arch, Apex Live Load, Pressure

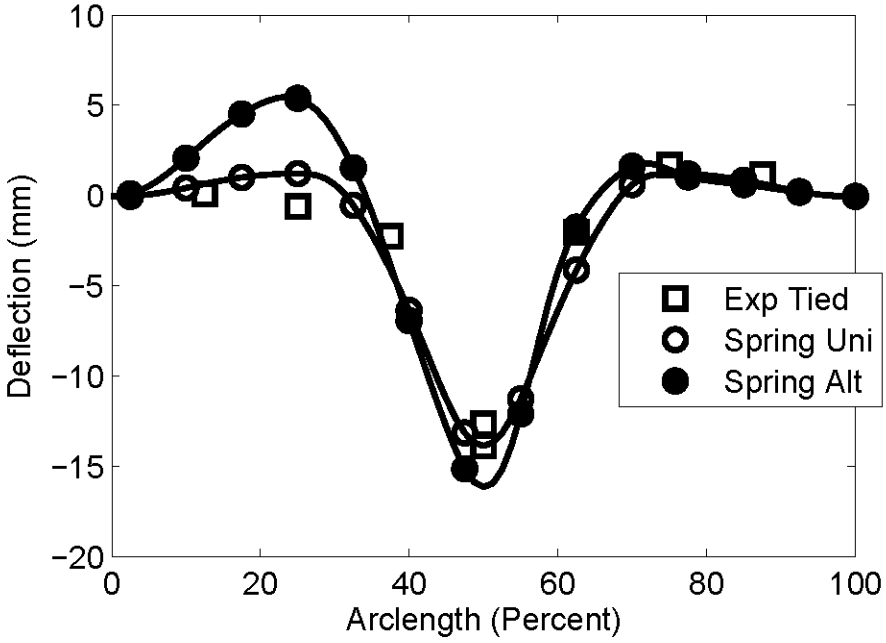

Figure 7.11. Tall CFFT Arch, Apex Live Load, Vertical Deflection

Also notice that the vertical deflections are closer to symmetric than the alternating model predicts, and the uniform lift model is almost exact for all gauge locations. The South measured deflections are negative (or close to zero), not more than double the North side deflections as predicted by the model alternating lift model. This may be directly attributable to measured pressure which indicates that instead of lifting upward the shoulders both experience vertical pressure increases on the order of 10 kPa, which is nearly half of the cover depth in the region. Added vertical restraint not considered by the model would limit vertical deflection. Horizontal deflection, shown in Figure 7.12, is predicted by the alternating lift model to have the proper shape (a peak at position 2, a gradual increase on the North side approaching the apex, but the alternating lift model predicts much larger magnitudes, particularly on the South side, where gauge deflections are predicted by greater than a 2:1 margin. The uniform model does not reflect the actual shape as well on the North side, but is much better at predicting the real magnitudes on the South side.

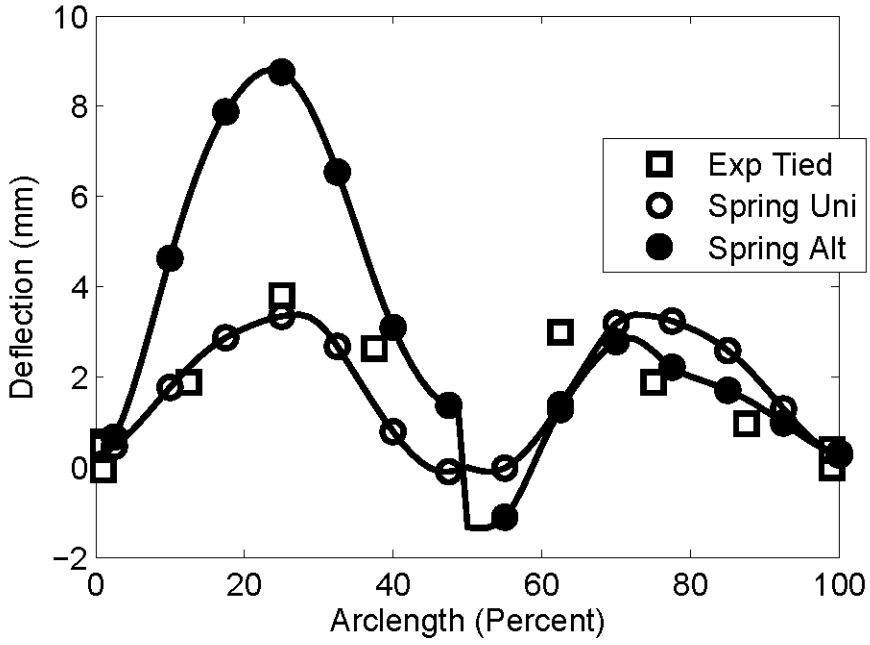

Figure 7.12. Tall CFFT Arch, Apex Live Load, Horizontal Deflection

Short CFFT top axis arch strains are well predicted by the model in Figure 7.13, and short CFFT bottom axis arch strains are well predicted in Figure 7.14. Notice that the top axis strains also have a much smaller magnitude than tall bridge results in Figure 7.8, and are therefore closer to the elastic region, where the moment-curvature relationship is better predicted. South foundation strains are overpredicted by the alternating lift model, but are well predicted by the uniform lift model and the measured foundation strains for both the North and South sides are nearly the same magnitude. Notice that there is considerable spread between the experimental foundation strains for individual arches: this is potentially a sign of different concrete cracking from prior loading. Notice that for the alternating lift model apex compression strains are overpredicted and apex tensile strains are underpredicted, each by approximately the same margin (meaning the curvature is very close to being correct). This suggests that axial compression is overpredicted by the model, as the section is in net greater tension than the model assumes. Apex curvature was overpredicted by the uniform lift model, but as both models predict similar responses, the apex curvature was still well predicted by the even lift model.

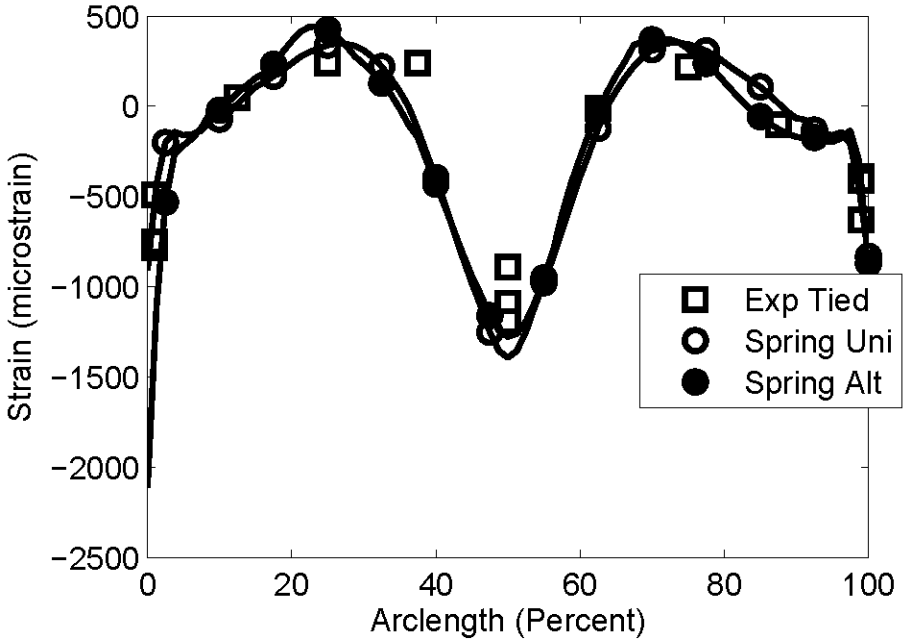

Figure 7.13. Short CFFT Arch, Apex Live Load, Top Strain

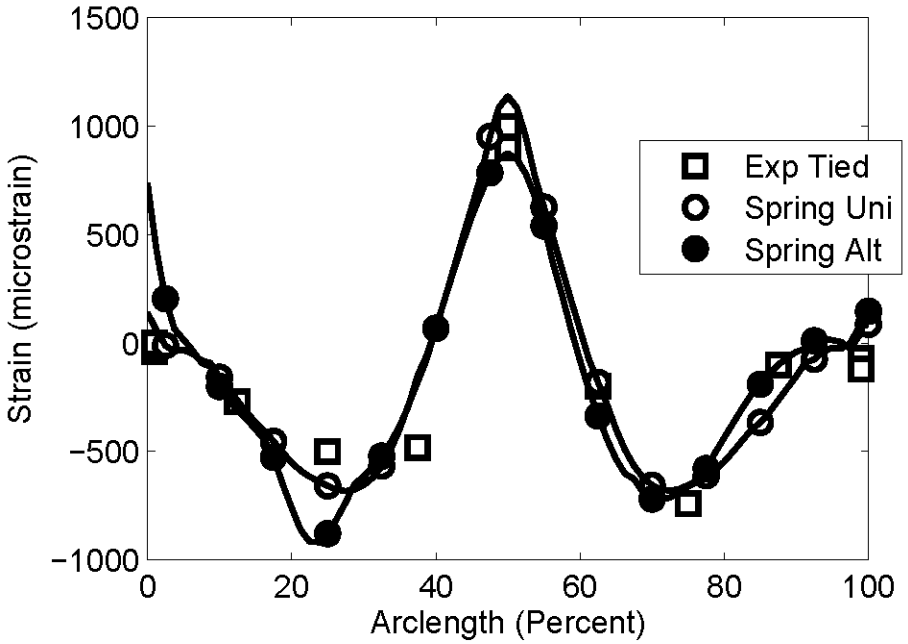

Figure 7.14. Short CFFT Arch, Apex Live Load, Bottom Strain

As anticipated by the quality of the apex strain prediction, the vertical deflection in Figure 7.15 is also well predicted by the models. The uniform lift model overpredicts the apex deflection, which is consistent with the overpredicted strains, but is superior for predicting the smaller deflections at the shoulders, which had a nearly symmetric response. Notice that, similar to Figure 7.11 for the tall bridge, the South side is predicted to have positive deflection near the shoulder of approximately 3 mm, but actual measurements indicate that the shoulder moves less than 1 mm. Likely, this is caused by a lack of modeled vertical restraint and passive soil arching as a result of the middle 25% of the bridge deflecting downward, but most likely it is due to the locked in deflections due to asymmetric backfill that were not correct for this structure..

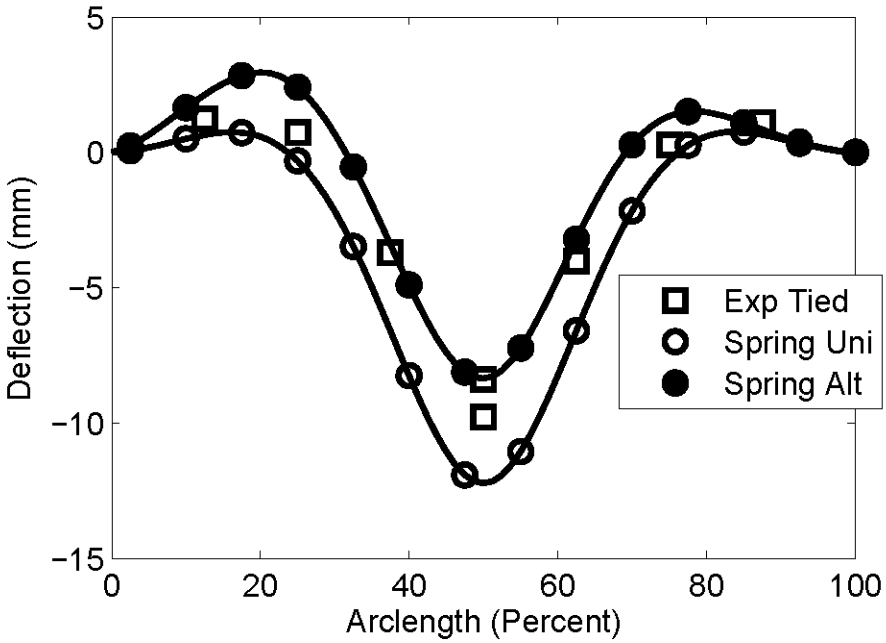

Figure 7.15. Short CFFT Arch, Apex Live Load, Vertical Deflection

Removal of soil cover should cause an increase in strain and displacement from a resulting load due to reduced load distribution. Standard testing is with 600 mm cover depth, but the short

CFFT arch system was also tested with a 300 mm cover depth and a smaller, 42 kN, live load due to concern over arch failure at the full 84 kN load used for other tests and a 450 mm cover depth tested to the same 84 kN live load as the full 600 mm cover depth bridges. The 450 mm cover depth bottom strain, Figure 7.16, response is also well-predicted by the alternating lift soil-spring model and both the experimental and modeled response is approximately 35% higher than the response for 600 mm of cover with the same load, implying an above linear strain difference relative to depth. Shallow cover, 300 mm, is not as well modeled: the experimental apex strain in Figure 7.17 is overpredicted by 38% by the alternating lift model. The uniform lift model overpredicts by 34%, but is a similar result. There are similar overpredictions in deflection and pressure, and the model's conservative result may have been caused by the added soil densification from previous loading applied with 600 mm of cover.

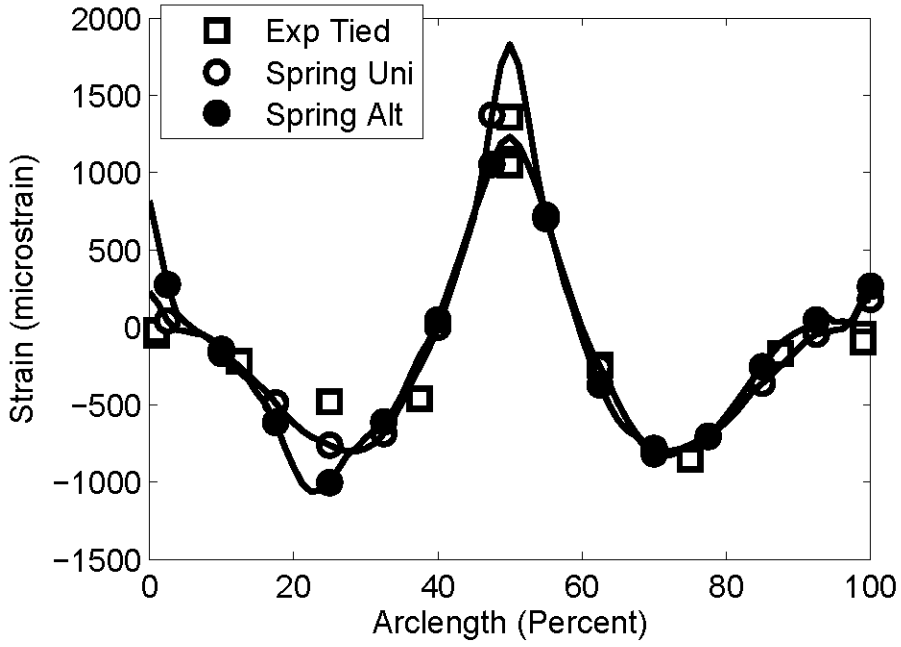

Figure 7.16. Short CFFT Arch, Apex Live Load, Bottom Strain, 450 mm Cover

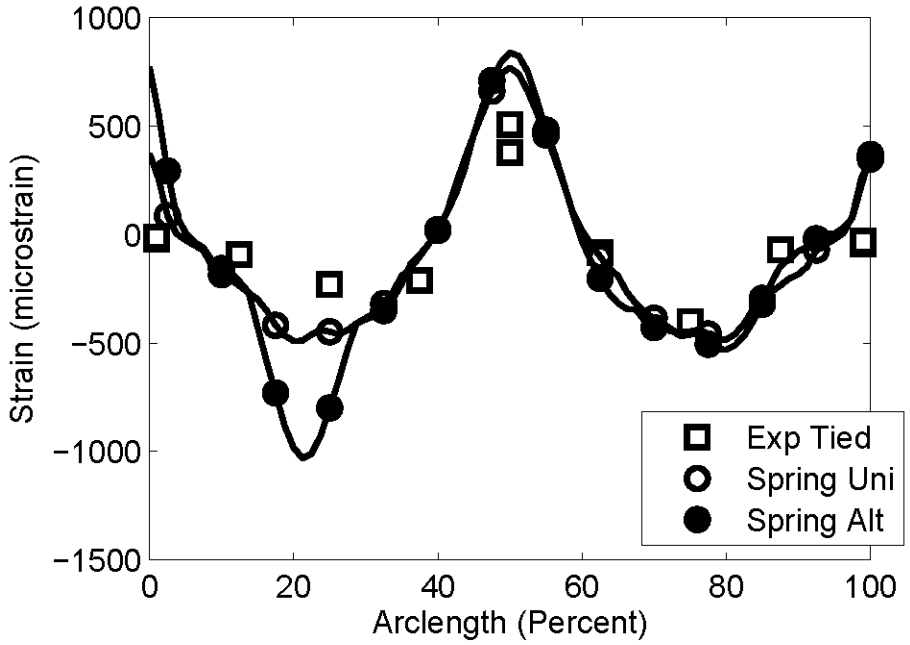

Figure 7.17. Short CFFT Arch, Apex Live Load, Bottom Strain, 450 mm Cover

7.3.2. 60% Offset Load

60% offset is the furthest offset load (from the apex) and induces side sway. Model and experimental results of steel and CFFT bridges indicates that this load has more effect on a short rise bridge than a tall rise bridge because the cover depth is 20% higher and the arch angle is 50% larger for the tall bridge, making the vertical forces smaller. This load is the controlling load case for a short rise bridge per steel results (Chapter 6), but a 40% offset controls taller bridge design. The live load moments are smaller for an offset load than an apex load, but the shoulder loads are additive with soil load moment and thus produce the worst-case design value; at the apex, live load moments oppose soil load moments.

For an offset load the model produces a less symmetric response for a CFFT arch bridge than for a steel bridge because the moment curvature relationship is outside the linear-elastic region during backfilling and each side of the arch has a different baseline cross-sectional stress state.

Figure 7.18 shows top strain for a 60% North offset load, tall bridge, and Figure 7.19 shows top strain for a 60% South offset, tall bridge. The experiment and the model show interesting apex strain results. The South side loading model indicates a higher apex strain, which is conservatively predicted, while the North side loading model is projected to be smaller, but is unconservative compared to the larger experimental strain. The apex strain difference is a direct effect of load sequence and using a non-hysteretic model that does not account for locked-in live load effects. 60% North offset follows apex load, which had locked in negative vertical apex deflection (compression on top). The South 60% offset load follows the North 60% offset load, and both loads produce positive vertical deflection at the apex. Because the soil around the apex is already locked into a similar stress state the strains in the arch are smaller. This is one example of how the experimental results and the decision to report step only strains rather than total strains can be misleading.

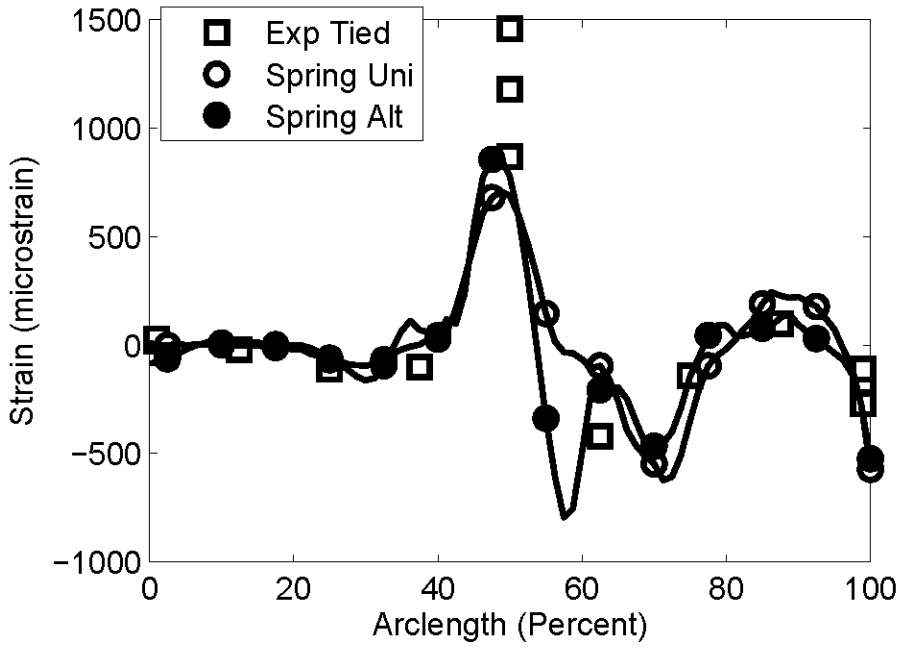

Figure 7.18. Tall CFFT Arch, 60% North Offset Load, Top Strain

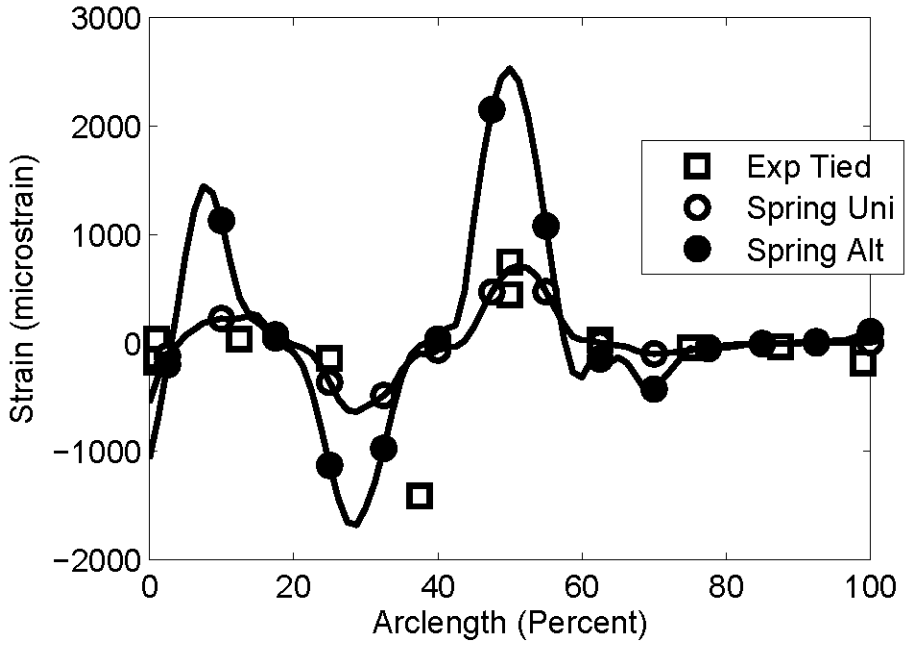

Figure 7.19. Tall CFFT Arch, 60% South Offset Load, Top Strain

The top total strain at the beginning of North 60% offset (caused by prior apex live loading and backfilling) is an average of 1810 microstrain below backfilling strain. North 60% offset locks in an average of 1150 microstrain, which makes the South 60% offset loading strain effect smaller. Total experimentally measured strain for North 60% offset is 1940 microstrain for the first load cycle and total strain for South 60% offset is 2570 microstrain for the first load cycle, which is more similar than indicated from plotted results, and is below the total strain predicted by the model of 4640 and 6400 microstrain, respectively.

The uniform lift model predicts a mirror image result for the North and South offset loads. This model fails to predict the large compression in gauge 3 top for a 60% North offset. This high measured strain was also a result of prior live load locked-in stress: in Figure 7.8, the tall CFFT bridge subject to apex loading, position 3 had a large top fiber tensile strain, which was

also not indicated by the model. The North 60% offset followed apex loading, thus the more locked-in strain from the prior test was easier to reverse than the model-assumed moment and axial strains at the start of this step.

The alternate lift model produces unrealistically asymmetric results with the CFFT arches and this may be most obvious with horizontal deflections. Figure 7.20 and Figure 7.21 are the tall CFFT horizontal deflections for a 60% offset load North and South respectively along the span of the arch. Notice that the experimental peak value (active loading side, either position 3 or 5) is approximately 4.5 mm for both load cases, and the peak deflection location disagrees with the model, which places peak deflection closer to points 2 and 6. The North offset load model predicts only 2.5 mm of negative deflection near position 5 and the South offset load model predicts approximately 6 mm of negative deflection at point 3. The average of the two model values is closer to the actual experimental values than either offset load model. This suggests that better live load results for CFFT arches may be obtained by running the model with uniform backfill lifts instead of staggering lifts below the apex. The uniform lift model underpredicts the peak horizontal deflection. The horizontal deflection at points 3 and 5 is underpredicted by the model for both 60% offset load cases. This may be a symptom of excessive horizontal soil stiffness near the apex.

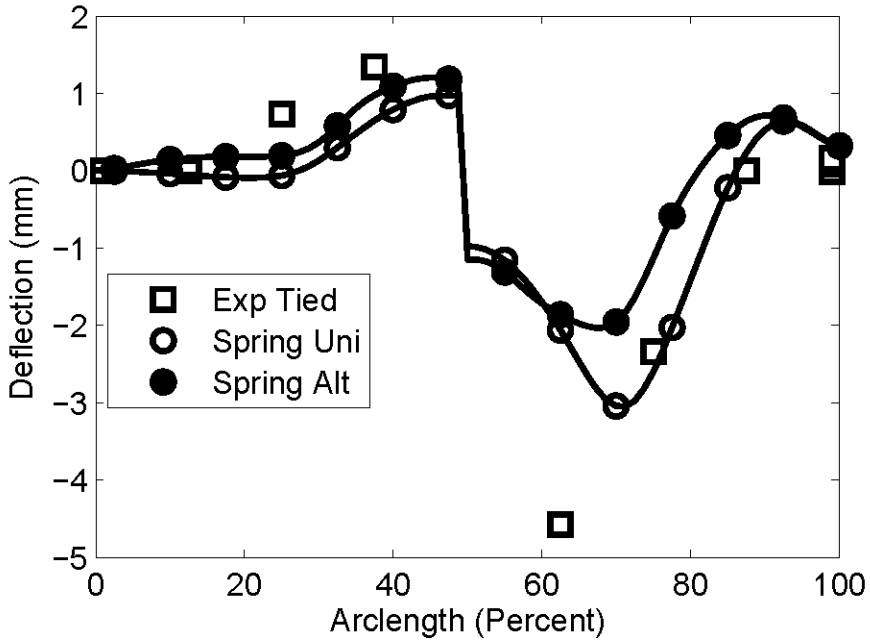

Figure 7.20. Tall CFFT Arch, 60% North Offset Load, Horizontal Deflection

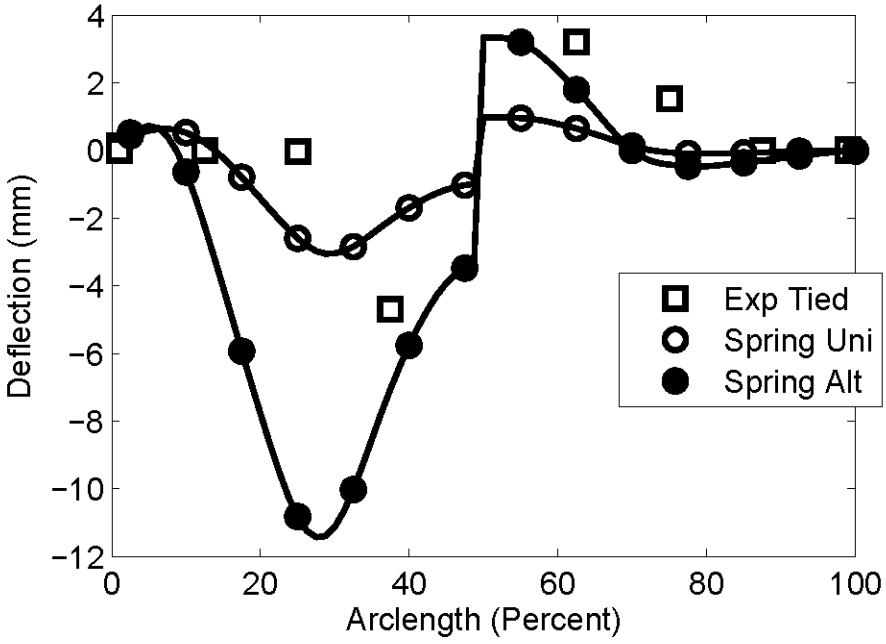

Figure 7.21. Tall CFFT Arch, 60% South Offset Load, Horizontal Deflection

The short CFFT bridge is problematic for comparing at this offset because the soil-spring model does not converge for the applied experimental load: the model predicts a hinge forming at the foundation on the side of load application. All model results in figures at this offset for the short bridge are for 80% of the applied load, and it becomes obvious that the model is not accurately capturing arch behavior. This is likely a combination of effects: an inaccurate soil restraint and an inaccurate representation of the stiffness of concrete in tension. The foundation moment caused by an offset load is predicted to be large and is the controlling load case, yet experimental values show a much smaller gain, as shown in the top strain diagrams in Figure 7.22 for North side loading and Figure 7.23 for South side loading.

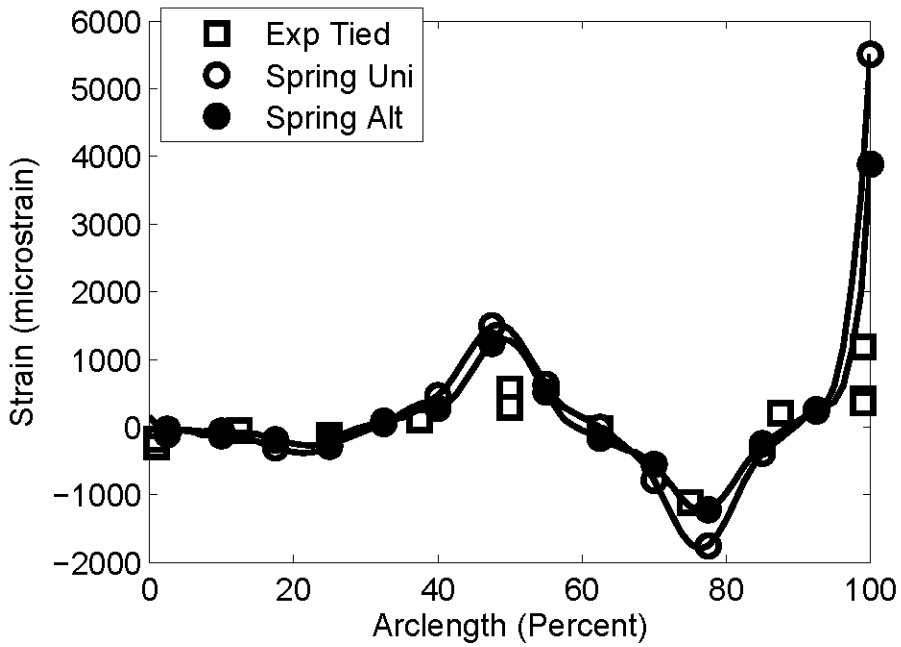

Figure 7.22. Short CFFT Arch, 60% North Offset Load, Top Strain

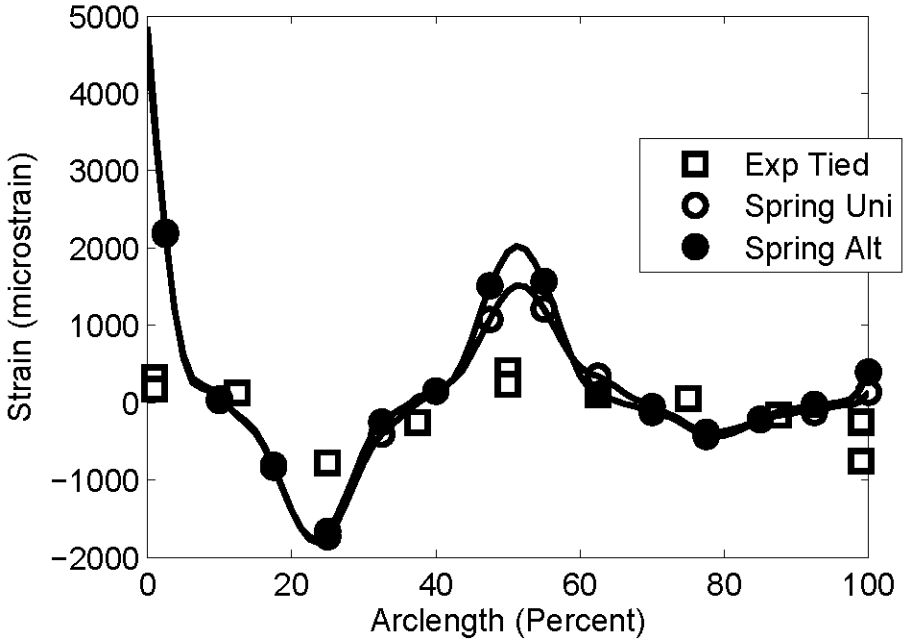

Figure 7.23. Short CFFT Arch, 60% South Offset Load, Top Strain

Also notice that the alternating lift model accurately predicts the North shoulder strain, which is a controlling load case. The South side loading overpredicts the strain by approximately a 2:1 ratio at the South shoulder. The uniform lift model predicts an 1800 microstrain strain at the North and South shoulder, which is conservative. The foundation strains on the loaded side are overpredicted by both models by a 10 to 1 margin. This is likely from two causes: primarily an overestimation of foundation moment (as was the case for the short offset steel bridge) and an overprediction of tensile strain as concrete cracks. Apex strains are also overpredicted by both models, which, when taken with the overpredicted foundation strains, is consistent with steel bridge results. The most likely cause of the large strains in both locations is driven by overestimating moment response due to inadequate vertical restraint. Figure 7.24 is the pressure from South 60% offset loading. The apex pressure and position 5 pressure are underpredicted by the model by about 4 to 7 kPa, or about one third or one half of the weight of the local

overburden weight. This in turn results in inaccurate apex deflection, which is overpredicted by the model, as shown in Figure 7.25. Another interesting feature of Figure 7.24 is that the vertical pressure above the point of load application is higher than predicted by the Bousinesq soil distribution, which is a consistent observation for most loads of this magnitude.

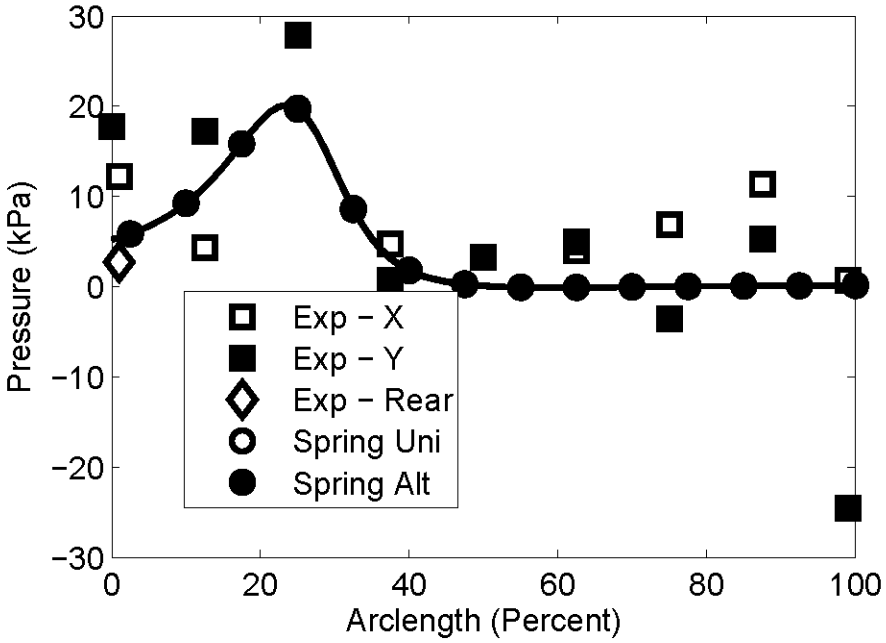

Figure 7.24. Short CFFT Arch, 60% South Offset Load, Pressure

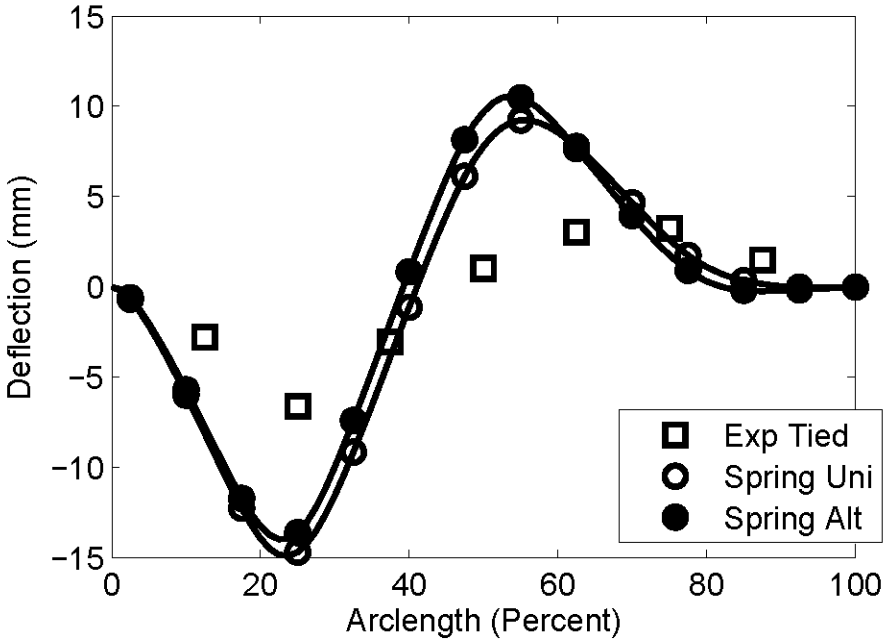

Figure 7.25. Short CFFT Arch, 60% South Offset Load, Vertical Deflection

7.3.3. 40% Offset Load

40% offset loading is the critical loading location for positive moment in a tall rise bridge: it adds the highest applied positive moments to the shoulder regions, which are the peak positive backfilling moments. The bottom strains for North 40% offset on the tall bridge are in Figure 7.26 and bottom strains for South 40% offset for the tall bridge are in Figure 7.27. The alternate lift model predicts a widely different response for both sides near the peak strain and predicts a peak strain that is 80% higher for the south loading case than the North loading case, or either experimental recorded maximum value. This is for identical applied vertical pressures and similar horizontal pressures for model loading cases. The model difference, which likely is not this severe in the actual structure, is caused by stress state differences in the moment curvature relationship as a result of alternating lift sides during backfilling. The uniform lift model does not exhibit strains of this magnitude and shows much better agreement with experimental results; it

exactly predicts the peak measured strain at position 3 or 5 depending on side of loading. The model does indicate that a 45% higher tensile strain is present about 5% of span closer to the footing than the peak gauge location. South loading for the uniform model predicts a larger negative response at the South shoulder (position 2) than measured by the experiment, but North side experimental loading response at the North shoulder (position 6) is close to the model response.

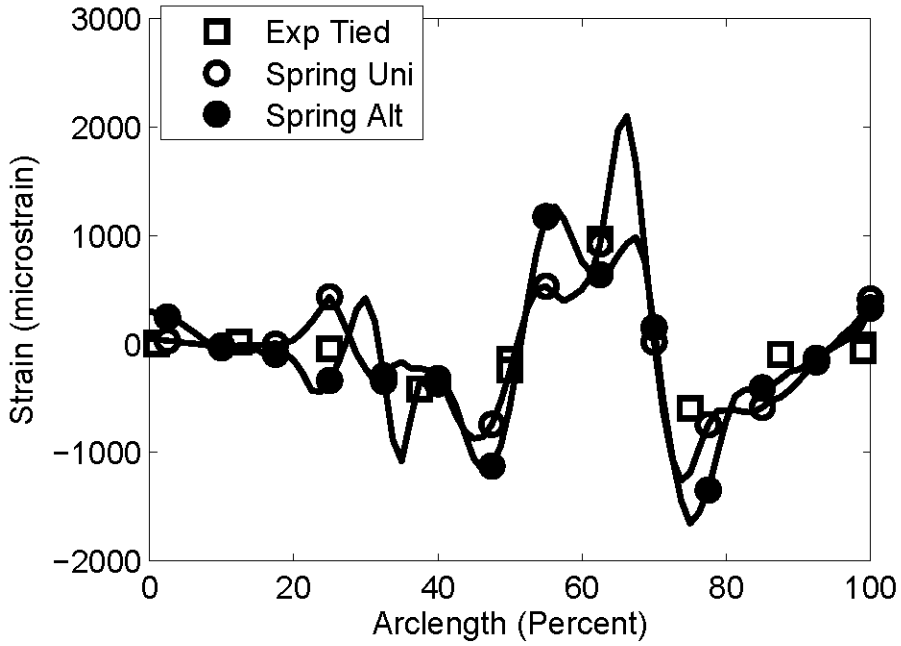

Figure 7.26. Tall CFFT Arch, 40% North Offset Load, Bottom Strain

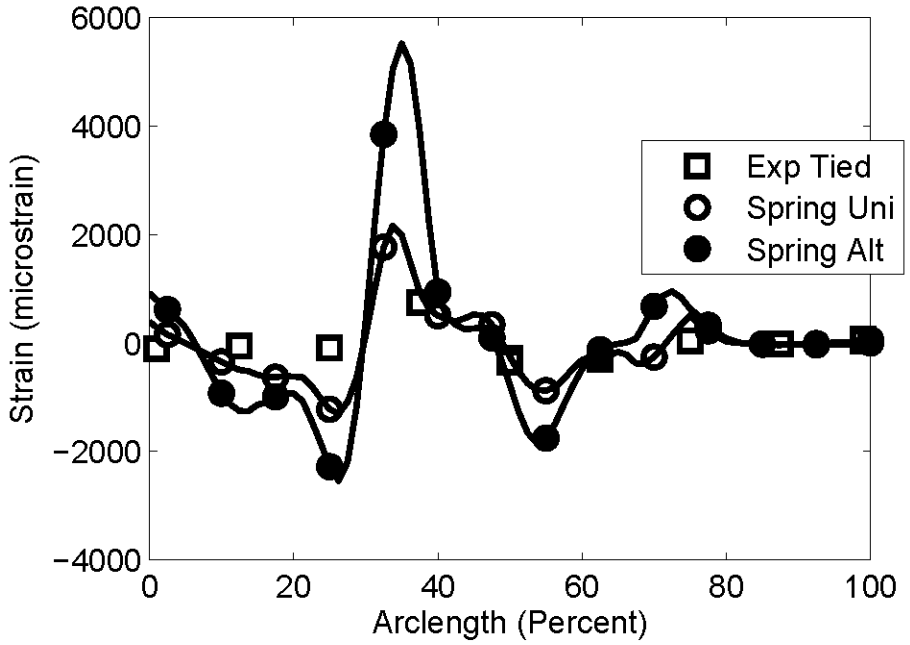

Figure 7.27. Tall CFFT Arch, 40% South Offset Load, Bottom Strain

The measured strain response for both 40% offset loading cases produces very similar peak moments for the uniform backfilling model (within 10%), but the extrapolated strains are very different (North peak strain is predicted to be more than 100% larger than the predicted South side strain). This further confirms the sensitivity of the model's response to moment curvature relationship. The South loading case is well represented, but the shape of the strain diagram is unexpected: there is no good reason for two peaks near the peak strain response instead of a single more rounded peak, and this trend was continued with the uniform loading model, thus it was likely a result of backfilling stored moments. To further investigate the odd strain response vertical deflections are plotted in Figure 7.28 for a North load and Figure 7.29 for a South load. Notice that the shape of the deflection diagram in Figure 7.28 and Figure 7.29 are both similar. Magnitude for the alternate lift model is considerably different side to side and this is not consistent with measured values, which indicate a nearly mirror response for the two 40% offset

load cases. Also, the uniform lift model vertical deflections are near experimental values at all measured locations for both offset loads.

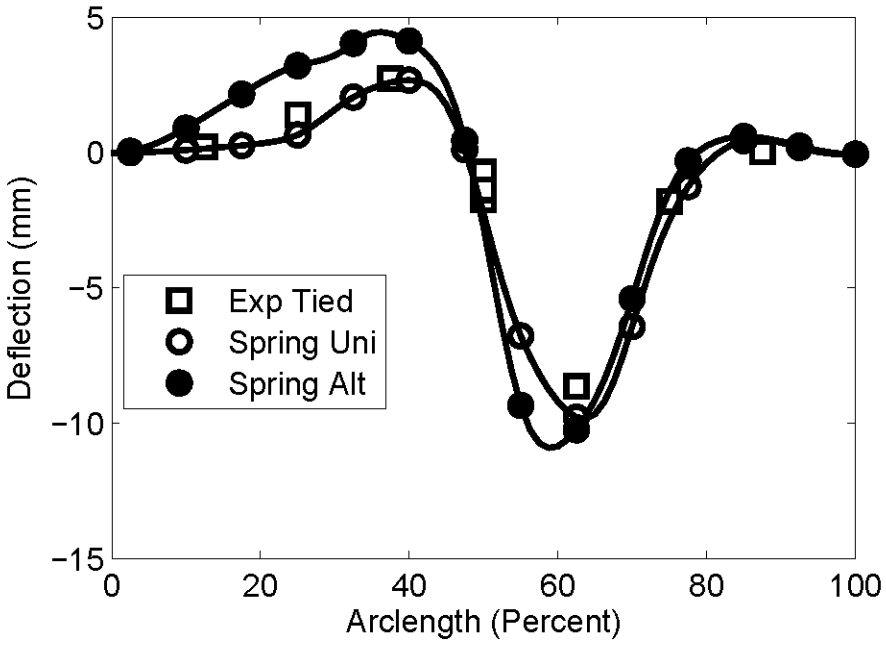

Figure 7.28. Tall CFFT Arch, 40% North Offset Load, Vertical Deflection

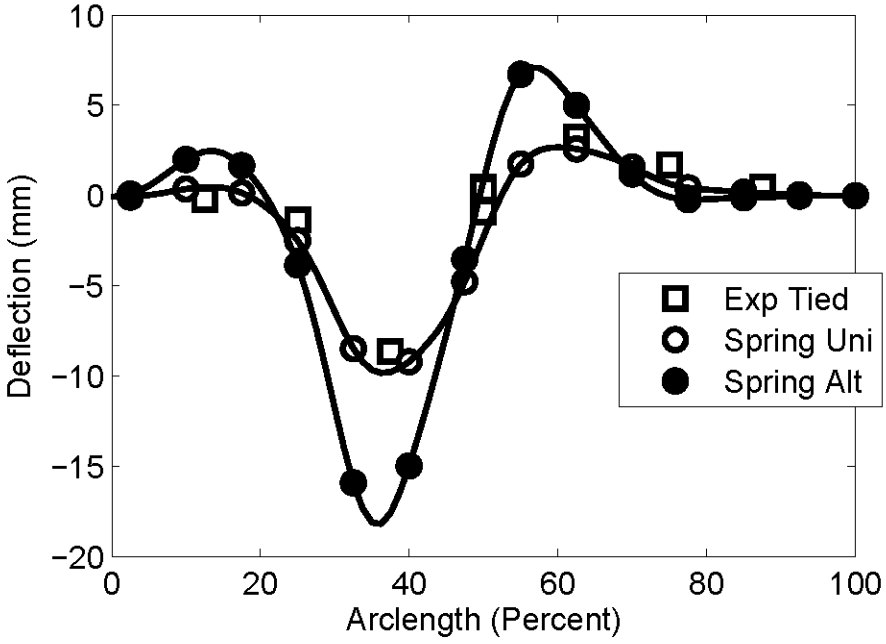

Figure 7.29. Tall CFFT Arch, 40% South Offset Load, Vertical Deflection

For a 40% offset load the short bridge comparisons are problematic again because the model is unable to converge due its prediction of a buckling failure. For this loading,a snap-through mode, not side sway, and is initiated near the point of load (where strains are high between gauge locations 5 and 6 for a North side load). Experimental bottom strain results are compared with the model for 80% of the applied load in Figure 7.30 and Figure 7.31. Peak strain is estimated to be approximately 5% of span closer to the foundation than the peak measured value, which also limits the value of comparison. The next recorded point (position 2 for South loading and position 6 for North loading) is overpredicted considerably by both models; thus it is unlikely that the peak strain predicted by the model is real. The elastic steel model predicts a maximum moment that is in the same location as peak strain for this loading case, so peak load effect region is consistent with different material properties. The uniform backfilling model accurately predicts peak positive measured strain. There is interesting disagreement between the strains in the models: the uniform model predicts higher North side strains than the alternate lift model, but is smaller for South side strains. This is not consistent with experimental results, which suggest higher peak strains for a South side load, as indicated by the alternating lift model.

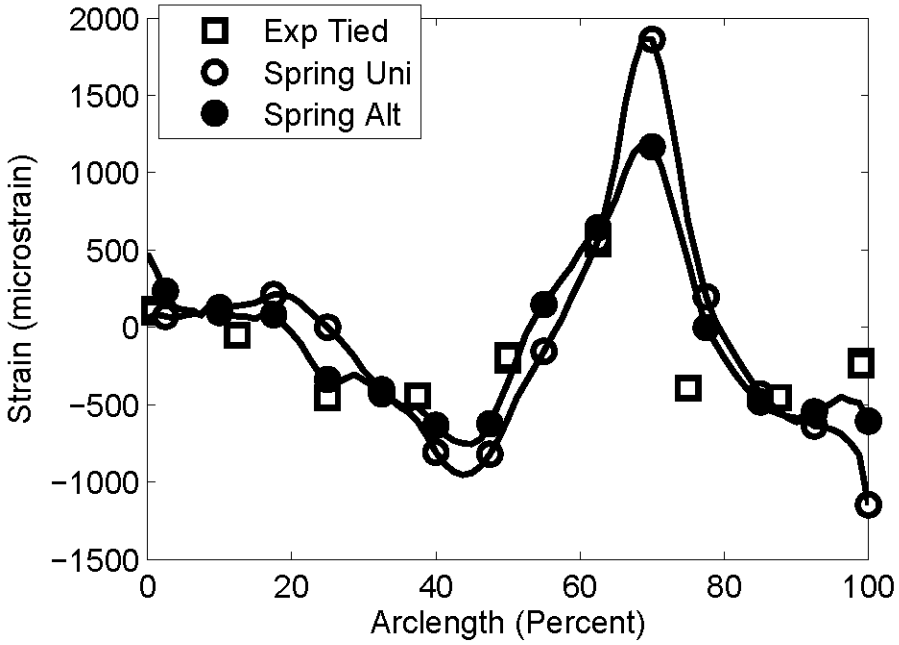

Figure 7.30. Short CFFT Arch, 40% North Offset Load, Bottom Strain

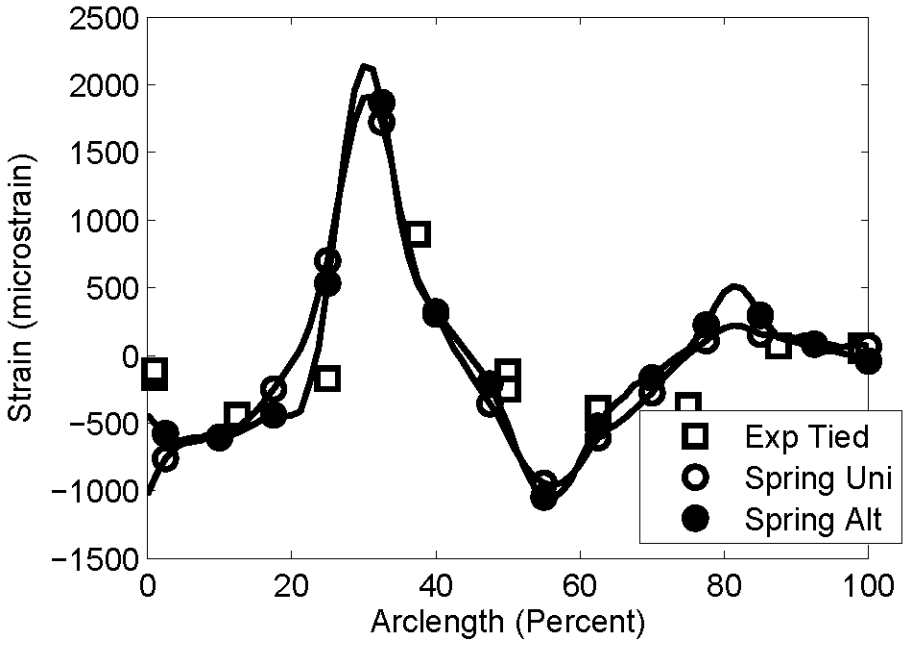

Figure 7.31. Short CFFT Arch, 40% South Offset Load, Bottom Strain

Strains are computed from moment and axial load, not from deflection. The axial load response is assumed elastic, which is inconsistent with the computed strains. This strain difference may be driving part of the difference between model and experimental results. This technique may be responsible for the unrealistic predicted strains. Figure 7.32 is the tall bridge measured and model predicted vertical deflections for a 40% North offset. The vertical deflection at the measured peak value (position 5) is well represented by the model. Also, as mentioned previously the measured strain at this point is well predicted by both models. The next position toward the foundation (position 6) is better predicted by the alternating lift model, which is consistent with the better strain prediction by the alternating lift model.

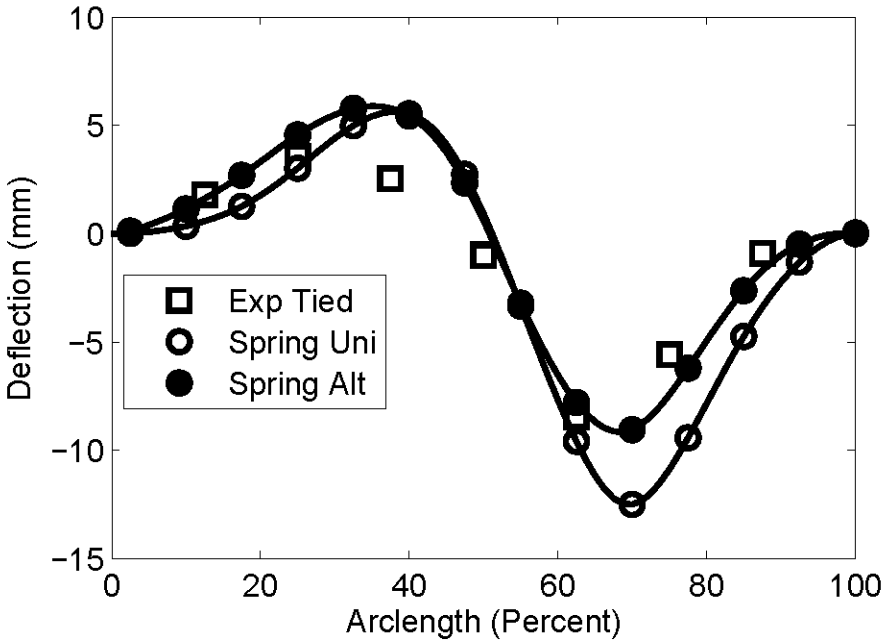

Figure 7.32. Short CFFT Arch, 40% North Offset Load, Vertical Deflection

7.3.4. 20% Offset Load

20% offset load response is similar to apex response. The outer offset loads drive the arch apex vertically upward, but a 20% offset drives the arch apex vertically downward. There may be no poorer alternating lift model response than South 20% offset load for the tall CFFT arch system. Figure 7.33Figure 7.34 is top strain and Figure 7.34 is bottom strain. Notice that the alternating lift model predicted strains are in excess of 5500 microstrain, which is very large, could threaten tensile rupture of the FRP shell when earlier strains are included, and is likely to cause compressive wrinkling of the shell on the top of the shell. Actual measured strains for this load case do not exceed 1000 microstrain, and are -260 and 70 at the point of peak predicted negative and positive strain.

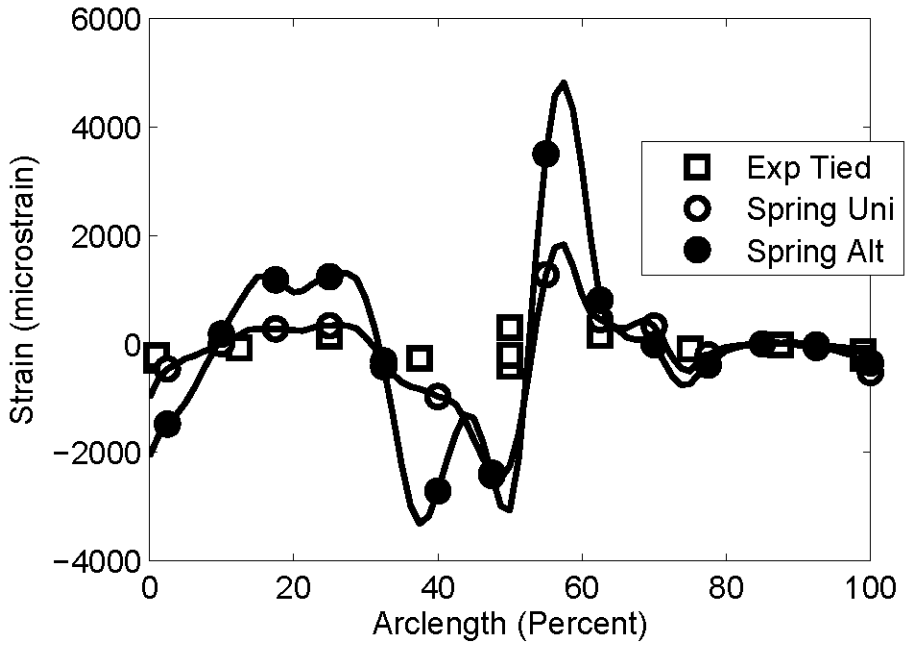

Figure 7.33. Tall CFFT Arch, 20% South Offset Load, Top Strain

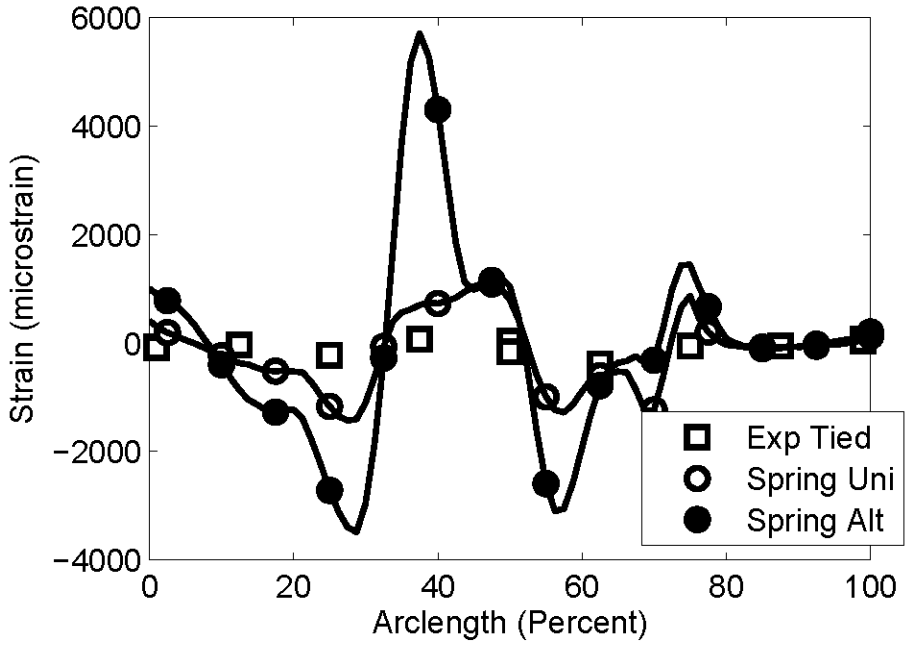

Figure 7.34. Tall CFFT Arch, 20% South Offset Load, Bottom Strain

South side load strains are overpredicted by the uniform lift model, but this model looks much better relative to the poor fit of the alternate lift model. Measured strains at point 3 are 70 microstrain tension on bottom and -260 microstrain compression on top, while the uniform model predicts approximately 800 microstrain tension and compression. Neither the measured or predicted strains for a uniform backfilling model control bridge design based on a 20% South offset, thus the 3 to 10 times overprediction at point 3 is not actually important. The nearly 100 times overprediction of strain in the alternating lift model is a problem, however, and shows the issues inherent with modeling CFFT arches.

North side loading top and bottom strains are displayed in Figure 7.35 and Figure 7.36. Model predictions have a much smaller response than South side loading, yet measured strain values are lower. In large part, this is due to load sequencing and stored strains from the prior analysis. The further offset loads, which precede the North load, push the apex upward, causing

stored tensile strain on top, compressive strain on bottom. North loading reverses this and therefore has a more compliant apex than South loading. The model does not store hysteretic effects and is unable to reflect this difference in experimental results. Both the alternating lift and uniform lift model could be appropriate for this response as no gauges were installed at the point of peak tensile response between the apex and position 5.

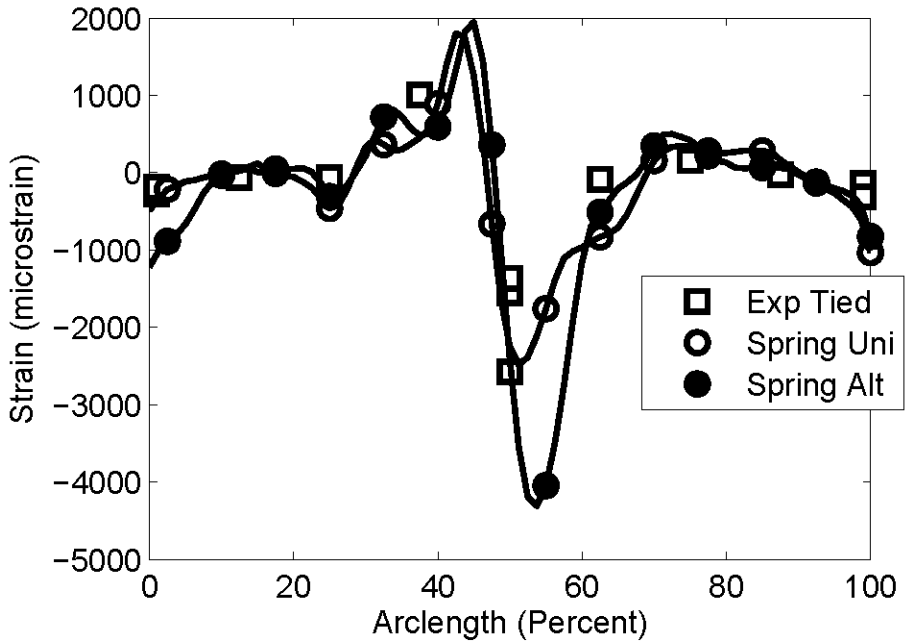

Figure 7.35. Tall CFFT Arch, 20% North Offset Load, Top Strain

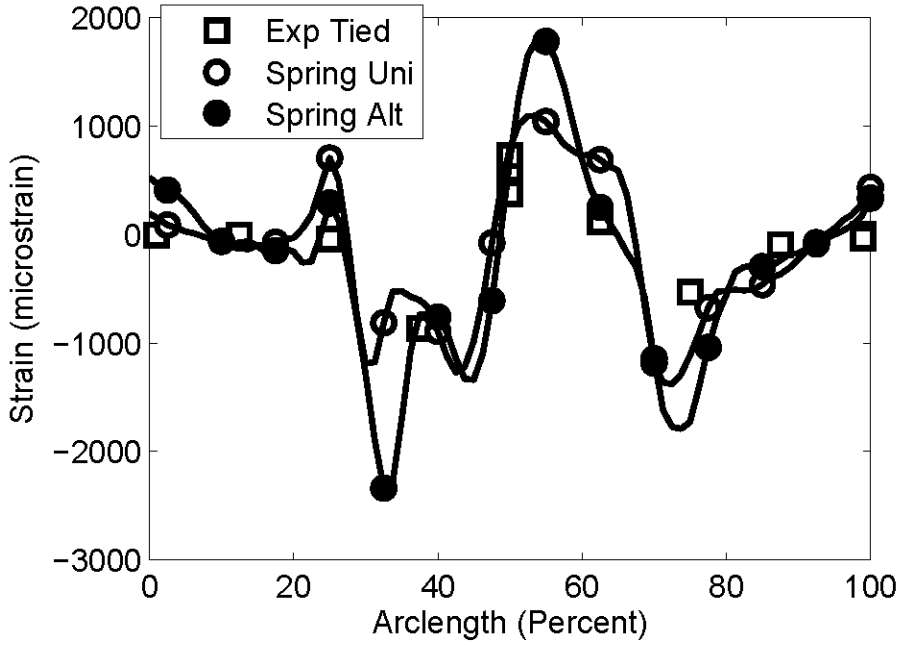

Figure 7.36. Tall CFFT Arch, 20% North Offset Load, Bottom Strain

Deflection for the tall rise South loading case is also overpredicted by the alternating lift model, as shown in Figure 7.37 (vertical) and Figure 7.38 (horizontal). Measured vertical deflections are small: peak deflection near the point of load application (position 3) is 7 mm, but the alternating lift model prediction is 24 mm and the uniform lift model predicts 12 mm of deflection. This helps explains the large difference in measured and predicted strain: there is less bending deformation, therefore less bending curvature, and less strain. The likely cause is the moment curvature relationship and the stress state imparted as a consequence of backfilling. Applied vertical pressures are approximately correct between model and experimental results (Figure 7.39), yet the deflection responses are different, which indicates that the arch is more than three times more flexible in bending than the experimental arch. This may be a combination of insufficient soil restraint and excessive arch flexibility. Measured horizontal deflection is nearly zero at all locations, indicating that soil restraint is part of the issue.

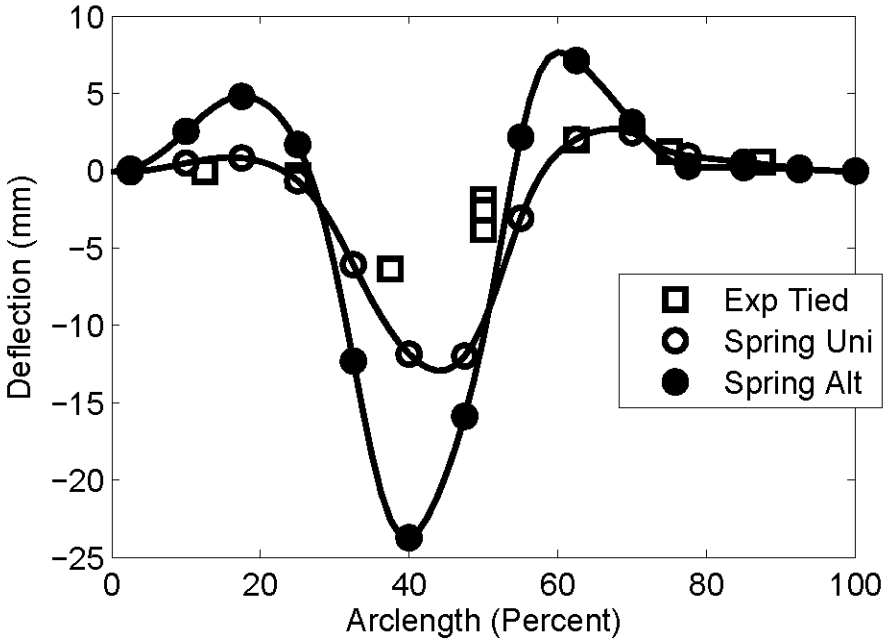

Figure 7.37. Tall CFFT Arch, 20% South Offset Load, Vertical Deflection

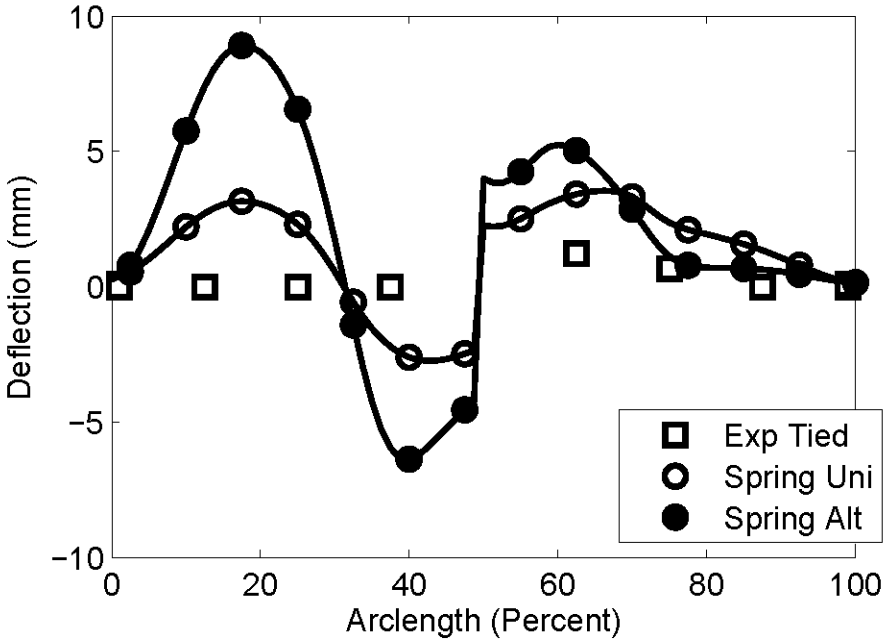

Figure 7.38. Tall CFFT Arch, 20% South Offset Load, Horizontal Deflection

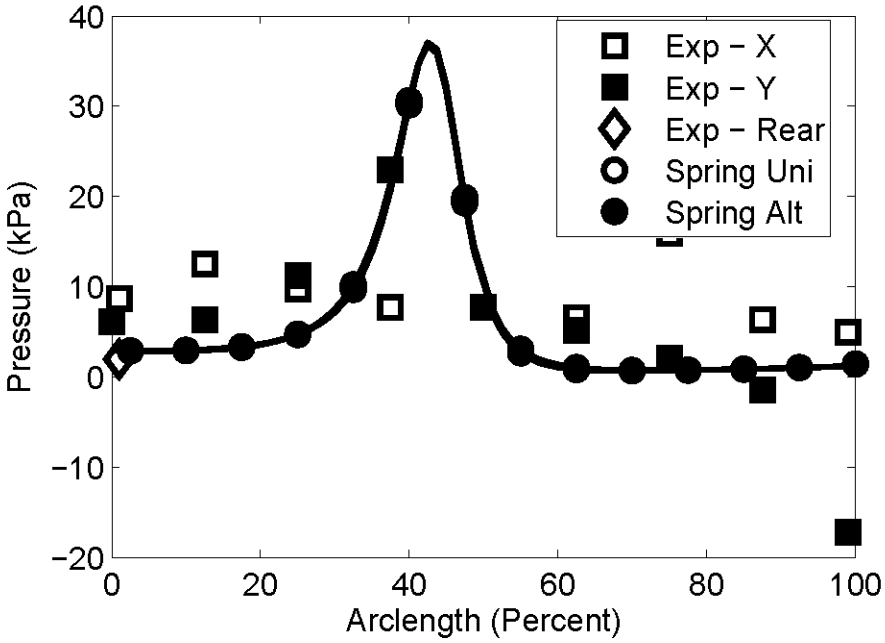

Figure 7.39. Tall CFFT Arch, 20% South Offset Load, Pressure

Unlike the tall rise arches, the short rise CFFT arch strains are well predicted by the alternating lift model for a 20% offset load, particularly a North offset load in Figure 7.40 and Figure 7.41. The peak strains are well represented by the model and even strains at other locations are reasonably representative. The South loading strains in Figure 7.42 and Figure 7.43 are not as well predicted. As has been common with other offset loads the South load peak strains are overpredicted by the model. The real measured strains are closer to the North strains, indicating that a uniform lift model may provide a better analysis for subsequent live load application. For the purposes of this study, earlier live load has a larger enduring effect than backfilling history; South response is generally smaller than North response. Uniform lift model response is better for South side loading, but worse for North side loading.

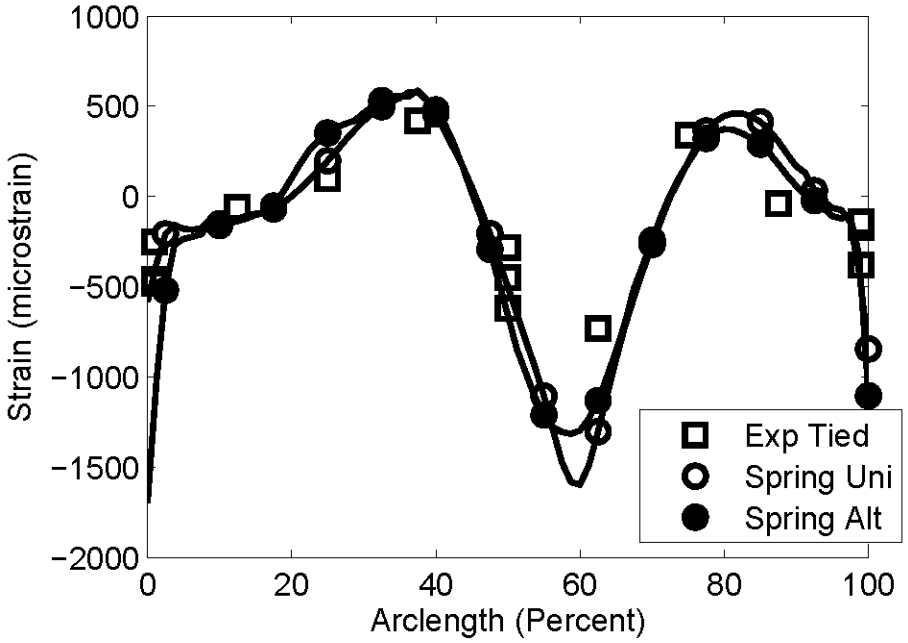

Figure 7.40. Short CFFT Arch, 20% North Offset Load, Top Strain

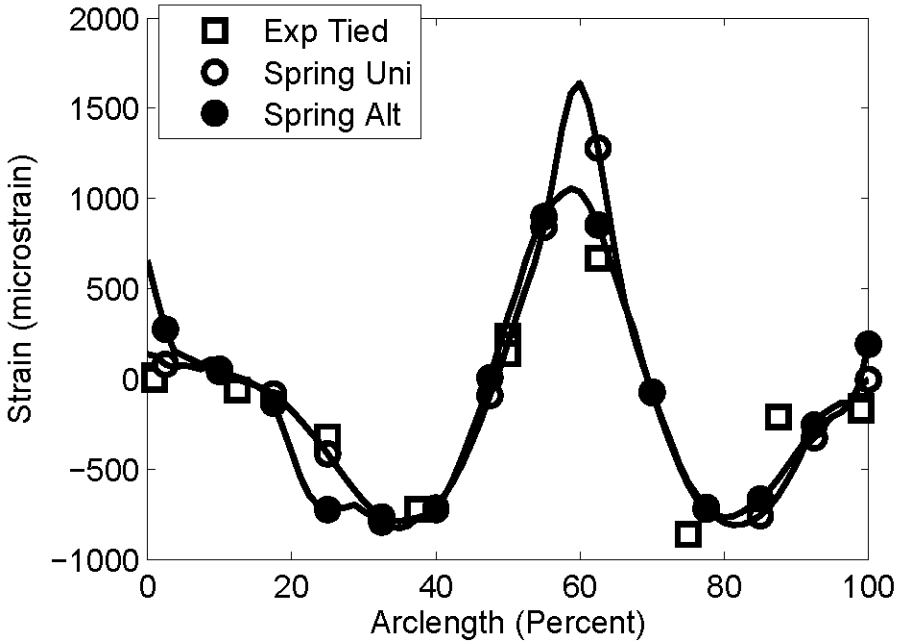

Figure 7.41. Short CFFT Arch, 20% North Offset Load, Bottom Strain

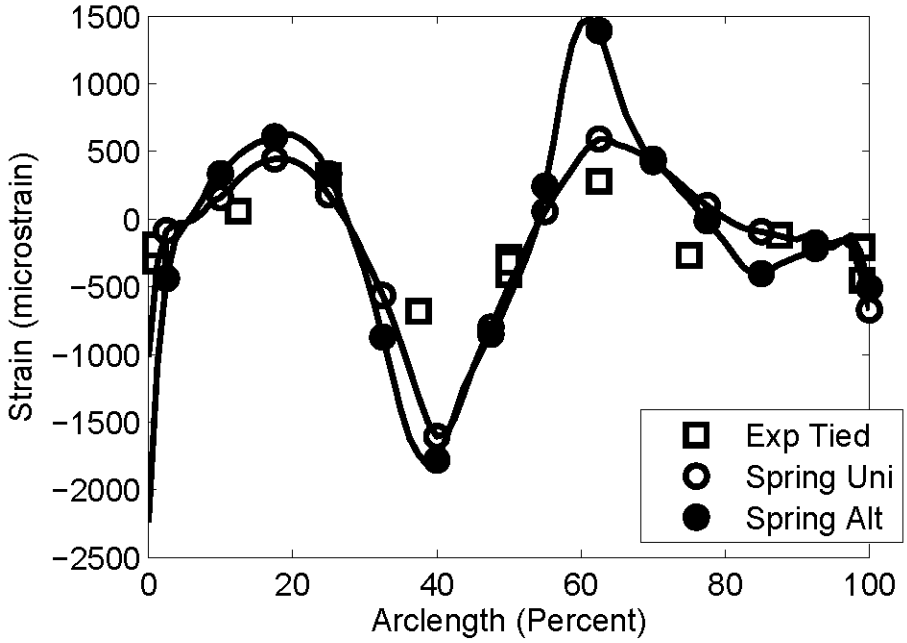

Figure 7.42. Short CFFT Arch, 20% South Offset Load, Top Strain

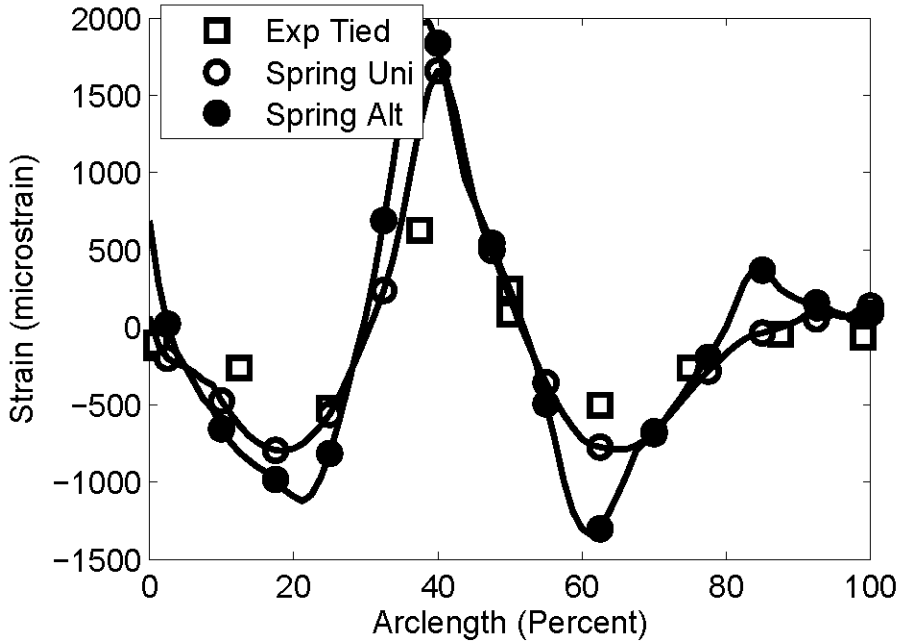

Figure 7.43. Short CFFT Arch, 20% South Offset Load, Bottom Strain

A trend for short CFFT arches is that the North side load alternate lift model response is better than the South side load response for the alternate lift model. The South side has a higher soil elevation when the lifts are not even, which creates greater deflection, moment, and horizontal soil stress on the South side of the arch. South side strains are overpredicted by the alternating lift model, a sign that the horizontal load effects during backfilling are too large. A possible solution would be to reduce the horizontal pressure coefficient which should decrease load effects and make a response closer to a uniform backfilling model.

7.4. Ultimate Load Response

The tall and short rise CFFT arches were both loaded in the same manner: an apex deflection controlled load applied to a wooden distribution pad to prevent soil bearing failure, which is described in more detail in Chapter 3. Ultimate load followed the full live load sequence, thus the arches were in a different configuration than at the end of backfilling. Specifically, ultimate load followed apex reloading with loose foundations, and this would tend to lock in soil stresses, resulting in smaller measured values of arch strain and deflection in the beginning of ultimate load, as was observed with the steel arches in Chapter 6.

Arch failure occurred at the apex and both bridges remained stable after the tensile rupture of the first (middle) arch. Apex bottom axis (tensile) strain is in Figure 7.44 for the tall bridge and Figure 7.45 for the short bridge with arch tensile rupture noted on the graph. For the tall bridge initial arch rupture occurred at a 201 kN load and a measured strain of only 0.3%, about 20% to 30% of the expected rupture strain (note that the failure occurred about 100 mm from the gauge and strains were likely higher at the failure location). After first arch failure the bridge continued to support additional load and achieved a peak capacity of 265 kN. Peak load occurred as the

central arch ruptured between the apex and the shoulder, after all three arches ruptured at the apex. The short bridge had a smaller spread between first rupture and ultimate load. First rupture of the middle arch occurred at 196 kN, and ultimate load was 200 kN. The bridge became unstable after the East arch ruptured; the west arch did not fail. Note that the East arch ruptured at a higher strain than the middle arch and deflection and strain were higher for the east arch than the west arch.

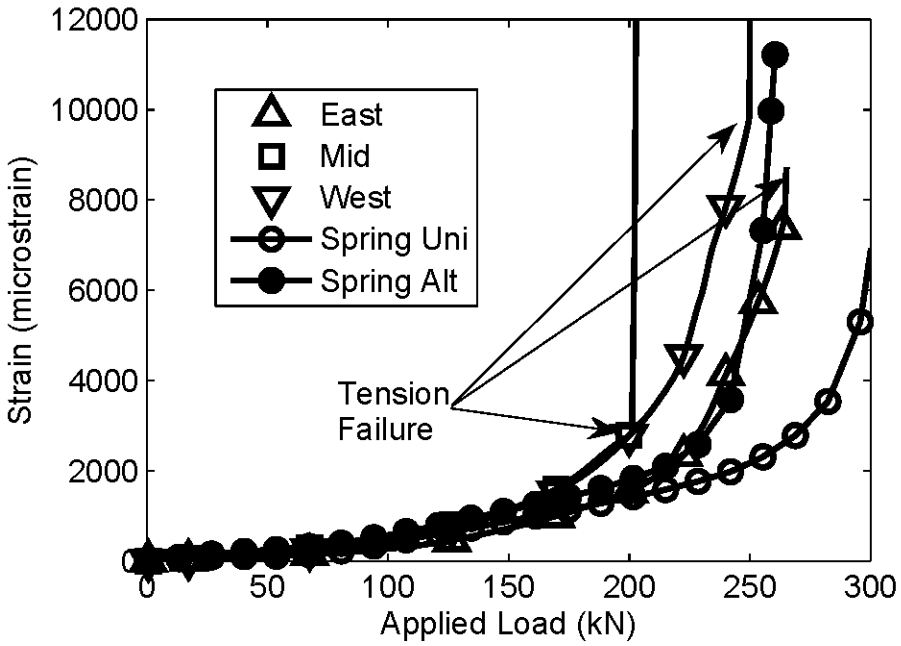

Figure 7.44. Tall CFFT Arch, Ultimate Load, Apex Bottom Strain

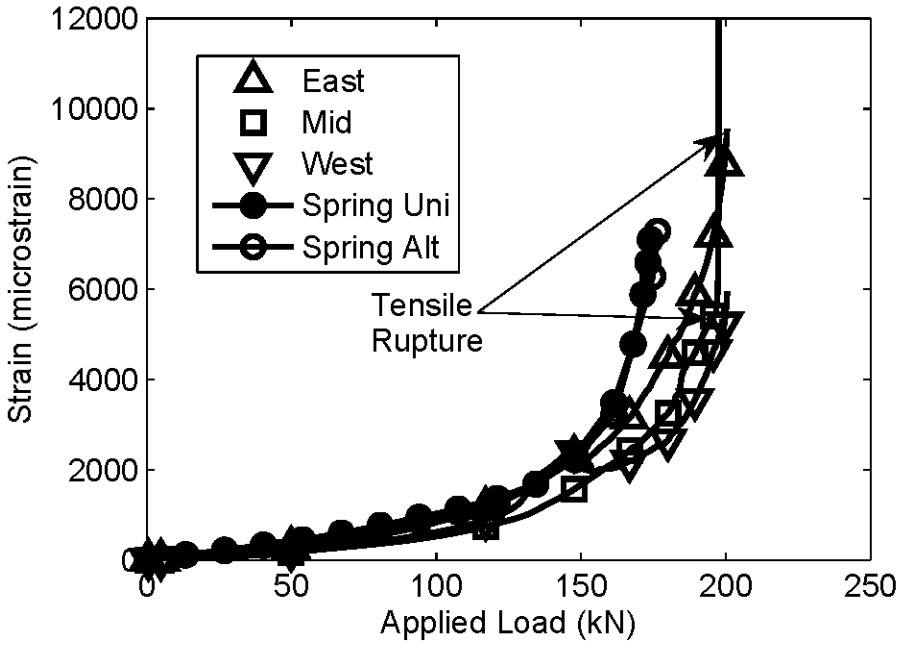

Figure 7.45. Short CFFT Arch, Ultimate Load, Apex Bottom Strain

A single isolated CFFT arch of both bridge geometries was tested to get a control value on strength. The isolated, fixed base arch test is described in detail in Chapter 3. Experimentally, the tall arch failed at an apex load of 12.1 kN and the short arch failed at an apex load of 15.4 kN. A large deformation corotational beam model was used to estimate the capacity of isolated arches using a moment curvature relationship tuned to mimic isolated arch apex deflection, as described in Chapter 3. The predicted failure load assuming a 1% tensile strain to failure (as indicated by experimental rupture of these arches) was 11.6 kN for the tall bridge and 16.1 kN for the short bridge. Both model estimates are within 5% of the experimental capacity. If the capacity of a single arch were extended to a three arch system the capacity for a bridge would be 36.3 kN for the tall bridge and 46.2 kN for the short bridge assuming no benefit from the soil. The tall bridge with soil achieved 5.5 times more live load capacity and the short bridge achieved 4.2 times

more live load capacity before first arch failure than three isolated arches with perfect load sharing.

For isolated arches the moment curvature relationship overpredicts the compressive strain at failure by 40% for both bridges: apex measured compressive strain was 0.29% for tall rise, 0.35% for short rise and model prediction was 0.41% for tall rise and 0.50% for short rise. This indicates that the model predicts more concrete cracking (a more flexible section) than experimentally observed for this cross section. This is consistent with experimental and model backfilling results for the tall bridge where the alternating lift model predicted more cracking, greater variation in strains and displacement side-to-side, and higher strains than experimentally observed.

Apex top strain is compressive, and is shown in Figure 7.46 for the tall CFFT arch and Figure 7.47 for the short CFFT arch. The model overestimates the compressive strain of the CFFT arches early in the ultimate loading process. This is more pronounced for the short bridge where the model also underestimates capacity. Likely, this was caused by an overprediction of the crack depth (higher tensile concrete strength results in stiffer arch response and lower compressive strain). As the experimental arches crack the difference between model and experimental results becomes less distinguishable.

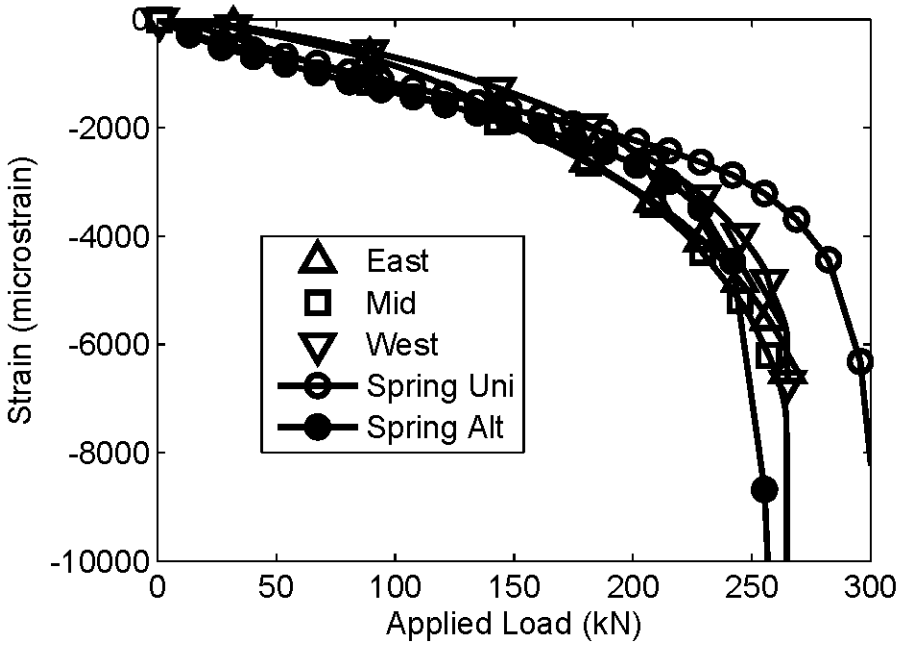

Figure 7.46. Tall CFFT Arch, Ultimate Load, Apex Top Strain

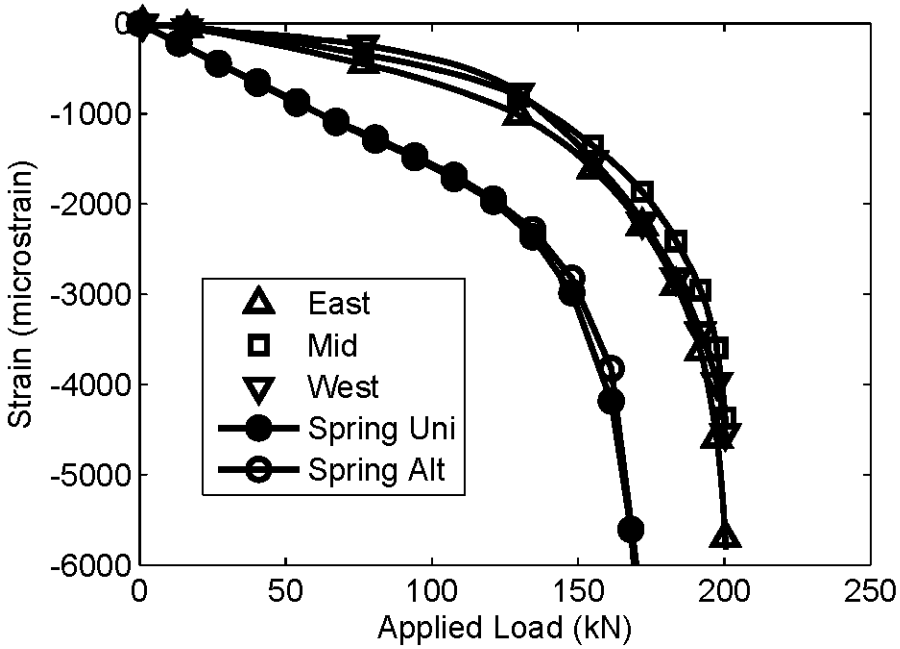

Figure 7.47. Short CFFT Arch, Ultimate Load, Apex Top Strain

Model predicted ultimate capacity for the Short bridge was 174 kN with uniform soil load and 176 kN with alternating soil lifts, nearly no difference between the two model types. These failure loads were 14% below the experimental ultimate capacity which is nearly the same amount of underprediction as the steel short bridge in Chapter 6. Model predicted capacity for the tall bridge was 260 kN with alternating soil lifts and 303 kN with uniform soil lifts, which is a significant difference between the two model types. The alternating lift model underpredicted the capacity by 2%, nearly an exact solution. The uniform lift model overpredicted the capacity by 13%, and is the only model to overpredict ultimate capacity. It is possible that the accurate prediction of the alternate lift model is a fortunate result and does not reflect more accurate modeling practice. The alternating lift model produced larger strains than expected throughout the live load sequence, which makes it seem fortuitous that the capacity during ultimate load is correct. Also, the ultimate apex strain for the middle arch was substantially lower than expected: the central arch failed at 20% of the expected failure strain, which indicates that there was prior damage to the middle arch apex and a stronger middle arch would have allowed greater bridge capacity.

Apex deflection is initially overpredicted by the model, supporting the theory that the model assumes greater concrete cracking than experimentally observed in Figure 7.48 and Figure 7.49. Also, the deflection difference is affected by the live load sequence. Earlier live loads experimentally change the deflected position of the arches, and lower the apex relative to the end of backfill position. The model predicts a similar deflection at ultimate load, however this is caused by the model predicting a smaller change in deflection 200 kN to 250 kN for the tall CFFT arches. While the model predicts a more compliant arch as load increases, the model does not predict individual arches failing and forming hinges, which results in a more compliant

structure. The short bridge deflections are better predicted by the model, possibly because the end of backfilling deflection is closer to zero for the short bridge. The deflection at model predicted peak load for the short bridge is accurate, but the experimental bridge has higher capacity and deflection continues to increase as load increases. This may be caused by apex pressure prediction issues in the model.

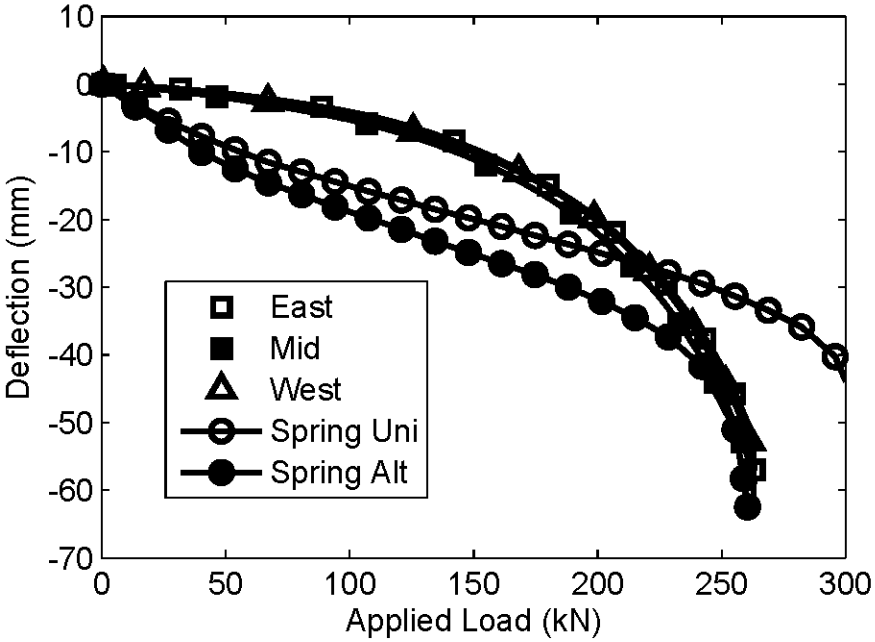

Figure 7.48. Tall CFFT Arch, Ultimate Load, Apex Deflection

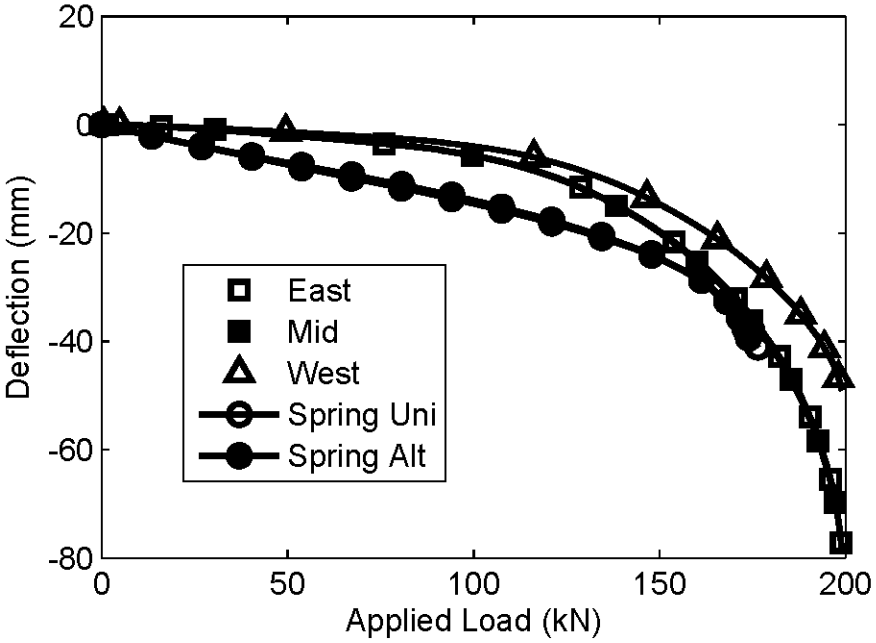

Figure 7.49. Short CFFT Arch, Ultimate Load, Apex Deflection

Apex vertical soil pressure is very different for both the tall and short bridge, shown in Figure 7.50. The tall bridge has nearly a linear relationship with load until directly near failure while the short bridge rapidly loses pressure after 120 kN and reaches zero pressure from live load. The difference in pressure may indicate part of the reason why the load is underpredicted for the short bridge and overpredicted for the tall bridge. The model predicted apex pressure (not shown) is linear with load and follows the initial slope of the short CFFT bridge apex pressure response. The tall bridge experimentally had a more concentrated load than assumed by the model, hence it failed at a lower load than assumed by the model .The short bridge had a higher model pressure than experimentally measured near peak load, because soil arching was important for this arch geometry, and the experimental capacity was higher than model predicted.

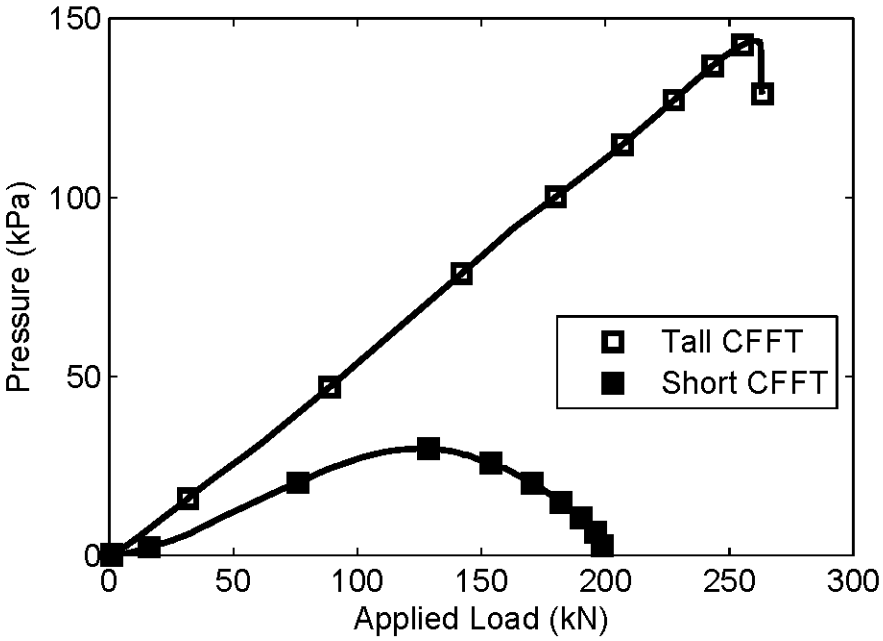

Figure 7.50. CFFT Arches, Ultimate Load, Apex Pressure

Despite a symmetric loading case the arches do not behave symmetrically, and this is apparent while looking at foundation pressures and deflections. As described in Chapter 3, on test construction, the South end wall is post-tensioned concrete and is rigid compared to the anticipated loads. The North wall is made from timber sheathing with steel H-pile soldier beams and is self-reacting with the South wall, tied with (6) 19 mm diameter cables. Thus it is able to move more. During ultimate load testing, soil box end wall construction differences are apparent when comparing side to side foundation deflection and pressure shown in Figure 7.51, Figure 7.52, Figure 7.53, and Figure 7.54 for the tall CFFT bridge. For the tall CFFT bridge the top foundation displacement (38 mm below the top of foundation) on the North side reaches an average of 5.2 mm deflection, the South side reaches an average of 2.3 mm deflection. Foundation base deflections on both sides are below 1 mm on average and indicate that base sliding was negligible for both foundations. Therefore, displacement primarily resulted in

foundation rotation. Horizontal pressure behind each foundation was nearly the same despite larger North side deflection: 20.3 kPa on the South end and 19.6 kPa on the North end, indicating that soil had a stiffer response on the South end. Vertical pressure response was different for both foundations. North foundation vertical pressures are much lower than South foundation pressures indicating substantial rotation away from the soil over the heel of the foundation.

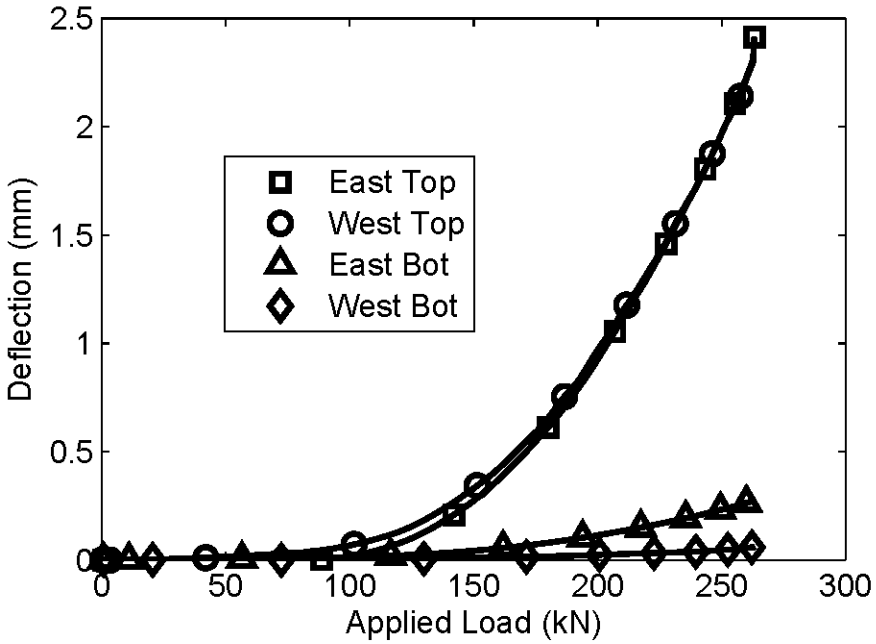

Figure 7.51. Tall CFFT Arch, Ultimate Load, South Foundation Deflection

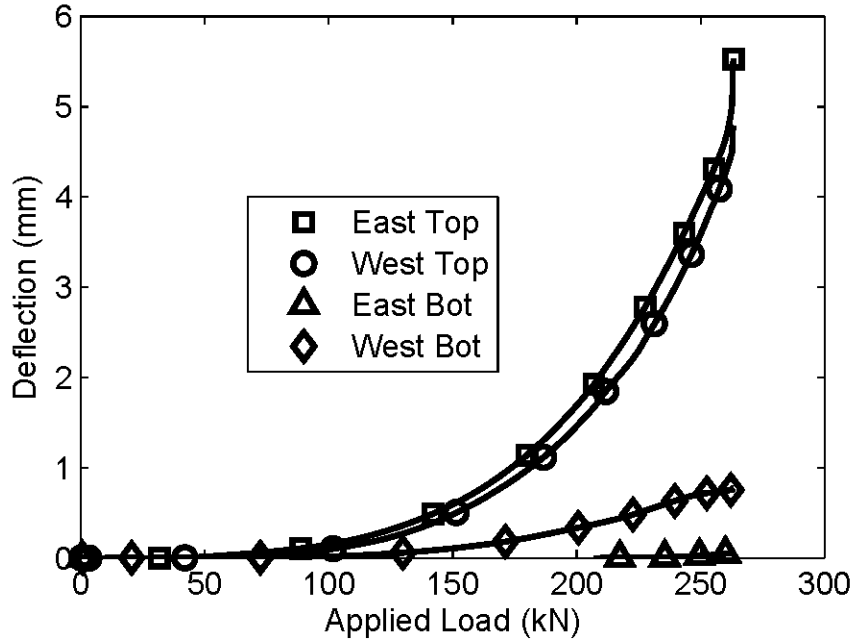

Figure 7.52. Tall CFFT Arch, Ultimate Load, North Foundation Deflection

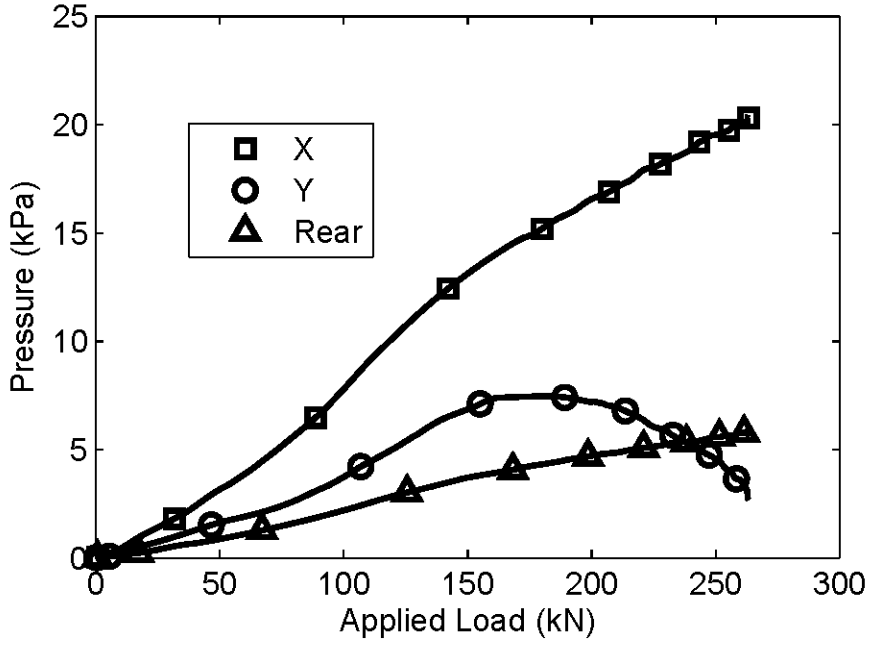

Figure 7.53. Tall CFFT Arch, Ultimate Load, South Foundation Pressure

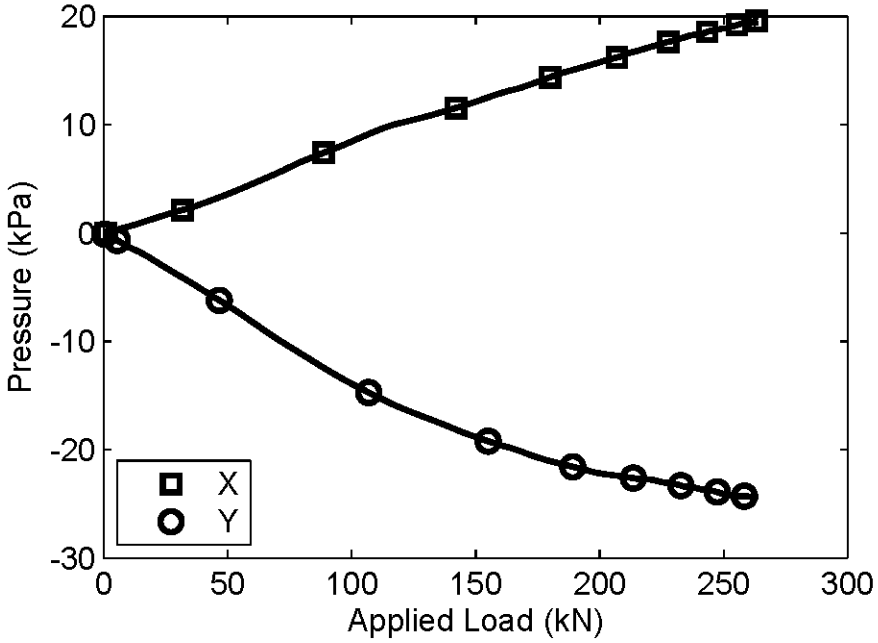

Figure 7.54. Tall CFFT Arch, Ultimate Load, North Foundation Pressure

7.5. Conclusions

Two CFFT buried arch bridge systems were constructed and tested under controlled laboratory conditions. Bridges were backfilled with soil, subjected to a series of live loads over the middle 60% of the span, and tested to failure with an apex load. This Chapter compared experimental results with a soil-spring model. The soil spring model was implemented assuming both uniform backfilling and alternate side backfilling, as used in bridge construction. Backfilling introduces locked in displacements and stresses that affect all subsequent responses. Significant results from this chapter are presented below:

- The moment-curvature relationship overpredicts compressive strain in isolated arches by 40% and overpredicts the compressive strain in buried structures. This indicates

that arches are less cracked and stiffer than predicted by the model. It also indicates that strains taken from the model for comparison with experimental results must be viewed with skepticism.

- The model is nonlinear elastic and soil and arches assume a non-hysteretic response meaning that there are no stored effects from temporary (live load) application. This is not consistent with experimental results, which indicated significant permanent strains and deformation that were stored after backfilling and each service load.
- Tall rise backfilling strain is overpredicted by the model. This may be caused by the at-rest earth pressure coefficient: a lower earth pressure coefficient would decrease backfilling strains and displacements.
- For a tall rise arch using the experimental arches the model calculates a large difference in backfilling effects from alternate side loading versus uniform side loading. This subsequently affects all future loads applied to the structure.
- The model predicts buckling of the short rise arch under offset service loading. This did not occur experimentally. This result is consistent with steel bridge results which indicated a high foundation moment with offset load that was several times higher than experimentally measured values.
- The lack of vertical arch restraint is a contribution to the poor model predicted response of the short rise bridge to offset loading. Elements near the apex are almost entirely horizontal, which gives very small area to the horizontal soil springs. The inclusion of soil friction or vertical restraint would oppose upward deformations caused by applied live load. Experimental results indicate apex and opposite side vertical pressures are near 7 kPa (about 50% of the weight of cover) higher than

assumed in the model. Applied load in this area produces moments opposing those produced by the applied load pressure, which would help stabilize the structure.

- As with the steel bridges, pressure under the point of live load application is underpredicted by the model, which was unexpected. It was anticipated that soil internal shear (soil arching) would direct load away from the deformed arch and cause greater pressure spread than assumed by the model.
- The moment curvature relationship overpredicts cracking: compressive strains are smaller than indicated. This becomes especially significant for a real structure with different load cases instead of monotonic loading.
- Predicted capacity of isolated arches was within 5% for both span to rise geometries, therefore the capacity of the small cross-section, isolated arches was adequately predicted by the model.
- Experimental capacity with soil was more than 4 times greater per arch than isolated arch capacity. The tall CFFT bridge reached a first arch failure 5.5 times greater than an isolated arch and a total bridge capacity 7 times greater than an isolated arch.
- Ultimate capacity of the tall CFFT bridge was overpredicted by the uniform fill model by 13%, and was the only bridge (steel or CFFT) to be overpredicted by the model. Possibly this was due to an abnormally low failure strain for the center arch indicating a critical defect that reduced capacity of the entire buried structure.

CHAPTER 8. CONCLUSION

8.1. Summary

Buried composite arch bridge structural members benefit from reduced bending compared to an isolated structural member as a result of soil restraint and vehicle load propagation through the soil. Placing soil lifts also generates potential deleterious effects due to the self-weight of soil, which may be higher during the backfilling process than in the final dead load position. Prior field testing has yielded unsatisfactory results, with small strains that show evidence of excessive conservatism in design. The goal of this report is to provide data and analysis of buried CFFT bridges to close the gap between expected behavior and measured behavior in commercial CFFT bridges. An extensive laboratory testing program was designed and implemented to resolve the knowledge gap between model and experimental results by having more control over the backfilling process and load history, higher confidence in instrumentation, and better knowledge of the structural and soil properties of all components of a buried arch bridge than in prior field studies.

Bridge response was scaled in Chapter 2 to be half as large as a typical (12.2 m) buried CFFT arch bridge using the design software currently used for commercial buried CFFT bridges, with only geometric scale modifications. Two bridge span-to-rise ratios were selected (5:1 and 2.67:1) which exhibit different behavior: the short rise bridge has higher foundation thrust and the tall rise bridge has larger backfilling effects. The scaling procedure suggested a 115 mm diameter CFFT arch for both rises and a 38 mm x 102 mm steel bar for the tall rise arch and a 51 mm x 51 mm steel bar for the short rise arch. Both steel sections were selected to mimic deflection of the

CFFT bridges during apex live load and to remain elastic throughout the backfilling and live load testing.

A timber soil box was erected to contain the scaled model tests, described in Chapter 3. Each bridge was installed in the soil box, wooden decking was fastened to the arches, and soil was placed in progressive lifts on alternating sides of the arch. Each bridge was also instrumented to measure arch strains, arch deflections, and soil pressures at eight points along the span of the middle of tree arches and the outer arches were instrumented at critical locations (at the foundations and at the apex).

The soil-spring model used for bridge design was detailed and modified in Chapter 4. The soil-spring model is a nonlinear elastic material model that uses 1D Euler beam elements and 1D horizontal springs connected to arch nodes. The stiffness of arch elements is based on axial-loaded CFFT tubes in bending (Burgueño 1999) and soil-spring stiffness is based on retaining wall movement versus stiffness (Barker et al. 1991). The soil-spring model also includes construction effects: it simulates all phases of response ranging from free-standing arches acted on only by self-weight, the progressive backfilling process, and also vehicular surcharge analysis on the completed structure. Modifications to this model discussed in this report include large deformation analysis, user adjustable soil properties, and user-defined foundation properties.

The soil-continuum model for steel arches was introduced in Chapter 5. Made using Abaqus (Abaqus 2011) commercial finite element software, the soil-continuum model is a more physically consistent model than the soil-spring model and was intended to extend understanding of soil-structure interaction. The soil-continuum model relies on a customized import analysis to simulate progressive backfilling: each lift loads the deformed mesh and stored stresses from the prior analysis, plus a custom fit geometry for a new soil lift. Each lift is meshed with triangular

continuum elements to fit the curved shape of the arch. Soil material is modeled with a depth-dependent stiffness and assuming Mohr-Coulomb plasticity. Mohr-Coulomb plasticity is elastic-perfectly plastic and elements in tension (exceeding internal shear capacity based on principal stresses) dilate with zero stiffness, which requires the use of an explicit dynamic solver. The soil-continuum model was not extended to CFFT arches due to the complicated nonlinear material model used in typical CFFT arch response, which would have been very difficult to model within Abaqus.

Response predictions for the steel arches with both the soil-spring and soil-continuum model were presented in Chapter 6. Experimental results from progressive backfilling, end of backfilling, live load, and ultimate load results are all presented in this chapter. The soil-spring model predicted more accurate results for backfilling process, end of backfilling, and ultimate load. The soil-continuum model more accurately predicted moment response due to live load at all points on the span of the arches. The soil-spring model did not accurately predict moment away from the applied live load for offset load cases.

Experimental results were analyzed for foundation thrust forces. The thrust in a high span to rise arch (2.67:1) was insignificant, and foundation spread with compacted soil was minimal. For a short span to rise arch (5:1) the foundation thrusts are higher, but with the soil and compaction used in this report there was no risk of arch failure due to foundation spread throughout backfilling and during live loading. A full analysis of foundation forces showed that a base friction coefficient of 0.34 was adequate to prevent sliding: a typical cast-in-place concrete-on-soil friction coefficient is 0.6 (NAVFAC 1986).

Predictions for CFFT arches using the soil-sopring model are presented in Chapter 7. The soil-spring model was modified to both a typical alternating load case and a uniform lift case

(staggered soil elevation increase on each side of the arch versus uniform soil height on both sides of the arch). The typical staggered backfilling case does not work well for tall CFFT arches because the predicted strains are large enough to be well out of the elastic range of the material. A limitation of the material model is that it has only been used successfully for monotonic loading of isolated CFFT arches, but during load cycling the response is not accurate. As concrete cracks and bending is reduced the cracks do not close uniformly and the stiffness during unloading is stiffer than the response during loading. This is a typical hysteretic response, but it is not captured by a nonlinear elastic model.

8.2. Conclusions

Continuum modeling is impractical for design purposes. The soil continuum model presented in this report proved to be a powerful tool for predicting live load response of buried arch bridges, but the prohibitively long solution time and the limitation to 2D modeling, which does not predict dissipation of true truck wheel load patches, makes this tool impractical for commercial bridges.

Large deformation soil-spring analysis is significant for subscale arches. The large-deformation solver used in this study predicted larger moments than the typical small deformation solution, caused primarily by P-delta effects (axial load acting through deformed geometry) by as much as 50% for an offset load. While deformations are small, on the order of 50 mm under combined live load and dead load, the axial loads are high due to the high compressive stiffness of concrete and the circular cross section, which is more efficient in compression than bending. As a result, service live loading may result in p-delta moments that are 20% of the ultimate capacity of a subscale arch. Full scale arches are stiffer in bending relative to axial than the subscale arches. Therefore, the P-delta effect should be smaller in full

scale bridges, but may still be relevant and the use of large deformation analysis in routine design should be explored further.

Soil properties matter in arch design. The measured results for tall steel arches with compacted and under-compacted soil are dramatically different: apex moment due to apex live load is more than twice as high with under-compacted soil. It is clear that stiffer soil benefits arch structural capacity by improving arch restraint. The model also predicts that stiffer soil results in a stronger structure. In Chapter 4, models are compared with three different friction angles and the loosest model predicts 49% higher apex moment due to apex load than the soil used in this study. Structural capacity of the arches can be improved by using better soil and the efficiency of design can be improved if designers are confident in the friction angle and relative compaction of the soil used in construction.

Boussinesq load distribution is more dispersed than experimental results. The measured pressure under the point of live load application is consistently 50% to 100% greater than the Boussinesq distribution pressure. This experimental pressure under live load application is contrary to the governing thought on soil arching: as the substructure moves away from load, soil internal shear stress should cause the soil to form its own structure using internal shear stress to spread load over a larger area than predicted by elastic (Boussinesq) distribution. Higher load spreading was observed during ultimate load of the short bridges, but was not observed in service load tests. While less load distribution should create an unconservative result, every indication (accurate apex loading moments, conservative offset loading moments) is that the effect is not large enough to warrant a change in model formulation. Load distribution is likely not critical enough to structural response to affect results because the load is not spreading that far due to shallow soil depth. The difference in internal arch moment is analogous to a point load versus a

distributed load over perhaps 20% of the span, which produce nearly the same moment. This may help guide future research: it is unlikely that load distribution is the governing factor for soil-spring model inaccuracy. Experimental live loads have a more localized effect than assumed by the models. This would analytically increase arch moments. Arch moments are currently conservatively predicted by the soil-spring model for steel bridges, which implies additional force is applied from soil resistance that was not considered by the soil-spring model.

Higher rise arches offer significant structural benefits. This study was limited to only two global arch geometries: 5:1 and 2.67:1 span to rise. The higher rise arch exhibited higher backfilling moments, but lower live load moments and was better modeled by the soil-spring model during live load analysis and offset live load analysis. The higher rise arch has higher cover over the shoulders and exhibits lower predicted and observed moment when load is applied in that region. Furthermore, foundation thrust becomes a non-issue for a higher rise structure because the angle between the foundation and the arch is closer to vertical.

Horizontal foundation thrust is resisted by soil pressure and base shear under service live load. During backfilling, shear stress at the arch-foundation interface is directed inward (toward the center of the arch) and during live loading the base shear in the arches is small compared to the end of backfilling shear force and the change in axial force due to live load. Early in backfilling, the at-rest soil pressure behind the foundation and the shear force drive the foundation inward. As soil is applied over the apex the axial load increases at a faster rate than other forces, and this generates an outward horizontal thrust force. Experimentally, the pressure behind the foundation was between active and at-rest for a compacted soil throughout backfilling and service live load sequence (deflections were small). The model indicates a concrete-to-soil friction coefficient of 0.4 is adequate to prevent footing sliding during service loading and a

typical design base shear value of 0.6 is adequate to prevent sliding in a 5:1 span to rise arch during any loads observed in this experiment. The actual friction coefficient in the experiment was intended to be lower than in a typical bridge: plastic was placed under the foundations to reduce friction instead of a soil base. Experimentally, the foundations began sliding during the ultimate load test, but only at a force that was three times a service level load. Foundations never reached fully passive pressure, and experimentally were below a horizontal pressure coefficient of 2. Passive pressure coefficient for this soil was close to 6. Foundation movements became high, therefore the soil behind the foundations was looser than predicted by the model. It is not appropriate to design bridges with full passive resistance at the foundation. The required foundation movement for full passive resistance is larger than the movements measured at ultimate load. Foundation movements of that magnitude will affect arch moment, and it is not appropriate to consider passive soil resistance with a fixed or pinned model. Foundations should be modeled to allow sliding if passive foundation resistance is required.

The soil-spring model does not accurately capture moments away from load application, but this is typically unimportant. The soil-spring model does a good job in all live load cases of predicting the peak positive moment. The moment at other locations is more poorly predicted. This is caused by a combination of inaccurately modeled arch restraint and a lack of modeled plasticity in the soil. In general, these moments are not important for design because they are considerably lower than the peak positive moment. The truck can be positioned in such a way that the peak positive moment can be maximized at any location along the span. The exception was short rise bridge foundation negative moment caused by a 60% offset, which is predicted to be 80% of the peak positive moment, but experimentally was close to zero. As foundation negative moment is a controlling design parameter, there is justification for improving the soil-

spring model's ability to better predict this result. More research is needed to find a justifiable approach to this problem. The continuum model is much more accurate for predicting arch moments due to offset loads, and underpredicts the foundation moment due to offset live load in a short rise bridge. This may be a deceptive result: the continuum model poorly predicts foundation moments during backfilling. The backfilling foundation moment predicted by the soil-continuum model was above the yield moment. Additional curvature would cause less moment because the arch is already yielded.

Foundation moments are overpredicted by the model during backfilling. The highest predicted moment in the structure is at the foundation when the soil elevation is near the apex of the arches. Experimental results agree with the model as to location and stage of construction with peak moment. However, predicted values are 60% higher for the soil-spring model than experimental values, but, at the end of backfilling there is good agreement. Thus, the spike predicted by the model was overpredicted compared to experimental results and backfilling moments were smaller than anticipated.

Total moment of vehicles exceeding past applied load can be predicted. The total moment and strain during ultimate apex load was well predicted by the soil-spring models once the applied load exceeded the maximum previously applied load. Previously applied loads deform the arches, and store soil stresses in the arch system. This changes the base point for future loads and creates a different initial stress state than at the end of backfilling (first apex load). This proves that load sequencing, which changes the initial condition of the arches, does not greatly affect how the arches respond to a new heavier load. This increases confidence in the model predictions for permit load rating for heavy trucks that exceed HL-93 design loads.

8.3. Future Work

Future work can be broadly divided into two topics: improvement to the testing program, which is unlikely to ever be repeated, and improvement to the models, mostly the design-oriented soil-spring model.

8.3.1. Future Testing Improvements

In future testing it is important to keep the backfilling process streamlined such that effort can be placed on speed of construction and on consistency. Moving platforms, installing through rods, and burying TPCs all cause added steps and confusion and lead to less accuracy in current soil elevation. But these processes were necessary and would need to be utilized in future testing. Improvement to the test could come in the form of simplifying quality control. This includes running the data acquisition unit for a full day instead of stopping between tests, which was implemented by the second bridge, and using a triggering mechanism to determine lifts, instead of determining lifts from post-processing of soil pressure data.

The biggest possible improvement to the testing procedure would have been to improve the boundary conditions of the test. The plastic under the foundations was compressible and causes a discrepancy between the soil-continuum model, the soil-spring model, and the experimental results. Greased sheet steel would have provided at least as low of a coefficient of friction and would have had the advantage of being relatively incompressible under the test loads. The side wall friction was a major obstacle that was not satisfactorily solved during testing. It may have contributed to the irregular failure pattern of the short CFFT arches, and it may have contributed to larger reductions in apex moment for the tall rise bridges at the end of backfilling than predicted by either model. Correcting this problem would not be trivial. First, the 4x4 timbers should have been planed to a uniform thickness (used 4SS 4x4 boards instead of rough sawn 4x4

timbers). Second, the plastic sheathing placed over the timber was inadequate for its task. The plastic should have been replaced with a more rigid sheathing such as sheet metal or even thicker plywood. Third, using two layers of sheathing was unsuccessful because soil slipped between the layers during backfilling. Instead, a single layer of sheathing should have been used. The decking should have been connected to mechanical rollers below the soil elevation that reacted on the wall sheathing. The small gap between the sheathing and the decking should have been bridged by thin sheeting plastic, as it was after the first bridge.

8.3.2. Future Analysis Improvements

There is still meaningful future work to be conducted with soil-spring and soil-continuum modeling. The soil-continuum modeling overpredicts foundation moments during backfilling and there is no obvious reason why this occurs. Possibly the issue is related to foundation stiffness, but the model becomes prohibitively slow if realistic materials are placed between the concrete foundation and the concrete floor. Another possible piece of future work would be to adapt the nonlinear moment-curvature model for the CFFT bridges to Abaqus for use with the continuum model.

More important future work would be improvements to the design soil-spring model. A failing in the model is the inability to accurately predict offset load moment response. While there is no single reason for this failing, because vertical loads are spread more in the model than in reality, the higher model moments compared to measured moments are likely caused by inadequate arch confinement. To review results, the tall arch overpredicts backfilling apex moments by 30%, but the short arch moments are accurately predicted (within 5%) during backfilling. The apex live load moment response is well predicted for both bridges (within 10% of the mean measured capacity for both briges). The offset load moment response is acceptable

for the tall rise bridge. The 40% offset positive moment is predicted within 10%, and offset foundation moments are predicted to be small, which agrees with measured values. The foundation negative moment for the short bridge was overpredicted by 300% of the predicted foundation moment, or by 60% of the peak positive moment.

While it is generally better to predict conservative results, there are possible ways to improve model accuracy. The tall bridge backfilling response is likely driven by the horizontal pressure coefficient. The shape of the tall bridge, with long, close to vertical legs, makes at-rest horizontal pressure an important contributor to moment in the structure, and having too stiff of a response may be causing the elevated backfilling load effects. This parameter is less critical for a short rise bridge because there is less vertical area along the legs to be driven by the applied soil lifts.

When passive movement (outward) is limited to portions of the arch with large vertical areas the model accurately predicts response, such as backfilling and apex load. During offset loading, when the passive movement (outward) occurs near the apex, the tall bridge more accurate predicts moment while the short bridge is inaccurate. Likely this is because the tall bridge has more vertical area above the shoulders and soil-spring modeled forces are higher with smaller pressures. Inadequate confinement near the apex is fairly observable throughout modeled results: horizontal and vertical deflection near the apex for offset loads, when the arch is moving into the soil at the apex, is overpredicted, yet the model predicts unrealistically high horizontal pressures, with a K near the apex that exceeds 5 at some nodes during service live loading. No measured horizontal pressures are near this value. Additional force is experimentally being applied that prevents the arch from developing the required deflection to become fully passive, and this is not captured b the soil-spring model. This likely comes from vertical soil confinement and arch-soil frictional shear.

To correct this problem, the analysis must consider vertical confinement and/or horizontal shear confinement. The arch elements near the arch apex are nearly horizontal, and with the current model formulation (based on a vertical retaining wall analysis), the tributary area for a soil spring is small. Shear stress acts over the element horizontal projection (large near the apex) instead of the element vertical projection (small near the apex), and the vertical normal stress also acts over the horizontal projection. Inclusion of both vertical confinement and arch-soil friction should improve model accuracy. Also, angled soil springs would include horizontal and vertical area and thus would increase soil stiffness near the apex and should improve model accuracy. This is the necessary next improvement to the modeling procedure, and the results obtained during this testing procedure could serve as a validation benchmark for those model improvements.

BIBLIOGRAPHY

AASHTO. (2012). *LRFD guide specification for design of concrete-filled FRP tubes, 1st ed.,* AASHTO, Washington D.C.

AASHTO. (2014). *LRFD Bridge design specifications*, 7th Ed., AASHTO, Washington D.C.

ABAQUS, (2011) 'ABAQUS Documentation', Dassault Systèmes, Providence, RI, USA.

APA (1998). *Plywood design specifications*. Engineered Wood Association, Tacoma, WA.

American Wood Council. (2005). *National Design Specification: Design Values for Wood Construction*. American Forest & Paper Association, Washington, D.C.

ASTM Standard A370, (2014), "Standard test method and definitions for mechanical testing of steel products." ASTM International, West Conshohocken, PA, DOI:10.1520/A0370-14.

ASTM Standard D422-63, (2007), "Standard test method for particle-size analysis of soils." ASTM International, West Conshohocken, PA, DOI:10.1520/D0422-63.

ASTM Standard D698-07, (2007), "Standard test methods for laboratory compaction characteristics of soil using standard effort." ASTM International, West Conshohocken, PA, DOI:10.1520/D0698-07E01.

ASTM Standard D1556-07, (2007), "Standard test method for density and unit weight of soil in place by sand-cone method." ASTM International, West Conshohocken, PA, DOI:10.1520/D1556-07.

ASTM Standard D1557-12, (2012), "Standard test methods for laboratory compaction characteristics of soil using modified effort." ASTM International, West Conshohocken, PA.

ASTM Standard D2216-10, (2010), "Standard test methods for laboratory determination of water (moisture) content of soil and rock by mass." ASTM International, West Conshohocken, PA.

ASTM Standard D3039, (2008), "ASTM D 3039: Standard test method for tensile properties of polymer matrix composite materials." ASTM International, West Conshohocken, PA.

ASTM Standard D3080-11, (2011), "Standard test methods for direct shear test of soils under consolidated drained conditions." ASTM International, West Conshohocken, PA.

Ates, S., Constantinou, M. C. (2011). "Example of application of response spectrum analyses for seismically isolated curved bridges including soil-foundation effects." *Soil Dynamics and Earthquake Engineering*, 31, 648-661.

Bannon, D. (2009). Characterization of concrete-filled fiber reinforced polymer arch members. (Masters thesis, University of Maine, 2009).

Barker, R.M., Duncan, J.M., Rojiani, K.B., Ooi, P.S.K., Tan, C.K., Kim, S.G. (1991). "*NCHRP 343: Manuals for the design of bridge foundations*." Transportation Research Board, Washington D.C.

Bayoglu Flener, E. (2009). "Response of long-span box type soil-steel composite structures during ultimate loading tests." *Journal of Bridge Engineering*, 14, 496-506.

Bayoglu Flener, E. (2010a). "Soil-steel interaction of long-span box culverts – performance during backfilling." *Journal of Geotechnical and Geoenvironmental Engineering*, 823-832.

Bayoglu Flener, E. (2010b). "Testing the response of box-type soil-steel structures under static service loads." *Journal of Bridge Engineering*, 15, 90-97.

Beben, D. (2013). "Field performance of corrugated steel plated road culvert under normal live-load conditions." *Journal of Performance of Constructed Facilities*, 27, 807-817.

Burgueño, R. (1999). System characterization and design of modular fiber reinforced polymer (FRP) short- and medium-span bridges. (Doctoral dissertation, University of California, San Diego, 1999) (UMI No. 9928617).

Chen, J. T., Farouz, E., Landers, P. (2010) "Development of project specific p-y curves for drilled shaft retaining wall design." Earth Retention Conference 3. 162-169.

Chung, J., Patil, A., Bollmann, H. (2011). *FB-Multipier API soil Model Validation.* Bridge Software Institute, Gainesville, FL.

Clapp, J.D. and Davids, W.G. (2011). "Simplified Modeling to Assess Soil-Structure Interaction." AEWC Report No. 11-30.

Clough, G.W., Duncan, J.M. (1990). "Earth pressures." *Foundation Engineering Handbook*, 2nd ed., editor: Fang H.S., Van Nostrand Reinhold, Norwell MA, 224-235.

Cox, B. N. and Dadkhah M. S. (1995). The macroscopic elasticity of 3D woven composites. *Journal of Composite Materials*, 29, 785-819.

Crisfield, M.A. (1991). Non-linear finite element analysis of solids and structures, volume 1, Wiley, Chichester.

Dagher, H.J., Bannon D.J., Davids, W.G., Lopez-Anido, R.A., Nagy, E., Goslin, K. (2012). "Bending behavior of concrete-filled tubular FRP arches for bridge structures." *Construction and Building Materials*, 37, 432-439.

Daniel, I. M. and Ishai, O. (2006). Engineering mechanics of composite materials, 2nd Edition. Oxford, NY.: Oxford University Press.

Davids, W.G., Walton, H.J., Clapp, J.D., Lopez-Anido, R., Goslin, K. and Dagher, H.J. (2012). "Response of Concrete-Filled Tubular FRP Arches to Construction-Induced Loading." *Proceedings of the 2012 International Bridge Conference*, Pittsburgh, PA, June 2012.

Demkowicz, M. (2011). "Environmental Durability of Hybrid Braided Polymer Matrix Composites for Infrastructure Applications." MS Thesis, Department of Civil and Environmental Engineering, University of Maine.

Drnevich, V.P., Evans, A.C., Prochaska, A.B. (2007). "A study of effective soil compaction control of granular soils." *Publication FHWA/IN/JTRP-2007/12*. Joint transportation research program, Indiana Department of Transportation and Purdue University, West Lafayette, Indiana.

Duncan, J.M., Byrne, P.M., Wong, K.S., Mabry, P.. (1980). "Strength, Stress-Strain and Bulk Modulus Parameters for Finite Element Analysis of Stress and Movements in Soil Masses," Report No. UCB/GT/80-01, University of California, Berkeley, Berkeley, CA.

El-Chiti, I. (2004). FRP-concrete arch. (Masters thesis, University of Maine, 2009).

Elshimi, T.M., Brachman, R.W.I., Moore, I.D. (2014). "Effect of truck position and multiple truck loading on response of long-span metal culverts." *Canadian Geotechnical Journal*, 51, 196-207.

Gerolymos, N. and Gazetas, G. (2006). "Development of Winkler model for static and dynamic response of caisson foundations with soil and interface nonlinearities." *Soil Dynamics and Earthquake Engineering*, 26, 363-376.

Goslin, K. Davids, W., Lopez-Anido, R., Walton, H., Clapp, J. (2015). "Technical Report 15-01, Bridge-in-a-Backpack Task 4: Monitoring and Load Rating." ME DOT report No. 15-01.

Greimann, L.F., Yang, P-S., Wolde-Tinsae, A.M., (1986). "Nonlinear Analysis of Integral Abutment Bridges." *J. Struct. Eng.*, 5(1), 1-10.

Holtz, R.D., Kovacs, W.D. (1981) *An Introduction to Geotechnical Engineering*, Prentice Hall, Upper Saddle River, New Jersey.

Jeong, S., Seo, D. (2004). "Analysis of tieback walls using proposed P-y curves for coupled soil springs." *Computers and Geotechnics*, 31, 443-456.

Kang, J., Parker, F., Yoo, C.H., (2008). “Soil-structure interaction for deeply buried corrugated steel pipes Part I: Embankment installation.” *Engineering Structures*, 30, 384-392.

Katona, M.G. (2015). ‘CANDE-2015 Culvert analysis and design user manual and guideline', Developed Under NCHRP 15-28, Gig Harbor, WA, USA.

Lehane, B.M., Keogh, D.L., O’Brien, E.J. (1999). “Simplified elastic model for restraining effects of backfill soil on integral bridges.” *Computers and Structures*, 73, 303-313.

Machelski, C., Michalski, J.B., Janusz L. (2009). “Deformation factors of buried corrugated structures.” *Transportation Reseaarch Record*, 2116, 70-75.

Mak, A.C., Brachman, R.W.I., Moore, I.D. (2009). “Measured response of a deeply corrugated box culvert to three-dimensional surface loads.” In *Proceedings of the Transportation Research Board Annual Conference*, Washington D.C.

Maine Department of Transportation. (2003). *Bridge Design Guide*. Maine Department of Transportation, Augusta, ME.

Mander, J.B., Priestley, M. J.N., Park R., (1988). "Theoretical stress strain model for confined concrete" ASCE Journal of Structural Engineering 114, 1804-1826.

MATLAB (2011), *MATLAB R2011b 7.13.0.564*, The MathWorks Inc., Natick, Massachusetts.

McCavour, T.C., Byrne, P.M., Morrison, T.D. (1998). “Long-span reinforced steel box culverts.” *Transportation Research Record*, 1624, 184-195.

Moore, I.D. and Taleb, B. (1999). “Metal culvert response to live loading: performance of three-dimensional analysis.” *Transportation Research Record*, 1656, 25-36.

Morrison T.D. (2000). “Long-span deep-corrugated structural plate arches with encased-concrete composite ribs.” *Transportation Research Record*, 1736, 81-93.

NAVFAC (1986), *DM 7.02 Foundations and Earth Structures*, Naval Facilities Engineering Command, Alexandria, Virginia.

Oettl, G., Stark, R.F., Hofstetter, G. (1998). “A comparison of elastic-plastic soil models for 2D FE analyses of tunneling.” *Computers and Geotechnics*, 23, 19-38.

Parry, H. (2013). “Splicing and Local Reinforcement of Concrete Filled FRP Tubes (CFFTs).” MS Thesis, Department of Civil and Environmental Engineering, University of Maine.

Petersen, D.L., Nelson, C.R., Li, G., McGrath, T.J., Kitane, Y. (2010). "*NCHRP 647: Recommended design specifications for live load distribution of buried structures*. Transportation Research Board, Washington DC.

Quinn, B.H., Civjan, S.A., Lahovich, A., Brena, S.F., Elnahal, S. (2013). "Monitoring of the first 'bridge-in-a-backpack' bridge in Massachusetts." Paper presented at *TRB 2013 Annual Meeting,* Washington D.C.

Reese L. C. and Wang S.T. (2006). "Verification of computer program *LPILE* as a valid tool for design of a single pile under lateral loading." www.ensoftinc.com.

Selig, E.T. (1988). "Soil Parameters for Design of Buried Pipelines." *Pipeline Infrastructure,* B. A. Bennett, Ed., ASCE, New York, NY, 99-116.

Sezen, H., Yeau, K.Y., Fox, P.J. (2008). "In-site load testing of corrugated steel pipe-arch culverts." *Journal of Performance of Constructed Facilities*, 22, 245-252.

SoilStructure.com (2013). Lateral Foundation v2.0 Software.

Taleb, B. and Moore, I.D. (1999). "Metal culvert response to earth loading: performance of two-dimensional analysis." *Transportation Research Record,* 1656, 25-36.

Tomblin, J. (2006). Buried frp-concete arches. (Masters thesis, University of Maine, 2006).

Vaslestad, J., Madaj, A., Janusz, L. (2002). "Field measurement of long-span corrugated steel culvert replacing corroded concrete bridge." *Transportation Research Record,* 1814, 164-170.

Walton, H.J. (2011). Response of FRP arches to concrete filling loads. (Masters thesis, University of Maine, 2011).

Wang, S.T. and Arrellaga, J. A. (2007). "Verification of computer program PYWALL as a valid tool for design of flexible retaining walls." www.ensoftinc.com.

Webb, M.C., Selig, E.T., Sussman, J.A., McGrath, T.J. (1999). "Field tests of a large-span metal culvert." *Transportation Research Record,* 1656, 14-24.

Yeau, K.Y., Sezen, H., and Fox, P.J. (2009). "Load perforce of in-situ corrugated steel highway culverts." *Journal of Performance of Constructed Facilities*, 23, 32-39.

BIOGRAPHY OF THE AUTHOR

Harold Joseph Walton was born in Portland, Maine on August 31, 1985. The son of William and Patty Jo Walton, Harold grew up in Portland and graduated from Deering High School in 2004. Harold enrolled at the University of Maine, fall, 2004 and earned a B.S. in Civil Engineering, May, 2008. Harold returned to the University of Maine for graduate studies in 2009 and earned a M.S. in Civil Engineering in August 2011. He is a candidate for the Doctor of Philosophy degree in Civil Engineering from the University of Maine in December 2015.